PACIFIC EARTHQUAKE ENGINEERING
RESEARCH CENTER

Nonlinear Analysis of a Soil-Drilled Pier System under Static and Dynamic Axial Loading

Gang Wang

and

Nicholas Sitar

University of California, Berkeley

PEER 2006/06
NOVEMBER 2006

Nonlinear Analysis of a Soil-Drilled Pier System under Static and Dynamic Axial Loading

Gang Wang and **Nicholas Sitar**
Department of Civil and Environmental Engineering
University of California, Berkeley

PEER Report 2006/06
Pacific Earthquake Engineering Research Center
College of Engineering
University of California, Berkeley

November 2006

ABSTRACT

Realistic time history simulation of a soil-drilled pier system under static and dynamic loading is essential for the development of effective performance-based earthquake design of deep foundations. Due to the nonlinear transient nature of the system and high computational requirements, to date the application of nonlinear finite element analyses to this problem has been limited. Thus, an important aspect of numerical modeling is a soil model that is simple enough to be computationally efficient yet able to capture the cyclic stress-strain behavior. In particular, it is essential to account for the modulus degradation and energy-dissipation characteristics during cyclic loading, which depend on the rate of loading and soil properties. In this study, a multi-axial cyclic bounding surface plasticity model proposed by Borja and Amies (1994) was developed in a general finite element framework called OpenSees. The model requires a minimal number of parameters that can be easily obtained through conventional site investigations. The stress point algorithm of this model is formulated in detail for finite element implementation. It is shown that the model can reasonably capture modulus degradation and hysteretic damping of nonlinear soil, and it is suitable for fully nonlinear analysis of soil-structure interaction as well as site-specific response analysis. The model is used to study load-displacement-capacity characteristics of an axially loaded soil-pier system at small and large strains by simulating a set of in-situ static and dynamic axial load tests on drilled piers performed at UC Berkeley. The numerical results are in excellent agreement with the field data and show that fully coupled nonlinear soil-structure interaction analyses can be successfully performed.

ACKNOWLEDGEMENTS

The PLT and static pier load tests were performed by American Piledriving, Inc. (API) of Pleasanton, California, under the direction of Dr. Gyimah Kasali of Rutherford & Chekene Consulting Engineers. His cooperation and support are gratefully acknowledged.

FISO Technologies of Canada fabricated the optical strain bars based on parameters provided by Lymon C. Reese and Associates, and the electrical strain bars were custom-built by Lymon C. Reese and Associates, who also monitored all the tests. An automated electronic data acquisition system was provided on loan by FISO. The authors also appreciate the support and advice of Craig Comartin of Comartin Associates, UC Berkeley Capital Projects group, and FISO Technologies throughout the test program.

The financial support for the test program was provided by UC Berkeley Capital Projects and the research was supported by a grant from Pacific Earthquake Engineering Research (PEER) Center under the NSF Award No. EEC-9701568.

Any opinions, findings, and conclusions or recommendations expressed in this material are those of the authors and do not necessarily reflect those of the National Science Foundation.

CONTENTS

LIST OF FIGURES

LIST OF TABLES

1 Introduction

1.1 OBJECTIVES

Use of pile/pier foundations as an economical means of transmitting the weight of structures down to the competent underlying soil strata can be traced back to prehistoric times. In China, there are numerous examples of timber piling supporting bridge foundations as early as THE Han Dynasty (202 BC - 220 AD). In Europe, remnants of timber pile foundations can be dated back to the Roman empire (Tomlinson, 1994). Today, timber has largely been replaced by newer construction materials like concrete, reinforced concrete, and steel. Pile foundations are also widely used in supporting transmission lines, bridges, buildings, and offshore platforms for gas and petroleum production.

Tomlinson (1994) in the preface of his monograph *Pile Design and Construction Practice* acclaims the use of pile in foundations as both an art and a science. The art is manifested for example in the selection of suitable pile types, configurations (length, diameter, spacing etc.) and method of installation for the proposed site conditions and loading conditions. Science enables prediction of the pile behavior, notably deflection and capacity, under specified design condition.

For many years, the science part of pile foundation design was mainly based on a combination of empiricism and experience, as the attempt at a realistic simulation is often deemed as *out of place* in view of complications arising from various uncertainties in pile installation and soil properties etc. Such a pessimistic attitude is best exemplified by the following remarks by Terzaghi (1943):

> *Because of the wide variety of soil conditions encountered in practice, any attempt to establish rules for the design of pile foundations necessarily involves radical simplifications, and the rules themselves are useful only as guides to judgement.*

For the same reason, theoretical refinements in dealing with pile problems, such as attempts to compute the distribution of load among the piles in a group by means of the theory of elasticity, are completely out of place and can be safely ignored.

Nevertheless, tremendous advancement has been made over the past half century in improving the understanding of a soil-pile/pier system and soil-pile/pier interaction. The effort branches largely into two general categories: One is based on experimental investigations including well-controlled model pile tests in the laboratory and well-explored in-situ pile tests in the field. The other is based on various analytical, numerical linear and nonlinear methods built on the strength of the fast-evolving computing technology and numerical modeling capacity.

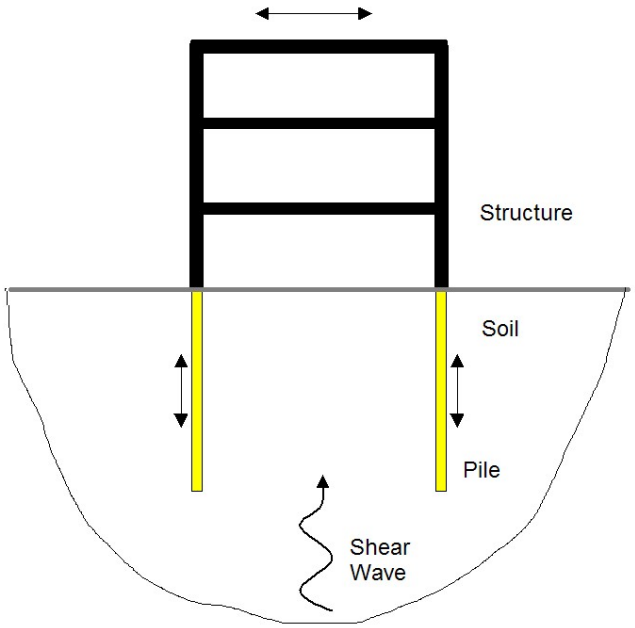

Fig. 1.1 System of Foundation-Soil-Structure Interaction (FSSI)

In the present study, the emphasis is on dynamic soil-pile/pier interaction. Among the many factors that influence the dynamic soil-pile-structure system, the system response is principally determined by structure stiffness, foundation stiffness, and energy-dissipation characteristics of the individual components. The foundation stiffness further relies on the loading characteristics, the soil properties (type, stress history, strain rate effect, and cyclic

degradation), pile properties (stiffness, geometry, and material), and pile installation methods. The energy dissipation comprises hysteretic damping due to internal friction of granular soils, viscous damping that depends on the velocity, and radiation damping that dissipates energy into the outer infinite domain.

In the past, much effort has been devoted to the study of the lateral response of soil-pile systems, but very few studies have addressed the axial behavior. Although seismic loads are usually viewed as being primarily horizontal, the action on the pile, when the interaction of the superstructure is involved, has a significant vertical component. As schematically illustrated in Fig. 1.1, vertically propagated shear waves during an earthquake cause rocking of the structure, which subsequently induces vertical up-and-down axial movement of piles. More importantly, the earthquake loading rate is about three orders of magnitude greater than the rate for which the static pile capacity is based. Thus, for earthquake design of pile foundations, proper consideration of dynamic effects may have important economic and safety implications (Kraft *et al.*, 1981). Such consideration is also critical in the design of oil platforms which are usually subjected to wave and storm loads.

The objective of this study was to investigate the behavior of the vertically loaded pile soil system. In particular, we examined the dynamic and static stiffness of the system, the nonlinear characteristics, and energy dissipation based on field pile load tests, and dealt with the challenges in the numerical modeling. The report is organized as follows: Chapter 1 and Chapter 2 provide a brief review of the state-of-the-practice design and state-of-the-art research on axially loaded piles, with a special focus on nonlinear axial behavior. Chapter 3 formulates the bounding surface plasticity model and its algorithmic implementation in the finite element framework. Chapter 4 documents a series of in-situ dynamic and static pile load tests recently performed at the University of California, Berkeley, campus. The response character of the pile in term of system stiffness, dynamic capacity, and accumulated displacements are analyzed, and the degradation after cyclic loading are also discussed. Chapter 5 presents the nonlinear finite element analysis of a single pile and the results are compared with the pile load tests. Chapter 6 provides conclusions including recommendations and suggestions for further research.

1.2 REVIEW OF FACTORS CONTROLLING AXIAL PILE PERFORMANCE

1.2.1 Effects of Pile Installation

Depending on the installation method, most piles could be classified as either non-displacement piles or displacement piles. Non-displacement piles are usually grout or cast concrete in pre-bored holes, and the disturbance to in-situ soil properties and stress state can be minimized to a certain extent. In contrast, displacement piles are inserted into the ground by displacing soils through hammer driving or jacking, and the process can significantly affect the soil-pile interface properties. Hence the installation method should be carefully chosen in the design phase, since it has great influence on the pile performance.

The effects of pile driving in clays, according to de Mello (1969) as cited in Poulos and Davis (1980), should take into account the following factors: (a) remolding or partial structural alternation of the soil surrounding the pile; (b) alternation of the stress state in the soil in the vicinity of the pile; (c) dissipation of the excess pore pressures developed around the pile; and (d) long-term phenomena of strength-regain in the soil. In addition, under continued large displacement during driving, strength reduction of softening soil may also be expected (Murff, 1980), and some reduction in capacity may be warranted to take into account the degradation of shaft friction. In general, the unit skin friction should not exceed the unconfined compression (UC) strength of cohesive soil in accordance with the ASTM D-2166-63T method. For detailed discussions and field measurements of the pile-driving effects in clays, one can also refer to Kraft *et al.* (1981), Randolph and Murphy (1985), Pestana *et al.* (2002), and Hunt *et al.* (2002).

In cohesionless soils, the effect of pile driving is mainly reflected in the change in the relative density and hence the friction angle of the soil. While loose soil below the pile tip is usually compacted by displacement and vibration, resulting in increased capacity, the soil in the immediate vicinity of the sides above the tip decreases in density and develops tensile strains. The pattern of displacements and strains around driven pile was investigated by Robinsky and Morrison (1964) in a series of model-pile tests in sand. Methods to estimate the extent of change in density and friction angle of soils around the driven pile in sand have been proposed by Meyerhof (1959) and Kishida (1967).

1.2.2 Loading Rate Effects

Rate-dependent soil response was first explored in the pioneering work of Taylor (1942) related to the study of secondary consolidation of soils. Although clay skeletons have been observed to obey non-linear viscous law, linear viscous law was used in the analysis due to its mathematical simplicity. Linear viscous damping was also used in the original work of Smith (1960) for numerical computation of pile driving by the wave equation, where the soil resistance from the damping was assumed to be proportional to the instantaneous velocity of the pile. [1]

However, the nonlinear nature of the viscosity of the soil at fast rates of deformation has been repeatedly observed in laboratory tests. Based on reviewing viscosity laws used by various researchers under different test conditions, Litkouhi and Poskitt (1980) conducted experiments to measure the point and side damping constants for small model piles driven at constant velocity into samples of soil, and they confirmed that a power law of the form

$$R_D = R_S(1 + JV^N) \tag{1.1}$$

fits many soil types over the range of velocities encountered during most pile-driving operations in their experiments, where R_D and R_S are dynamic and static soil resistance, respectively. V is the loading velocity, and J and N are factors depending on the nature of soil. Litkouhi and Poskitt (1980) as well as Randolph and Deeks (1992) also recommended $N \approx 0.2$ for both point and side resistances, and, J ranges from 0.1 for sand to 1.0 for clay. Their test data are summarized in Fig. 1.2. Eq.(1.1) is also analogous to the formula proposed earlier by Coyle and Gibson (1970). A similar formula was also suggested by El Naggar and Novak (1994b) to relate the dynamic ultimate soil resistance to the ultimate soil resistance at a reference velocity.

Accordingly, the axial pile capacity can significantly increase with the loading rate. In Fig. 1.3, Audibert and Dover (1982) compiled field pile load tests at varying loading rate conducted in clay sites from Kraft *et al.* (1981), Dubose (1955), Seed and Reese (1955), Ginzburg (1973), Goncharov (1966), Bea and Doyle (1975), Fuller and Hoy (1970) and others. Although a large amount of scatter can be noted in the figure, the ratio of ultimate

[1] To take into account the fact that soil under the pile tip is displaced very rapidly as the pile is driven downward, bigger damping constant is suggested for resistance at the pile tip than along the side. Damping constant is assumed to be 0.15 for the resistance at the pile tip and 0.05 along the side in Smith (1960).

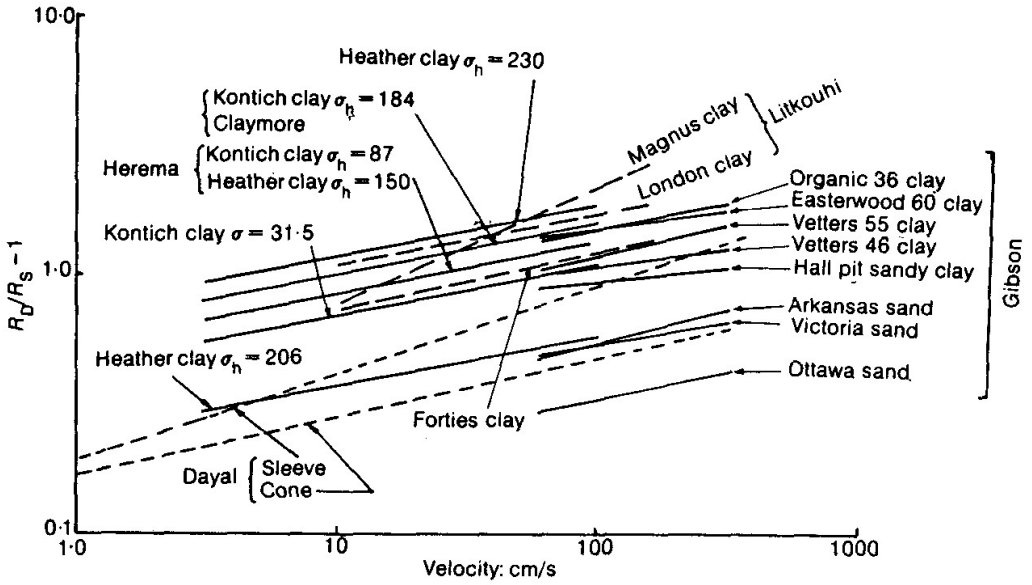

Fig. 1.2. Nonlinear Viscous Resistance of Soil, from Litkouhi and Poskitt (1980)

dynamic capacity to the static capacity shows a definite trend with increased loading rate. In the range corresponding to wave and earthquake forces, the ultimate axial capacity of a pile increases by 20% – 80%. Interestingly, the loading rate effect obtained from pile load tests is in general agreement with that from laboratory triaxial tests on soil samples. Fig. 1.4 overlays the increase of the dynamic axial capacity of the pile and the increase of the undrained shear strength of soil samples, in which their general trends show great similarity. It is also worth pointing out that in these figures, the rate of loading is expressed as a percentage of the static ultimate capacity of the pile per unit of time to allow for comparison between piles of differing size and capacity.

1.2.3 Cyclic Loading Effects

In general, cyclic loads tend to counteract rate effects such that capacity and stiffness degrade with repeated loading cycles. An idealized cyclic response curve is illustrated in Fig. 1.5, in which the cyclic behavior is bounded by the corresponding static stress-strain curve. To facilitate quantitative analysis, several parameters need to be defined first as follows: The cyclic ratios, R_1 and R_2, are used to describe the normalized cyclic amplitude and the

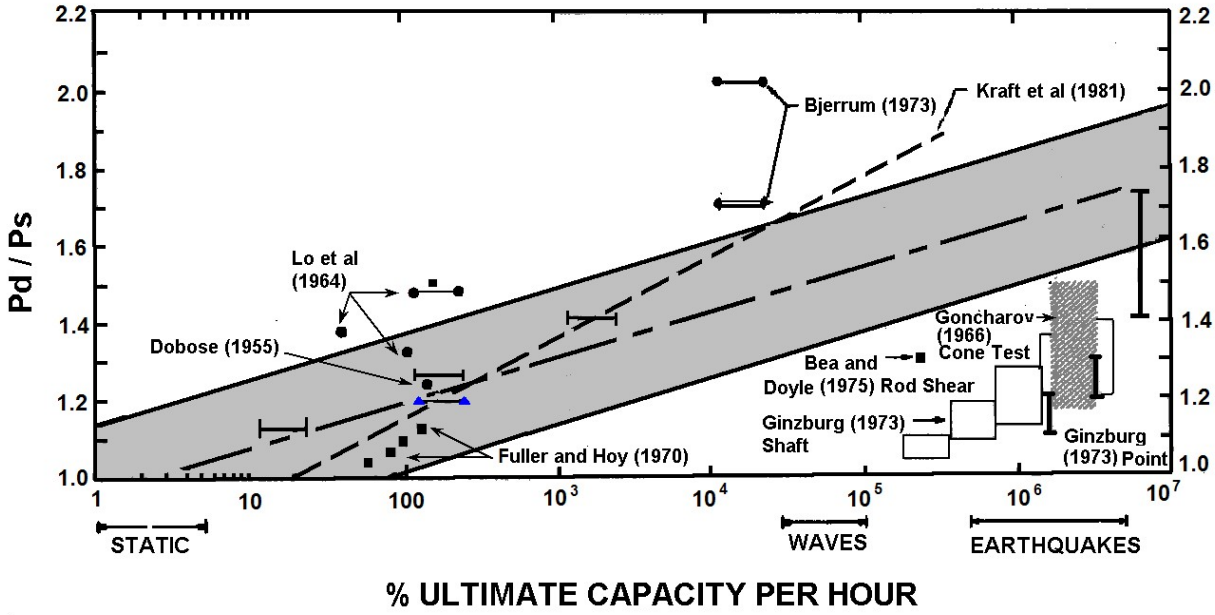

Fig. 1.3. Rate of Loading Effects on Axial Pile Capacity, from Audibert and Dover (1982)

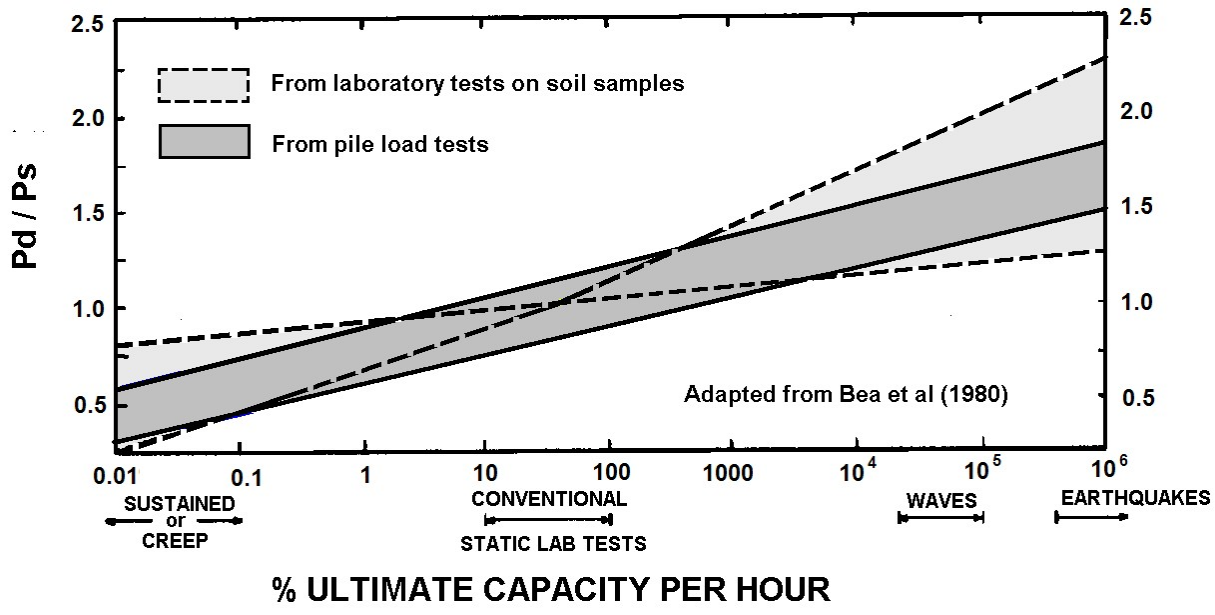

Fig. 1.4. Rate of Loading Effects on Soil Samples, from Audibert and Dover (1982)

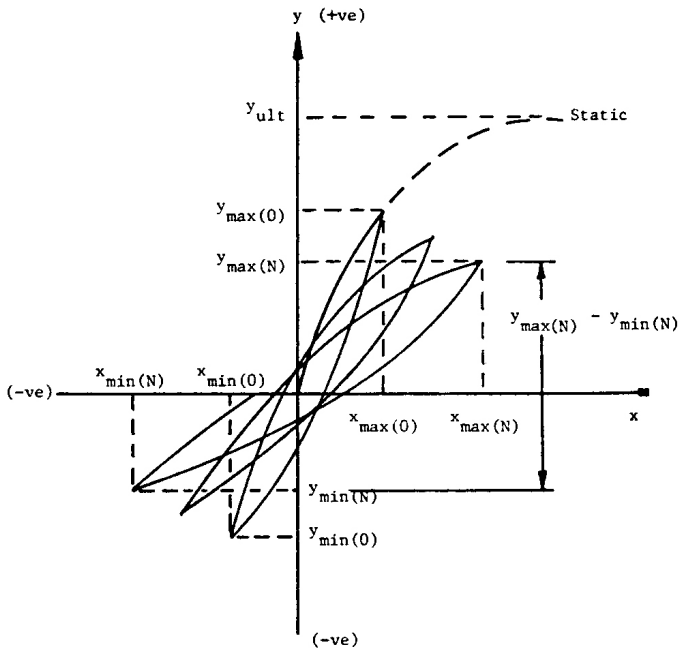

Fig. 1.5 Definition of Cyclic Parameters, from Briaud and Fellio (1986)

normalized mean cyclic stress

$$R_1 = \frac{y_{max(0)} - y_{min(0)}}{2y_{ult}} \tag{1.2}$$

$$R_2 = \frac{y_{max(0)} + y_{min(0)}}{2y_{ult}} \tag{1.3}$$

with parameters defined in Fig. 1.5. Thus, $R_1 + R_2$ specifies the ratio of the peak cyclic stress over the ultimate static capacity. In general, a higher cyclic stress level leads to more severe cyclic degradation. Hence a threshold value $(R_1 + R_2)_t$ can be defined, below which some degradation of the soil or the soil-pile interface may occur but increasing the number cycles does not produce excessive damage or failure. Above the "threshold", failure of the soil or soil-pile system would be expected. For each cycle N, secant stiffness $G_{S(N)}$ and cyclic stiffness $G_{C(N)}$ are defined as

$$G_{S(N)} = \frac{y_{max(N)}}{x_{max(N)}} \tag{1.4}$$

$$G_{C(N)} = \frac{y_{max(N)} - y_{min(N)}}{x_{max(N)} - x_{min(N)}} \tag{1.5}$$

To quantify the stiffness degradation during cyclic tests, the secant stiffness degradation parameter β and the cyclic stiffness degradation parameter δ are used to compare the quantities

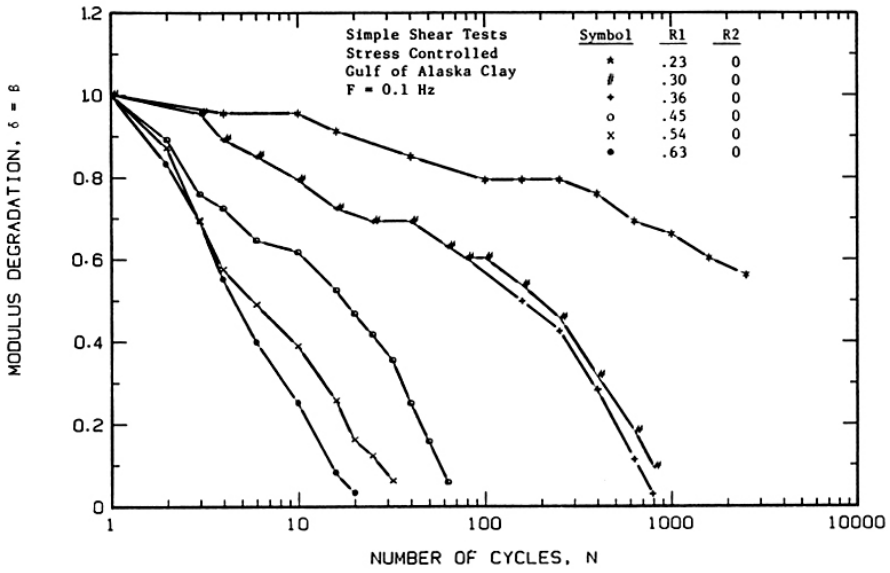

Fig. 1.6. Modulus Degradation Curves for Gulf of Alaska Clay, from Briaud and Fellio (1986), whose data were compiled from Floess (1979)

in cycle number N and the first loading by

$$\beta = \frac{G_{S(N)}}{G_{S(0)}} \tag{1.6}$$

$$\delta = \frac{G_{C(N)}}{G_{C(0)}} \tag{1.7}$$

The following power law is usually adopted to quantify the rate of degradation with cycle number N,

$$\beta = N^{-a} \tag{1.8}$$

$$\delta = N^{-b} \tag{1.9}$$

Eqs. (1.8) and (1.9) have been used successfully by various researchers, for example in Idriss *et al.* (1978), Briaud and Fellio (1986), Poulos (1981), and Bouckovalas (1996). From the strain-controlled cyclic test on soft clay, Idriss *et al.* (1978) concluded that parameters a and b are strongly dependent on the cyclic strain level and that the values appear to be uniquely determined by the applied cyclic strain for a wide range of initial confinement. Fig. 1.6 shows an example of the $\beta(\delta) \sim N$ degradation curve for various stress ratios $R_1 + R_2$ in stress-controlled tests on Gulf of Alaska clay (Briaud and Fellio, 1986). A similar relationship was also used by Poulos (1981) to study the cyclic degradation of axially load single pile.

Degradation parameters seem to be strongly related to the peak cyclic stress ratio. By reviewing published data on 9 cyclic tests on the clay samples in laboratory, 10 cyclic load tests on model pile and 16 full-scale cyclic pile load tests in clay, Briaud and Fellio (1986) observed the general trend of such a correlation. The values of a and b versus peak cyclic stress ratio $R_1 + R_2$ are calculated by best-fit regression analysis for each cyclic stress-strain curve from cyclic laboratory tests of soil samples and pile head load-displacement curves from full-scale load tests. Although quite scattered, the data show that the degradation parameters for full-scale piles are much less than those measured from laboratory tests on soil specimens. For full-scale piles, the best-fit straight lines through the origin, see Fig. 1.7, follow

$$a = 0.09(R_1 + R_2) \tag{1.10}$$

$$b = 0.03(R_1 + R_2) \tag{1.11}$$

While for soil specimens, the best-fit lines follow

$$a = 0.6(R_1 + R_2) \tag{1.12}$$

$$b = 0.6(R_1 + R_2) \tag{1.13}$$

The difference can be explained by the stress distribution in the soil surrounding a loaded pile. For a given $R_1 + R_2$ value measured on the pile head, the actual shear stress level in the soil decreases radially away from the pile, and the soil is also less stressed at greater depth. In another words, the cyclic degradation is non-uniform in a pile-soil system, and the integrated response of cyclic degradation is apparently less severe compared to that measured from a simple shear test. A proper way of using laboratory measurement in prediction of pile response should integrate the soil response in the radial direction and consider the compressibility of the pile, as was suggested, for example, by Bea *et al.* (1984).

The effect of cyclic loading on the ultimate pile capacity seems at first glance to be quite contrary to the observed behavior in cyclic pile load tests. On the one hand, large cyclic capacity degradation was observed under cyclic *displacement-controlled* tests (Grosch and Reese, 1980); on the other hand, the ultimate axial capacity was only slightly (10% – 15%) affected under one-way cyclic *load-controlled* tests, as summarized in Fig. 1.8. This finding also corroborates that reported in Kraft *et al.* (1981), where the pile capacity after cyclic loading was observed to exceed its static capacity, i.e., no apparent reduction of ultimate

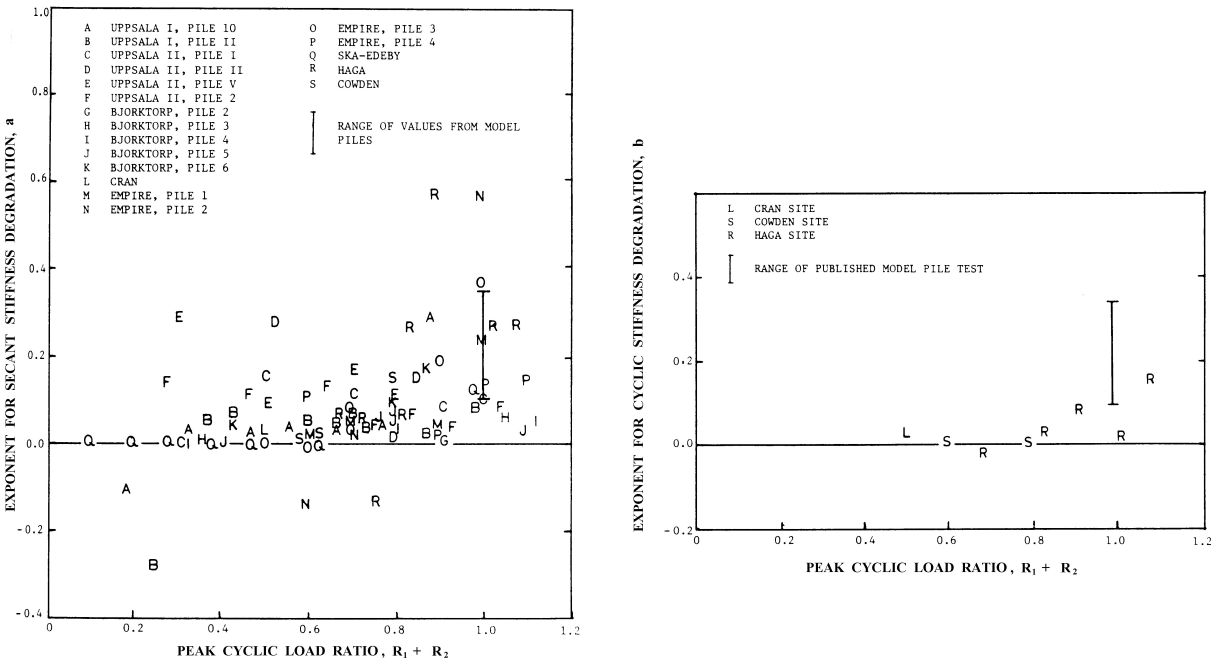

Fig. 1.7. Power Law Exponents a, b versus $R_1 + R_2$ for Full-scale Pile Test Data, from Briaud and Fellio (1986)

static capacity after the cyclic load test. Therefore they suggested that "the total effects of the loading history must be evaluated together with loading rate."

So we must distinguish two different forms of cyclic load tests. A one-way cyclic test imposes cyclic loading without reversal of the load (e.g., compression only), while the load in the two-way cyclic test reverses (e.g., applying both compression and extension). Complete stress reversal in a two-way cyclic test induces much more severe structural damage in the soil due to remolding along the shafts and at the tip, causing more rapid and severe pile loading capacity and stiffness degradation compared to that in the one-way cyclic test. Figs. 1.9 and 1.10 show the repeated one-way and two-way loading tests on model piles reported in Matlock and Homquist (1976). The two-way loading test is displacement controlled in which the ultimate displacement exceeds yield displacement by a factor of 10. Considerable degradation in strength and stiffness can easily be seen in that case.

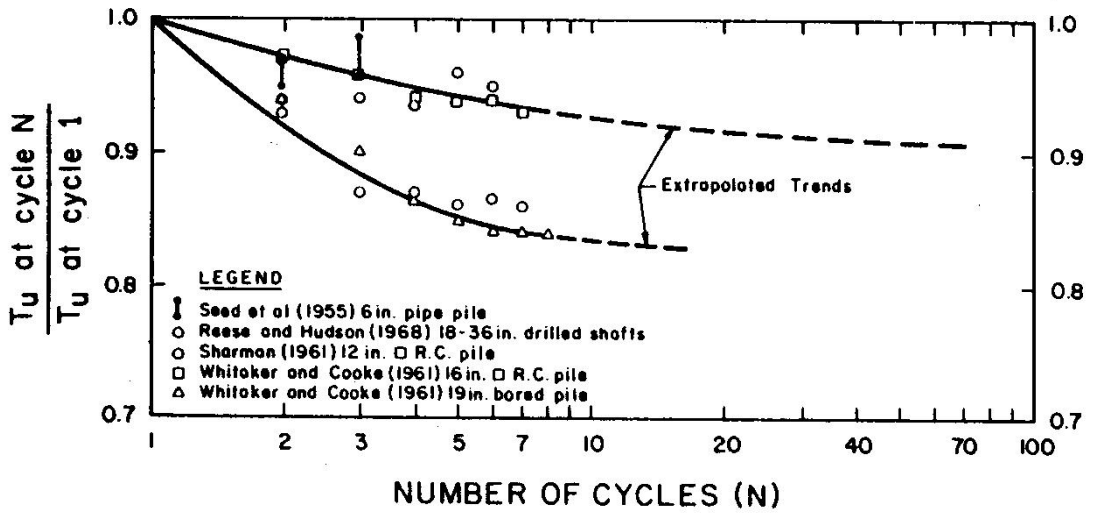

Fig. 1.8 Effect of Cycles on Axial Pile Capacity, from Bea *et al.* (1980)

1.2.4 Combined Effect of Cyclic Loading and Rate of Loading

The overall effect of strain-rate and cyclic loading on soil can be illustrated in Fig. 1.11 (from Bea, 1992). A general cyclic stress can be decomposed into a steady (mean) component and cyclic component. In the figure, two diagonal lines divide the plot into four regions. One diagonal line (termed as "equal strength line") indicates that the applied peak cyclic stress equals the static strength, the other diagonal line (termed as "stress reversal line") separates the cases of stress reversal and no stress reversal. Contours of the numbers of cycles to failure (defined as 20% strain) are plotted. For cases of no stress reversal, the presence of the rate effect results in the contours exceeding the equal strength line. Reduction in cyclic strength is seen when the soil experiences stress reversals.

The cyclic stability diagram, first proposed by Poulos (1988), is also a useful tool to describe the effect of cyclic loading on the stability of the pile system. The diagram was further extended by Lee and Poulos (1993) to four main regions, as shown in Fig. 1.12. Region A is called the cyclically *stable* region, in which cyclic loading has no influence on the axial capacity of the pile when the cyclic component is relatively small; Region B is a cyclically *metastable* region in which cyclic loading causes some reduction of axial load capacity, but the pile does not fail within the specified number of cycles. Region C is called the *serviceability loss* region, in which excessive permanent displacement of the pile

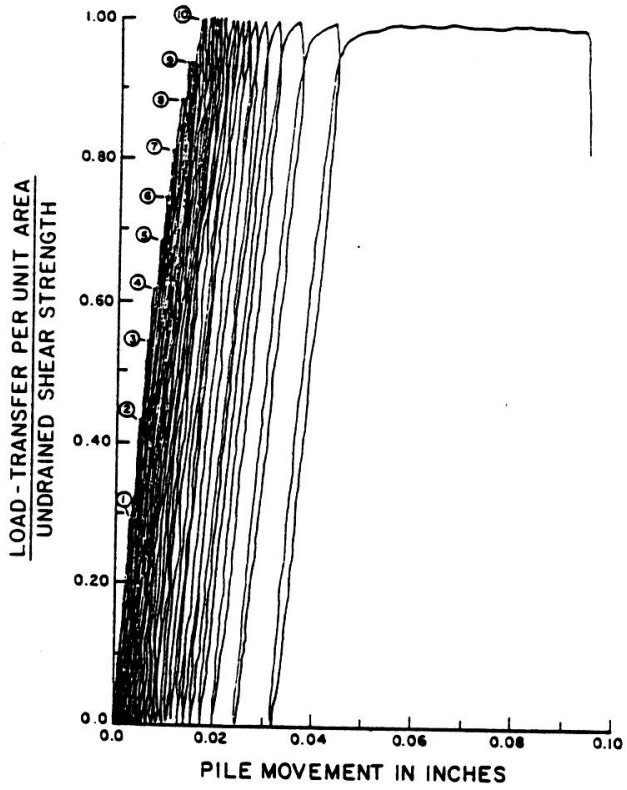

Fig. 1.9. Repeated One-way Loading on Pile, reproduced from Bea (1980) from Matlock and Homquist (1976)

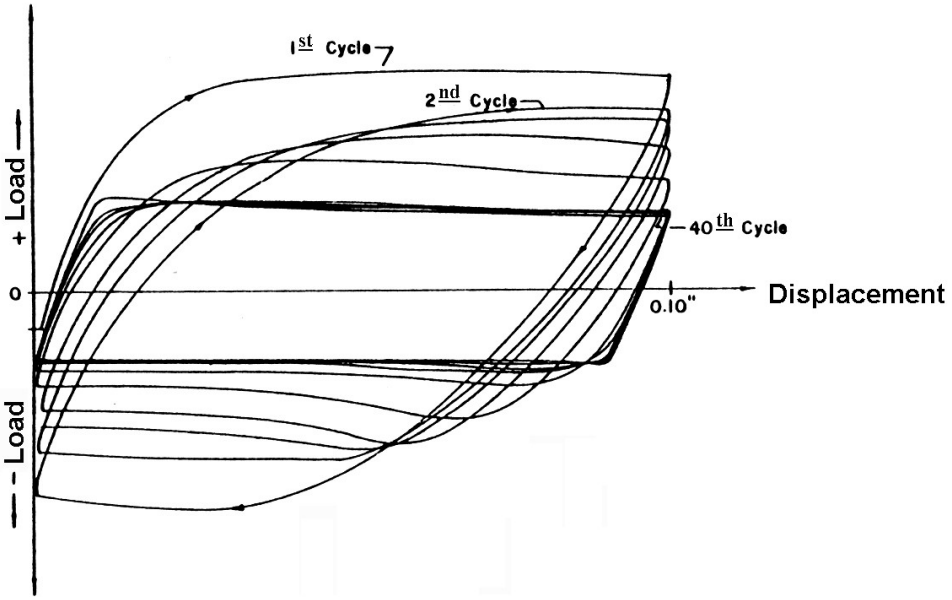

Fig. 1.10. Repeated Two-way Loading on Pile, reproduced from Bea (1980) from Matlock and Homquist (1976)

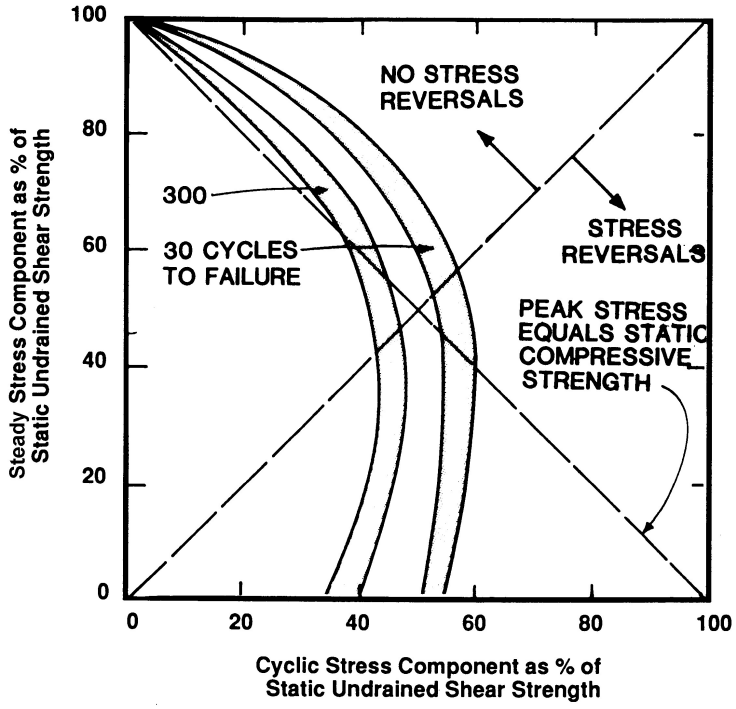

Fig. 1.11. Effect of Steady and Cyclic Shear Stress Ratios on Numbers of Cycles to Failure (20% strain), from Bea (1992)

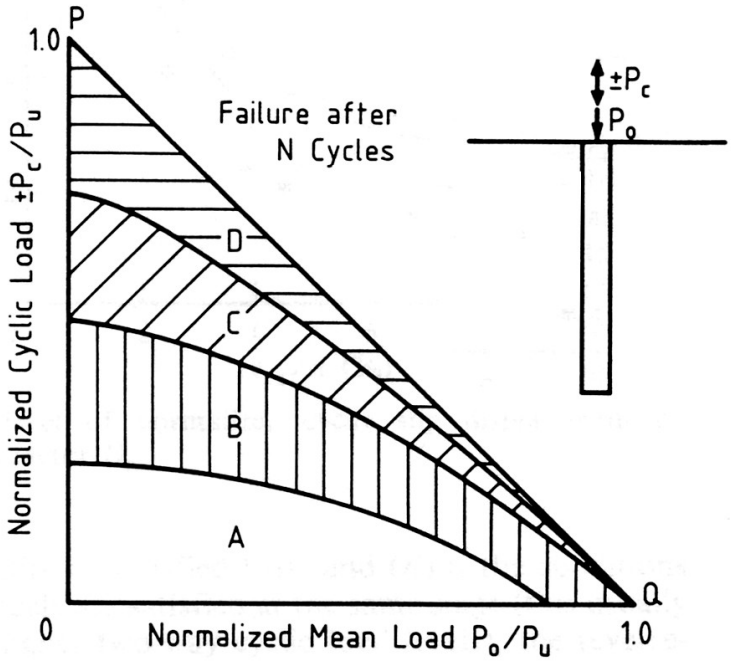

Fig. 1.12 Extended Cyclic Stability Diagrams, from Lee and Poulos (1993)

due to cyclic loading is beyond the allowable value so that the pile functionality is greatly diminished. Region D is called the cyclically *unstable* region, in which cyclic loading causes a sufficient reduction of axial pile capacity, with the pile failing within the specified number of load cycles.

1.2.5 Pile Group Effects

Compared to an isolated single pile, loading of adjacent piles will increase the settlement of a pile in the pile group. To quantify this effect, an interaction factor (Poulos, 1968) can be introduced, which is defined as the ratio of the increased settlement to the settlement of the single pile. For pile groups in homogeneous soil, the interaction factors can be derived as functions of pile spacing (Poulos and Davis, 1980). For more general cases such as pile groups in finite soil layers, one can refer to (Chin *et al.*, 1990). Since the solutions are obtained through boundary element procedure where soil is essentially assumed elastic, how the interaction factors change with evolving soil nonlinearities is absent in their work. With our focus on a single pile behavior, the group effect is beyond the scope of this report.

1.2.6 Static Ultimate Bearing Capacity

To satisfy the functional requirement of supporting superstructures, the bearing capacity of piles has been the primary concern of pile design. In this section, the state-of-the-practice pile foundations design guidance is outlined based on the latest design code *Recommended Practice for Planning, Designing and Constructing Fixed Offshore Platforms* by American Petroleum Institute (API, 2002).

Although many alternative interpretations exist, the axial capacity of a pile can be defined as the maximum axial resistance under which a pile maintains a specified service requirement (e.g., a specified pile head displacement). The bearing capacity of a pile can be written as the summation of the skin friction and end bearing as,

$$Q_d = Q_f + Q_p = f A_s + q A_p \tag{1.14}$$

where

$$\begin{aligned} Q_f &= \text{skin friction resistance, } lb(kN) \\ Q_p &= \text{total end bearing, } lb(kN) \\ f &= \text{unit skin friction capacity, } lb/ft^2(kPa) \\ q &= \text{unit end bearing capacity, } lb/ft^2(kPa) \\ A_s &= \text{side surface area of pile, } ft^2(m^2) \\ A_p &= \text{gross end area of pile, } ft^2(m^2) \end{aligned}$$

Direct summation in Eq. (1.14) implies the maximum skin friction and the maximum end bearing are mobilized simultaneously, which may not necessarily be true in some circumstances, where explicit consideration of different skin and end bearing behavior may be warranted.

For piles in **cohesive** soils, the unit skin friction f and unit end bearing capacity q can be related to the undrained shear strength of the soil by the following equations,

$$f = \alpha\, S_u \tag{1.15}$$

$$q = 9\, S_u \tag{1.16}$$

where

$$\begin{aligned} \alpha &= \text{a dimensionless factor} \\ S_u &= \text{undrained strength of the soil, } lb/ft^2(kPa) \end{aligned}$$

The reduction factor α here is presented to take into account the influence of many factors, including pile type, soil type, and installation methods we have discussed before. Ideally, α should be determined from a pile-load test. Besides other correlations (see Poulos and Davis, 1980, pp.20), API recommends that it can be empirically estimated as a function of undrained strength S_u and effective overburden pressure p_0' via

$$\alpha = 0.5\Psi^{-0.5}, \quad \Psi \leq 1.0 \tag{1.17}$$

$$\alpha = 0.5\Psi^{-0.25}, \quad \Psi > 1.0 \tag{1.18}$$

where $\Psi = S_u/p_0'$, and $\alpha \leq 1.0$ is constrained for the above equation.

For piles in **cohesionless** soils, the unit shaft friction f is a function of the effective overburden pressure p'_0, the coefficient of lateral earth pressure K_0, and the friction angle between the soil and pile wall δ, and is expressed in the form of the Coulomb frictional law

$$f = K_0 p'_0 \tan\delta \tag{1.19}$$

and the end bearing capacity is expressed in terms of the effective overburden pressure p'_0 at the pile tip, and a bearing capacity factor N_q which depends on the internal friction angle of the cohesionless soil.

$$q = p'_0 N_q \tag{1.20}$$

where

$$\begin{aligned} p'_0 &= \text{effective overburden pressure at the pile tip} \\ N_q &= \text{dimensionless bearing capacity factor} \end{aligned}$$

Table 1.1 summarizes the design parameters for cohesionless siliceous soils, which are categorized according to the soil type and density. Field observations also show that the unit skin friction and unit end bearing do not increase infinitely with depth but tend to reach their limiting values – a phenomena that has been explained by many researchers as the "arching effect". This effect curtails the increase of the overburden pressure and of the lateral earth pressure with depth. The recommended limiting values of f and q are also provided in the table.

The above recommendation should be applied cautiously to piles in calcareous sands. In comparison to non-calcareous sands, calcareous sands are more suspectable to crushing during pile driving; moreover, cementation may prevent the development of lateral pressure on the pile wall (McClelland, 1974). Particle crushing and cementation in calcareous sands are known to affect the axial pile capacity significantly. According to Datta *et al.* (1980), the capacity can be reduced to 1/3 of that in non-calcareous sands.

Besides API's recommendation, numerous other empirical methods have been developed to predict axial pile capacities. Briaud and Tucker (1988) exercised 13 methods published in the literature to predict the ultimate load of 98 full-scale pile load tests. These methods are listed in Table 1.2 with corresponding references included. Basic parameters

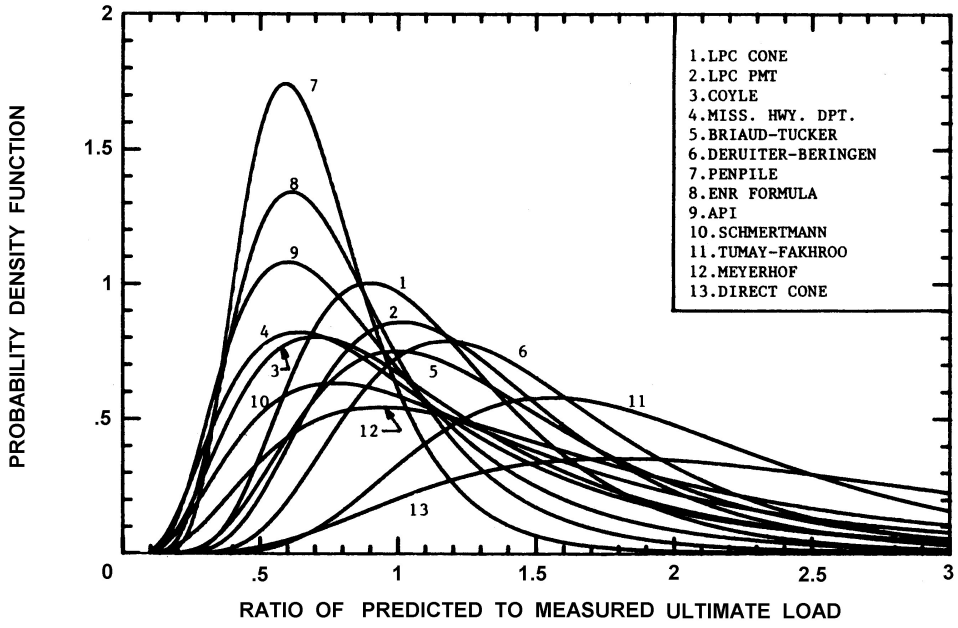

Fig. 1.13. Statistical Distribution for Ultimate Pile Load Prediction, from Briaud and Tucker (1988)

used in predictions are based on the standard penetration test (SPT), the cone penetrometer test (CPT) or pressuremeter tests (PMT), as well as laboratory tests, including undrained triaxial tests and unconfined compression tests for undrained shear strength S_u of clays. The predictive capacities of these methods are varying, and one way to compare them is to plot the ratio of the predicted ultimate load vs. the actual measured value [2], as shown in Fig. 1.13. Some methods tend to overpredict the ultimate capacity whereas some underpredict. Overall, the better methods have a mean of the ratio between 0.9 – 1.2, with the coefficient of variation 0.40 – 0.45.

[2]The ultimate load was defined as the load inducing a settlement of one tenth of the pile diameter plus the elastic compression of the pile.

Table 1.1. API Recommended Design Parameters for Cohesionless Siliceous Soil (from API, 2002)

Density	Soil Description	Soil-pile Friction $\delta(^o)$	Limiting f value $kips/ft^2(kPa)$	N_q	Limiting q value $kips/ft^2(kPa)$
Very Loose Loose Medium	Sand Sand-Silt Silt	15	1.0 (47.8)	8	40 (1.9)
Loose Medium Dense	Sand Sand-Silt Silt	20	1.4 (67.0)	12	60 (2.9)
Medium Dense	Sand Sand-Silt	25	1.7 (81.3)	20	100 (4.8)
Dense Very Dense	Sand Sand-Silt	30	2.0 (95.7)	40	200 (9.6)
Dense Very Dense	Gravel Sand	35	2.4 (114.8)	50	250 (12.0)

Table 1.2. Methods for Ultimate Pile Capacity Prediction, from Briaud and Tucker (1988)

Method	Reference	Basic Parameters Clay	Sand
Coyle	Coyle and Castello (1981)	S_u	SPT data
API	API (1984)	S_u	SPT data
Briaud-Tucker	Briaud and Tucker (1984)	S_u	SPT data
Meyerhof	Meyerhof (1976)	S_u	SPT data
Mississippi State Highway Dept.	MSHD (1972)	S_u	SPT data-direct shear
Direct Cone	Briaud (1986)	CPT data	CPT data
De Ruiter	De Ruiter and Beringen (1979)	CPT data	CPT data
LPC Cone	Bustamante and Gianeselli (1983)	CPT data	CPT data
Schmertmann	Schmertmann (1978)	CPT data	CPT data
Tumay-Frakhroo	Tumay and Fakhroo (1981)	CPT data	CPT data
Penpile	Clisby (1978)	CPT data	CPT data
LPC PMT	Bustamante and Gianeselli (1982)	PMT data	PMT data
EN Formula	Peck *et al.* (1974)	Blow count	Blow count

1.2.7 Empirical Load Transfer Curves

$t - z$ and $Q - z$ Curves for Clays and Sands

As the axial resistance of the soil is provided by a combination of load transfer along the sides of the pile and end bearing resistance at the pile tip, the pile and the resistance can be modelled as "Beam on Nonlinear Winkler Foundation" (BNWF). This approach assumes that the reaction (force-displacement) of the system at a depth is independent of interaction between different depths. Usually, the relationship between mobilized soil-pile shear transfer t and local pile deflection z at a depth is described using a nonlinear relation called $t - z$ curve. Similarly, the relationship between mobilized end bearing resistance Q and axial tip deflection z is described using a $Q - z$ curve, such that the resistance can be discretized along the pile length and at the pile tip.

In the absence of more definitive criteria, API (2002, section 6.7) recommended $t - z$ and $Q - z$ curves for non-carbonate soils are presented in Figs. 1.14 and 1.15. As illustrated in these figures, there are several distinctive features in API's recommendations as follows:

- Maximum side resistance is more easily mobilized in sands than clays, especially for large diameter piles. Similarly, maximum side resistance is more easily mobilized than tip resistance. As suggested by the direct addition in Eq.(1.14) for calculating ultimate bearing capacity, both of the maximum side and tip resistances are mobilized simultaneously, which may overestimate the capacity in some circumstances.

- Sands are interpolated as perfectly elastic-plastic material, while clays behave nonlinearly even at the small strain range. The $t - z$ curve for clays may exhibit various degrees of softening, once relative displacement between pile and clay is fully mobilized (beyond $z/D = 0.01$, where D is pile diameter). Residual side adhesion drops down to 0.70 to 0.90 of the maximum adhesion, whose values are a function of soil stress-strain behavior, stress history, installation method, pile load sequence and other factors. Laboratory, in-situ or model pile tests can be used to provide information for determination of these values for various soils.

- Same tip load-displacement curve is suggested for both sand and clays. The tip resis-

tance is mobilized parabolically to its full strength at the tip displacement of 0.10 pile diameter.

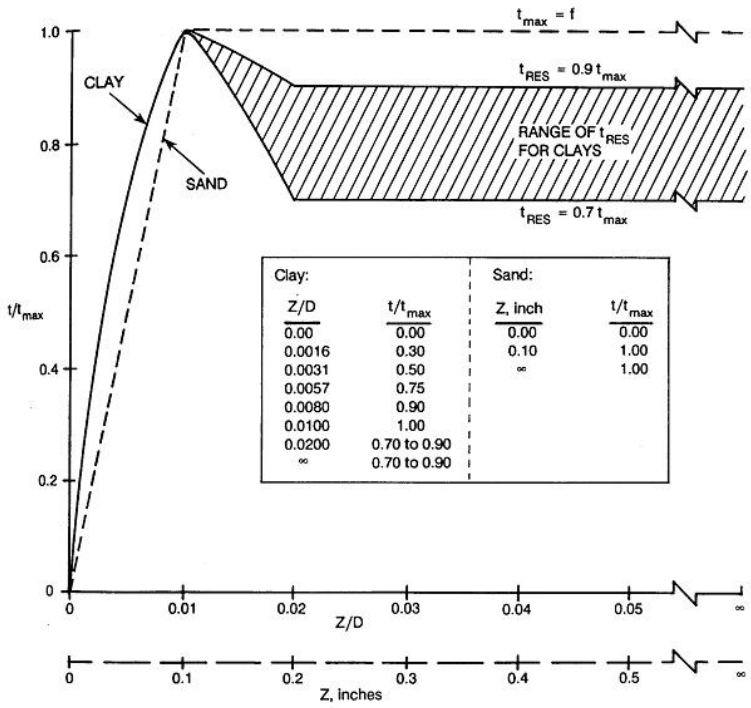

Fig. 1.14. Typical Axial Pile Load Transfer-Displacement ($t - z$) Curves, from API (2002)

$p - y$ Curves for Soft Clays

Similar to $t - z$ and $Q - z$ curves for axially loaded piles, various $p - y$ curves have been formulated for lateral loaded pile reaction, which have been summarized for example in Mosher and Dawkins (2000). Compared to a vertically loaded pile where soil resistances are unidirectional, laterally loaded pile movement is at least two-dimensional. Distinctive failure mechanisms are associated with upper and lower portions of the soil respectively – near the ground surface, wedge type failure of the soil is expected due to lateral pile movement, while in the lower position, the soil fails through plastic yielding. Correspondingly, different load transfer mechanisms should be considered for these different regions.

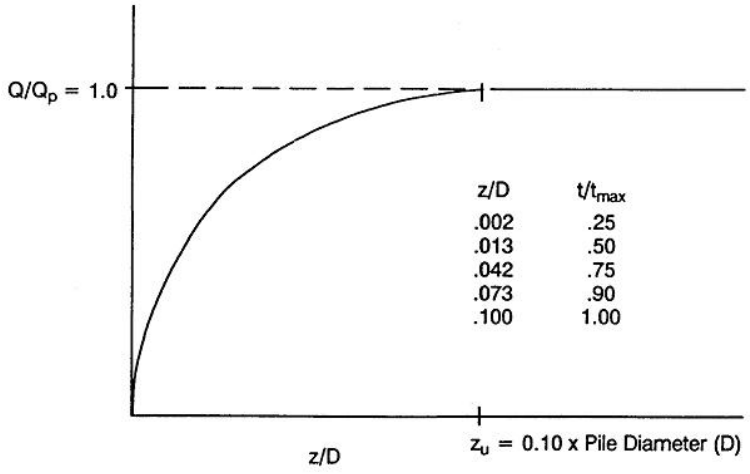

Fig. 1.15 Pile Tip Load-Displacement ($Q - z$) Curves, from API (2002)

Matlock (1970) recommended the following procedure to construct $p - y$ curves for soft clays, also see Fig. 1.16(a):

$$\frac{P}{P_u} = 0.5\left(\frac{Y}{Y_c}\right)^{\frac{1}{3}} \qquad (Y < 8Y_c) \tag{1.21}$$

$$\frac{P}{P_u} = 1 \qquad (Y > 8Y_c) \tag{1.22}$$

where

Y_c = $2.5D\varepsilon_c$, is the lateral displacement at one half of the ultimate resistance

D = the diameter of the pile

ε_c = strain at one half the maximum stress in a laboratory undrained compression test of undisturbed soil samples

P = lateral static soil resistance per unit pile length

P_u = ultimate lateral static soil resistance per unit pile length

Y = lateral displacement of pile relative to the soil

The static ultimate resistance can be related to pile diameter (D) and undrained shear strength of the soil (S_u) through a dimensionless ultimate resistance coefficient N_p as follows

$$P_u = N_p \; S_u \; D \tag{1.23}$$

Matlock (1970) recommended a linear variation of N_p to a constant limiting value at depth

$$N_p = 3 + \frac{\gamma'}{S_u} Z + \frac{J}{D} Z \qquad (Z < Z_{cr}) \tag{1.24}$$

$$N_p = 9 \qquad (Z > Z_{cr}) \tag{1.25}$$

in which Z is depth below ground surface and Z_{cr} is a critical depth where soil wedge failure transforms to flow failure, and γ' is the effective unit weight of the soil. It is also recommended $J = 0.5$ for a soft clay and 0.25 for a medium stiff clay. Note that the normalized consolidated condition estimates $\dfrac{\gamma' Z}{S_u} \simeq 0.3$ for normally consolidated clays, so N_p varies from around 3 near the surface to 9 at the critical depth Z_{cr} [3]. On the other hand, the critical depth which differentiates the wedge failure on the surface and the flow failure at the depth can be obtained by equating Eq. (1.24) and Eq. (1.25),

$$Z_{cr} = \frac{6 S_u D}{\gamma' D + J S_u} \tag{1.26}$$

Fig. 1.16 summarizes the recommended $p - y$ curves for soft clays under static and dynamic loading. Same exponential function is used for the nonlinear pre-yielding behavior in both cases except that the dynamic curve is truncated at $Y/Y_c = 3$ and considerable reduction of the ultimate resistance occurs in the dynamic case in Fig. 1.16 (b). Moreover, the intensity of strain softening is assumed to vary linearly with depth Z until no softening is assumed to occur for soils deeper than Z_{cr}.

$p - y$ Curves for Stiff Clays

Stiff clays are usually more brittle than soft clays and capacity degradation has to be considered. Reese *et al.* (1975) proposed curves with five segments to describe strain softening response of the overconsolidated stiff clay (see Fig. 1.17). The initial stiffness of the $p - y$ curve is the product of static or cyclic stiffness parameters (k_s or k_c) and the depth Z at which the curve is applied. For the static case, the second segment in Fig. 1.17 (a) is of the following form

$$\frac{P}{P_c} = 0.5 \left(\frac{Y}{Y_c} \right)^{0.5} \tag{1.27}$$

[3] Stevens and Audibert (1979) noticed the above relations were based on field load tests on relatively small diameter piles. By synthesizing a broader database, they proposed a modification of N_p profile, which assumes a higher value than that of Matlock.

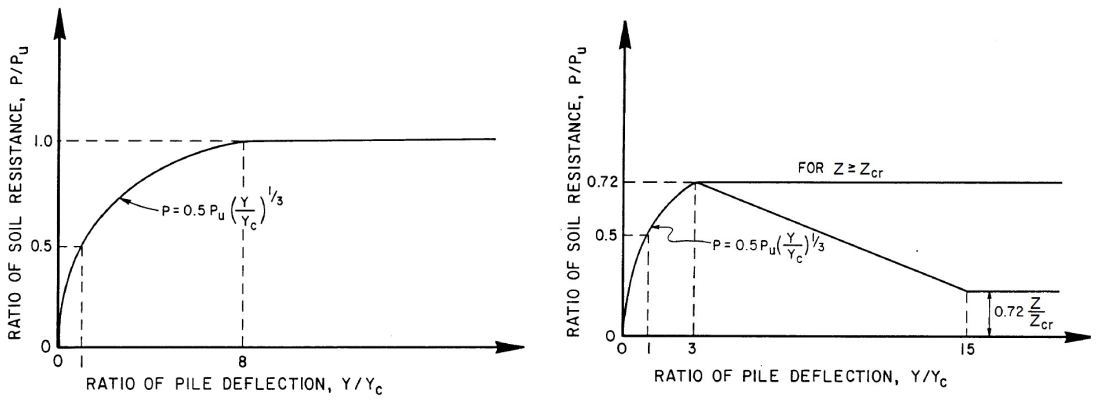

(a) Static (b) Dynamic

Fig. 1.16 p-y Curves for Soft Clay, from Matlock (1970)

with P_c taken as the smaller of

$$P_c = \left(2 + \frac{\gamma'}{S_u}Z + 2.83\frac{Z}{D}\right) S_u D \tag{1.28}$$

for wedge failure near the ground, or

$$P_c = 11 S_u D \tag{1.29}$$

for flow failure at depth. $Y_c = \varepsilon_c D$, A is a displacement parameter related to the depth. The third segment is

$$\frac{P}{P_c} = 0.5\left(\frac{Y}{Y_c}\right)^{0.5} - 0.055\left(\frac{Y}{AY_c} - 1\right)^{1.25} \tag{1.30}$$

After linear degradation, the residual resistance remains constant beyond $18A$. Similar construction for dynamic case was also proposed in Fig. 1.17(b).

$p - y$ Curves for Sands

Based on a series of static and cyclic lateral load tests on pipe piles driven in submerged sands, Reese *et al.* (1974) proposed a $p - y$ relation for use in the sand. Fig. 1.18(a) represents a characteristic curve, where two straight line segments OA and BU are connected by a parabolic curve AB. A constant resistance is assumed beyond U.

O'Neill and Murchison (1983) also conducted a systematic study of proposed $p - y$ relationships in sands and proposed a single expression as follows, also refer to Fig. 1.18(b).

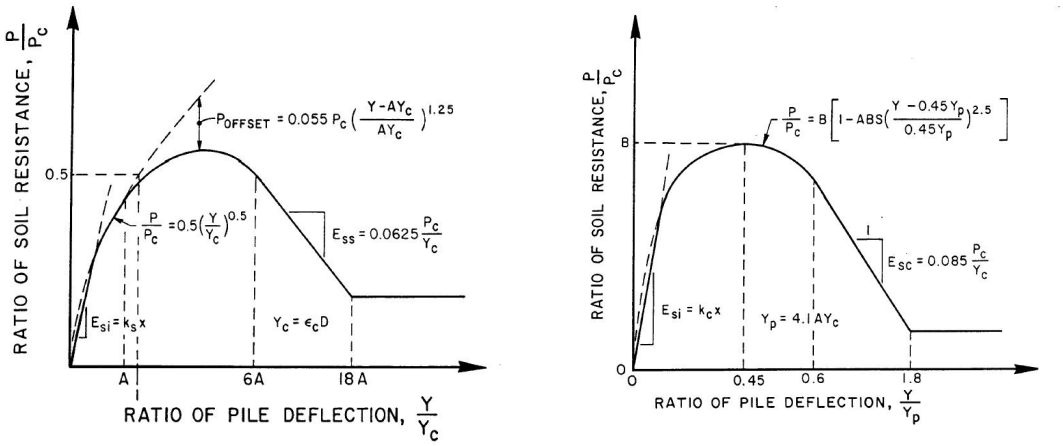

(a) Static (b) Dynamic

Fig. 1.17 p-y Curves for Stiff Clay, from Reese *et al.* (1975)

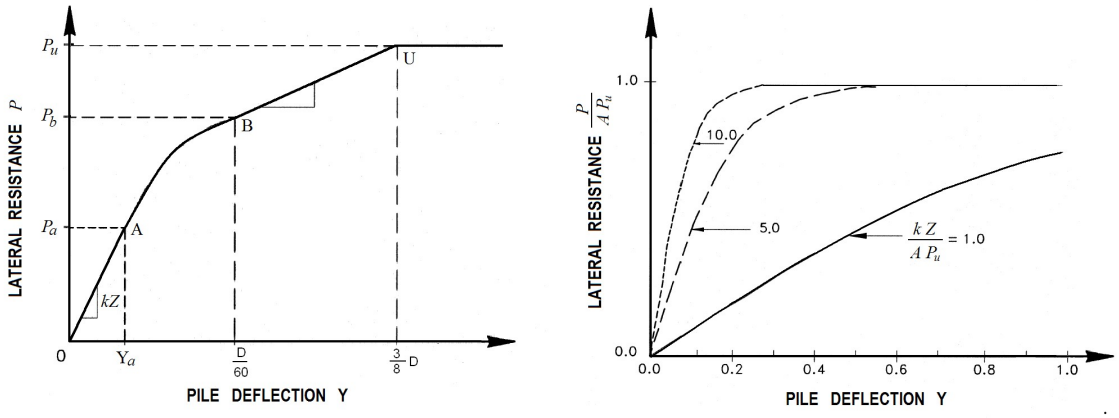

(a) Reese *et al.* (1975) (b) O'Neill and Murchison (1983)

Fig. 1.18 p-y Curves for Sand

$$\frac{P}{P_u} = nA \tanh\left(\frac{kZ}{AP_u}Y\right) \tag{1.31}$$

where n is geometry factor, it takes 1.5 for tapered piles and 1.0 for prismatic piles; A is a factor to account for cyclic or static loading condition. $A = 0.9$ for cyclic loading and $A = 3.0 - 0.8\dfrac{Z}{D} \geq 0.9$ for static loading; k is the initial modulus of subgrade reaction, and it can be determined from Fig. 1.19(a) as a function of the internal friction angle.

The ultimate lateral resistance per unit pile length is determined as the smaller value

of the follows

$$P_u = (C_1 Z + C_2 D)\gamma' Z \tag{1.32}$$

for a wedge failure near the ground surface, or

$$P_u = C_3 D \gamma' Z \tag{1.33}$$

for a flow failure at depth. Coefficients C_1, C_2, C_3 are determined from Fig. 1.19 (b) as a function of the internal friction angle of the sand.

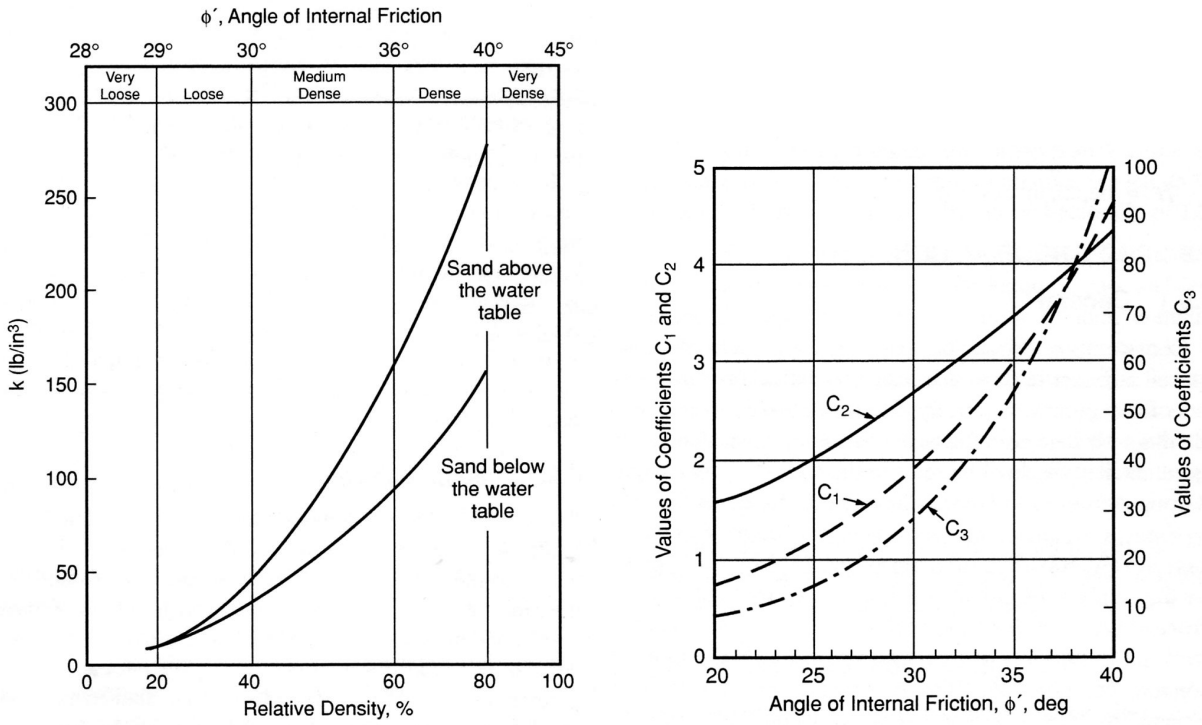

(a) Determination of k

(b) Determination of C_1, C_2, C_3

Fig. 1.19 p-y Curves Parameters for Sand, from API (2002)

$p-y$ curves proposed by Reese *et al.* (1974) define the initial stiffness increasing linearly with depth Z and the initial modulus of subgrade reaction coefficient k. As commented in Boulanger *et al.* (1999), a constant k value overestimates the $p-y$ stiffness at depths larger than a few pile diameters, since the stiffness of sand generally increases in proportion to the square root (not the value) of confinement. Instead, they suggested using the elastic theory

proposed by Vesic (1961):

$$k^e = 0.65\sqrt{\frac{E_s D^4}{EI}}\frac{E_s}{1-\nu^2} \tag{1.34}$$

where E_s = Young's modulus of the soil $= 2G_{max}(1+\nu)G_{max}$, and G_{max} is the small-strain shear modulus of the sand, which can be either obtained by site investigation or empirical correlations; ν is the soil's Poisson's ratio; D is the pile diameter, and EI is the bending stiffness of the pile.

A similar adjustment can also be applied for clay. For example, $p-y$ curve for soft clay in Matlock (1970) implies an infinite initial stiffness, which is not appropriate for dynamic analysis. Wang *et al.* (1998) proposed to use a computed k^e from Eq.(1.34) to replace Matlock's exponential curve Eq.(1.21) up to the point of their intersection. Typically the intersection corresponds to 35% P_u.

2 Review of Analytical and Numerical Models for Axially Loaded Piles

Numerous analytical and numerical models for static and dynamic load transfer of axially loaded piles were developed over the years. The purpose of this review is to provide a context for the numerical solution presented later and to examine typical assumptions made in the analysis of the behavior of axially loaded piles.

2.1 ANALYTICAL STATIC LOAD TRANSFER MODELS

2.1.1 Randolph-Wroth Solution

Analytical models seek closed-form solutions of the pile behavior for the idealized soil response and simplified boundary conditions. For a vertically loaded pile in an infinite linear elastic half-space, the approximate analytical solution proposed by Randolph and Wroth (1978) is often used to establish the load transfer function for the pile shaft and pile tip. This solution is important because it forms the basis for the development of other methods.

To determine the load transfer of the shaft resistance, Randolph and Wroth (1978) idealize the deformation pattern of soil around the pile shaft as shearing of concentric cylinders. It can be further assumed that the radial soil displacements due to pile loads are negligible compared with vertical displacement w. For this idealized model, the vertical equilibrium of a soil element at radius r at depth z is governed by the following differential equation

$$\frac{\partial}{\partial r}(r\tau) + r\frac{\partial \sigma_z}{\partial z} = 0 \tag{2.1}$$

in which τ and σ_z are the shear stress increment and vertical stress increment (taking compression as positive), respectively. When the pile is loaded, the increase in shear stress τ is

much greater than the increase in vertical stress σ_z, so the second term in Eq.(2.1) can be dropped [1] and Eq.(2.1) may be approximated as

$$\frac{\partial}{\partial r}(r\tau) = 0 \tag{2.2}$$

Eq.(2.2) can be integrated to give the shear stress τ distribution in radial direction, written in terms of shear stress τ_0 at the pile shaft r_0 as

$$\tau = \frac{\tau_0 r_0}{r} \tag{2.3}$$

Considering the fact that the gradient of the vertical displacement of the soil w is much greater than that of radial displacement u, the shear strain (reduction in angle taken as positive) is simplified as

$$\gamma = \frac{\partial u}{\partial z} + \frac{\partial w}{\partial r} \approx \frac{\partial w}{\partial r} \tag{2.4}$$

Assuming that the stress-strain relation of the soil is linearly elastic, with a constant shear modulus G, Eq. (2.4) can be written as

$$\gamma = \frac{\tau}{G} = \frac{\tau_0 r_0}{rG} \approx \frac{\partial w}{\partial r} \tag{2.5}$$

Integration of the above equation leads to approximation of the settlement of the pile shaft, w_0, as

$$w_0 \approx \int_{r_0}^{\infty} \gamma dr = \tau_0 r_0 \int_{r_0}^{\infty} \frac{dr}{Gr} \tag{2.6}$$

Unfortunately, the above integral solution is unbounded and the usual assumption is that there is some radius, r_m, beyond which the shear stress and strain become negligible, i.e., $w(r_m) = 0$. Accordingly, the shaft displacement w_0 can be related to the local shaft stress τ_0 and modulus G as

$$w_0 \approx \tau_0 r_0 \int_{r_0}^{r_m} \frac{dr}{Gr} = \frac{\tau_0 r_0}{G} \ln\left(\frac{r_m}{r_0}\right) = \zeta \frac{\tau_0 r_0}{G} \tag{2.7}$$

in which $\zeta = \ln(r_m/r_0)$ is defined as the shaft load transfer factor. The settlement at a radial distance r may be expressed as

$$w(r) = w_0 - \frac{\tau_0 r_0}{G} \ln\left(\frac{r}{r_0}\right) \tag{2.8}$$

[1] A more rigorous solution to incorporate σ_z is given by Mylonakis (2001).

Obviously, the choice of r_m is crucial to quantify local mobilized stress and strain along the shaft. Randolph and Wroth (1978) proposed the following empirical relation

$$r_m = 2.5\ \rho\ L\ (1-\nu) \tag{2.9}$$

where L is the length of the pile, and $\rho = G(L/2)/G(L)$ is an inhomogeneity factor, which is defined as a ratio of the soil shear modulus at the pile mid-depth to that at the pile base. So $\zeta = \ln(r_m/r_0)$ depends on the slenderness ratio L/r_0 of the pile and Poisson's ratio ν of the soil, and its value is usually around 4. Since the above formula is for a single pile in an infinite homogeneous soil, modifications of r_m to account for the influence of pile geometry, inhomogeneous soil and layered soil stratigraphy are given by Guo and Randolph (1997) and Chin and Poulos (1991). For more general soil profiles, r_m may have to be determined from a numerical procedure such as finite element analysis.

The solution for pile tip settlement, suggested by Randolph and Wroth (1978), is similar to that of a rigid punch acting on the surface of an elastic half-space (Timoshenko and Goodier, 1951, pp.372), and it can be estimated as

$$w_b = \frac{P_b\ (1-\nu)}{4\ r_0\ G_b}\ \eta \tag{2.10}$$

where P_b is the mobilized base load, G_b is the shear modulus of soil beneath the tip of the pile. Compared with the original solution of Timoshenko and Goodier (1951), the additional parameter η is introduced to account for the depth of the pile tip below the surface, i.e., the interaction of the soil layer above with the layer below. Although there has been much debate and confusion over the coefficient η [2], it can be generally chosen as unity if plastic yielding of the soil is considered.

By adding the results of the pile tip and shaft load transfer models, a reasonable estimate of the deformation of an elastic pile in a homogeneous linearly elastic soil can be obtained in closed-form. Considering the compressibility of an elastic pile, the pile load over length $P(z)$ can be determined by the elastic compression of the pile, as

$$P(z) = -AE_p \frac{\partial w_0(z)}{\partial z} \tag{2.11}$$

[2]For example, Fox (1948) showed $\eta = 0.5$ should be used considering a loaded area embedded in a soil mass at depth, and it was used by Burland and Cooke (1974). For plate loading testing conducted at the bottom of an open borehole, Burland (1969) showed by finite element analyses that the limiting value for η was about 0.85.

in which E_p = Young's modulus of the pile material; A = cross sectional area of the pile. The gradient of pile load, $P(z)$, can be related to the vertical soil reaction per unit pile length, $f(z)$, by

$$\frac{\partial P(z)}{\partial z} = -f(z) = -k(z)w_0(z) \tag{2.12}$$

where $k(z) \equiv \dfrac{f(z)}{w_0(z)}$ is often referred to as the *modulus of subgrade reaction*, in units of $force/length^2$. It is well known that $k(z)$ depends on both soil and pile properties, and it varies with depth even for a homogeneous soil profile when the compressiblity of the pile is considered. For circular piles, the vertical soil reaction per unit pile length $f(z)$ is simply the integration of shear stress, i.e.,

$$f(z) = 2\pi r_0 \tau_0(z) \tag{2.13}$$

Substituting Eq.(2.11) into Eq.(2.12) gives the one-dimensional equilibrium equation of a single pile embedded in soils:

$$-E_p A \frac{\partial^2 w_0(z)}{\partial z^2} + k(z)w_0(z) = 0 \tag{2.14}$$

Note that this governing equation is restricted only to the assumption of an elastic pile, and it can be used for more general case of nonlinear soils. Considering the shaft load-displacement relation of Eq. (2.7), the following governing differential equation can be derived from Eqs. (2.14)

$$\frac{\partial^2 w_0(z)}{\partial z^2} - \frac{2}{r_0^2 \zeta \lambda} w_0(z) = 0 \tag{2.15}$$

in which $\lambda = E_p/G$ is the stiffness ratio between the pile material and the soil. The second-order PDE can be solved by substituting the boundary conditions of Eqs.(2.10, 2.11) at the tip of the pile

$$w_0(L) = w_b = \frac{P_b\ (1-\nu)}{4\ r_0\ G}\ \eta \tag{2.16}$$

$$\left.\frac{\partial w_0(z)}{\partial z}\right|_{z=L} = -\frac{P_b}{AE_p} \tag{2.17}$$

Eq.(2.15) can be solved as

$$w_0(z) = \frac{1}{2}\frac{P_b}{r_0 G}\left\{\left[\frac{\eta(1-\nu)}{4} - \frac{1}{\pi r_0 \lambda \mu}\right] e^{-\mu(L-z)} + \left[\frac{\eta(1-\nu)}{4} + \frac{1}{\pi r_0 \lambda \mu}\right] e^{\mu(L-z)}\right\} \tag{2.18}$$

with $\mu = \sqrt{\dfrac{2}{\zeta\lambda}}\ \dfrac{1}{r_0}$. Due to the high stiffness contrast of pile and soil, the term $(\pi r_0 \lambda \mu)^{-1}$ can be ignored. Hence the solution of shaft displacement as a function depth can be simplified

as

$$w_0(z) = w_b \cosh\left(\mu\ (L - z)\ \right) \tag{2.19}$$

In particular, the pile head displacement($z = 0$) may be expressed in terms of the settlement of the pile tip by

$$w_t = w_0(0) = w_b \cosh\left(\mu L\right) \tag{2.20}$$

and total load supported by the pile may be obtained by integrating Eq. (2.12), and utilizing Eqs.(2.13) and (2.18)

$$P(z) = \frac{2\pi P_b}{\zeta r_0}\left\{\frac{\eta(1-\nu)}{4\mu}\sinh[\mu(L-z)] + \frac{\zeta r_0}{2\pi}\cosh[\mu(L-z)]\right\} \tag{2.21}$$

and the pile load on top can be found as

$$P_t = P(0) = \frac{2\pi P_b}{\zeta r_0}\left\{\frac{\eta(1-\nu)}{4\mu}\sinh(\mu L) + \frac{\zeta r_0}{2\pi}\cosh(\mu L)\right\} \tag{2.22}$$

Finally, using Eqs.(2.20, 2.22, 2.10), the global stiffness of the soil-pile system, expressed as a ratio of pile load on top and pile head displacement, can be evaluated as

$$k_t = \frac{P_t}{w_t} = G\ r_0\left[\frac{4}{\eta(1-\nu)} + \frac{2\pi}{\zeta}\frac{L}{r_0}\frac{\tanh(\mu L)}{\mu L}\right]\left[1 + \frac{4}{\eta(1-\nu)}\frac{1}{\pi\lambda}\frac{L}{r_0}\frac{\tanh(\mu L)}{\mu L}\right]^{-1} \tag{2.23}$$

The expression for the effective stiffness of the system Eq. (2.23) explicitly accounts for the effect of the pile stiffness ratio λ, slenderness ratio L/r_0, and Poisson's ratio etc. It should be noted that the result might become unstable for long compressible piles. Also, the influence of the magnitude of the load is absent in this formulation because the soil is considered linearly elastic, so the stiffness of the soil-pile system is also linearly elastic. The above solution can degenerate to the limiting case of a rigid pile as $\lambda \to \infty$ and $\mu \to 0$

$$k_t = \frac{P_t}{w_t} = k_t^{tip} + k_t^{shaft} = \frac{4G\ r_0}{\eta(1-\nu)} + \frac{2\pi G\ L}{\zeta} \tag{2.24}$$

where the first and second part of the above expression are contributions from tip resistance and shaft resistance, respectively.

In summary, in seeking an approximated analytical solution for a vertically loaded pile, the displacement pattern is assumed to have the form of shearing of the concentric cylinders and the materials are assumed to be isotropic elastic. The approximation is made such that radial displacements are assumed negligible, and shear stresses are assumed negligible beyond a radial distance r_m. The zone of influence r_m is usually taken as an average

value along the shaft, and is a function of pile length L and the Poisson's ratio ν of the soil. The Randolph-Wroth solution is limited to homogeneous elastic soils, and the predicted load-displacement is in good agreement only with the *linear elastic part* of the measured pile settlement (Lee and Poulos, 1990). Various extensions to include nonlinearity and non-homogeneity of soils have been attempted in the past and are discussed in the following sections.

2.1.2 Vertical Variations in Soil Modulus

The analytical method can be extended to several special cases of nonhomogeneous soil profiles. Randolph and Wroth (1978) first considered linearly increasing soil modulus with depth. A more general vertical variation of soil shear modulus can be assumed as a power function of depth z (Guo and Randolph, 1997; Guo, 2000a) and the solution procedure for this case is briefly outlined below.

Assume that the shear modulus has the following general form

$$G = A_g(\alpha_g + z)^n \tag{2.25}$$

where n, A_g, and α_g are constants. The above assumption is general enough to represent both normally consolidated soil where shear modulus at the ground surface is usually assumed to be zero and overconsolidated soil profiles where the shear modulus at ground surface is nonzero.

Below the pile tip, shear modulus is assumed to be constant G_b, which may be different from the shear modulus G_L at just above the pile tip. The jump in the shear modulus at the pile tip can be described by the so-called end-bearing factor $\xi = G_L/G_b$, and the stiffness ratio is defined as $\lambda = E_p/G_L$. The shaft load transfer equation of Eq.(2.7) can be rewritten as

$$w_0(z) = \zeta\frac{\tau_0(z)r_0}{G} = \zeta\frac{\tau_0(z)r_0}{A_g(\alpha_g + z)^n} \tag{2.26}$$

Combining with the governing equation Eq.(2.14), we get the basic differential equation for the axial pile displacement

$$\frac{\partial^2 w_0(z)}{\partial z^2} = \frac{A_g}{\pi r_0^2 E_p}\frac{2\pi}{\zeta}(\alpha_g + z)^n w_0(z) \tag{2.27}$$

The solution of Eq.(2.27) takes the form of modified Bessel functions of the non-integer order. Again, the unknown constants can be found through the stress and deformation compatibility boundary conditions at the pile tip, i.e.,

$$w_0(L) = \frac{P_b\ (1-\nu)}{4\ r_0\ G}\ \eta = w_b \tag{2.28}$$

and

$$\left.\frac{\partial w_0(z)}{\partial z}\right|_{z=L} = -\frac{P_b}{\pi {r_0}^2 E_p} \tag{2.29}$$

After elaborate derivation, the final expression for the displacement and load at any depth of z can be expressed as

$$w_0(z) = w_b \left(\frac{\alpha_g + z}{\alpha_g + L}\right)^{1/2} \left(\frac{C_3(z) + \chi_v C_4(z)}{C_3(L)}\right) \tag{2.30}$$

$$P(z) = k_s E_p \pi r_0^2 w_b (\alpha_g + z)^{n/2} \left(\frac{\alpha_g + z}{\alpha_g + L}\right)^{1/2} \left(\frac{C_1(z) + \chi_v C_2(z)}{C_3(L)}\right) \tag{2.31}$$

where

$$\begin{aligned}
k_s &= \frac{\alpha_g + L}{r_0}\sqrt{\frac{2}{\lambda\zeta}}\left(\frac{1}{\alpha_g + L}\right)^{\frac{1}{2m}} \\
\chi_v &= \frac{2\sqrt{2}}{\pi(1-\nu)\eta\xi}\sqrt{\frac{\zeta}{\lambda}} \\
C_1(z) &= -K_{m-1}(L)I_{m-1}(y) + K_{m-1}(z)I_{m-1}(L) \\
C_2(z) &= K_{m-1}(L)I_{m-1}(y) + K_{m-1}(z)I_m(L) \\
C_3(z) &= K_{m-1}(L)I_m(y) + K_m(z)I_{m-1}(L) \\
C_4(z) &= -K_m(L)I_m(y) + K_m(z)I_m(L)
\end{aligned} \tag{2.32}$$

and I_m, I_{m-1} are modified Bessel functions of the first kind of non-integer order m, $m-1$ respectively. K_m, K_{m-1} are modified Bessel functions of the second kind of non-integer order m, $m-1$ respectively. The order m and variable y of the function can be calculated as $m = 1/(2+n)$, and $y = 2mk_s(\alpha_g + z)^{1/(2m)}$. The stiffness of the soil-pile system at any depth z can be determined as

$$\frac{P(z)}{w_0(z)} = \sqrt{2}\pi r_0 G_L \sqrt{\frac{\lambda}{\zeta}} C_v(z) \tag{2.33}$$

$$C_v(z) = \left(\frac{\alpha_g + z}{\alpha_g + L}\right)^{n/2} \left(\frac{C_1(z) + \chi_v C_2(z)}{C_3(L) + \chi_v C_4(z)}\right) \tag{2.34}$$

Hence we now have an analytical solution for the vertical variation in soil modulus; however, the soil is still assumed to be linearly elastic.

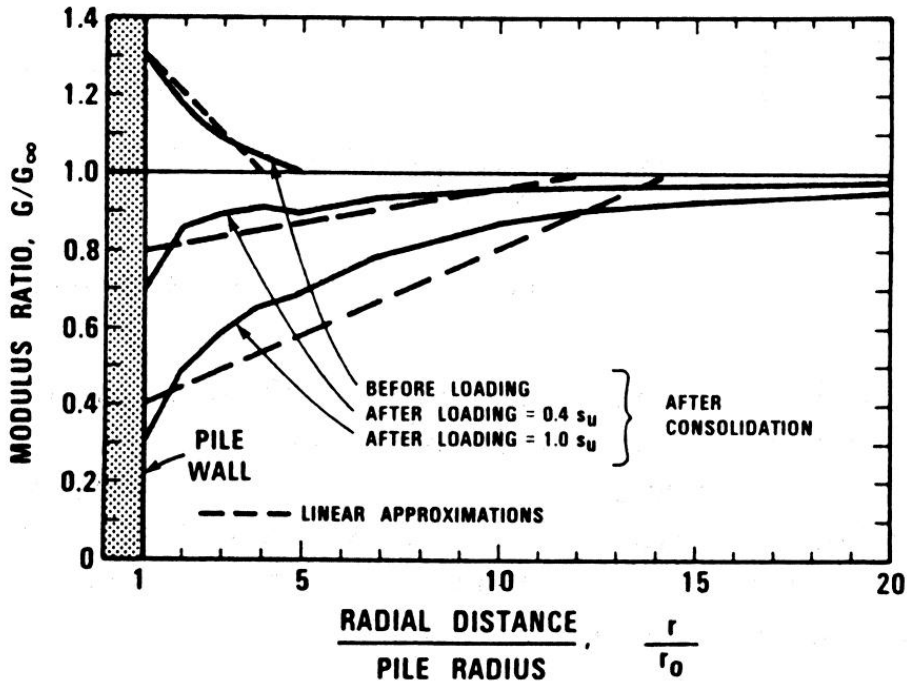

Fig. 2.1. Estimated Radial Distribution of Soil Modulus Ratio, from Kraft *et al.* (1981)

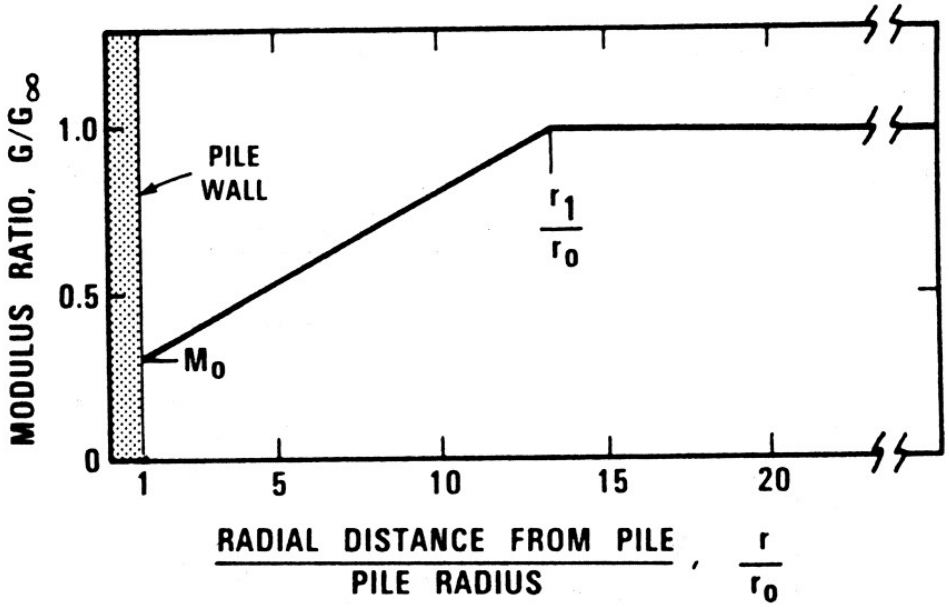

Fig. 2.2. Idealized Radial Distribution of Soil Modulus Ratio, from Kraft *et al.* (1981)

2.1.3 Radial Variations in Soil Modulus

In practice, the radial variation in the soil modulus may be the result of pile installation, and soil consolidation and, more significantly, due to reduction in the soil modulus at large strains associated with pile loading especially as the pile capacity is reached or exceeded. As schematically illustrated in Fig. 2.1, after pile-driving compaction and consolidation, the soil modulus becomes stiffer around pile wall. Loading of the pile results in significant reduction in the soil modulus. The reduction depends on load intensity and can be approximated by a linear variation in radial direction.

Novak and Sheta (1980) were the first to examine the importance of the highly non-linear region around the pile. They divided the soil around the pile into an outer and inner hollow cylinder with distinctive modulus assigned. Hence the radial variation in the soil modulus is prescribed in a piecewise constant manner. Kraft *et al.* (1981) proposed a linear variation in the modulus (Fig. 2.2) based on cavity expansion and consolidation results by Randolph *et al.* (1979). The average soil modulus for this case can be evaluated as

$$G_{ave} = G_{\infty} \frac{\ln\left(\frac{r_m}{r_0}\right)}{\frac{\left(\frac{r_1}{r_0}\right) - 1}{\left(\frac{M_0 r_1}{r_0}\right) - 1} \ln\left(\frac{M_0 r_1}{r_0}\right) + \ln\left(\frac{r_m}{r_1}\right)} \tag{2.35}$$

in which G_{ave} = equivalent shear modulus for the soil-pile system; G_{∞} = shear modulus at great distance from pile; and r_1, M_0 are defined in Fig. 2.2.

2.1.4 Soil Nonlinearity

The theoretical work of Randolph and Wroth (1978) can be extended to consider the non-linear stress-strain behavior of soils. Recall that the load-displacement relationship at the pile shaft is given by Eq. (2.7),

$$w_0 = \tau_0 r_0 \int_{r_0}^{r_m} \frac{dr}{Gr} \tag{2.36}$$

The following hyperbolic shear stress - shear strain relationship was considered by Kraft *et al.* (1981),

$$G = G_i \left(1 - \frac{\tau R_f}{\tau_f}\right) = G_i \left(1 - \psi\right) \tag{2.37}$$

in which G_i = initial small strain shear modulus; G = *secant* modulus at applied stress level; τ = shear stress; τ_f = shear stress at failure; R_f = hyperbolic curve-fitting constant, it takes value R_{fs} for the shaft and R_{fb} for the tip reaction; $\psi = \tau R_f/\tau_f$ is defined as a nondimensional parameter for loading intensity, and it has assumed values ψ_s for points along the shaft and ψ_b at the pile tip.

Utilizing Eqs. (2.36) and (2.37), the following load-transfer relationship can be obtained (Kraft *et al.*, 1981):

$$w_0 = \frac{\tau_0 r_0}{G_i} \ln\left(\frac{r_m/r_0 - \psi_s}{1 - \psi_s}\right) \tag{2.38}$$

From which the *secant* stiffness for the pile shaft segment of unit length can be obtained as

$$k_s^{shaft} = \frac{2\pi G_i}{\ln\left(\dfrac{r_m/r_0 - \psi_s}{1 - \psi_s}\right)} \tag{2.39}$$

where $\psi_s = \tau_0 R_f/\tau_f$ is the loading intensity parameter evaluated at points along the shaft. The result coincides with the Randolph-Wroth solution if linearly elastic soil (i.e., $\psi_s = 0$) is assumed.

To facilitate incremental load-displacement analysis, the secant modulus in Eq.(2.37) can be replaced by a corresponding *tangent* modulus as

$$G_t = G_i \left(1 - \frac{\tau R_f}{\tau_f}\right)^2 = G_i \left(1 - \psi\right)^2 \tag{2.40}$$

The resulting *tangent* stiffness for the pile shaft segment of the unit length can also be obtained (Chow, 1986) as:

$$k_t^{shaft} = \frac{2\pi G_i}{\ln\left(\dfrac{r_m/r_0 - \psi_s}{1 - \psi_s}\right) + \dfrac{\psi_s \left(r_m/r_0 - 1\right)}{(r_m/r_0 - 1)(1 - \psi_s)}} \tag{2.41}$$

and the *tangent* stiffness for the tip is:

$$k_t^{tip} = \frac{4 G_i r_0}{1 - \nu}(1 - \psi_b)^2 \tag{2.42}$$

in which $\psi_b = P_b R_{fb}/P_f$; P_b = mobilized tip load; P_f = limiting tip load; and ν= Poisson's ratio at the pile tip. Based on limited experience Poulos (1989) suggests the following hyperbolic curve fitting constants: $R_{fs} = 0 \sim 0.5$ and $R_{fb} \approx 0.9$. It is interesting to note that the above formula coincides with Randolph-Wroth solution Eq.(2.24) at the initial loading stage ($\tau_0 \to 0$), or for the special case of linearly elastic soil ($R_{fs} = R_{fb} = 0$).

For some other cases of nonlinear soil behavior, the equivalent stiffness of the soil-pile system has also been derived analytically. For example, the viscoelastic effect has been accounted for by integration of a generalized visco-elastic stress-strain model for the soil (Guo, 2000b).

2.2 ANALYTICAL DYNAMIC LOAD TRANSFER MODELS

2.2.1 Dynamic Stiffness of SDF System

To illustrate the concept of dynamic stiffness, it is convenient to examine a single-degree-of-freedom (SDF) dynamic system consisting of a mass M, a spring k, and a dashpot c, subjected to external load F. The governing equation for the system is

$$M\ddot{u}(t) + c\dot{u}(t) + ku = F(t) \tag{2.43}$$

The natural frequency of the undamped system, ω, can be determined by the spring stiffness k and mass M,

$$\omega = \sqrt{\frac{k}{M}} \tag{2.44}$$

It is also customary to introduce the fraction of critical damping given by

$$\beta = \frac{c}{2\sqrt{kM}} = \frac{1}{2}\frac{c}{k}\omega \tag{2.45}$$

The analytical solutions of this simple system are briefly reviewed here because the various terms appear later in other formulations.

(1) Free vibration: Free vibration of a SDF system induced by the prescribed initial displacement u_0 of the mass is exponentially damped harmonic oscillation of the form

$$u = u_0 e^{-\beta\omega t}\left(\cos\omega_D t + \frac{\beta\omega}{\omega_D}\sin\omega_D t\right) \tag{2.46}$$

where the damped natural frequency $\omega_D = \omega\sqrt{1-\beta^2}$, and the period of vibration $T = \dfrac{2\pi}{\omega_D}$. The amplitude of the vibration after each cycle is damped by a constant factor as follows,

$$\frac{u(t)}{u(t+\frac{2\pi}{\omega_D})} = e^{2\pi\beta\omega/\omega_D} = e^{2\pi\beta/\sqrt{1-\beta^2}} \tag{2.47}$$

and the above solution is often used in a small strain dynamic test, such as the resonant column test, to determine the damping coefficient β or c.

(2) Harmonic excitation: A harmonic load F with frequency Ω

$$F = P\sin\Omega t \tag{2.48}$$

results in steady-state vibration of the system given by a harmonic function with phase delay Ψ,

$$u = A\sin\left(\Omega\ t + \Psi\right) \tag{2.49}$$

where the amplitude $A = \dfrac{P}{\sqrt{(k-M\Omega^2)^2 + 4\beta^2\Omega^2/\omega^2}} = \dfrac{P}{\sqrt{(k-M\Omega^2)^2 + c^2\Omega^2}}$, and the phase is delayed by $\tan\Psi = -\dfrac{2\beta\Omega/\omega}{1-\Omega^2/\omega^2} = -\dfrac{c\Omega}{k-\Omega^2 M}$

With the steady-state solution of harmonic excitation, it is straightforward to generalize the above solution to an external load F of the following complex form

$$F = Pe^{i\Omega t} \tag{2.50}$$

and the displacement solution is given by

$$u = Ae^{i(\Omega t+\Psi)} \tag{2.51}$$

The real and imaginary part of u correspond to the steady-state response of external excitations $P\cos\Omega t$ and $P\sin\Omega t$, respectively.

The dynamic stiffness k^*, also in complex form, can be introduced to relate the force and displacement as

$$F = k^* u \tag{2.52}$$

and direct calculation reveals k^* is quantified as

$$k^* = (k - M\Omega^2) + i\ c\ \Omega = k(k_1 + ik_2) \tag{2.53}$$

where $k_1 = 1 - \dfrac{\Omega^2}{\omega^2}$ and $k_2 = \dfrac{2\beta\Omega}{\omega}$.

Although the dynamic stiffness is cast as a complex number, Eq. (2.53) has direct physical meaning. The real part of dynamic stiffness includes the effects of spring stiffness k and inertia M, and is a quadratic function of frequency Ω, while the imaginary part represents energy dissipation through viscous damping c, and is a linear function of frequency Ω. The energy dissipation by viscous damping can be evaluated through the ratio of the dissipated energy to the maximum strain energy per cycle as

$$ER = \frac{\pi c \Omega A^2}{\frac{1}{2} k A^2} = 4\pi \frac{\beta \Omega}{\omega} = 2\pi \frac{c\Omega}{k} \tag{2.54}$$

(3) Linearized hysteretic system: Physical systems rarely have an actual viscous dashpot. Thus, the assumption of linear viscous damping is useful mainly for its mathematical simplicity, since it is easier to get the analytical solution of linear ODE with constant coefficients than a nonlinear differential equation. For the nonlinear hysteretic spring, the equivalent linear system can be defined to match the load-displacement relation and the energy ratio. At a given amplitude of motion, the equivalent secant stiffness k_{eq} can be determined from the load-displacement relation, and the damping ratio D can be defined as

$$ER = \frac{\Delta W}{W} = 4\pi D \tag{2.55}$$

As an analogy to Eq. (2.53), the dynamic stiffness of the equivalent system is determined as

$$k^* = k_{eq} \left(1 - \frac{\Omega^2}{\omega_{eq}^2} + 2\ i\ D \right) \tag{2.56}$$

with

$$\omega_{eq} = \sqrt{\frac{k_{eq}}{M}} \tag{2.57}$$

In this formulation the hysteretic damping ratio, D, is independent of frequency. The key point of Eq. (2.56) is to replace the original nonlinear system with a linear hysteretic system such that the secant load-displacement relation and energy ratio are preserved. This is also equivalent to a viscous system with c inversely proportional to frequency.

Finally, the dynamic stiffness of combined system with hysteretic spring and viscous damping c can be found via simple addition if c is not affected by spring nonlinearity

$$k^* = k_{eq} \left[1 - \frac{\Omega^2}{\omega_{eq}^2} + 2\ i\ \left(D + \frac{\beta \Omega}{\omega_{eq}} \right) \right] \tag{2.58}$$

As mentioned above, the linearization is equivalent in terms of the secant load-displacement relation and energy dissipation. While this simplification captures the key aspects of dynamic behavior, the real time-history of the load and deformation is not followed and the quantitative evaluation of the actual tangential stiffness is very difficult. Hence, the approximation is good only to the first order and is suitable for the steady-state harmonic oscillation.

2.2.2 Equivalent Linearization of Axial Response of Piles

Equivalent linearization is frequently employed to derive the appropriate properties for a dynamic soil-pile system. Early approximate solutions are mainly based on the assumption that soils are radially homogeneous. Novak and Sheta (1980) were among the first to include the highly nonlinear region around the pile. In their model, the soils are divided into an outer infinite region and a massless inner layer (hollow cylinder) surrounding the pile, as shown in Fig. 2.3. Soil nonlinearity, as well as weakened bond and slippage are approximately accounted for by a reduced shear modulus and increased material damping of the inner layer. Both soil zones are assumed to be homogeneous, isotropic and viscoelastic with frequency-independent material damping (linear hysteretic damping).

Axial stiffness of the composite system can be obtained by assuming that the mode of displacement is predominately under vertical harmonic excitation, and that horizontal displacement can be ignored; i.e., vertical displacement $w(t) = w(r) \exp i\Omega t$ with harmonic motion of frequency Ω. For this linear viscoelastic system, the governing differential equation for a vertically excited soil layer of unit thickness is

$$G^* \frac{\partial^2 w}{dr^2} + \frac{G^*}{r} \frac{\partial w}{\partial r} = \rho \frac{\partial^2 w}{\partial t^2} \tag{2.59}$$

where G^* is the complex stiffness of soil, with its real part representing shear modulus, and its imaginary component taking into account the hysteretic material damping. Eq. (2.59) holds for all media, except that the inner cylinder is assumed massless ($\rho = 0$), which is necessary to eliminate spurious wave reflections across the interface of two distinct soil regions. Further assumptions are made such that there is no separation between the soil and pile, and the pile cylinder is rigid, circular, and infinitely long. Considering the displacement compatibility condition between the interface of two soil regions, the dynamic axial stiffness of the soil-pile

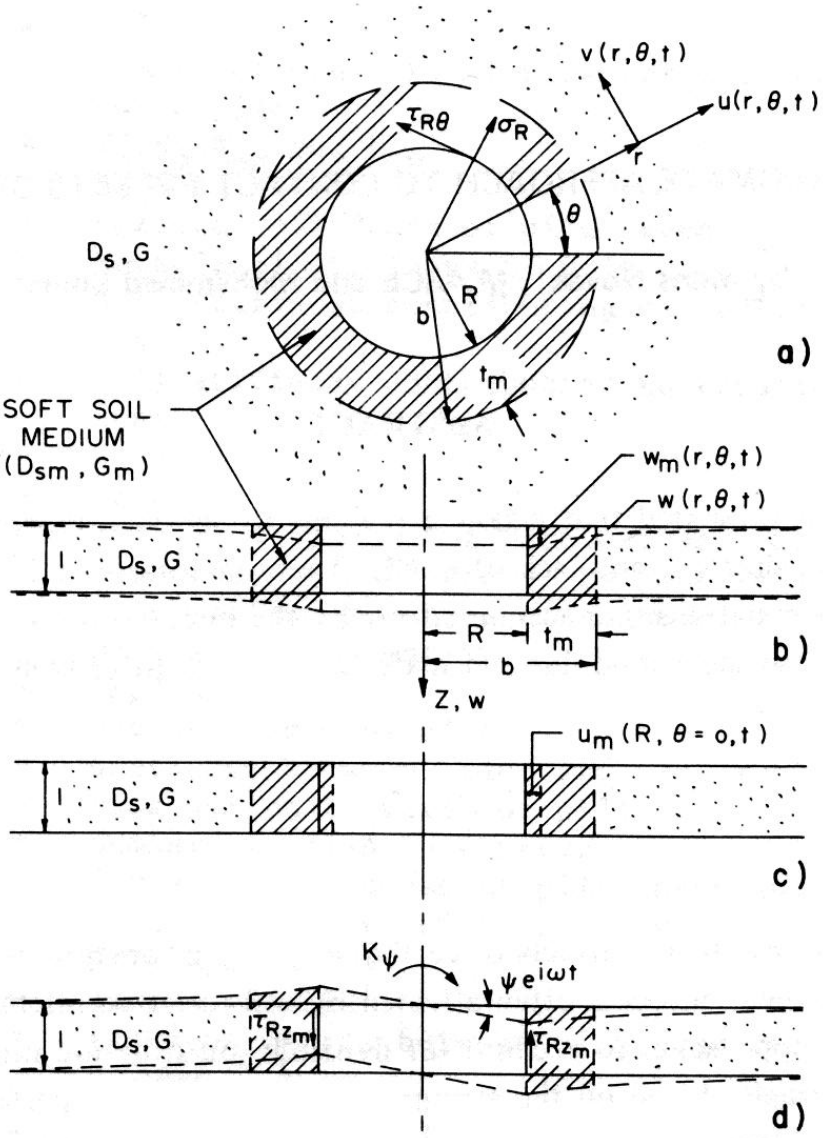

Fig. 2.3 Composite Soil Medium, from Novak and Sheta (1980)

system can be derived explicitly from Eq. (2.59) as

$$k_w^* = \frac{2\pi G_m^*}{-\ln\dfrac{R}{b} + \dfrac{G_m^*}{G_s^*}\dfrac{K_0(sb)}{(sb)\ K_1(sb)}} = G(S_{w1} + iS_{w2}) \tag{2.60}$$

where $G_s^* = G(1 + iD_s)$ is the complex stiffness of the outer soil region, $G_m^* = G_m(1 + iD_{sm})$ is the complex stiffness of the inner soil region, and K_0 and K_1 are modified Bessel functions of order zero and order one, respectively. Parameter b is the radius of the soil interface, $s = \dfrac{\Omega\ i}{V_s\sqrt{1+iD_s}}$, $V_s = \sqrt{G/\rho}$, and R is the pile radius. The dimensionless stiffness and damping parameters S_{w1} and S_{w2} depend on the dimensionless frequency parameter ($a_0 = R\Omega/V_s$), inner layer and pile radius ratio, as well as stiffness and damping contrast between inner and outer soil layers.

Further development includes considering continuous radial variation of soil stiffness (secant modulus), as proposed by Gazetas and Dobry (1984) and later refined by Michaelides *et al.* (1997). As shown in Eq.(2.3), shear stresses developed in the soil are inversely proportional to the radial distance from the pile. The radial variation of stress and strain requires a strain compatible shear modulus to be used in the analysis. The idea is to replace the actual nonlinear but radially homogeneous soils with linear but radially inhomogeneous soils through equivalent linearization procedure. The governing differential equation for a vertically excited soil layer taking account of radial variation in modulus is modified as,

$$G^*\frac{d^2w}{dr^2} + \left(\frac{dG^*}{dr} + \frac{G^*}{r}\right)\frac{dw}{dr} = \rho\frac{\partial^2 w}{\partial t^2} \tag{2.61}$$

where $G^* = G(1 + 2\ i\ \xi)$ is the complex stiffness of the soil. Using experimental data from Vucetic and Dobry (1991), Michaelides *et al.* (1997) proposed the following variation of shear modulus and damping ratio

$$\frac{G(r)}{G_{max}} = 1 - \left\{\Lambda\frac{R}{r}F(a_r)\right\}^{0.72} \tag{2.62}$$

$$\xi = \begin{cases} 2 + [18 - 0.08(I_p - 15)](1 - G/G_{max}) & \text{if} \quad 0 \le I_p < 100 \\ 2 + 11.2(1 - G/G_{max}) & \text{if} \quad I_p \ge 100 \end{cases} \tag{2.63}$$

where Λ is called the loading intensity factor. It can be related to the amplitude of imposed cyclic shear stress at the soil-pile interface (τ_0), and the plasticity index of the soil ((I_p)) as follows

$$\Lambda = 2700\frac{\tau_0}{G_{max}}10^{-(1.4I_p/\lambda)} \tag{2.64}$$

and λ is a function of plasticity index I_p

$$\lambda \approx 0.002(I_p)^2 + 0.25(I_p) + 60 \tag{2.65}$$

The radial distribution function

$$F(a_r) \approx \begin{cases} 1 & \text{if} \quad a_r < 1 \\ a_r^{0.57} & \text{if} \quad a_r > 1 \end{cases} \tag{2.66}$$

where the argument is a dimensionless frequency parameter defined as

$$a_r = r\ \Omega / V_s(r) \tag{2.67}$$

and Ω is the frequency of excitation. Unfortunately, the introduction of Eq.(2.62) precludes an analytical solution of Eq.(2.61). Instead, Eq.(2.62) can be fitted piecewisely by polynominals, leading to a solution in terms of Hankel functions.

The complex stiffness of soil-pile system, $k_w^* = k_w + i\ c_w\Omega$ can also be obtained. Michaelides *et al.* (1997) showed that with increasing load intensity factor Λ, soil nonlinearity increases, and the equivalent stiffness k_w of the soil-pile system decreases. The damping c_w includes both the hysteretic damping of the soil and radiation damping of the infinite space. The former increases and the latter decreases with increasing nonlinearity.

2.3 NUMERICAL METHODS

While analytical models are theoretically sound, but their limitations are that the site condition and material properties have to be overly simplified. Numerical methods have been introduced in recent years because, theoretically, they offer much greater flexibility in modelling complex problems including heterogeneity, anisotropy and nonlinearity. In this section, we review four types of most frequently used numerical methods in pile simulation: wave equation analysis, the nonlinear Winkler model, the boundary element method and the finite element method.

2.3.1 Wave Equation Analysis

From the pile design perspective, pile behavior derived from the pile-driving test itself is desirable, since it has the advantage for both cost savings and incorporation of the site-

specific condition. The initial attempts of this kind can be traced back to various dynamic pile formulas proposed over the last 100 years. The dynamic formulas are usually based on Newtonian mechanics of rigid body impact, and use only the simplest measurement available (i.e., permanent set per hammer blow). In general, dynamic formulas are empirical in nature and the predictions are not satisfactory.

It was not until the early 1930s that researchers realized that the pile-driving mechanism is more of a wave propagation problem and that the effects of soil-pile interaction should also be addressed. For these purposes, the Smith model is perhaps the most widely accepted in practice (Smith, 1960). The model introduces a one-dimensional wave equation to analyze the elastic pile subjected to hammer blows and the induced soil resistance. As illustrated in Fig. 2.4, the pile segments and driving elements (ram, capblock, and the pile cap) are idealized by a series of discrete weights and springs. Simple constitutive relations are specified for the capblock, and the soil resistance at any depth along the pile is modeled by an elastic-perfectly plastic spring and dashpot in parallel. The one-dimensional wave equation to the discrete system is solved by a simple numerical integration to provide the response of each weight and spring for each time step. Since pile driving usually generates a fairly long wave form, Smith recommended the division of the pile into lengths of 5 ft to 10 ft and a time interval of about $1/4,000$ second for a computational step. Although numerous improvements have been made ever since, Smith's model continues to form the basis for modern wave equation analysis.

One of the major applications of wave equation analysis is to estimate the pile capacity from force and velocity measurements during pile driving. Researchers from the Case Institute of Technology (now Case Western Reserve University) developed a computer program called CAPWAP ©(CAse Pile Wave Analysis Program) in the late 1960's to fully take advantage of the accurate force and acceleration measurements from the driving system (Rausche, 1970). Based on wave theory, the Case method evolves to a "signal matching" iterative process: Direct measurements at the pile top for each hammer blow (usually the velocity integrated from the measured acceleration) are used as input to replace the hammer model. The computed force is then compared with the measured force, therefore soil resistance distribution can be back-analyzed accordingly to generate a good agreement between these two records (Rausche *et al.*, 1972). It is also shown that the resistance distribution

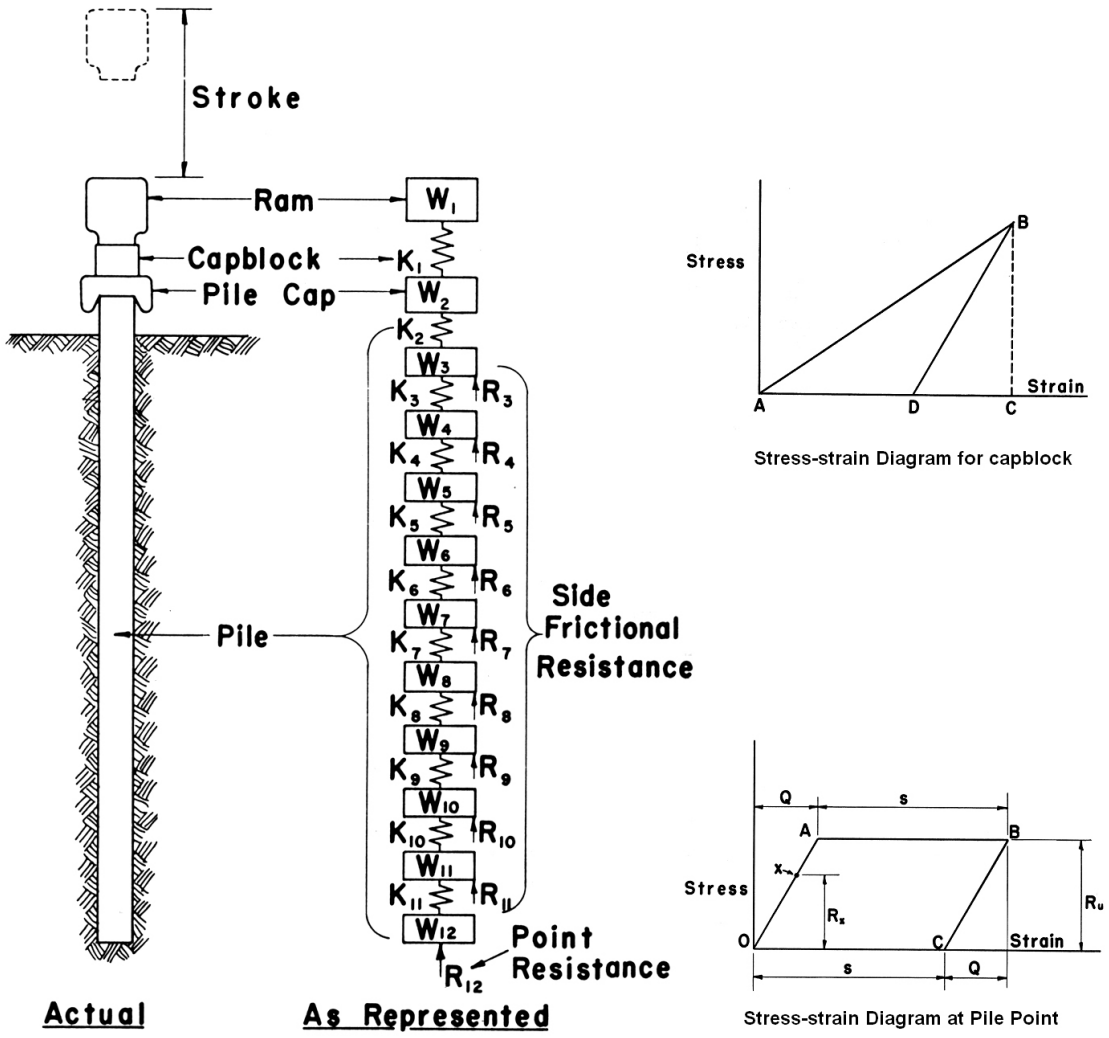

Fig. 2.4 Smith Model for Pile Driving Analysis, from Smith (1960)

calculated by CAPWAP is unique, from which the total pile capacity can be reasonably estimated. The static pile capacity can also be obtained by subtracting the dynamic part from the total driving resistance, which is usually assumed to be in proportion to the pile tip velocity (Rausche *et al.*, 1985). Several guidelines were also proposed in order to obtain reliable pile capacity prediction. For example, the hammer impact energy during the test should be sufficient to fully mobilize the soil resistance. If the hammer input is small, the method will result in a conservative prediction, since the dynamic test will activate only a portion of pile resistance. Also, due to setup or relaxation effects, the pile capacity can change with time, so the dynamic method gives only the static capacity at the time of testing. Restrike tests are recommended after an appropriate waiting period to obtain the long-term pile capacity (Likins, 2004).

Because of the simplicity and the capacity to be calibrated with field pile-driving tests, the wave equation method and computer programs have found wide application in industry. It is estimated that over 5000 job sites are tested and analyzed annually based on this method. The on-going *International Conference on the Application of Stress-Wave Theory to Piles* has been devoted to exercise this approach in the past twenty years, and a large amount of literature has been accumulated from the conference proceedings. A much-detailed historical account of the development can be found in a recent review paper by Hussein and Goble (2004).

However, the wave equation analysis method today still suffers many drawbacks. One major limitation is its reliance on an overly simplistic soil model, which cannot described the dynamic response of the soil accurately. Parameters used for the soil, namely the maximum elastic deformation (termed as the "Quake" Q) and damping coefficients, are non-standard and empirical in nature. It has been recognized that these parameters are not a function of soil only, but also depend on pile properties. Since they cannot be independently obtained from laboratory tests and then used in the analysis, there has been much debate on how to sensibly choose them. Typically, they should be back-analyzed from the prototype field tests or empirical correlations. Furthermore, discretization of a pile as a number of masses and springs for wave equation analysis leads to discrete fields of displacement, velocity and acceleration over the pile length, and the solution could be considerably improved if a continuous interpolation and implicit time integration scheme was used; see Borja (1988). Since

the soil is modelled only through distributed reaction forces, inertial effect of the soil mass is not considered. Significant energy loss by wave radiation from the pile to the soil mass is also absent in the modelling. More importantly, the method is designed for estimating the capacity of piles, and it is not suitable for the general purpose of soil-pile interaction modelling.

2.3.2 Nonlinear Winkler Foundation Model

To analyze soil-pile interaction, the nonlinear Winkler foundation model is widely used due to its simplicity. This model idealizes the effect of the soil surrounding the pile into a combination of discrete springs, sliders, dashpots, lumped masses, with each component representing the effect of soil nonlinearity, pile-soil slip and separation (gapping), energy dissipation, inertia etc. In this section, we give a few examples to illustrate the main features of this method.

In the case of a dynamic axially loaded pile, strong nonlinear soil-pile interaction occurs in the near field, and the far field soil is primarily linear elastic. El Naggar and Novak (1994b) presented a nonlinear Winkler foundation model as shown in Fig. 2.5, where the soil is differentiated into a slip zone, an inner field and an outer field. Masses are lumped in soil nodes of the inner field to account for inertial effect. The slip zone is a rigid plastic slider between the pile and soil nodes, enabling slippage between the pile and soil at a limiting load. The inner soil field can develop high nonlinearity, and it can be modelled, for example, by a hyperbolic stress-strain relation suggested by Kondner (1963),

$$\frac{\gamma}{\gamma_r} = \frac{\eta}{1-\eta} \tag{2.68}$$

where $\eta = \tau/\tau_f$ in which τ_f is the ultimate shear strength; $\gamma_r = \tau_f/G_{max}$ is the reference shear strain, and G_{max} is the maximum soil shear modulus at small strain. Equivalent linearized stiffness and hysteresis damping parameters are assigned to soil springs and dashpots. As derived in previous sections, the equivalent stiffness of the inner field spring for a unit of the shaft length, after integrating the stress-strain relation over the thickness of the inner zone

and the perimeter of the shaft, can be expressed as

$$K_{nl} = \frac{2\pi G_{max}}{\ln\left(\dfrac{r_1/r_0 - \eta_0}{1-\eta_0}\right)} \tag{2.69}$$

where $\eta_0 = \dfrac{\tau_0}{\tau_f}$ represents the loading intensity, τ_0 is stress at pile surface ($r = r_0$), and r_0,r_1 are the pile and inner field radii, respectively. To model the hysteretic behavior of the soil, unloading stiffness can be assumed completely elastic as

$$K_{nl} = \frac{2\pi G_{max}}{\ln\left(\dfrac{r_1}{r_0}\right)} \tag{2.70}$$

Since stress intensity is usually low in the outer field, the outer field soil can be modelled by an elastic spring with a dashpot for radiation damping. The linear stiffness K_l and damping parameter C should be chosen to accurately represent radiation damping, and they can be approximated for example by the plane strain solution for an infinitely long massless cylinder vibrating in an infinite elastic medium (Novak *et al.*, 1978) as,

$$K_l = G_{max}\, S_1 \tag{2.71}$$

$$C = \frac{G_{max} r_0}{V_s}\, S_2 \tag{2.72}$$

where S_1 and S_2 are constants, and they can be chosen based on the dominant dimensionless frequency parameter $a_0 = \Omega r_0/V_s$, where Ω is the frequency of excitation, r_0 is the pile radius, and V_s is the shear wave velocity of soils.

The Winkler model can also incorporate the loading rate effect and cyclic stiffness degradation by proper modification of the ultimate resistance and loading/unloading stiffness of the nonlinear soil spring (El Naggar, 2004). In the case of a dynamic laterally loaded pile, a more sophisticated model by Boulanger *et al.* (1999) is also capable of simulating drag force, gapping and closure etc. The nonlinear $p - y$ behavior is conceptually divided into three components in a series, namely, the elastic component ($p - y^e$), plastic component ($p - y^p$), and gap component $p - y^g$, shown in Fig. 2.6(a). Radiation damping is included by a dashpot in parallel with the elastic components. The effect of gapping is modeled by a drag and closure nonlinear springs in parallel. Physically, the drag force is caused by mobilized residual soil resistance on the sides of the pile as it moves within the gap, and its maximum value can be set as a suitable portion of the ultimate capacity. Component

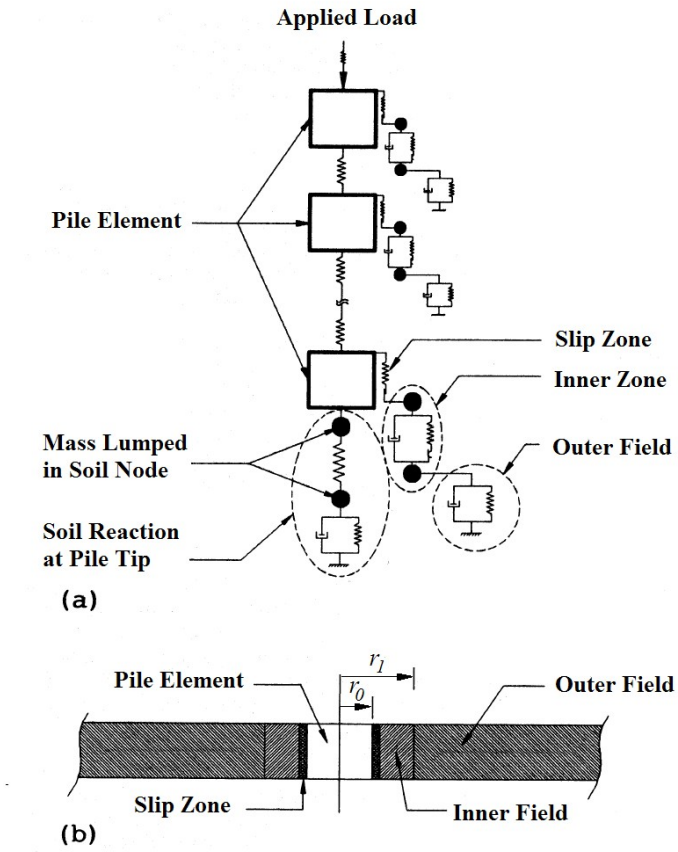

Fig. 2.5. Nonlinear Winkler Model for Dynamic Analysis of a Single Pile, from El Naggar and Novak (1994b)

behavior and combined response are shown in Fig. 2.6(b). The reliability of the Winkler model was validated through a series of centrifuge model pile tests.

In the past, researchers have used a variety of dashpot-spring combinations, and there is no unanimous agreement on the details of the arrangement. The predicted response for various combinations of nonlinear springs (representing nonlinear soil response in the near field) and linear viscous dashpots (representing radiation damping in the far field) has been examined by Wang *et al.* (1998) and compared with model pile centrifuge tests. They concluded that combination in a series is technically superior to a parallel arrangement, since the latter would produce excessive damping forces and the viscous force may dominate (or pollute) the solution. Serial arrangement is also more representative of the physics, since energy tends to pass successively from the near field to the far field. Hence, if serial radiation damping is used, the solution depends more sensitively on the soil properties and improves the predicted frequency content of the system.

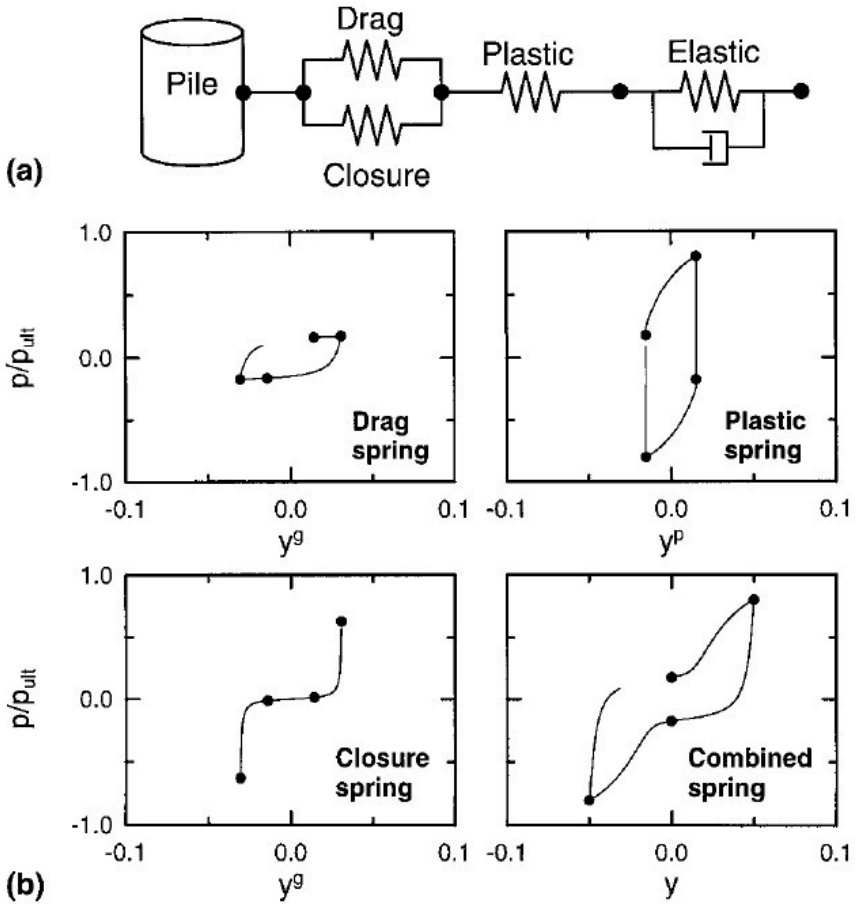

Fig. 2.6 A Nonlinear $p-y$ Element, from Boulanger *et al.* (1999)

In a seismic soil-pile interaction analysis, the response of the free-field soil column can be analyzed separately using an equivalent linear site response program such as SHAKE (Schnabel *et al.*, 1970; Idriss and Sun, 1991). The free field response is then prescribed as input motion to the Winkler soil at depths. Alternatively, a hybrid Winkler and finite element model can be used, as schematically illustrated in Fig. 2.7. In this model, a far-field soil column is modelled by finite element to generate site-specific ground motion input for near-field soils, where highly nonlinear interactions between the pile and near-field soils are modelled through the discrete springs and dashpots. Various empirical rules were proposed by Bea *et al.* (1984) for initial loading, unloading/reloading, load reversal, gapping and cyclic degradation etc., as shown in Fig. 2.8. The system has the capacity to analyze cyclic, strain rate, gapping, and damping effects for piles embedded in cohesive and cohesionless soils.

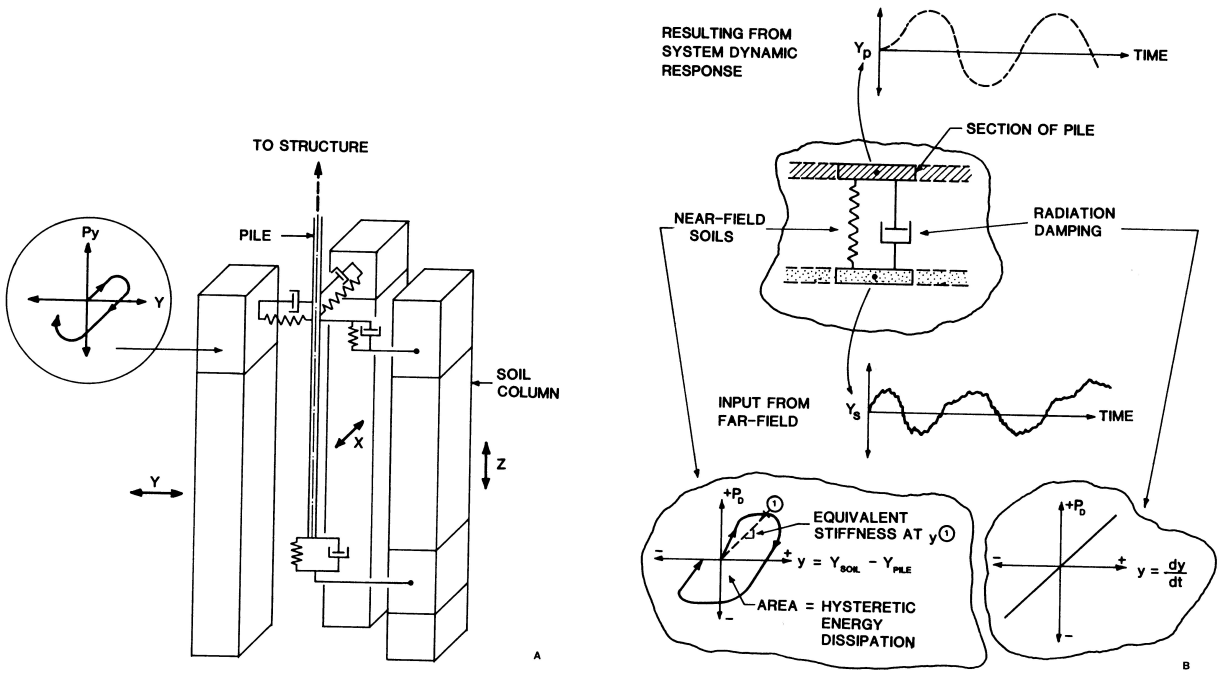

Fig. 2.7 Pile Soil Analysis System, from Bea *et al.* (1984)

In summary, the Winkler method has been extensively developed and used in the past due to its simplicity. The model has been reported to give a satisfactory result for geometrically simple soil-structure systems. However, the performance of the Winkler method is still debatable if it is applied to more complex systems or pile group. Disregarding soil continuity makes it impossible to model pile-to-pile interaction rigorously, albeit a few approximations have been proposed to incorporate the group effect, for example, see El Naggar and Novak (1994a); Mostafa and El Naggar (2002). More importantly, simplification of the continuum soil into discrete springs and dashpots makes model parameters empirical or semi-empirical in nature. They are not intrinsic soil properties but also depend on the pile properties and loading conditions. For most cases, they have to be adjusted to fit the experimental data. The shortcomings may be removed by means of continuum-based numerical methods, particularly by the boundary element method and the finite element method.

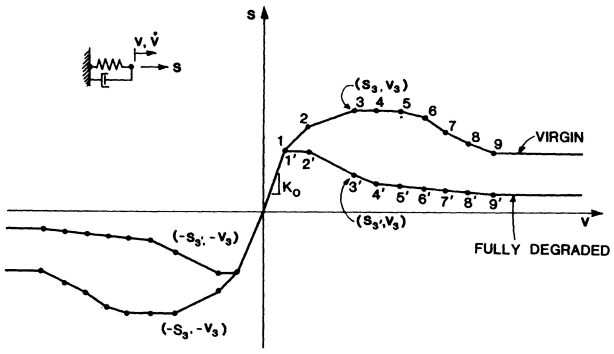

Rule 1: Initial loading (backbone) curve

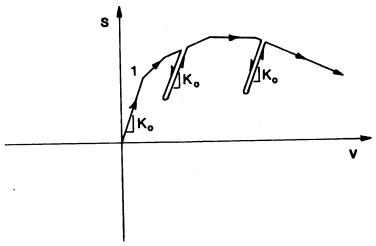

Rule 2: Unloading / reloading

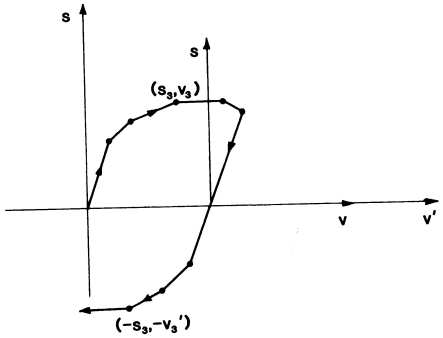

Rule 3: Load reversal

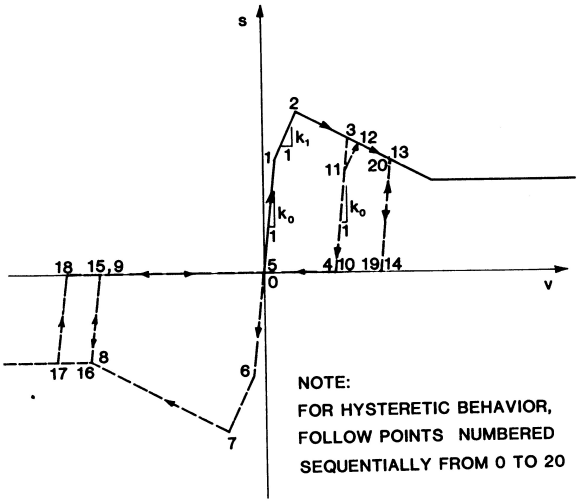

Rule 4: Load reversal — full gap

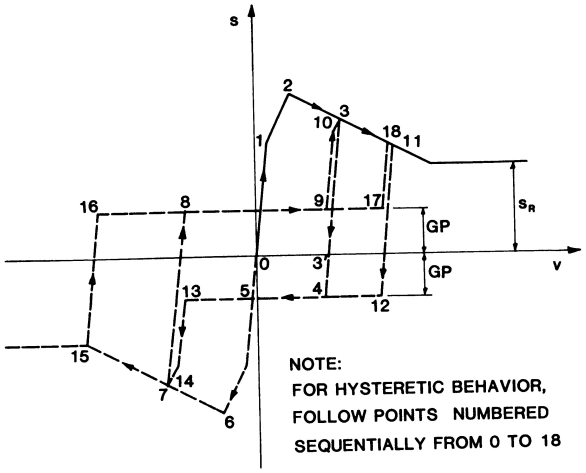

Rule 5: Load reversal — partial gap

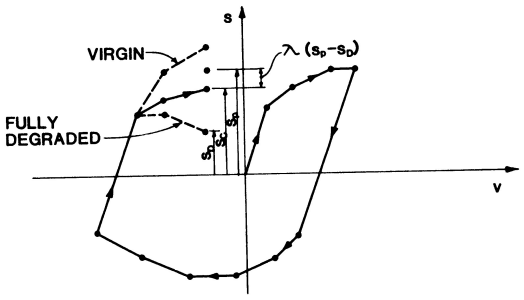

Rule 6: Cyclic degradation

Fig. 2.8 Generalized Nonlinear Rules, from Bea *et al.* (1984)

2.3.3 Boundary Element Method

The boundary element method (also known as the integral equation method) is probably among the earliest continuum methods developed for the soil-pile interaction analyses. Compared to other continuum methods, such as the finite element method, the boundary element method has considerable advantage of computational efficiency, since only the boundary of the simulation domain needs to be discretized. For a pile embedded in a infinite soil, only the ground surface and soil-pile interface need to be meshed.

In the discrete setting, the boundary element method calculates displacement in the k direction at node i (written as w_{ki} with two subscript indices) as the summation of contribution from the nodal force P_{kj} in the k direction acting on node j over all nodes,

$$w_{ki} = \sum_{j=1}^{n} f_{ij} P_{kj} \tag{2.73}$$

where f_{ij} is the flexibility coefficient, representing the displacement at node i due to unit point load at node j, and n is the total number of nodes.

The flexibility coefficient crucially depends on fundamental solutions of a given material property and geometry. To date, only a few closed-form solutions exist for the simplest materials. Mindlin's solutions (Mindlin, 1936) for a point load in the interior of an elastic *half space* is usually employed in most boundary element analyses; however, the solution is suitable only for piles embedded in homogeneous, isotropic and elastic soils.

Many ad-hoc procedures have been proposed in the past to extend the boundary element method to suit for more realistic soil responses and distributions. Considering a pile embedded in a horizontally layered soil where the moduli of adjacent layers differ abruptly, Poulos (1979), Lee and Poulos (1990) suggested an empirical modification of the soil moduli and used them in Mindlin's solutions. The modified soil modulus is a weighted average taking into account the stiffness differences and distances between layers empirically. More theoretically sound approaches directly take advantage of fundamental solutions for layered soils. Although solutions for general multi-layered soil profile are not available at the present, solutions for a point load in the *interior* and the *interface* of a two-layered elastic half-space (Chan *et al.*, 1974; Davies and Banerjee, 1978) have been used (Chin *et al.*, 1990).

Since the development of the boundary element method requires the availability of the

fundamental solution, severe restriction is imposed on the constitutive behavior of modelled materials. Poulos and Davis (1980) devised an approximate method to treat the effect of pile-soil slippage by loosening the constraint of vertical displacement compatibility. It should be noted that soil displacements in their analyses are still given by elastic theory. The dynamic problem is also cumbersome to solve in the time domain. Although time-domain boundary element methods were proposed to analyze the transient response of a vertical pile, for example in (Tham *et al.*, 1996), the development is mainly limited to elastic soil. More sophisticated material behavior such as nonlinearity, plasticity, hardening, and strain localization, and more complex soil stratigraphy are, if not impossible, extremely difficult to accommodate in boundary element analyses. With the advancements in computational technology, computational costs are no longer a major concern. As a result, at present, the interest in boundary element methods is diminishing, and the current trend is in favor of more powerful and flexible finite element methods.

2.3.4 Finite Element Method

Although nonlinear discrete systems have been extensively used due to its simplicity, severe limitations remain in the proper assessment of the empirical model parameters. With the advancement of computing technology, the finite element method is increasingly attractive as a versatile and powerful tool for realistic soil-structure interaction analyses.

Early finite element simulations of soil-pile interaction employed simple constitutive relations to represent soils. Ottaviani (1975) assumed that the pile was embedded in linearly elastic and homogeneous soil and studied a vertical loaded single pile as well as a pile group. Amir and Sokolov (1976) also modelled the soil as linearly elastic to study the behavior of piles in expansive soils. A trilinear elastic stress-strain relationship for soils was used by Ellison *et al.* (1971) to study the load-deformation mechanism of bored piles in London clay. Kuhlemeyer (1979) adopted a power law to study static and dynamic laterally loaded floating piles. An axisymmetric model with elastic-perfectly plastic soil was used by Pressley and Poulos (1986) for the pile group.

The hyperbolic family of soil models was often used to describe nonlinear stress-strain behavior (Kondner, 1963; Duncan and Chang, 1970; Hardin and Drnevich, 1972; Fahey and

Carter, 1993). Desai (1974) used the Duncan-Chang hyperbolic soil model for finite element analysis of piles in sands. To model vertical pile movement in expansive soils, Mohamedzein *et al.* (1999) introduced swell-induced strains in the Duncan-Chang model, and related swell-induced strains to change in soil suction. Lee and Salgado (1999) reformulated the hyperbolic equation initially proposed by Fahey and Carter (1993) to the 3D stress condition, with non-associative Drucker-Prager criterion as the failure surface. The effect of sand density, which can be related to the cone resistance from CPT test, was correlated to determine the tip resistance of axially loaded piles.

Simple plasticity models, such as Mohr-Coulomb, von Mises and Drucker-Prager model (Drucker and Prager, 1952), have also been often used for soils due to their relative simplicity. For example, a comprehensive nonlinear finite element analysis of a vertically loaded single pile was carried out using $ABAQUS^{TM}$ (Trochanis *et al.*, 1991). In this study, the soil was modeled using an extended Drucker-Prager plasticity, while piles were modeled as linearly elastic material. Non-associative Drucker-Prager and von Mises models were also used by Yang and Jeremic (2002, 2005) to study interaction between distinct soil layers for a laterally loaded pile in multi-layered soil profiles. A non-associative Mohr-Coulomb model for the soil was used in finite element by Lee *et al.* (2002) to compute the distribution of dragloads due to negative skin friction in pile groups. They concluded that the dragload is normally overestimated from empirical methods and elastic analyses. A nonlinear finite element model, with proper stiffness and soil slip included, is necessary for an accurate prediction. Although these previous analyses dealt with soil-pile interaction with various degrees of success, uncertainties and limitations associated with these simple plasticity models were not fully addressed. Wang and Sitar (2004) have conducted a parametric study of the influence of various model assumptions, i.e., friction angle approximation, volumetric dilatancy etc., on predicted axial pile behaviors in cohesionless and cohesive soils.

Provided soil parameters can be sensibly determined, distinctive models can provide similarly satisfactory performance. Four different constitutive soil models, namely, the linear elastic model (LEM), the Duncan-Chang's hyperbolic model (DCM), the Modified Cam-clay model (MCM), and Yin's two yield surface elastoplastic model (YM), were used separately to simulate a benchmark static pile load test (Cheung and Lee, 1991). The computed load-settlement of the single pile was compared with field measurements. It was found that the

system response cannot be properly captured by a linear elastic model, and consideration of soil nonlinearity in one way or another is necessary.

A more advanced model has also been developed to study statically loaded axial piles. Geordiadis *et al.* (2003) have examined the influence of partial soil saturation on axial pile behavior by a total stress elasto-plastic model. They found that the presence of an unsaturated zone has significant importance for shallow foundations, which gives a higher static bearing capacity due to suction, and it is subjected to the influence of ground water table fluctuation.

An elasto-plastic model was also used in the dynamic finite element analysis of piles (Wu *et al.*, 1989). To simulate pile-driving dynamics, Liyanapathirana *et al.* (2000, 2001) used von Mises material to model the soil and an Eulerian-like algorithm to accommodate large accumulated displacements of piles subjected to multiple hammer blows. More complicated effective stress analyses were performed by Mabsout *et al.* (1995) and Mabsout and Sadek (2003) to model the pile-driving process in saturated clays. The soil model adopted is a simplified version of bounding surface plasticity (Dafalias and Herrmann, 1986) proposed by Kaliakin and Dafalias (1989). The soil model has 13 parameters: six parameters are typical of critical-state soil mechanics (λ, κ, M_c, M_e, G, ν), two parameters for the geometry of the bounding surface, and the remaining five parameters to describe the hardening function. To accommodate large deformation experienced during penetration, an updated Lagrangian scheme was used. Coulomb-type frictional elements via the penalty method were also used along the soil-pile interface. Although the model simulated the time history of pile penetrations and pore-pressure generation, it has not been calibrated against an experimental or an actual pile-driving test.

For a soil-pile-structure system under earthquake loading, most research efforts have been devoted to study laterally loaded pile response. Bentley and El Naggar (2000) numerically evaluated the kinematic interaction effects on the pile response under earthquake excitation using the Drucker-Prager soil model and considered the influence of soil plasticity, pile-soil interface and radiation damping. The bounding surface plasticity model of Dafalias and Herrmann (1986) has also been used in a two-dimensional finite element analysis of a pile-supported structure under earthquake excitations and the results compared well with a series of centrifuge model experiments (Anandarajah *et al.*, 1995). The hierarchical

single surface (HiSS) model, proposed by Wathugala and Desai (1993), was first used in dynamic axial pile simulation by Desai *et al.* (1993). This model was later employed by Cai *et al.* (2000) in a peudo-3D finite element analysis of the soil-pile-structure system with a successive-coupling scheme to bind the foundation and structure subsystems. Using the same soil model and coupling scheme, Maheshwari *et al.* (2004, 2005) further compared the dynamic pile response under harmonic and seismic excitations with the solution in an elastic soil. They found soil nonlinearity has significant effects on the pile response at low and moderate frequencies, while the difference is negligible at high frequencies.

Slippage and separation of the soil and the pile usually occur under axial and lateral loading. More importantly, pile installation may affect the interface property, therefore an accurate modelling of soil-pile interface is very important in order to obtain realistic solutions (Trochanis *et al.*, 1991; Bentley and El Naggar, 2000; Lee *et al.*, 2002). To be used in finite element simulation, a simple but robust interface element is particularly desirable. One of the first interface elements was introduced by Goodman *et al.* (1968) in their finite element analysis of jointed rock masses. The element is a four-node element of zero thickness, in which the normal and tangential behaviors are linearly elastic until the yield state is reached. The strength envelope of the interface usually relates normal stress and tangential stress by Mohr-Coulomb frictional law. The shear stress and displacement of the interface has been modified to hyperbolic relation by Clough and Duncan (1971), and recently extended by Gomez *et al.* (2003) to accommodate arbitrary stress path directions. More complex constitutive laws for interface elements have also been reported to include the effects of strain hardening, softening, volumetric dilatancy, rate effect, cyclic effect, grain crushing, and creeping etc. (Boulon and Nova, 1990; Shahrour and Rezaie, 1997; Zeghal and Edil, 2002; Karabatakis and Hatzigogos, 2002; Hu and Pu, 2004).

From a mathematical point of view, the constraint of inpenetration and the interface law for two bodies in contact impose variational inequalities on a physical system, which can add significant mathematical complication and may cause the boundary value problem to be ill-posed (Oden and Pires, 1983). To date, only the simplest frictionless or Mohr-Coulomb type frictional contact problems have been thoroughly studied for improved numerical stability in computational mechanics community. Typically, numerical methods that convert the constraint inequalities into suitable equality for finite element formulation fall into two

categories: the penalty method and the Lagrange multiplier method. For the frictional contact problem, the penalty method is usually more straightforward and offers a distinct advantage, although the numerical accuracy and stability pivot on the choice of penalty numbers. A continuum-based implicit algorithm for large deformation frictional contact problems was proposed in the pioneering work of Laursen and Simo (1993). One important feature of this effort is the formulation of a frictional law in an appropriate convected basis; therefore the frame invariance of the constitutive behavior under finite deformation is assured. The penalty method and backward Euler integration have been used in their work, and the complete linearization of the global statement of virtual work provides a quadratic rate of numerical convergence. In dynamic contact/compact computations, a choice of time integrators is usually made between explicit and implicit ones. Although an explicit formula (e.g., forward Euler) provides straightforward and less expensive implementation, an implicit scheme (e.g., backward Euler) is preferred for better enforcement of constraints and ensuing numerical stability especially for dynamic problems of long time duration. The features of implicit integrators for dynamic frictional contact were further explored by Armero and Petocz (1998, 1999). In their work, a modified midpoint rule was shown to be energy conserving for frictionless contact and dissipative for frictional contact. Variational constraints can be numerically prescribed more precisely using methods of Lagrange multipliers. One may refer to, for example, the work by Jones and Papadopoulos (2001) and Papadopoulos and Taylor (1992, 1993).

As an alternative to the zero thickness element, Desai *et al.* (1984) proposed the idea of a thin-layer element for interfaces and joints. They argued that the interface behavior is often localized within a "smear zone" of finite thickness, which has different properties from the surrounding materials. So a thin-layer element is essentially a solid element, and its implementation is rather straightforward. Element penetration can be avoided using the thin-layer element, so it can be more computationally stable than the zero thickness element. However, the aspect ratio of a thin-layer element can affect the numerical solution, and it needs to be sensibly selected.

Since the finite-element simulation domain is of finite size, spurious wave reflections from the finite element boundary could significantly pollute dynamic simulation. Although the simplest solution to this problem is to enlarge the simulation domain so that the truncated

boundary does not affect the results, it is often computationally inefficient or infeasible to do so. Finite elements can also be coupled with boundary elements or infinite elements, but it is more convenient to use a transmitting boundary to dissipate outgoing waves. For its simplicity, a Kelvin element (spring and dashpot in parallel) is often used to represent infinite soil medium. The stiffness and damping parameters are frequency dependent, which can be determined by the predominant frequency of input motion (Novak and Mitwally, 1988; Novak *et al.*, 1978). The Lysmer-Kuhlemeyer transmitting boundary (Lysmer and Kuhlemeyer, 1969) is also commonly used in dynamic soil-structure interaction analysis. The boundary amounts to representing the infinite soil by a viscous dashpot and an equivalent force that are proportional to the incident wave velocity. These transmitting boundaries are easy to implement in a finite element model; however, the efficiency depends either on wave frequency or angles of incidence. The state-of-the art absorbing boundary is the perfectly matched layer (PML), first introduced in a study of electromagnetic waves in the 1990s. PML is a solid layer designed to absorb waves of any incident angles and at any frequencies. The waves can be completely attenuated within the PML layer by appropriate choice of the attenuation function and the depth of the layer. Displacement-based PMLs for elastodynamics were recently formulated for both time-harmonic and transient wave motion, and have been used in soil-structure interaction analysis by Basu and Chopra (2003, 2004).

In summary, the finite element method has been actively pursued in the past to simulate soil-pile-structure interaction. However, the endeavor is still quite limited in engineering design practice. One major constraint is that the soil model is usually quite complicated in that the parameters cannot be easily obtained by conventional site investigation. Many advanced soil models require a considerable large set of parameters, and they need to be determined from a series of high-quality laboratory tests. For example, the disturbed state concept (DSC) model has been successfully used to characterize the cyclic behavior of saturated clays and clay-steel pile interface (Desai and Shao, 2000). The DSC model uses up to 25 parameters to describe a continuous transformation of the soil from a relatively intact state to a fully adjusted (critical) state, the disturbance and loading-unloading behaviors. The model parameters need to be obtained from triaxial compression tests, consolidation tests, simple shear tests, and direct shear tests. However, in view of the unavoidable sampling disturbance, the heterogeneity of nature soil deposits, and more importantly, various

approximations made in *any* kind of numerical approach, estimating soil parameters directly from in-situ field tests is highly desirable. High computational cost further inhibits the applicability of finite element method in day-to-day design practice. For example, as documented in the pile-driving analysis performed by Mabsout *et al.* (1999), 70 hours CPU time on a Pentium 90 MHz personal computer is needed for an analysis of 2800 steps (28 blows). Bentley and El Naggar (2000) reported a simulation of soil-pile system under a 20 sec earthquake excitation lasting approximately 10 days on a Pentium 233 MHz personal computer. The excessive computational cost in dynamic analysis can be greatly reduced only by using simplistic models, for example, the modified equivalent linear method by Wu and Finn (1997). They proposed to update the strain-dependent soil properties (e.g., effective secant shear modulus and damping ratio) every 0.5 sec based on the peak strain calculated at the previous time interval, and the CPU time is reported to be within a reasonable range (3 hours on PC-486 30 MHz to run a full seismic quasi-3D analysis). However, soil nonlinearity is actually modelled in an empirical fashion, and the solution scheme is ad-hoc in nature, which can hardly be generalized. To push finite element simulation a step further, there is great demand to implement a simple yet realistic cyclic soil model.

3 Constitutive Model for Cyclic Soil Response

3.1 INTRODUCTION

The behavior of a pile subjected to lateral or axial dynamic loading is a three-dimensional, nonlinear transient problem. Due to the complexity of the system and high computational requirements, to date the application of nonlinear finite element analysis to this problem has been limited. One of the primary interests in the numerical modelling scheme is a soil model which is simple enough to be computationally efficient, yet able to capture the cyclic stress-strain behavior, i.e., the modulus degradation and energy dissipation during cyclic loadings; and the model should have the potential to be used in three-dimensional site response and soil-structure interaction analysis.

Since the early 1970s, many different nonlinear constitutive models of soil behavior were developed for various applications and a comprehensive review of the various approaches can be found in Zienkiewicz *et al.* (1999); and Potts and Zdravkovic (1999, 2001). For the purpose of the research herein, the models based on the concept of nested yield surfaces (Prevost, 1977, 1985; Mroz *et al.*, 1979) provided the greatest degree of flexibility to model cyclic soil response. As shown in Fig. 3.1, the basic concept is that a collection of nested yield surfaces defines the contours of constant shear moduli. A constant plastic shear modulus is associated with each of the yield surfaces whose initial position and the value of the plastic modulus can be determined from laboratory stress-strain curves. The outermost yield surface plays the role of a failure surface, beyond which the stress state is inadmissible. The associative flow rule, i.e., plastic flow occurs in the direction normal to the yield surface, is usually assumed for each yield surface. Upon loading, the active surface (the locus of stress point) is translated kinematically, touching and pushing other yield surfaces consecutively without intersecting them. Upon loading reversal (see Fig. 3.2), the stress point reverses the

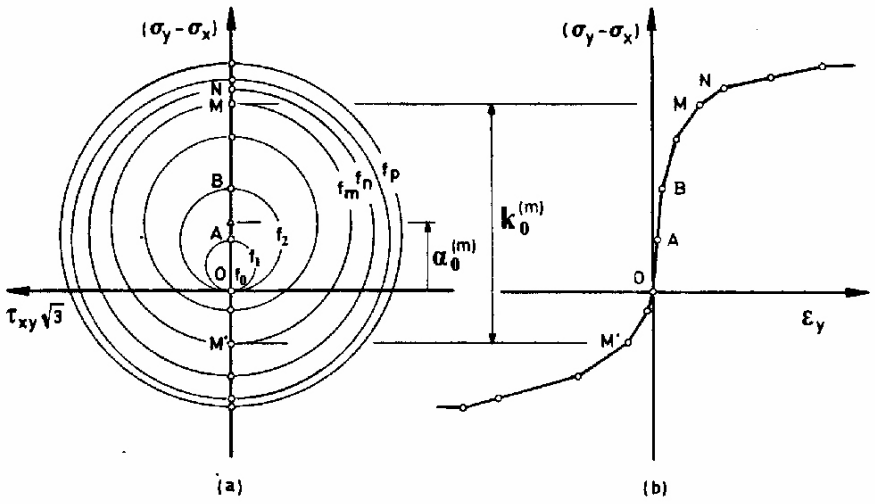

(a) π Plane (b) Stress-Strain Curve

Fig. 3.1. Nested Yield Surface Model: Monotonic Triaxial Compression and Extension, from Prevost (1977)

flow direction at point N and translates the surfaces in the new direction. The introduction of nested yield surfaces essentially breaks down the the complexity of the nonlinear stress-strain relation into a discrete set of relatively simple relations and, in principle, it can describe any kind of experimental hardening law.

For clays under undrained condition, the yield surfaces can be assumed to be pressure independent, and are nested cylinders in the principal stress space. They can also be modified to be nested cones, as illustrated in Fig. 3.3, to describe the pressure-dependent behavior such as that of the granular soils. By incorporating a phase transformation (PT) surface delimitating phases of contraction and dilation, the model can also be further extended to analyze the cyclic mobility of the sand and post-liquefaction site response (Elgamal *et al.*, 2002, 2003).

Since the nested yield surface model approximates nonlinear soil behavior in a discrete sense, it requires significant computer storage for a robust numerical implementation. Motivated by the need for a smooth evolution of nonlinearity, Borja and Amies (1994) proposed a J_2 bounding surface plasticity model with a vanishing elastic region, called multi-axial cyclic plasticity model for cyclic clay behavior. The model is based on the pioneering concept of bounding surface plasticity by Dafalias and Popov (1977). Similar to the classical plasticity, a stress function (called bounding surface) is used in the bounding surface plasticity to de-

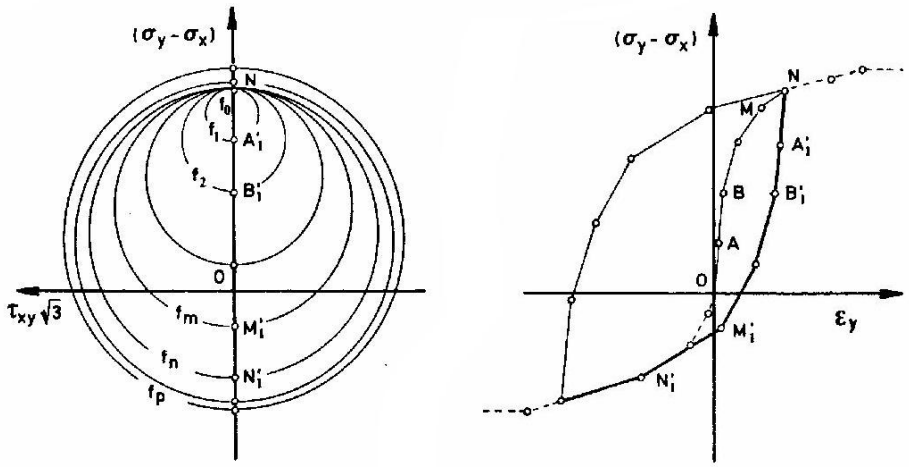

(a) Yield Surfaces upon Reach N in compression (b) Cyclic Stress-Strain Curve

Fig. 3.2. Nested Yield Surface Model: Cyclic Triaxial Test, from Prevost (1977)

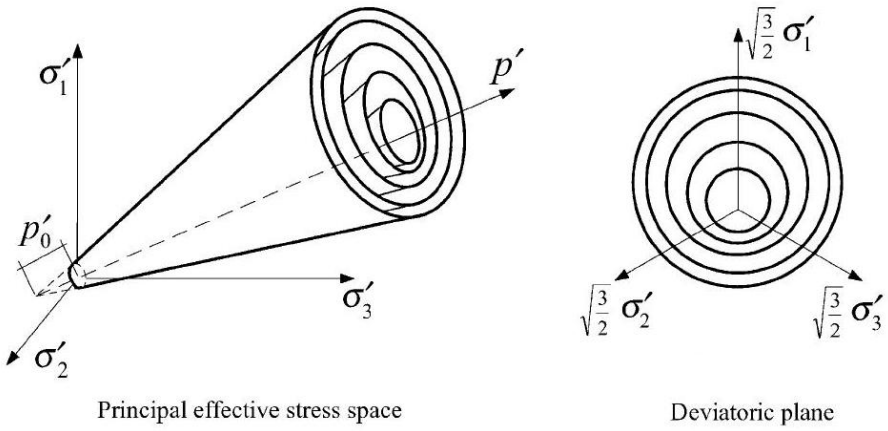

Fig. 3.3. Pressure-Dependent Nested Yield Surface Model: Conical Yield Surfaces, from Prevost (1985)

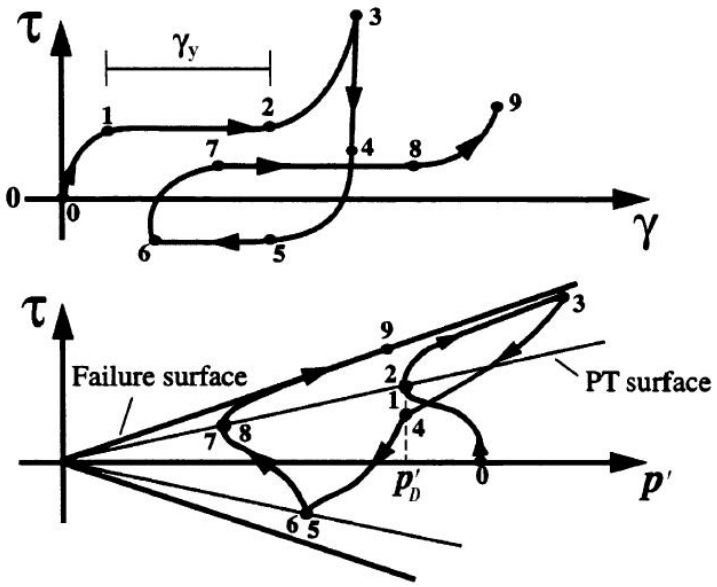

Fig. 3.4. Pressure Dependent Nested Yield Surface Model: Schematic of Constitutive Response, from Elgamal *et al.* (2002)

scribe a full plastic state. But plasticity also occurs for a stress state within the bounding surface, whose plastic modulus is determined by a smooth mapping rule between the stress state and its image point on the bounding surface.

Montáns and Borja further extended this type of J_2 bounding surface plasticity model to incorporate extended Masing behavior (Montans, 2000a); Prager's translation rule (Montans and Borja, 2002); the multilayer J_2 plasticity model with the Mróz translation rule (Montans, 2000b); Prager's translation rule (Montans, 2001); Prager-Ziegler translation rule (Montans, 2004); and Cam-clay version of bounding surface model (Borja *et al.*, 2001).

Due to its simplicity, the multi-axial cyclic plasticity model can be effectively utilized in a numerical procedure such as a finite element scheme. Borja and Wu (1994) used this type of model for three-dimensional finite element analysis of vibration of undrained clay foundations; for nonlinear site response of Lotung LSST during the 20 May 1986 Taiwan earthquake (Borja *et al.*, 1999a,b, 2000); and for the nonlinear site response of the Gilroy 2 reference site during the 17 October 1989 Loma Prieta earthquake (Borja *et al.*, 2000). This model was also successfully used to characterize nonlinear site-specific response under the near-fault ground motions (Rodriguez-Marek, 2000). These previous studies have demonstrated the success of the model in modelling site-specific response as well as its numerical stability. However, to the author's knowledge, this type of model has not been used in the

analysis of a strongly kinematically coupled problem, such as the pile-structure system, or for modelling of behavior in the full range from very small to very large strains. For example, the mobilized maximum shear strain of soils in Lotung site analysis (Borja *et al.*, 1999a) was only on the order of 0.2 % and, accordingly, the shear modulus of soil has degraded to, at the most, 20% from its maximum value.

3.2 J_2 BOUNDING SURFACE PLASTICITY

3.2.1 Constitutive Relation

In the classical theory of plasticity, yield surface, flow rule, and hardening law are three fundamental ingredients to describe constitutive behavior. The yield surface, usually expressed in the stress space, specifies the state at which plastic flow occurs. The flow rule defines the flow direction of the plastic strain increment. For the simplest case, the flow direction can be assumed normal (associative) to the yield surface, although in general the non-associative flow rule can be used. Finally, the hardening law describes the way the yield surface changes during plastic flow. A combination of the isotropic and kinematic plastic hardening laws can describe the change in the size and translation of the yield surface in stress space.

The basic concept of bounding surface plasticity is that there is no purely elastic region in the stress-strain relationship; instead, the nonlinearity of the soil is modelled by smoothly transforming the modulus from its initial value at small strain to full plastic state through a state dependent hardening modulus. In the following sections, the model of Borja and Amies (1994) is reformulated, with several features extended, including a revised loading-unloading criterion, hardening of the bounding surface, and operator split for the stress-strain transition from inside the bounding surface to the full plastic stage.

Within the framework of the bounding surface plasticity, a stress function, called bounding surface $\mathcal{B}$, is used to specify the full plastic state. The yield surface $\mathcal{Q}$ is always inside the interior of the bounding surface $\mathcal{B}$; see Fig. 3.5. The projection of these two functions on the π plane are two circles. For clays under undrained condition, the bounding surface is assumed pressure independent, which is circular if viewed in the deviatoric stress

plane (π plane),

$$\mathcal{B} := \|\hat{\boldsymbol{\sigma}}' - \boldsymbol{\beta}\| - R = 0 \tag{3.1}$$

where $\hat{\boldsymbol{\sigma}}'$ is the stress image point, $\boldsymbol{\beta}$ is the deviatoric back stress of the bounding surface, and R is the radius of the bounding surface. Prime ($'$) is used exclusively to signify that a tensor is deviatoric. The image stress point is located on the bounding surface, and it is projected from the current stress point $\boldsymbol{\sigma}'$ and the last stress reversal point $\boldsymbol{\sigma}'_0$ (Fig. 3.5). The radius of the bounding surface R can be related to the undrained shear strength S_u, determined from an unconfined compressive strength test on a normally consolidated clay, through

$$R = \sqrt{\frac{8}{3}} S_u \tag{3.2}$$

As is customary, the tensorial strain rate can be additively decomposed into elastic and plastic parts, i.e.,

$$\dot{\boldsymbol{\epsilon}} = \dot{\boldsymbol{\epsilon}}^e + \dot{\boldsymbol{\epsilon}}^p \tag{3.3}$$

where superscripts "e" and "p" denote the elastic part and plastic part, respectively. The plastic strain rate $\dot{\boldsymbol{\epsilon}}^p$ is determined by the flow rule

$$\dot{\boldsymbol{\epsilon}}^p = \lambda \tilde{\mathbf{n}} \tag{3.4}$$

where λ is the plastic consistency parameter, and $\tilde{\mathbf{n}}$ specifies the direction of the plastic strain rate, which can be chosen as outward normal to the yield surface. So the rate form of the constitutive stress-strain relation is

$$\dot{\boldsymbol{\sigma}} = \mathbf{C}^e : (\dot{\boldsymbol{\epsilon}} - \dot{\boldsymbol{\epsilon}}^p) = \mathbf{C}^e : \dot{\boldsymbol{\epsilon}} - 2G\lambda\tilde{\mathbf{n}} \tag{3.5}$$

where the fourth-order elasticity tensor $\mathbf{C}^e$ is defined through elastic bulk modulus K and elastic shear modulus G as

$$\mathbf{C}^e = K\ \mathbf{1} \otimes \mathbf{1} + 2G\ \mathbf{II}_{dev} \tag{3.6}$$

where $\mathbf{1} = \delta_{ij}\mathbf{e}_i \otimes \mathbf{e}_j$ is the second-order identity tensor; $\mathbf{II}_{dev} = \mathbf{II} - \frac{1}{3}\mathbf{1} \otimes \mathbf{1}$; $\mathbf{II} = \frac{1}{2}(\delta_{ik}\delta_{jl} + \delta_{il}\delta_{jk})\ \mathbf{e}_i \otimes \mathbf{e}_j \otimes \mathbf{e}_k \otimes \mathbf{e}_l$ is the fourth-order (symmetric) identity tensor.

Yield surface $\mathcal{Q}$ can be written as

$$\mathcal{Q} := \|\boldsymbol{\sigma}' - \tilde{\boldsymbol{\alpha}}\| - Y = 0 \tag{3.7}$$

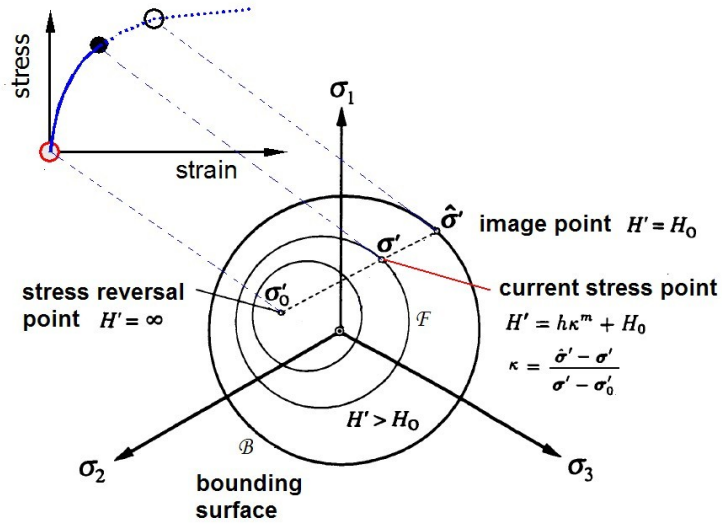

Fig. 3.5 Bounding Surface Plasticity (in Deviatoric π Plane)

in which Y is the radius of the yield surface $\mathcal{Q}$ and $\tilde{\alpha}$ is the deviatoric back stress representing the center. Then the unit outward normal to the yield surface $\mathcal{Q}$ is defined as

$$\tilde{\mathbf{n}} = \frac{\boldsymbol{\sigma}' - \tilde{\boldsymbol{\alpha}}}{\|\boldsymbol{\sigma}' - \tilde{\boldsymbol{\alpha}}\|} \tag{3.8}$$

Now assume the back stress of the yield function $\dot{\tilde{\boldsymbol{\alpha}}}$ obeys Prager's translation rule (Prager, 1956)

$$\dot{\tilde{\boldsymbol{\alpha}}} = \|\dot{\tilde{\boldsymbol{\alpha}}}\|\tilde{\mathbf{n}} = \frac{2}{3}H'\lambda\tilde{\mathbf{n}} \tag{3.9}$$

where H' is the hardening modulus, which will be discussed in detail later. In the limit case of the vanishing elastic region ($Y \to 0$), the persistency condition $\dot{\mathcal{Q}} = 0$ simply means $\dot{\boldsymbol{\sigma}}' - \dot{\tilde{\boldsymbol{\alpha}}} = 0$, so $\dot{\boldsymbol{\sigma}}'$ and $\tilde{\mathbf{n}}$ becomes coaxial, i.e.,

$$\dot{\tilde{\boldsymbol{\alpha}}} = \dot{\boldsymbol{\sigma}}' = \|\dot{\tilde{\boldsymbol{\alpha}}}\|\tilde{\mathbf{n}} \tag{3.10}$$

So the outward normal $\tilde{\mathbf{n}}$ can be easily evaluated at the limit as

$$\mathbf{n} = \lim_{Y \to 0}\left(\frac{\boldsymbol{\sigma}' - \boldsymbol{\alpha}}{\|\boldsymbol{\sigma}' - \boldsymbol{\alpha}\|}\right) = \frac{\dot{\boldsymbol{\sigma}}'}{\|\dot{\boldsymbol{\sigma}}'\|} \tag{3.11}$$

The rate form of the constitutive relation $\dot{\boldsymbol{\sigma}}' = 2G\,(\dot{\boldsymbol{\epsilon}}' - \dot{\boldsymbol{\epsilon}}'^{p})$ becomes

$$\dot{\boldsymbol{\sigma}}' = 2G\left(\dot{\boldsymbol{\epsilon}}' - \lambda\frac{\dot{\boldsymbol{\sigma}}'}{\|\dot{\boldsymbol{\sigma}}'\|}\right) \tag{3.12}$$

which implies $\dot{\boldsymbol{\sigma}}'$ and $\dot{\boldsymbol{\epsilon}}'$ are also coaxial. Further, Eq.(3.12) implies:

$$\|\dot{\boldsymbol{\sigma}}'\| = 2G\|\dot{\boldsymbol{\epsilon}}'\| - 2G\lambda \tag{3.13}$$

Substituting the above into Eq. (3.9), Eq. (3.11) and Eq. (3.12), we obtained

$$\dot{\boldsymbol{\sigma}}' = \dot{\boldsymbol{\alpha}} = \frac{2}{3}H'\lambda\tilde{\mathbf{n}} = \frac{2}{3}H'\lambda\left(\frac{\dot{\boldsymbol{\sigma}}'}{2G\|\dot{\boldsymbol{\epsilon}}'\| - 2G\lambda}\right) \tag{3.14}$$

and it solves the plastic multiplier

$$\lambda = \frac{3G}{3G + H'}\|\dot{\boldsymbol{\epsilon}}'\| \tag{3.15}$$

Note that $\dfrac{\dot{\boldsymbol{\sigma}}'}{\|\dot{\boldsymbol{\sigma}}'\|} = \dfrac{\dot{\boldsymbol{\epsilon}}'}{\|\dot{\boldsymbol{\epsilon}}'\|}$ since $\dot{\boldsymbol{\sigma}}'$ and $\dot{\boldsymbol{\epsilon}}'$ are coaxial. So Eq.(3.12) and Eq.(3.15) leads to the following nonlinear stress and strain relation

$$\dot{\boldsymbol{\sigma}}' = 2G\left(1 + \frac{3G}{H'}\right)^{-1}\dot{\boldsymbol{\epsilon}}' = \Psi\dot{\boldsymbol{\epsilon}}' \tag{3.16}$$

in which the nonlinear shear modulus Ψ is defined as:

$$\Psi = 2G\left(1 + \frac{3G}{H'}\right)^{-1} = 2G\left(1 - \frac{2G}{2G + \dfrac{2}{3}H'}\right) \tag{3.17}$$

Finally, we obtained the constitutive relation written in the rate form as

$$\dot{\boldsymbol{\sigma}} = K\ \dot{\theta}\ \mathbf{I} + \Psi\dot{\boldsymbol{\epsilon}}' \tag{3.18}$$

During the foregoing derivations, the introduction of vanishing elastic region imposes no singularity in the resulting constitutive equation. The results are derived from the framework of classical plasticity, but interestingly enough, Eq.(3.18) is more reminiscent of nonlinear elasticity than plasticity, since $\dot{\boldsymbol{\sigma}}'$ and $\dot{\boldsymbol{\epsilon}}'$ are coaxial. This feature greatly simplifies its numerical implementation, since provided H' is known, Eq. (3.18) can be easily integrated.

3.2.2 Hardening Law

The development of nonlinearity is fully manifested in the evolution of hardening modulus H' and shear modulus Ψ. Among many interpolation schemes, the radial mapping rule is

most widely used in the bounding surface plasticity, in that the hardening modulus depends on the radial position of the current stress point.

Given a most recent stress reversal point $\boldsymbol{\sigma}'_0$, the current deviatoric stress $\boldsymbol{\sigma}'$ and its image point $\hat{\boldsymbol{\sigma}}'$ on the bounding surface $\mathcal{B}$ (see Fig. 3.5), a dimensionless scalar κ can be defined to measure the relative distance of these stress points

$$\kappa = \frac{\hat{\boldsymbol{\sigma}}' - \boldsymbol{\sigma}'}{\boldsymbol{\sigma}' - \boldsymbol{\sigma}'_0} \tag{3.19}$$

It is easy to see that κ is non-negative, taking values from infinity (when $\boldsymbol{\sigma}' = \boldsymbol{\sigma}'_0$) to zero (when $\boldsymbol{\sigma}' = \hat{\boldsymbol{\sigma}}'$). Accordingly, the hardening modulus H' can be specified as a smooth monotonically increasing function of κ, $H' = H'(\kappa)$, such that $H' \to \infty$ as $\boldsymbol{\sigma}' \to \boldsymbol{\sigma}'_0$, and $H' = H_0$ (constant) if $\boldsymbol{\sigma}'$ lies on the bounding surface $\mathcal{B}$. We will show later that contour surfaces for constant H' are nested circles emanating from the latest stress reversal point $\boldsymbol{\sigma}'_0$ in the π plane, and we denote the one passing the current stress point as *loading surface* $\mathcal{F}$. The properties of the loading surface will be examined in Section 3.3.

One example of such a hardening law can be chosen as the exponential function

$$H' = h\kappa^m + H_0 \tag{3.20}$$

in which h is a modulus parameter and m is a dimensionless scalar. They control the rate of shear stiffness degradation. H_0 is the hardening modulus associated with the bounding surface. Using Eq.(3.20), the soil behaves instantaneously elastic upon unloading ($H' \to \infty$), and transits asymptotically towards fully plastic stage on the bounding surface ($H' = H_0$).

3.2.3 Modified Loading/Unloading Criterion

According to Borja and Amies (1994), the unloading condition can be interpreted as the instance that the hardening modulus increases, i.e., $\dot{H}' > 0$

$$\dot{H}' = \frac{dH'}{d\kappa}\dot{\kappa} > 0 \tag{3.21}$$

Since H' is a monotonically increasing function of κ, i.e., $\dfrac{dH'}{d\kappa} > 0$, the unloading is implied by the condition $\dot{\kappa} > 0$. Taking the time variation of Eq. (3.1) and considering the condition

that $\dot{\boldsymbol{\sigma}}'$ and $\dot{\boldsymbol{\epsilon}}'$ are coaxial, Borja and Amies (1994) proposed the following criterion for the unloading condition:

$$\chi = -\frac{(1+\kappa)(\boldsymbol{\sigma}'-\boldsymbol{\beta})+\kappa(1+\kappa)(\boldsymbol{\sigma}'-\boldsymbol{\sigma}'_0)}{(\boldsymbol{\sigma}'-\boldsymbol{\beta}):(\boldsymbol{\sigma}'-\boldsymbol{\sigma}'_0)+\kappa(\boldsymbol{\sigma}'-\boldsymbol{\sigma}'_0):(\boldsymbol{\sigma}'-\boldsymbol{\sigma}'_0)} : \dot{\boldsymbol{\epsilon}}' > 0 \tag{3.22}$$

However, the above criterion lacks obvious geometrical interpretation. Alternatively, we will provide a simplified loading/unloading criterion and prove that they are essentially equivalent, but the new criterion has distinctive geometrical significance. As will be shown in Section 3.3, the center of loading surface $\mathcal{F}$, $\boldsymbol{\alpha}$, can be expressed as

$$\boldsymbol{\alpha} = \frac{\kappa\boldsymbol{\sigma}'_0+\boldsymbol{\beta}}{1+\kappa} \tag{3.23}$$

Hence

$$(\boldsymbol{\sigma}'-\boldsymbol{\beta})+\kappa(\boldsymbol{\sigma}'-\boldsymbol{\sigma}'_0) = (1+\kappa)(\boldsymbol{\sigma}'-\boldsymbol{\alpha}) \tag{3.24}$$

Using above equation, the condition Eq.(3.22) can be simplified as

$$\begin{aligned}
\chi &= -\frac{(1+\kappa)(\boldsymbol{\sigma}'-\boldsymbol{\beta})+\kappa(1+\kappa)(\boldsymbol{\sigma}'-\boldsymbol{\sigma}'_0)}{(\boldsymbol{\sigma}'-\boldsymbol{\beta}):(\boldsymbol{\sigma}'-\boldsymbol{\sigma}'_0)+\kappa(\boldsymbol{\sigma}'-\boldsymbol{\sigma}'_0):(\boldsymbol{\sigma}'-\boldsymbol{\sigma}'_0)} : \dot{\boldsymbol{\epsilon}}' \\
&= -\frac{(1+\kappa)\left((\boldsymbol{\sigma}'-\boldsymbol{\beta})+\kappa(\boldsymbol{\sigma}'-\boldsymbol{\sigma}'_0)\right)}{(\boldsymbol{\sigma}'-\boldsymbol{\sigma}'_0):\left((\boldsymbol{\sigma}'-\boldsymbol{\beta})+\kappa(\boldsymbol{\sigma}'-\boldsymbol{\sigma}'_0)\right)} : \dot{\boldsymbol{\epsilon}}' > 0 \\
&= -\frac{(1+\kappa)(\boldsymbol{\sigma}'-\boldsymbol{\alpha})}{(\boldsymbol{\sigma}'-\boldsymbol{\sigma}'_0):(\boldsymbol{\sigma}'-\boldsymbol{\alpha})} : \dot{\boldsymbol{\epsilon}}'
\end{aligned} \tag{3.25}$$

We can further simplify the above expression. It is easy to prove that the following inequity always holds by observing that $\boldsymbol{\sigma}'_0$ and $\boldsymbol{\alpha}$ are all inside the circle $\mathcal{F}$

$$(\boldsymbol{\sigma}'-\boldsymbol{\sigma}'_0):(\boldsymbol{\sigma}'-\boldsymbol{\alpha}) > 0 \tag{3.26}$$

Finally, Eq.(3.25) is simplified to a new loading condition for the bounding surface plasticity model

$$\chi = -(\boldsymbol{\sigma}'-\boldsymbol{\alpha}) : \dot{\boldsymbol{\epsilon}}' > 0 \tag{3.27}$$

Since only the sign of χ matters, the above unloading criterion is preferably written in the following way

$$\chi = \frac{\boldsymbol{\sigma}'-\boldsymbol{\alpha}}{\|\boldsymbol{\sigma}'-\boldsymbol{\alpha}\|} : \dot{\boldsymbol{\epsilon}}' = \mathbf{n} : \dot{\boldsymbol{\epsilon}}' < 0 \tag{3.28}$$

The above expression has a straightforward geometrical interpretation, and the loading/unloading criterion can be stated as the following: the material is undergoing *loading*

if the strain increment $\dot{\boldsymbol{\epsilon}}'$ points outward from surface $\mathcal{F}$; *unloading* if $\dot{\boldsymbol{\epsilon}}'$ points inward; and *neutral loading* if $\dot{\boldsymbol{\epsilon}}'$ is tangential to $\mathcal{F}$. The criterion is summarized in Eq.(3.29) and illustrated in Fig. 3.6 for this geometrical interpretation. Compared with Eq.(3.22), the new criterion is more intuitive and is similar to the loading/unloading condition in classical theory of plasticity.

$$\chi = \mathbf{n} : \dot{\boldsymbol{\epsilon}}' \begin{cases} > 0, & \text{loading} \\ = 0, & \text{neutral loading} \\ < 0, & \text{unloading} \end{cases} \tag{3.29}$$

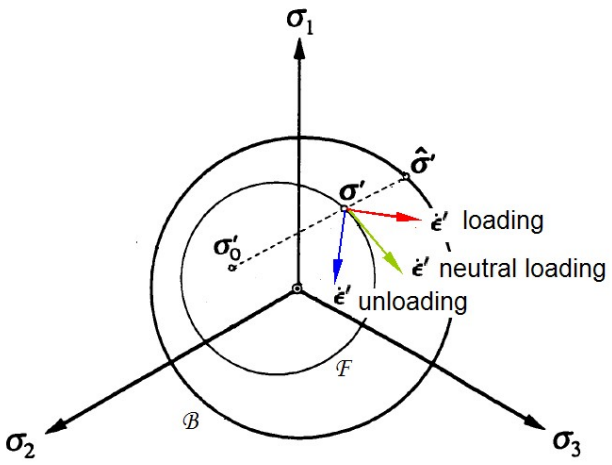

Fig. 3.6 Loading/Unloading Criterion

Identification of loading/unloading is critical for the cyclic material model. Once the unloading is identified, the previous $\mathcal{F}$ surfaces dissolve. The stress reversal point $\boldsymbol{\sigma}'_0$ is updated to the new stress unloading point (which coincides with $\boldsymbol{\sigma}'$ upon just unloading), and new $\mathcal{F}$ surfaces for constant hardening modulus H' are re-centered about the new position to interpolate the subsequent **loading** process. Fig. 3.7 illustrates the model response upon unloading being detected.

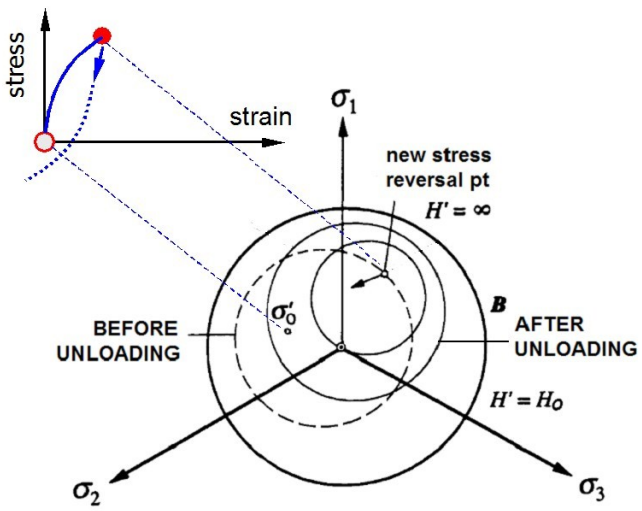

Fig. 3.7 Response upon Unloading

3.3 MATHEMATICAL PROPERTIES OF LOADING SURFACE

3.3.1 Consistency Condition

In this section, we examine the intrinsic mathematical properties of the loading surface $\mathcal{F}$. Recalling that the bounding surface $\mathcal{B}$ is circular in the deviatoric stress space,

$$\mathcal{B} := \|\hat{\boldsymbol{\sigma}}' - \boldsymbol{\beta}\| - R = 0. \tag{3.30}$$

Substituting the mapping $\hat{\boldsymbol{\sigma}}' = \boldsymbol{\sigma}' + \kappa(\boldsymbol{\sigma}' - \boldsymbol{\sigma}'_0)$ into above, the current stress state $\boldsymbol{\sigma}'$ satisfies

$$\mathcal{B} = \|(1+\kappa)\boldsymbol{\sigma}' - (\kappa\boldsymbol{\sigma}'_0 + \boldsymbol{\beta})\| - R = 0 \tag{3.31}$$

When divided by $(1+\kappa)$, it reads

$$\frac{\mathcal{B}}{(1+\kappa)} = \|\boldsymbol{\sigma}' - \frac{\kappa\boldsymbol{\sigma}'_0 + \boldsymbol{\beta}}{1+\kappa}\| - \frac{R}{1+\kappa} = 0 \tag{3.32}$$

Hence the contour of a constant κ passing through $\boldsymbol{\sigma}'$ defines a loading surface $\mathcal{F}$ as

$$\mathcal{F} := \frac{\mathcal{B}}{(1+\kappa)} = \|\boldsymbol{\sigma}' - \boldsymbol{\alpha}\| - r = 0 \tag{3.33}$$

The loading surface $\mathcal{F}$ is circular in the deviatoric stress space, with its center $\boldsymbol{\alpha}$ determined through

$$\boldsymbol{\alpha} = \frac{\kappa\boldsymbol{\sigma}'_0 + \boldsymbol{\beta}}{1+\kappa} \tag{3.34}$$

The radius r of $\mathcal{F}$ scales down R through

$$r = \frac{R}{1+\kappa} \tag{3.35}$$

Rewriting $\hat{\boldsymbol{\sigma}}' = \boldsymbol{\sigma}' + \kappa(\boldsymbol{\sigma}' - \boldsymbol{\sigma}'_0)$, a similar mapping rule as Eq.(3.34) also holds between $\boldsymbol{\sigma}'_0$, $\boldsymbol{\sigma}'$ and $\hat{\boldsymbol{\sigma}}'$

$$\boldsymbol{\sigma}' = \frac{\kappa\boldsymbol{\sigma}'_0 + \hat{\boldsymbol{\sigma}}'}{1+\kappa} \tag{3.36}$$

This implies $\boldsymbol{\sigma}'_0$, $\boldsymbol{\alpha}$, and $\boldsymbol{\beta}$ are aligned, and the outward normal at the image stress point $\hat{\boldsymbol{\sigma}}'$ on $\mathcal{B}$ has the same direction as the outward normal at the stress point $\boldsymbol{\sigma}'$ on $\mathcal{F}$, i.e., $\mathbf{n} = \hat{\mathbf{n}}$, as illustrated in Fig. 3.8. The statement can be formally proven as follows,

$$\hat{\mathbf{n}} = \frac{\partial\mathcal{B}}{\partial\hat{\boldsymbol{\sigma}}'} = \frac{\hat{\boldsymbol{\sigma}}' - \boldsymbol{\beta}}{\|\hat{\boldsymbol{\sigma}}' - \boldsymbol{\beta}\|} = \frac{(1+\kappa)(\boldsymbol{\sigma}' - \boldsymbol{\alpha})}{R} = \frac{\boldsymbol{\sigma}' - \boldsymbol{\alpha}}{\|\boldsymbol{\sigma}' - \boldsymbol{\alpha}\|} \tag{3.37}$$

$$\mathbf{n} = \frac{\partial\mathcal{F}}{\partial\boldsymbol{\sigma}'} = \frac{\boldsymbol{\sigma}' - \boldsymbol{\alpha}}{\|\boldsymbol{\sigma}' - \boldsymbol{\alpha}\|} \tag{3.38}$$

Moreover, the consistency condition on the bounding surface $\mathcal{B}$ is equivalent to the consistency condition on the loading surface $\mathcal{F}$, i.e.

$$\mathcal{B} = \dot{\mathcal{B}} = 0 \quad \text{implies} \quad \mathcal{F} = \dot{\mathcal{F}} = 0 \tag{3.39}$$

The result $\mathcal{F} = 0$ if $\mathcal{B} = 0$ can be easily seen from Eq.(3.33). Taking the time derivative of $\mathcal{B}$ gives $\dot{\mathcal{B}} = (1+\kappa)\dot{\mathcal{F}} + \dot{\kappa}\mathcal{F}$. Since $\mathcal{F} = 0$, it follows that $\dot{\mathcal{F}} = 0$ if $\mathcal{B} = \dot{\mathcal{B}} = 0$. This amenable feature allows all attributes of the standard return mapping algorithm for classical plasticity to be carried out in the settings of bounding surface plasticity with minimum modifications. The loading surface $\mathcal{F}$ can thus be practically treated as a yield surface, but it is not a yield surface, since $\mathcal{F} = 0$ is always enforced.

3.3.2 Hardening Behavior

In this section, we examine the hardening behavior of the loading surface. To simplify analysis, we assume during a loading step that the bounding surface remains stationary, i.e., $\boldsymbol{\beta}$, $\boldsymbol{\sigma}'_0$ and R are constants. Define a parameter ϱ as

$$\varrho \equiv \frac{1}{1+\kappa} \tag{3.40}$$

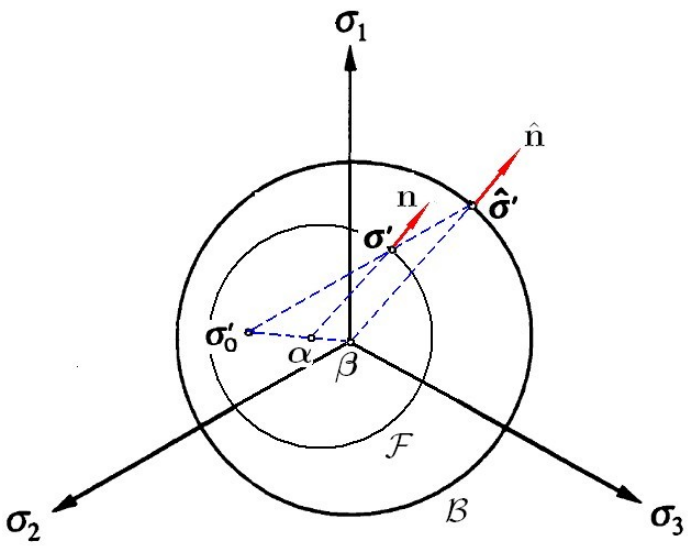

Fig. 3.8 Bounding and Loading Surfaces

so its variation can be evaluated as

$$\dot{\varrho} = -\frac{\dot{\kappa}}{(1+\kappa)^2} = -\varrho^2 \, \dot{\kappa} \tag{3.41}$$

Using parameter ϱ, the radius of loading surface $\mathcal{F}$ is simply $r = \varrho R$, and the backstress $\boldsymbol{\alpha}$ becomes

$$\boldsymbol{\alpha} = \frac{\kappa \boldsymbol{\sigma}'_0 + \boldsymbol{\beta}}{1+\kappa} = \boldsymbol{\sigma}'_0 + \varrho \, (\boldsymbol{\beta} - \boldsymbol{\sigma}'_0) \tag{3.42}$$

It evolves according to the following expression

$$\dot{\boldsymbol{\alpha}} = \dot{\varrho} \, (\boldsymbol{\beta} - \boldsymbol{\sigma}'_0) \tag{3.43}$$

From Eq.(3.33) and Eq.(3.43), the consistency condition $\dot{\mathcal{F}} = 0$ gives

$$\begin{aligned} \dot{\mathcal{F}} &= \frac{\boldsymbol{\sigma}' - \boldsymbol{\alpha}}{\|\boldsymbol{\sigma}' - \boldsymbol{\alpha}\|} : (\dot{\boldsymbol{\sigma}}' - \dot{\boldsymbol{\alpha}}) - \dot{\varrho} \, R \\ &= \mathbf{n} : \dot{\boldsymbol{\sigma}}' - \dot{\varrho} \, [\mathbf{n} : (\boldsymbol{\beta} - \boldsymbol{\sigma}'_0) + R] = 0 \end{aligned} \tag{3.44}$$

which implies the time derivative of p can be evaluated as

$$\dot{\varrho} = \frac{\mathbf{n}}{\mathbf{n} : (\boldsymbol{\beta} - \boldsymbol{\sigma}'_0) + R} : \dot{\boldsymbol{\sigma}}' \tag{3.45}$$

Comparing Eqs. (3.41) and (3.45), we obtain

$$\frac{\partial \dot{\kappa}}{\partial \dot{\boldsymbol{\sigma}}'} = -\frac{\mathbf{n}}{\varrho^2 \left[\mathbf{n} : (\boldsymbol{\beta} - \boldsymbol{\sigma}_0') + R\right]} \tag{3.46}$$

Defining a fourth-order hardening tensor through

$$\frac{\partial \dot{\boldsymbol{\sigma}}'}{\partial \dot{\boldsymbol{\epsilon}}'^p} = H' \mathbf{n} \otimes \mathbf{n} \tag{3.47}$$

So using the chain rule, the time derivative of κ can be evaluated as

$$\dot{\kappa} = \frac{\partial \dot{\kappa}}{\partial \dot{\boldsymbol{\sigma}}'} : \frac{\partial \dot{\boldsymbol{\sigma}}'}{\partial \dot{\boldsymbol{\epsilon}}'^p} : \dot{\boldsymbol{\epsilon}}'^p = -\frac{H'\lambda}{\varrho^2 \left[\mathbf{n} : (\boldsymbol{\beta} - \boldsymbol{\sigma}_0') + R\right]} \tag{3.48}$$

Correspondingly, the time derivative of ϱ is obtained

$$\dot{\varrho} = -\varrho^2 \dot{\kappa} = \frac{H'\lambda}{\mathbf{n} : (\boldsymbol{\beta} - \boldsymbol{\sigma}_0') + R} \tag{3.49}$$

So $\dot{\varrho}\left[\mathbf{n} : (\boldsymbol{\beta} - \boldsymbol{\sigma}_0') + R\right] = H'\lambda$, and the consistency condition Eq.(3.44) can be simplified as

$$\dot{\mathcal{F}} = \mathbf{n} : \dot{\boldsymbol{\sigma}}' - H'\lambda = 0 \tag{3.50}$$

giving a useful relation

$$H'\lambda = \mathbf{n} : \dot{\boldsymbol{\sigma}}' \tag{3.51}$$

Finally the evolution of the back stress is found to be

$$\begin{aligned}
\dot{\boldsymbol{\alpha}} &= \dot{\varrho}\,(\boldsymbol{\beta} - \boldsymbol{\sigma}_0') = \frac{\boldsymbol{\beta} - \boldsymbol{\sigma}_0'}{\mathbf{n} : (\boldsymbol{\beta} - \boldsymbol{\sigma}_0') + R} H'\lambda \\
&= \frac{(\mathbf{n} : \dot{\boldsymbol{\sigma}}')\,(\boldsymbol{\beta} - \boldsymbol{\sigma}_0')}{\mathbf{n} : (\boldsymbol{\beta} - \boldsymbol{\sigma}_0') + R} = \left[\frac{\mathbf{n} : (\boldsymbol{\beta} - \boldsymbol{\sigma}_0')}{\mathbf{n} : (\boldsymbol{\beta} - \boldsymbol{\sigma}_0') + R}\right] \left[\frac{(\mathbf{n} : \dot{\boldsymbol{\sigma}}')\,(\boldsymbol{\beta} - \boldsymbol{\sigma}_0')}{\mathbf{n} : (\boldsymbol{\beta} - \boldsymbol{\sigma}_0')}\right] \\
&= (1 - \zeta)\, \frac{\mathbf{n} : \dot{\boldsymbol{\sigma}}'}{\mathbf{n} : (\boldsymbol{\beta} - \boldsymbol{\sigma}_0')} (\boldsymbol{\beta} - \boldsymbol{\sigma}_0') \\
&= (1 - \zeta)\, \frac{\mathbf{n} : \dot{\boldsymbol{\sigma}}'}{\mathbf{n} : \boldsymbol{\Lambda}} \boldsymbol{\Lambda} = (1 - \zeta)\, H'\lambda \frac{\boldsymbol{\Lambda}}{\mathbf{n} : \boldsymbol{\Lambda}}
\end{aligned} \tag{3.52}$$

with parameter ζ defined as

$$\zeta = \frac{R}{\mathbf{n} : (\boldsymbol{\beta} - \boldsymbol{\sigma}_0') + R} \tag{3.53}$$

and the unit tensor $\boldsymbol{\Lambda}$ specifies the hardening direction, which is defined as

$$\boldsymbol{\Lambda} = \frac{\boldsymbol{\beta} - \boldsymbol{\sigma}_0'}{\|\boldsymbol{\beta} - \boldsymbol{\sigma}_0'\|} \tag{3.54}$$

The evolution of radius r can be obtained from equity $r = \|\boldsymbol{\sigma}' - \boldsymbol{\alpha}\|$, Eqs.(3.51,3.52)

$$\begin{aligned} \dot{r} &= \frac{\boldsymbol{\sigma}' - \boldsymbol{\alpha}}{\|\boldsymbol{\sigma}' - \boldsymbol{\alpha}\|} : (\dot{\boldsymbol{\sigma}}' - \dot{\boldsymbol{\alpha}}) = \mathbf{n} : (\dot{\boldsymbol{\sigma}}' - \dot{\boldsymbol{\alpha}}) \\ &= \lambda H' - \frac{\mathbf{n} : (\boldsymbol{\beta} - \boldsymbol{\sigma}'_0)}{\mathbf{n} : (\boldsymbol{\beta} - \boldsymbol{\sigma}'_0) + R}\ \lambda H' = \frac{R}{\mathbf{n} : (\boldsymbol{\beta} - \boldsymbol{\sigma}'_0) + R}\ \lambda H' \\ &= \zeta\ \lambda H' \end{aligned} \tag{3.55}$$

Next, we proceed to explore the physical meaning of Eq. (3.52) and Eq.(3.55). The consistency condition of $\mathcal{F}$ is

$$\dot{\mathcal{F}} = \mathbf{n} : (\dot{\boldsymbol{\sigma}}' - \dot{\boldsymbol{\alpha}}) - \dot{r} = 0 \tag{3.56}$$

If $\mathcal{F}$ is assumed to harden *purely kinematically*, i.e., $\dot{r} = 0$, we find the following relation

$$\mathbf{n} : \dot{\boldsymbol{\sigma}}' = \mathbf{n} : \dot{\boldsymbol{\alpha}} \tag{3.57}$$

Since $\dot{\boldsymbol{\alpha}}$ is in the direction of $\boldsymbol{\Lambda}$, we have $\dot{\boldsymbol{\alpha}} = \|\dot{\boldsymbol{\alpha}}\|\boldsymbol{\Lambda}$. When it is double contracted with $\mathbf{n}$ and considering Eq. (3.57), we obtain $\|\dot{\boldsymbol{\alpha}}\| = \dfrac{\mathbf{n} : \dot{\boldsymbol{\sigma}}'}{\mathbf{n} : \boldsymbol{\Lambda}}$, hence

$$\dot{\boldsymbol{\alpha}} = \frac{\mathbf{n} : \dot{\boldsymbol{\sigma}}'}{\mathbf{n} : \boldsymbol{\Lambda}}\boldsymbol{\Lambda} = H'\lambda\frac{\boldsymbol{\Lambda}}{\mathbf{n} : \boldsymbol{\Lambda}} \tag{3.58}$$

Comparing to Eq. (3.52), it is clear that they are different only to the scale of $(1 - \zeta)$. Moreover, if it is assumed $\mathcal{F}$ hardens *purely isotropically*, i.e., $\dot{\boldsymbol{\alpha}} = 0$, then the consistency condition gives

$$\dot{r} = \mathbf{n} : \dot{\boldsymbol{\sigma}}' = \lambda H' \tag{3.59}$$

It only differs from Eq.(3.55) by a scalar coefficient ζ. The above analysis sheds light on the hardening nature of loading surface $\mathcal{F}$. The hardening behavior of $\mathcal{F}$ is a combined kinematic hardening and isotropic hardening. The kinematic hardening part scales a pure kinematic hardening by factor $(1-\zeta)$, and the isotropic hardening part scales a pure isotropic hardening by ζ. This type of combination is very similar to that used in classical computational plasticity (Simo and Hughes, 1997). However, the combination is not linear, since in general ζ is not a constant during a loading history, and it may keep changing in the process of stress evolution. It is also worth pointing out that although two types of hardening are combined through ζ, neither the plastic multiplier nor the resulting continuum elastoplastic tangent depends on the variables ζ and $\boldsymbol{\Lambda}$. In fact, using Eqs.(3.52, 3.55), the consistency condition

becomes

$$\begin{aligned}\dot{\mathcal{F}} &= \frac{\partial \mathcal{F}}{\partial\left(\boldsymbol{\sigma}' - \boldsymbol{\alpha}\right)} : \left(\dot{\boldsymbol{\sigma}}' - \dot{\boldsymbol{\alpha}}\right) + \frac{\partial \mathcal{F}}{\partial r}\dot{r} = \mathbf{n} : \left(\dot{\boldsymbol{\sigma}}' - \dot{\boldsymbol{\alpha}}\right) + \frac{\partial F}{\partial r}\dot{r} \\ &= \mathbf{n} : \dot{\boldsymbol{\sigma}}' - (1-\zeta)\frac{\mathbf{n} : \dot{\boldsymbol{\sigma}}'}{\mathbf{n} : \boldsymbol{\Lambda}}\mathbf{n} : \boldsymbol{\Lambda} - \zeta\lambda H' \\ &= \zeta(\mathbf{n} : \dot{\boldsymbol{\sigma}}' - \lambda H') = 0 \end{aligned} \tag{3.60}$$

which rules out the influence of the factor ζ. As a final remark to conclude this section, treating loading surface $\mathcal{F}$ as a yield surface unifies the bounding surface plasticity with the classical framework. The only distinction is that hardening modulus H' in the bounding surface model should be determined from the mapping rule discussed before.

3.4 FINITE ELEMENT IMPLEMENTATION

3.4.1 Nonlinear FEM Framework

The cyclic soil model can be easily implemented in a nonlinear finite element framework such as FEAP (Taylor, 2002) and OpenSees (2005). For the nonlinear-transient problem the finite element method uses semidiscrete formulation, where nodal displacements are usually assumed as the primary unknowns to interpolate the displacement field from nodal displacements (Hughes, 1987). After spatial discretization of the weak form by the finite element scheme, the system to solve reduces to a system of algebraic equations, writing in residual vector form as

$$\mathbf{R}(\mathbf{u}, \dot{\mathbf{u}}, \ddot{\mathbf{u}}) = \mathbf{F}^{ext} - \mathbf{M}\ddot{\mathbf{u}} - \mathbf{D}\dot{\mathbf{u}} - \mathbf{F}^{int}(\boldsymbol{\sigma}) = 0 \tag{3.61}$$

where

$$\mathbf{F}^{int}(\boldsymbol{\sigma}) = \sum_e \int_{\Omega_e} \mathbf{B}^T \boldsymbol{\sigma}\ d\Omega \tag{3.62}$$

is the internal nodal force vector and $\mathbf{B}$ is the strain-displacement matrix. The integration is taken over the element domain Ω_e, and summation $\sum_e$ should be understood as the element assemblage operator. $\mathbf{F}^{ext}$ is the external nodal force vector; $\mathbf{M}$ is the consistent mass matrix,

$$\mathbf{M} = \sum_e \int_{\Omega_e} \mathbf{N}^T \rho \mathbf{N}\ d\Omega \tag{3.63}$$

and $\mathbf{D}$ is the viscous damping matrix which will be discussed later.

To model incompressible materials such as undrained clays, finite element interpolation should be designed to avoid the volumetric locking phenomenon at the incompressibility limit, i.e., as Poisson's ratio $\nu \to \frac{1}{2}$. Locking arises from the existence of parasitic shear in the standard element formulation. Several techniques, either ad hoc or mathematically rigorous, are designed to combat this difficulty, such as the method of incompatible modes (QM6), selective reduced integration, the $\bar{B}$ method, and the mixed formulation (Zienkiewicz and Taylor, 2000). $\bar{\mathbf{B}}$ method is related to mixed methods. The essence of the $\bar{\mathbf{B}}$ formulation is to modify the term associated with volumetric strain in the element such that incompressibility is satisfied in a volume average sense without the need to reinforce it point-wise at each Gaussian point. Accordingly, the internal force can be split into deviatoric and volumetric parts by introducing the following decomposition

$$\mathbf{B} = \mathbf{B}_{dev} + \mathbf{B}_{vol}, \tag{3.64}$$

where the selective reduced integration scheme can be used for the volumetric part, which reduces the rank of stiffness matrix.

To solve the above nonlinear set of ordinary differential equations, various direct integration schemes can be used to relate the velocity and acceleration to a displacement increment $\Delta\mathbf{u}_{n+1} = \mathbf{u}_{n+1} - \mathbf{u}_n$. For example, the popular Newmark method specifies the following update to advance a solution from t_n to t_{n+1},

$$\begin{aligned} \mathbf{v}_{n+1} &= \left(1 - \frac{\gamma}{\beta}\right)\mathbf{v}_n + \frac{\gamma}{\beta\Delta t}\Delta\mathbf{u}_{n+1} + \Delta t\left(1 - \frac{\gamma}{2\beta}\right)\mathbf{a}_n \\ \mathbf{a}_{n+1} &= \left(1 - \frac{1}{2\beta}\right)\mathbf{a}_n + \frac{1}{\beta\Delta t^2}\Delta\mathbf{u}_{n+1} - \frac{1}{\beta\Delta t}\mathbf{v}_n \end{aligned} \tag{3.65}$$

in which $\mathbf{u}_n$, $\mathbf{v}_n$, and $\mathbf{a}_n$ are approximations of $\mathbf{u}(t_n)$, $\dot{\mathbf{u}}(t_n)$, $\ddot{\mathbf{u}}(t_n)$ at time step t_n; Δt is the time step; β and γ are numerical parameters which control the stability and numerical dissipation of the integration scheme respectively. β primarily controls the stability but also influences the form of the matrix problem. For $\beta = 0$, the formulation is reduced to *explicit* method, and the solution step can be greatly simplified especially if the lumped mass matrix is used. However, the explicit method is only conditionally stable and very small time steps are needed. For $\beta \neq 0$, the method is *implicit*, which improves the stability so quite large time steps can be taken. For example, if $\beta = 0.25$, the method for linear problems

is unconditionally stable, which is commonly called *trapezoidal rule* or *constant average acceleration*. Values of β less than 0.25 shouldn't be used, since they are only conditionally stable (Zienkiewicz and Taylor, 2000). Since the Newmark integration scheme is linear and has scalar coefficients, the primary unknowns in basic equation (3.61) can be reduced to a single vector, which can be chosen as either the displacement $\mathbf{u}_{n+1}$, the velocity $\mathbf{v}_{n+1}$, or the acceleration $\mathbf{a}_{n+1}$. Here we select $\mathbf{u}_{n+1}$ as the primary unknowns and solve the following residual equation at time step t_{n+1},

$$\mathbf{R}_{n+1} = \mathbf{R}(\mathbf{u}_{n+1}) = \mathbf{F}^{ext}_{n+1} - \mathbf{M}\mathbf{a}_{n+1} - \mathbf{D}\mathbf{v}_{n+1} - \mathbf{F}^{int}(\boldsymbol{\sigma}_{n+1}) = 0 \tag{3.66}$$

Given solutions at time t_n, solutions of the above global system of nonlinear implicit equations at time t_{n+1} can be obtained using an iterative procedure, such as Newton-Raphson or quasi-Newton techniques. The sequence of approximation $\mathbf{u}^{(i)}_{n+1}, i = 0, 1, 2...$ can be calculated by iteration, which (one hopes) converges to the solution $\mathbf{u}_{n+1}$. Consistent with Newmark integration (3.65), the initial values to start the iteration can be set as follows,

$$\mathbf{u}^{(0)}_{n+1} = \mathbf{u}_n \tag{3.67}$$

$$\mathbf{v}^{(0)}_{n+1} = \left(1 - \frac{\gamma}{\beta}\right)\mathbf{v}_n + \Delta t\left(1 - \frac{\gamma}{2\beta}\right)\mathbf{a}_n \tag{3.68}$$

$$\mathbf{a}^{(0)}_{n+1} = -\frac{1}{\beta\Delta t}\mathbf{v}_n + \left(1 - \frac{1}{2\beta}\right)\mathbf{a}_n \tag{3.69}$$

Using Newton-Raphson iterative scheme, the residual form (3.66) can be linearized around $\mathbf{u}^{(i)}_{n+1}$,

$$\begin{aligned}\mathbf{R}\left(\mathbf{u}^{(i+1)}_{n+1}\right) &= \mathbf{R}\left(\mathbf{u}^{(i)}_{n+1}\right) + \left[\frac{\partial \mathbf{R}(\mathbf{u}_{n+1})}{\partial \mathbf{u}_{n+1}}\right]_{\mathbf{u}^{(i)}_{n+1}}\left(\mathbf{u}^{(i+1)}_{n+1} - \mathbf{u}^{(i)}_{n+1}\right) \\ &= \mathbf{R}\left(\mathbf{u}^{(i)}_{n+1}\right) - \mathbf{K}^{*(i)}\left(\mathbf{u}^{(i+1)}_{n+1} - \mathbf{u}^{(i)}_{n+1}\right) = 0\end{aligned} \tag{3.70}$$

where

$$\mathbf{K}^{*(i)} = -\left[\frac{\partial \mathbf{R}(\mathbf{u}_{n+1})}{\partial \mathbf{u}_{n+1}}\right]_{\mathbf{u}^{(i)}_{n+1}} = \frac{\partial \mathbf{a_{n+1}}}{\partial \mathbf{u}_{n+1}}\mathbf{M} + \frac{\partial \mathbf{v_{n+1}}}{\partial \mathbf{u}_{n+1}}\mathbf{D} + \frac{\partial \mathbf{F}^{int}(\boldsymbol{\sigma}_{n+1})}{\partial \mathbf{u}_{n+1}} \tag{3.71}$$

To evaluate the above, Newmark integration (3.65) can be linearized as

$$\frac{\partial \mathbf{a_{n+1}}}{\partial \mathbf{u}_{n+1}} = \frac{1}{\beta\Delta t^2} \tag{3.72}$$

$$\frac{\partial \mathbf{v_{n+1}}}{\partial \mathbf{u}_{n+1}} = \frac{\gamma}{\beta\Delta t} \tag{3.73}$$

Also we can evaluate

$$\frac{\partial \mathbf{F}^{int}(\boldsymbol{\sigma}_{n+1})}{\partial \mathbf{u}_{n+1}} = \sum_e \int_{\Omega_e} \mathbf{B}^T \frac{\partial \boldsymbol{\sigma}_{n+1}}{\partial \boldsymbol{\epsilon}_{n+1}} \mathbf{B} \; d\Omega \tag{3.74}$$

We further define the material's *algorithmic consistent tangent* $\mathbf{C}^{alg}$ as the exact linearization of the material's constitutive relation at the step t_{n+1} as,

$$\mathbf{C}^{alg} = \frac{\partial \boldsymbol{\sigma}_{n+1}}{\partial \boldsymbol{\epsilon}_{n+1}} \tag{3.75}$$

Hence

$$\frac{\partial \mathbf{F}^{int}(\boldsymbol{\sigma}_{n+1})}{\partial \mathbf{u}_{n+1}} = \sum_e \int_{\Omega_e} \mathbf{B}^T \mathbf{C}^{alg} \mathbf{B} \; d\Omega = \mathbf{K}^{alg} \tag{3.76}$$

Finally $\mathbf{u}_{n+1}^{(i+1)}$ can be solved from the following

$$\mathbf{K}^{*(i)} \left(\mathbf{u}_{n+1}^{(i+1)} - \mathbf{u}_{n+1}^{(i)} \right) = \mathbf{R}(\mathbf{u}_{n+1}^{(i)}) \tag{3.77}$$

where

$$\mathbf{K}^{*(i)} = \mathbf{K}^{alg} + \frac{\gamma}{\beta \Delta t} \mathbf{D} + \frac{1}{\beta \Delta t^2} \mathbf{M} \tag{3.78}$$

In practice, Rayleigh damping is often used so that the damping matrix $\mathbf{D}$ can be assumed as a linear combination of mass matrix $\mathbf{M}$ and stiffness matrix $\mathbf{K}$

$$\mathbf{D} = \alpha_1 \; \mathbf{M} + \alpha_2 \; \mathbf{K} \tag{3.79}$$

To produce a designed damping ratio ξ, constants α_1 and α_2 are determined by

$$\alpha_1 = \frac{2\xi}{\omega_1 + \omega_2} \tag{3.80}$$

$$\alpha_2 = \frac{2\omega_1 \omega_2 \xi}{\omega_1 + \omega_2} = \omega_1 \omega_2 \alpha_1 \tag{3.81}$$

and ω_1 and ω_2 are chosen to cover the desired frequency range (encompassing the natural period of the soil and the predominant period of input motion). Alternatively, the damping matrix can be directly assumed to be proportional to the initial modulus via

$$\mathbf{D} = \frac{2\xi_0}{\omega} \mathbf{K}^e \tag{3.82}$$

where ω is the predominant frequency of input motion and ξ_0 is the damping ratio at the limit of zero shear strain, which is usually assumed to be quite small for soil (typical value 1%).

As a general remark to conclude this section, the importance of the algorithmic consistent tangent has to be emphasized. The algorithmic consistent tangent can be the same as the continuum tangent for a linear elastic material, but they are distinctive for a general nonelastic material. The algorithmic consistent tangent is derived from the exact linearization of the *discrete* constitutive relation, and it is compatible with the use of the Newton-Raphson iterative scheme in solving the global system of equations. As pointed out by Simo and Taylor (1985), the use of the algorithmic consistent tangent $\mathbf{C}^{alg}$ is essential to preserve the asymptotic global *quadratic rate of convergence* of the Newton-Raphson scheme, while using the continuum tangent may deteriorate the efficiency and only results in a linear rate of convergence.

3.4.2 Algorithmic Tangent Operator

To be implemented in a numerical analysis program, the rate constitutive equation of the nonlinear material model needs to be numerically integrated. As commonly used in a displacement-based finite element procedure, integration of the local constitutive equation is usually treated as a strain-driven problem, i.e., given a strain increment $\Delta\boldsymbol{\epsilon}_{n+1} = \boldsymbol{\epsilon}_{n+1} - \boldsymbol{\epsilon}_n$ and state variables at time t_n, one seeks to obtain the stress and state variables at the next discrete time step t_{n+1}. Obviously, the accuracy and stability of the local integration algorithm will directly influence the accuracy and stability of the global system.

Now consider the rate constitutive equation we have obtained in previous section

$$\dot{\boldsymbol{\sigma}} = K\dot{\theta}\mathbf{1} + 2G\left(1 + \frac{3G}{H'}\right)^{-1}\dot{\boldsymbol{\epsilon}}' \tag{3.83}$$

The deviatoric components of stress increment can be integrated from t_n to t_{n+1},

$$\boldsymbol{\sigma}'_{n+1} - \boldsymbol{\sigma}'_n = \Delta\boldsymbol{\sigma}'_{n+1} = 2G\int_{t_n}^{t_{n+1}}\left(1 + \frac{3G}{H'}\right)^{-1} d\,\boldsymbol{\epsilon}' \tag{3.84}$$

Since H' is not a constant, a trapezoidal rule can be applied to integrate the above equation

$$\Delta\boldsymbol{\sigma}'_{n+1}\left[1 + 3G\left(\frac{1-\beta}{H'_n} + \frac{\beta}{H'_{n+1}}\right)\right] = 2G\Delta\boldsymbol{\epsilon}'_{n+1} \tag{3.85}$$

where $H'_n = h\kappa_n^m + H_0$ and $H'_{n+1} = h\kappa_{n+1}^m + H_0$ are hardening moduli evaluated at time t_n and t_{n+1}, respectively. The parameter β is an integration parameter such that the integration

is explicit if $\beta = 0$ and fully implicit if $\beta = 1$. Since it has been shown that the stress increment and strain increment are coaxial, we can assume $\Delta\boldsymbol{\sigma}'_{n+1} = \Psi\Delta\boldsymbol{\epsilon}'_{n+1}$, then the above equation yields a residual equation:

$$\mathcal{G}_1 := 2G - \Psi\left[1 + 3G\left(\frac{1-\beta}{H'_n} + \frac{\beta}{H'_{n+1}}\right)\right] = 0 \tag{3.86}$$

in which $H'_{n+1} = h\kappa^m_{n+1} + H_0$, and parameters Ψ and κ_{n+1} remains unknown. We need another restriction to solve these two unknowns. Imposing the following condition at t_{n+1}

$$\|\hat{\boldsymbol{\sigma}}'_{n+1} - \boldsymbol{\beta}_{n+1}\| = \|\boldsymbol{\sigma}'_{n+1} - \boldsymbol{\beta}_{n+1} + \kappa_{n+1}(\boldsymbol{\sigma}'_{n+1} - \boldsymbol{\sigma}'_0)\| = R \tag{3.87}$$

If the stress state of t_{n+1} still remains *within* the bounding surface $\mathcal{B}$, then $\boldsymbol{\beta}_{n+1} = \boldsymbol{\beta}_n$ since kinematic hardening of $\mathcal{B}$ will not occur in this case. We obtained the second residual equation:

$$\mathcal{G}_2 := R - \|\boldsymbol{\sigma}'_n - \boldsymbol{\beta}_n + \Psi\ \Delta\boldsymbol{\epsilon}'_{n+1} + \kappa_{n+1}(\boldsymbol{\sigma}'_n + \Psi\ \Delta\boldsymbol{\epsilon}'_{n+1} - \boldsymbol{\sigma}'_0)\| = 0 \tag{3.88}$$

We propose to solve Eqs.(3.86) and (3.88) simultaneously for Ψ and κ_{n+1} using the Newton-Raphson iterative scheme. The procedure is outlined by pseudo-code in Algorithm 2. Once Ψ is obtained, the stress point $\boldsymbol{\sigma}_{n+1}$ can be updated accordingly:

$$\boldsymbol{\sigma}_{n+1} = \boldsymbol{\sigma}_n + K\Delta\theta\mathbf{1} + \Psi\Delta\boldsymbol{\epsilon}'_{n+1} \tag{3.89}$$

In the context of nonlinear finite element analyses, the consistent algorithmic tangent is usually needed to improve the stability and efficiency of the global solution scheme. The consistent algorithmic tangent can be obtained through complete linearization of constitutive relation in discrete form:

$$\mathbf{C}^{alg}_F = \frac{\partial\boldsymbol{\sigma}_{n+1}}{\partial\boldsymbol{\epsilon}_{n+1}} = K\mathbf{I}\otimes\mathbf{I} + \Psi\ \mathbf{II}_{dev} + \frac{\partial\Psi}{\partial\boldsymbol{\epsilon}'_{n+1}}\otimes\Delta\boldsymbol{\epsilon}'_{n+1} \tag{3.90}$$

In particular, $\dfrac{\partial\Psi}{\partial\boldsymbol{\epsilon}'_{n+1}}$ can be obtained by differentiation of Eqs.(3.86) and (3.88) as follows:

$$\frac{\partial\mathcal{G}_1}{\partial\boldsymbol{\epsilon}'_{n+1}} = \left[1 + 3G\left(\frac{1-\beta}{H'_n} + \frac{\beta}{H'_{n+1}}\right)\right]\frac{\partial\Psi}{\partial\boldsymbol{\epsilon}'_{n+1}} - \left[\frac{3G\Psi\beta}{H'^{\,2}_{n+1}}\frac{\partial H'_{n+1}}{\partial\kappa_{n+1}}\right]\frac{\partial\kappa_{n+1}}{\partial\boldsymbol{\epsilon}'_{n+1}} = 0 \tag{3.91}$$

$$\begin{aligned}\frac{\partial\mathcal{G}_2}{\partial\boldsymbol{\epsilon}'_{n+1}} &= (1+\kappa_{n+1})\hat{\boldsymbol{\xi}}_{n+1} : \Delta\boldsymbol{\epsilon}'_{n+1}\ \frac{\partial\Psi}{\partial\boldsymbol{\epsilon}'_{n+1}} + \hat{\boldsymbol{\xi}}_{n+1} : (\boldsymbol{\sigma}'_n + \Psi\ \Delta\boldsymbol{\epsilon}'_{n+1} - \boldsymbol{\sigma}'_0)\ \frac{\partial\kappa_{n+1}}{\partial\boldsymbol{\epsilon}'_{n+1}} \\ &\quad +(1+\kappa_{n+1})\Psi\hat{\boldsymbol{\xi}}_{n+1} = 0\end{aligned} \tag{3.92}$$

where $\hat{\boldsymbol{\xi}}_{n+1} = \hat{\boldsymbol{\sigma}}'_{n+1} - \boldsymbol{\beta}_{n+1} = \boldsymbol{\sigma}'_n - \boldsymbol{\beta}_n + \Psi\ \Delta\boldsymbol{\epsilon}'_{n+1} + \kappa_{n+1}(\boldsymbol{\sigma}'_n + \Psi\ \Delta\boldsymbol{\epsilon}'_{n+1} - \boldsymbol{\sigma}'_0)$ is image stress, and it points to the radial direction. Solving the above equations leads to

$$\frac{\partial \Psi}{\partial \boldsymbol{\epsilon}'_{n+1}} \otimes \Delta\boldsymbol{\epsilon}'_{n+1} = -\frac{\Psi(1+\kappa_{n+1})}{\theta_1}\ \hat{\boldsymbol{\xi}}_{n+1} \otimes \Delta\boldsymbol{\epsilon}'_{n+1} \tag{3.93}$$

where

$$\theta_1 = (1+\kappa_{n+1})(\hat{\boldsymbol{\xi}}_{n+1} : \Delta\boldsymbol{\epsilon}'_{n+1}) + \hat{\boldsymbol{\xi}}_{n+1} : (\boldsymbol{\sigma}'_n + \Psi\ \Delta\boldsymbol{\epsilon}'_{n+1} - \boldsymbol{\sigma}'_0)\theta_2 \tag{3.94}$$

$$\theta_2 = \left(\frac{3G\Psi\beta}{H'^{\,2}_{n+1}}\frac{\partial H'_{n+1}}{\partial \kappa_{n+1}}\right)^{-1}\left[1 + 3G\left(\frac{1-\beta}{H'_n} + \frac{\beta}{H'_{n+1}}\right)\right] \tag{3.95}$$

As we can see from the above expression, $\dfrac{\partial \Psi}{\partial \boldsymbol{\epsilon}'_{n+1}}$ is in line with $\hat{\boldsymbol{\xi}}_{n+1}$, i.e., it points to the radial direction. So the term $\dfrac{\partial \Psi}{\partial \boldsymbol{\epsilon}'_{n+1}} \otimes \Delta\boldsymbol{\epsilon}'_{n+1}$ has no major symmetry for a general loading path, and the exact evaluation of it is cumbersome. To preserve symmetry and simplicity, we propose to drop this term and use the following tangent modulus in the algorithm:

$$\mathbf{C}_F^{alg} = K\mathbf{I} \otimes \mathbf{I} + \Psi\ \mathbf{II}_{dev} \tag{3.96}$$

It is also worth pointing out that the simplification slightly influences the convergence rate of global solution iterations, but it will not affect the accuracy of the solution.

3.4.3 Operator Split across Bounding Surface

Given a strain increment, a special case must be considered in the stress update process, i.e., the initial stress point is inside the bounding surface $\mathcal{B}$, but the stress point hits $\mathcal{B}$ at $t_{n+\gamma}$ and pushes $\mathcal{B}$ together in the remaining time. For a given strain increment $\Delta\boldsymbol{\epsilon}'$, it can be additively decomposed into two parts,

$$\Delta\boldsymbol{\epsilon}' = \Delta\boldsymbol{\epsilon}'^F + \Delta\boldsymbol{\epsilon}'^B \tag{3.97}$$

where $\Delta\boldsymbol{\epsilon}'^F$ is the strain increment that drives the stress state right onto the bounding surface $\mathcal{B}$, and $\Delta\boldsymbol{\epsilon}'^B$ is the plastic strain persistent on the bounding surface.

Introducing a dimensionless strain split parameter $0 \le \gamma \le 1$ such that

$$\Delta\boldsymbol{\epsilon}'^F = \gamma\Delta\boldsymbol{\epsilon}' \qquad \text{and} \qquad \Delta\boldsymbol{\epsilon}'^B = (1-\gamma)\Delta\boldsymbol{\epsilon}' \tag{3.98}$$

Secant modulus Ψ_γ is the interpolation between H'_n and $H'_{n+\gamma}(= H_0)$

$$\Psi_\gamma = \frac{2G}{1 + 3G\left(\dfrac{1-\beta}{H'_n} + \dfrac{\beta}{H_0}\right)} \tag{3.99}$$

To avoid singularity that would occur to evaluate terms as $H' \to 0$, an alternative expression for secant modulus Ψ_γ can be written as

$$\Psi_\gamma = 2G\left(1 - \frac{G}{G + \dfrac{1}{3}\left((1-\beta)H'_n + \beta H_0\right)}\right) \tag{3.100}$$

It should be noted that these two relations are not equivalent, since in general

$$\frac{1-\beta}{H'_n} + \frac{\beta}{H_0} \neq \frac{1}{(1-\beta)H'_n + \beta H_0} \tag{3.101}$$

The left- and right-hand sides are trapezoidal integrations of H' and $1/H'$, respectively. Although Eq. (3.99) is proposed by Borja and Amies (1994), Eq. (3.100) is preferred, since the variation of H' is much less compared with the drastic change of $1/H'$ as $H' \to 0$. Considering the fact that $\boldsymbol{\xi}_{n+\gamma}$ is on the bounding surface $\mathcal{B}$, i.e.,

$$\|\boldsymbol{\xi}_{n+\gamma}\|^2 = \|\boldsymbol{\xi}_n + \Psi_\gamma \gamma \Delta\boldsymbol{\epsilon}'\|^2 = R^2 \tag{3.102}$$

where $\boldsymbol{\xi}_n = \boldsymbol{\sigma}'_n - \boldsymbol{\beta}_n$ The parameter γ could be solved as the positive root of the above quadratic equation,

$$\gamma = \frac{-\boldsymbol{\xi}_n : \Delta\boldsymbol{\epsilon}' + \sqrt{(\boldsymbol{\xi}_n : \Delta\boldsymbol{\epsilon}')^2 + \Delta\boldsymbol{\epsilon}' : \Delta\boldsymbol{\epsilon}'(R^2 - \boldsymbol{\xi}_n : \boldsymbol{\xi}_n)}}{\Psi_\gamma \Delta\boldsymbol{\epsilon}' : \Delta\boldsymbol{\epsilon}'} \tag{3.103}$$

The above equation must be carefully examined to guarantee the solution $0 \leq \gamma \leq 1$. we propose the the following criteria for the operator split:

$$\text{(a)} \quad \|\boldsymbol{\xi}_n\|^2 < R^2 \tag{3.104}$$

$$\text{(b)} \quad \boldsymbol{\xi}_n : \Delta\boldsymbol{\epsilon}' > 0 \tag{3.105}$$

$$\text{(c)} \quad \|\boldsymbol{\xi}^{tr}\|^2 = \|\boldsymbol{\xi}_n + \Psi_\gamma \Delta\boldsymbol{\epsilon}'\|^2 \geq R^2 \tag{3.106}$$

That is, if (a) the previous state is inside the bounding surface, (b) the strain increment step is loading, and (c) the trial state $\boldsymbol{\xi}^{tr}$ is outside the bounding surface, the strain split should be performed. For the bounding surface which is perfectly plastic or hardening ($H_0 \geq 0$),

from Eq. (3.100) it is obvious $\Psi_\gamma > 0$, since $H'_n = h\kappa_n^m + H_0 > H_0 \geq 0$. Together with condition (a), it can be assured $\gamma > 0$ in Eq. (3.103). Further, since

$$\|\boldsymbol{\xi}_n + \Psi_\gamma \Delta\boldsymbol{\epsilon}'\|^2 = \boldsymbol{\xi}_n : \boldsymbol{\xi}_n + 2\Psi_\gamma \boldsymbol{\xi}_n : \Delta\boldsymbol{\epsilon}' + \Psi_\gamma^2 \Delta\boldsymbol{\epsilon}' : \Delta\boldsymbol{\epsilon}' \geq R^2 \tag{3.107}$$

$$\|\boldsymbol{\xi}_n + \Psi_\gamma \gamma \Delta\boldsymbol{\epsilon}'\|^2 = \boldsymbol{\xi}_n : \boldsymbol{\xi}_n + 2\Psi_\gamma \gamma \boldsymbol{\xi}_n : \Delta\boldsymbol{\epsilon}' + \Psi_\gamma^2 \gamma^2 \Delta\boldsymbol{\epsilon}' : \Delta\boldsymbol{\epsilon}' = R^2 \tag{3.108}$$

which implies

$$(1-\gamma)\left(2\Psi_\gamma \boldsymbol{\xi}_n : \Delta\boldsymbol{\epsilon}' + \Psi_\gamma^2 (1+\gamma)\Delta\boldsymbol{\epsilon}' : \Delta\boldsymbol{\epsilon}'\right) \geq 0 \tag{3.109}$$

considering loading condition $\boldsymbol{\xi}_n : \Delta\boldsymbol{\epsilon}' > 0$, so $\gamma \leq 1$ is proved.

For the case that the bounding surface is kinematically softening ($H_0 < 0$), difficulties can be seen by inspecting the above conditions. For the t_n state close enough to the bounding surface, it is likely that $H'_n = h\kappa_n^m + H_0 < 0$, which yields a trial modulus $\Psi_\gamma < 0$. Even if the trial state is loading, the predictor is strain softening and so the bounding surface will never be reached. An ad-hoc remedy can be proposed to interpolate $H'_n =< H_0 > + h\kappa_n^m > 0$ inside the bounding surface. So for the softening bounding surface, $< H_0 >= 0$ and the stationary point $H' = 0$ is achieved when trail stress crosses the bounding surface. For the ensuing persistent plastic loading, the bounding surface softens according to the assigned value $H_0 < 0$.

To compute the plastic strain $(1-\gamma)\Delta\boldsymbol{\epsilon}'$, the classical return mapping scheme for J_2 plasticity can be applied (Simo and Hughes, 1997). Finally, the state variables at t_{n+1} can be updated as a linear combination

$$\boldsymbol{\sigma}_{n+1} = \boldsymbol{\sigma}_n + K\ \Delta\theta\ \mathbf{I} + \gamma\Psi_\gamma \Delta\boldsymbol{\epsilon}' + 2G\ \left((1-\gamma)\Delta\boldsymbol{\epsilon}' - \lambda_B\ \hat{\mathbf{n}}_B\right) \tag{3.110}$$

$$\boldsymbol{\beta}_{n+1} = \boldsymbol{\beta}_n + \frac{2}{3} H_0 \lambda_B\ \hat{\mathbf{n}}_B \tag{3.111}$$

$$\lambda_B = (1-\gamma)\left(\frac{G}{G + H_0/3}\right)\|\Delta\boldsymbol{\epsilon}'\| \tag{3.112}$$

and the resulting algorithmic consistent tangent is simply a linear combination of two types of tangent operators as

$$\mathbf{C}^{alg} = \gamma\ \mathbf{C}_F^{alg} + (1-\gamma)\ \mathbf{C}_B^{alg} \tag{3.113}$$

The operator split algorithm is summarized in Algorithm 3.

Algorithm 1 Classical J2 plasticity return mapping algorithm

1. For stress state $\boldsymbol{\sigma}_n$ on the bounding surface, elastic predictor:

$$\boldsymbol{\sigma}^{tr}_{n+1} = \boldsymbol{\sigma}_n + \mathbf{C}^e : \Delta\boldsymbol{\epsilon}_{n+1} \tag{3.114}$$

where $\Delta\boldsymbol{\epsilon}_{n+1} = \frac{1}{3}\Delta\theta_{n+1}\ \mathbf{I} + \Delta\boldsymbol{\epsilon}'_{n+1}$; $\mathbf{C}^e = K\mathbf{I}\otimes\mathbf{I} + 2G\ \mathbf{II}_{dev}$

$$\boldsymbol{\xi}^{tr}_{n+1} = \boldsymbol{\sigma}^{tr}_{n+1} - \boldsymbol{\beta}_n \tag{3.115}$$

$$f^{tr}_{n+1} = \|\boldsymbol{\xi}^{tr}_{n+1}\| - R \tag{3.116}$$

2. Loading/unloading check

   If unloading, then set unloading point $\boldsymbol{\sigma}_0$ to current stress, and proceed to Alg. 2 or else CONTINUE

3. Compute plastic multiplier and normal

$$\Delta\lambda_B = \frac{f^{tr}_{n+1}}{2G + \frac{2}{3}H_0} \tag{3.117}$$

$$\hat{\mathbf{n}}_B = \frac{\boldsymbol{\xi}^{tr}_{n+1}}{\|\boldsymbol{\xi}^{tr}_{n+1}\|} \tag{3.118}$$

4. Update stress and back stress of bounding surface $\mathcal{B}$

$$\boldsymbol{\sigma}_{n+1} = \boldsymbol{\sigma}_n + K\ \Delta\theta_{n+1}\ \mathbf{I} + 2G\ (\Delta\boldsymbol{\epsilon}'_{n+1} - \Delta\lambda_B\ \hat{\mathbf{n}}_B) \tag{3.119}$$

$$\boldsymbol{\beta}_{n+1} = \boldsymbol{\beta}_n + \frac{2}{3}H_0\Delta\lambda_B\ \hat{\mathbf{n}}_B \tag{3.120}$$

5. Consistent elasto-plastic tangent

$$\mathbf{C}^{alg}_B = K\mathbf{I}\otimes\mathbf{I} + 2G\ \theta_1\mathbf{II}_{dev} - 2G\ \theta_2\hat{\mathbf{n}}_B\otimes\hat{\mathbf{n}}_B \tag{3.121}$$

where

$$\theta_1 = 1 - \frac{2G\Delta\lambda_B}{\|\boldsymbol{\xi}^{tr}_{n+1}\|},\ \theta_2 = \frac{1}{1+\frac{H_0}{3G}} - (1-\theta_1) \tag{3.122}$$

Algorithm 2 Integration of bounding surface plasticity

1. **Newton Iteration to solve Ψ and κ**

Initialize

$$\begin{bmatrix} \Psi_{n+1} \\ \kappa_{n+1} \end{bmatrix}^{(0)} = \begin{bmatrix} \Psi_n \\ \kappa_n \end{bmatrix} \tag{3.123}$$

$$\mathcal{G}_1 := 2G - \Psi \left[1 + 3G \left(\frac{1-\beta}{H'_n} + \frac{\beta}{H'_{n+1}} \right) \right] \tag{3.124}$$

$$\mathcal{G}_2 := R - \| \boldsymbol{\xi}_n + \Psi \ \Delta \boldsymbol{\epsilon}'_{n+1} + \kappa_{n+1} (\boldsymbol{\sigma}'_n + \Psi \ \Delta \boldsymbol{\epsilon}'_{n+1} - \boldsymbol{\sigma}'_0) \| \tag{3.125}$$

Compute Jacobian

$$[\mathbf{J}^{(k)}] = \begin{bmatrix} \dfrac{\partial \mathcal{G}_1}{\partial \Psi} & \dfrac{\partial \mathcal{G}_1}{\partial \kappa} \\ \dfrac{\partial \mathcal{G}_2}{\partial \Psi} & \dfrac{\partial \mathcal{G}_2}{\partial \kappa} \end{bmatrix}_{(\Psi_{n+1}, \kappa_{n+1})^{(k)}} \tag{3.126}$$

while $\| \mathcal{G}_1^2 + \mathcal{G}_2^2 \| < TOL$ **do**

Update solution

$$\begin{bmatrix} \Psi_{n+1} \\ \kappa_{n+1} \end{bmatrix}^{(k+1)} = \begin{bmatrix} \Psi_{n+1} \\ \kappa_{n+1} \end{bmatrix}^{(k)} - [\mathbf{J}^{(k)}]^{-1} \begin{bmatrix} \mathcal{G}_1 \\ \mathcal{G}_2 \end{bmatrix}^{(k)} \tag{3.127}$$

Update $\mathcal{G}_1$, $\mathcal{G}_2$

end while

2. Update stress

$$\boldsymbol{\sigma}_{n+1} = \boldsymbol{\sigma}_n + K \ \Delta\theta_{n+1} \ \mathbf{I} + \Psi \Delta \boldsymbol{\epsilon}'_{n+1} \tag{3.128}$$

3. Elasto-plastic tangent (symmetric version)

$$\mathbf{C}_F^{alg} = K \mathbf{I} \otimes \mathbf{I} + \Psi \ \mathbf{II}_{dev} \tag{3.129}$$

Algorithm 3 Strain Step Split

1. Decompose the deviatoric strain into

$$\Delta\boldsymbol{\epsilon}' = \Delta\boldsymbol{\epsilon}'^F + \Delta\boldsymbol{\epsilon}'^B \tag{3.130}$$

where $\Delta\boldsymbol{\epsilon}'^F$ is the strain that loads the soil to the bounding surface B at time $t_{n+\gamma}$, and $\Delta\boldsymbol{\epsilon}'^B$ is the deviatoric strain the soil experiences after reaching the bounding surface.

$$\Delta\boldsymbol{\epsilon}'^F = \gamma\Delta\boldsymbol{\epsilon}' \tag{3.131}$$

2. Solve for secant modulus split

$$\Psi_\gamma = \frac{2G}{1 + 3G\left(\dfrac{1-\beta}{H'_n} + \dfrac{\beta}{H_0}\right)} \tag{3.132}$$

3. Solve for split parameter γ

$$\gamma = \frac{-\boldsymbol{\xi}_n : \Delta\boldsymbol{\epsilon} + \sqrt{(\boldsymbol{\xi}_n : \Delta\boldsymbol{\epsilon})^2 + \Delta\boldsymbol{\epsilon} : \Delta\boldsymbol{\epsilon}(R^2 - \boldsymbol{\xi}_n : \boldsymbol{\xi}_n)}}{\Psi_\gamma \Delta\boldsymbol{\epsilon} : \Delta\boldsymbol{\epsilon}} \tag{3.133}$$

where

$$\boldsymbol{\xi}_n = \boldsymbol{\sigma}'_n - \boldsymbol{\beta}_n \tag{3.134}$$

4. Linear interpolation of the tangent modulus

$$\mathbf{C}^{alg} = \gamma\ \mathbf{C}_F^{alg} + (1-\gamma)\ \mathbf{C}_B^{alg} \tag{3.135}$$

where $\mathbf{C}_F^{alg}$ and $\mathbf{C}_B^{alg}$ are from Algorithm 1 and 2.

3.5 DETERMINATION OF MODEL PARAMETERS

In previous sections, the cyclic soil model has been formulated in a general three-dimensional stress space, and a detailed numerical implementation has been derived. Fig. 3.9 schematically illustrates a cyclic soil response simulated by the model. Starting from the initial stress point ①, the nonlinear stress-strain curve from ① to ② is governed by a bounding surface hardening law. The shear modulus smoothly degenerates from maximum value at point ① to a constant residual value at point ②, where the stress point hits the bounding surface $\mathcal{B}_1$. The full plastic stage is reached from point ② to ③, and the bounding surface hardens kinematically from $\mathcal{B}_1$ to $\mathcal{B}_2$. Once the unloading condition is detected at point ③, the stress reversal point is updated to that point, and a new interpolated nonlinear stress-strain relation is developed until the stress point reaches the bounding surface again at point ④. After $\mathcal{B}_2$ hardens to $\mathcal{B}_3$, i.e., from point ④ to point ⑤, the soil is reloaded to point ⑥.

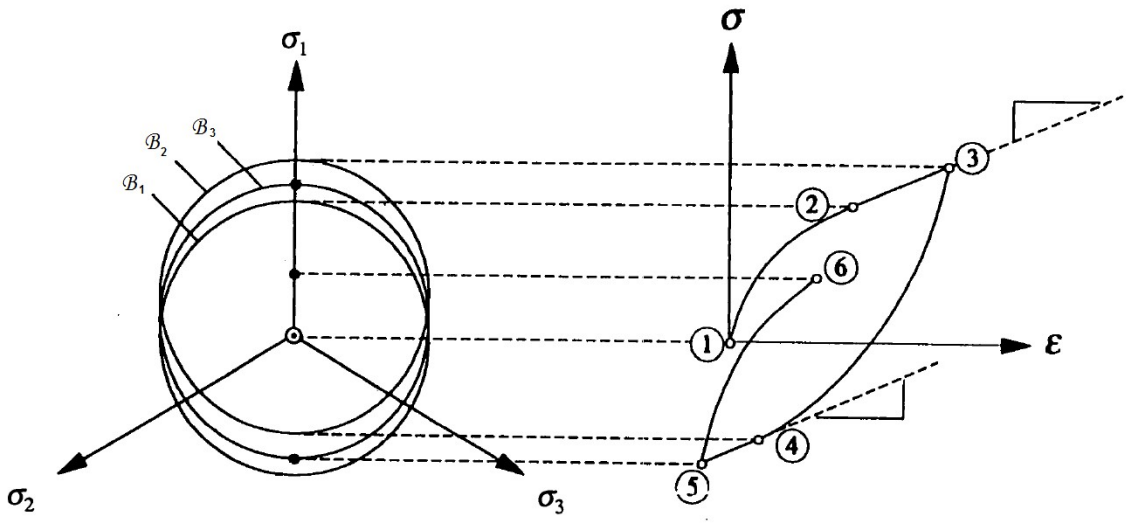

Fig. 3.9 Schematic Cyclic Soil Response

Table 3.1 summarizes recommended methods to determine model parameters. The maximum shear modulus at small strain, G_{max}, which was previously denoted as G for brevity, can be computed from the shear wave velocity profile,

$$G_{max} = \rho_s \, V_s^2 \tag{3.136}$$

Table 3.1 Determination of Model Parameters

Model Parameters		Calibration Methods
Elastic Parameters	G_{max}	From from shear wave velocity profile
	ν	Poisson's ratio
Strength Parameter	S_u	From unconfined compression test or SPT correlation
Hardening Parameters	$h,\ m$	Shear modulus reduction curves
	H_0	Tangential shear modulus at large strain

where ρ_s is soil density, and V_s is the measured shear wave velocity of the soil. The undrained shear strength, S_u, which determines the radius of the bounding surface R, can be determined from an unconfined compression (UC) test or empirical correlation such as standard penetration test (SPT) data.

As described before, the nonlinear stress-strain relation within the bounding surface is governed by the exponential hardening law. The two hardening parameters h and m control the rate of modulus degradation. Fig. 3.10 presents the cyclic simple shear response produced by a strain-controlled single finite element test. The soil element is assumed to have maximum shear modulus $G_{max} = 1.67 \times 10^5$ kPa, Possion's ratio $\nu = 0.49$, and undrained shear strength determined from unconfined compressive strength test $S_u = 100$ kPa. The hardening modulus for the bounding surface is assumed to be zero ($H_0 = 0$). As shown in Fig. 3.10(a), for a given $m = 0.8$, larger h predicts a more elastic cyclic response. As a limit case, the perfectly elasto-plastic J_2 response can be approximated using a large h value ($h \geq 10$ in this case). Fig. 3.10(b) gives the predicted cyclic loops for a given $h = 0.7\ G_{max}$ and a varying m from 0.8 to 2.0. The stress-strain relation for a larger m is more elastic right upon stress reversal; however, the curve bends over more quickly at large stress level. Since a very small tangential modulus has been developed well before the stress point reaches the bounding surface, the soil apparently experiences premature yielding for the case of larger m. Fig. 3.10(c) plots cyclic stress-strain curves with increasing magnitude of control strains. It can be observed that the Masing rule is well approximated by the cyclic curves. Note that as highlighted in Fig. 3.10(d) for a single cyclic curve, a closed loop is not immediately formed

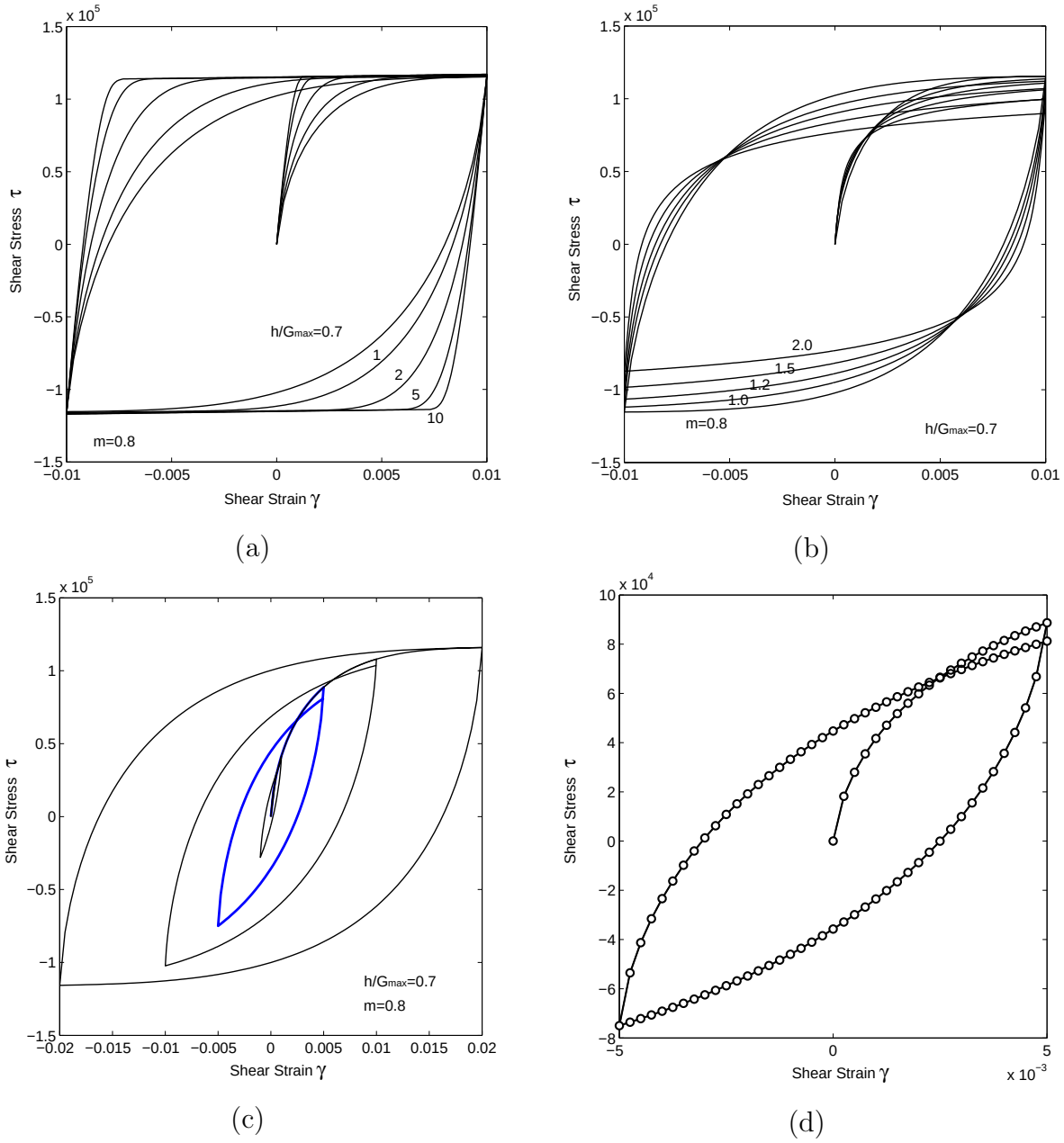

Fig. 3.10 Modeled Cyclic Simple Shear Response

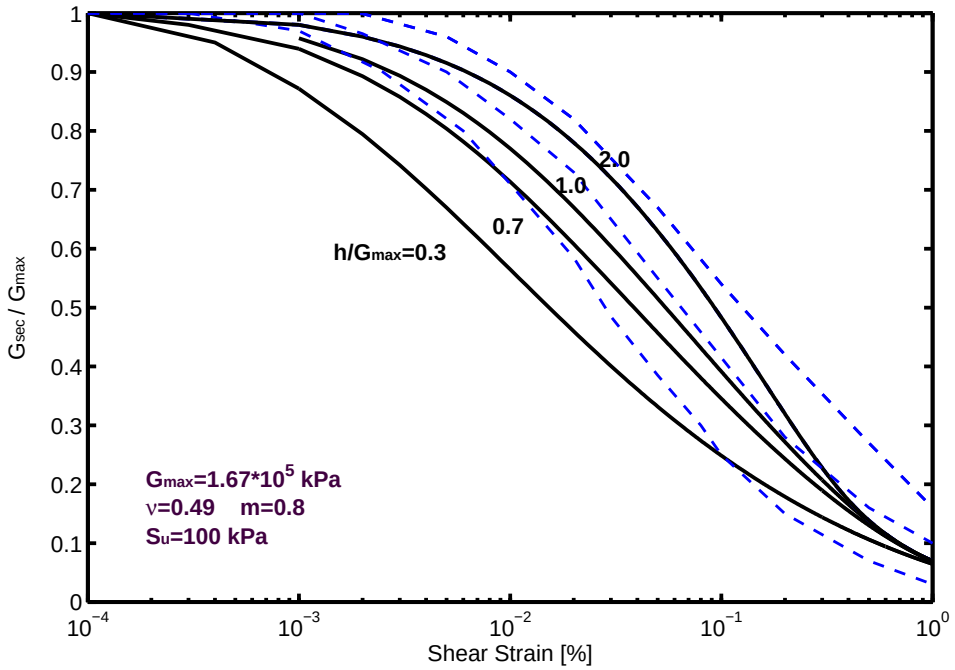

(a) variation in h

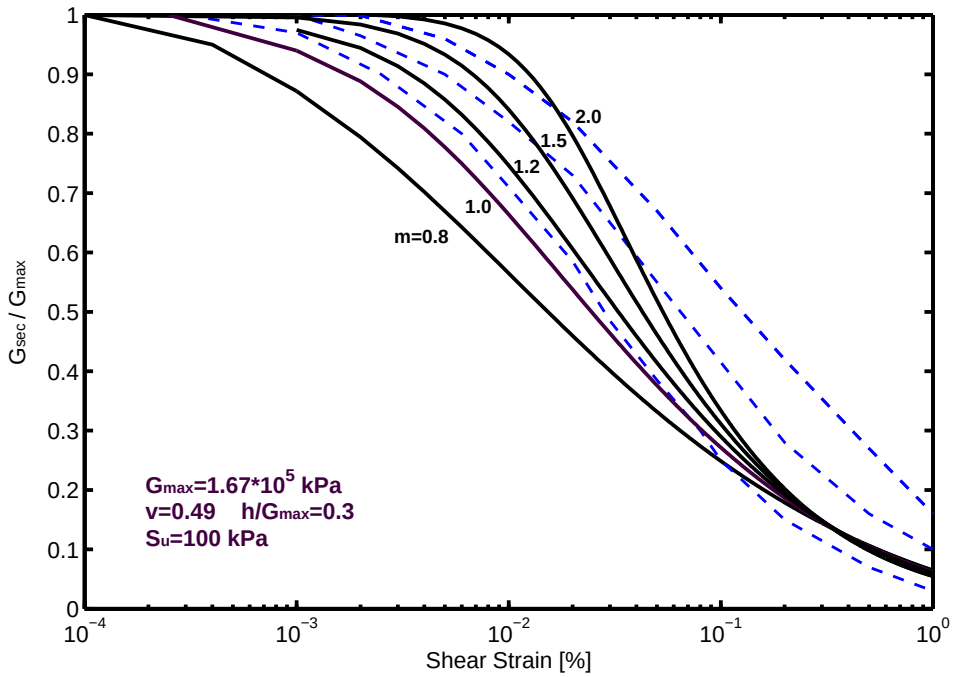

(b) variation in m

Fig. 3.11. Computed Modulus Reduction Curves, Dashed lines: PI=0,15,30 from Vucetic and Dobry (1991)

after one cycle of loading. Instead, a slight strength degradation is captured naturally by the model.

The cyclic stress-strain responses can also be represented in the form of modulus reduction curves. The modulus reduction curve plots the ratio of *secant shear modulus* and *maximum shear modulus* versus shear strains applied, and was found to be dependent on the plasticity index (PI) for clays. As presented in Fig. 3.11, variations in h and m result in a family of modulus reduction curves. Modulus reduction curves for clays (PI=0,15,30 in dashed lines, left to right) from Vucetic and Dobry (1991) are also illustrated for comparison. Although increases in h and m both shift modulus reduction curves to the right of the strain axis, their ranges of influence are different: variation in h affects the curve shape over a small to large strain range (10^{-4} % – 1 %), while variation in m mainly changes the curve shape over small to medium strain levels (10^{-4} % – 10^{-1} %). The suitable combination of h and m can be determined by fitting through two points on a measured modulus degradation curve, so the parameters can be related to fundamental properties of the soil. The hardening modulus of the bounding surface, H_0, can be determined by fitting the tangential shear modulus at large strains.

In summary, the bounding surface cyclic soil model has analytical features that can simulate three-dimensional nonlinear cyclic soil response more realistically, and it can capture the most important aspects of dynamic simulation, namely, the modulus reduction and hysteretic energy dissipation. Furthermore, the model requires minimal parameters that can be easily calibrated through a conventional field investigation. The cyclic soil model provides physical simplicity and numerical efficiency that is very much needed in a general nonlinear soil-structure analysis. The goal of this study is to use this model to simulate the nonlinear soil-pile response, and the feasibility of the numerical model is examined directly by analyzing prototype pile load tests.

4 Static and Dynamic Load Tests on Prototype Piers at UC Berkeley

4.1 INTRODUCTION

A number of seismic retrofit and new construction projects on the UC Berkeley campus relied on drilled piers to handle the expected dynamic loads. In most of these cases, the drilled piers were a relatively costly component; therefore, there was a considerable interest in making the design as cost effective as possible. In particular, the earthquake loading rate is about three orders of magnitude greater than the rate for which the static pier capacity is based. Thus, for earthquake design of pile foundations, consideration of the loading rate for piers may have important economic and safety implications (Kraft *et al.*, 1981). To be useful in the earthquake design, the loading rate in a test should be typical of an earthquake loading. The time-histories of the displacement and load should be well monitored and the pier should be loaded to a wide range of mobilized strains so that the tests can be used to explore the energy-dissipation pattern of the system from low to high strains. The capacity and stiffness degradation of the soil-pier system after the pier load test should also be investigated.

To address all these concerns and collect valuable data, a full-scale load test program on drilled cast-in-placed concrete piers was recently performed adjacent to the campus of the University of California, Berkeley (Kasali, 2002). The test results are documented and discussed in detail in the following sections.

4.2 SITE CONDITION

4.2.1 Stratigraphy

The drilled pier load test program was performed at Underhill Parking Lot near the University of California, Berkeley, campus as a part of the student residence halls Unit 1 and Unit 2 seismic retrofit project. The site is located near the seismically active Hayward fault geomorphic zone, which passes through the campus some 1,500 feet northeast of the site. The site is underlain by alluvial deposits of the Temescal Formation, and mainly consists of silts and clays of mottled yellowish / olive gray color. Fig. 4.1(a) shows the vicinity map of the test area, where the parking lot is bounded to the north by Channing Way, to the east by College Ave, to the south by Haste Street, and to the west by a construction site for the proposed new Dining/Student Services building and an exiting apartment building. As shown in Fig. 4.1(b), the Unit 1 and Unit 2 Residence Halls are located immediately north and south of the Underhill Parking Lot. It should be noted that the Underhill Parking Lot was constructed by excavating up to about 10 to 20 feet of native soil to form a relatively level area.

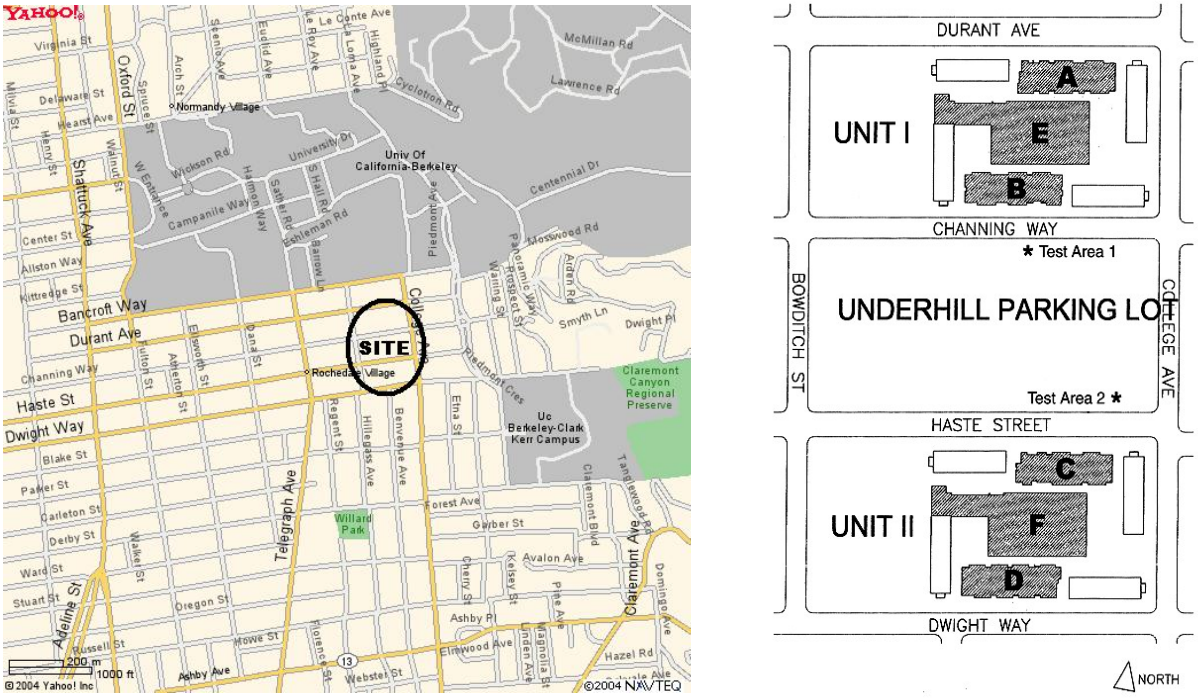

(a) Test Site (b) Close-up

Fig. 4.1 Test Area Vicinity Map

The two test areas were chosen located quite close to the locations of geotechnical borings drilled by Geomatrix Consultants in 1997. Test Area 1 (close to Channing Way) is near to boring B-2, and Test Area 2 (close to Haste Street) is located near to boring B-4. The soil profiles derived from the geotechnical investigation are schematically illustrated in Fig. 4.2 for Test Area 1 and Fig. 4.3 for Test Area 2, respectively. The surface elevations of test areas 1 and 2 are 272.5 ft and 277.5 ft (MSL), respectively. As shown in these figures, the site is underlain by stiff clay with varying amounts of silt, sand, and/or gravel. The degree of saturation varies considerably throughout the site. Groundwater was reportedly encountered at 21.5 feet in depth at Test Area 1, and 10 - 11.5 feet in depth at Test Area 2. The plasticity index of stiff clay is around 10 in the site. Thus, according to the criterion proposed by Seed and Idriss (1982), the clayey and silty soils at the site should not experience severe strength degradation during strong ground shaking.

4.2.2 Shear Wave Velocity Profile

As a part of site investigation, SASW (Spectral Analysis of Surface Waves) measurements were conducted along two arrays by Rutherford & Chekene on June 22-24, 2001. Test locations of SASW array 1 and array 2 were chosen to coincide with the locations of test piers site 1 and site 2, respectively [1]. SASW method is an in-situ geophysical method in which surface waves (Rayleigh waves) of different wavelengths are generated at a point, and the average of the wave velocity are measured along the array. Since different wave lengths penetrate into different depths of soils, a profile of soil properties can be back analyzed. The results provide a good "global" estimate of the small strain material properties along the arrays.

The shear-wave velocity profiles for arrays 1 and 2 are presented in Fig. 4.4. Average shear wave velocities to a depth of 30 m (V_s30) were found to be 456 m/s (1496 ft/s) for array 1 and 545 m/s (1788 ft/s) for array 2, classifying the vicinity of the test area as class C (very dense soil and soft rock) according to the 1997 Uniform Building Code. At the depth of interest for our modelling, the average shear velocities of soil are 288–292 m/s for the top

[1] Array 1 was located in the west side of the parking lot, close to pier test site 1; and array 2 was located in the east side of the parking lot, close to pier test site 2.

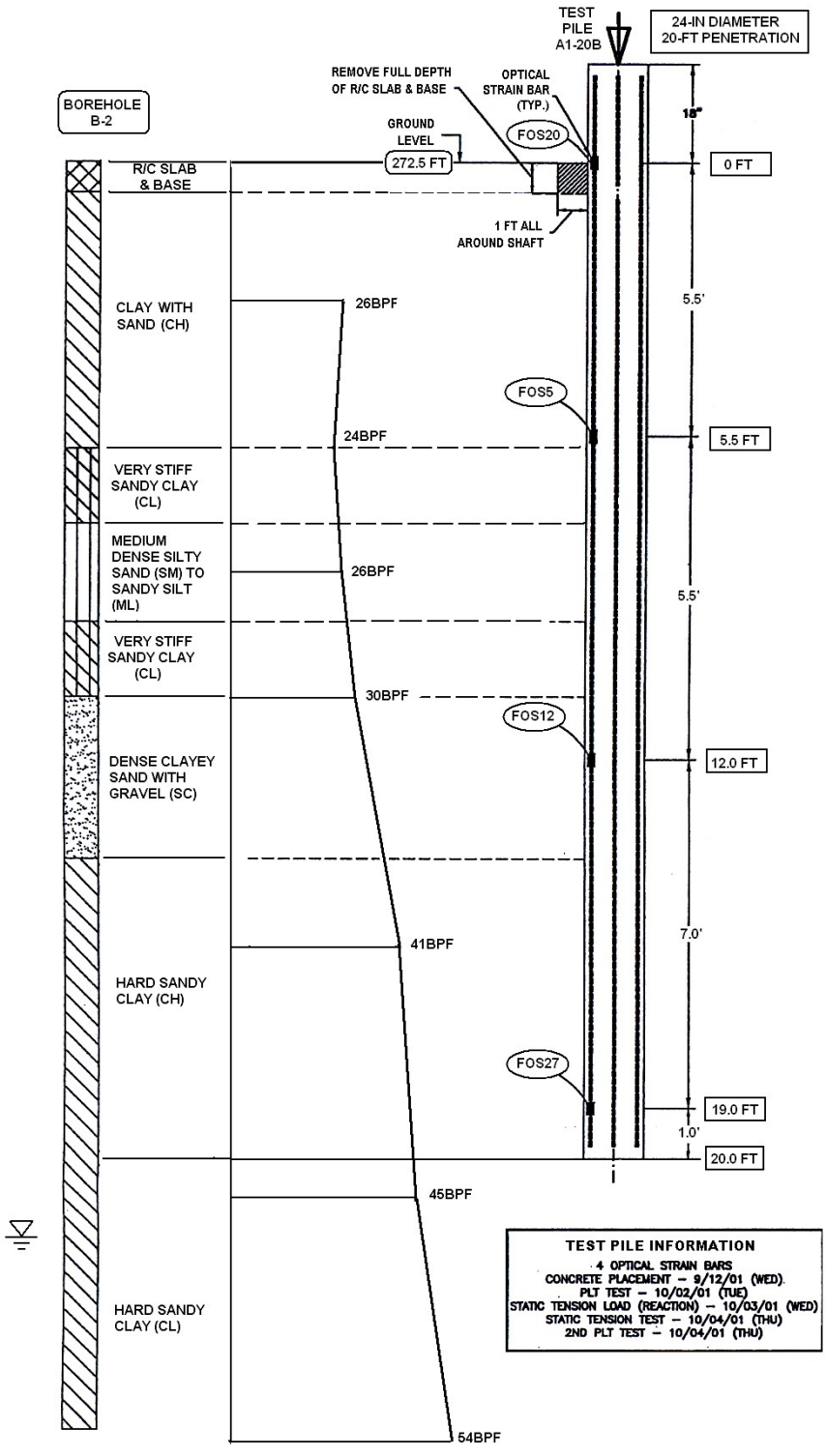

Fig. 4.2 Schematic Soil Profile of Test Area 1 and Test Pier

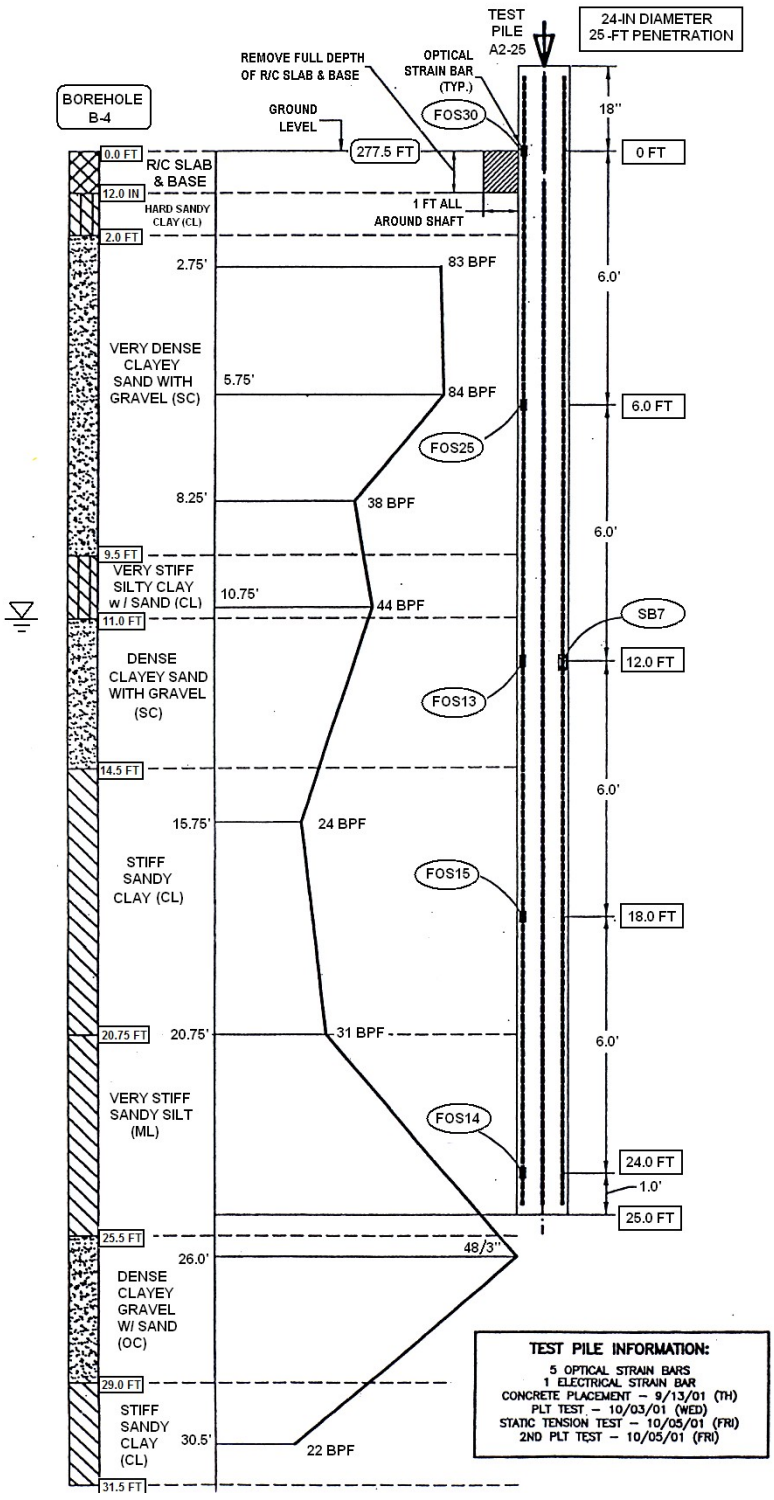

Fig. 4.3 Schematic Soil Profile of Test Area 2 and Test Pier

20–30 ft along array 1, and 280–307 m/s for the top 20-30 ft along array 2, respectively. It should be noted that the V_s profile of array 1 is more uniform than that of array 2.

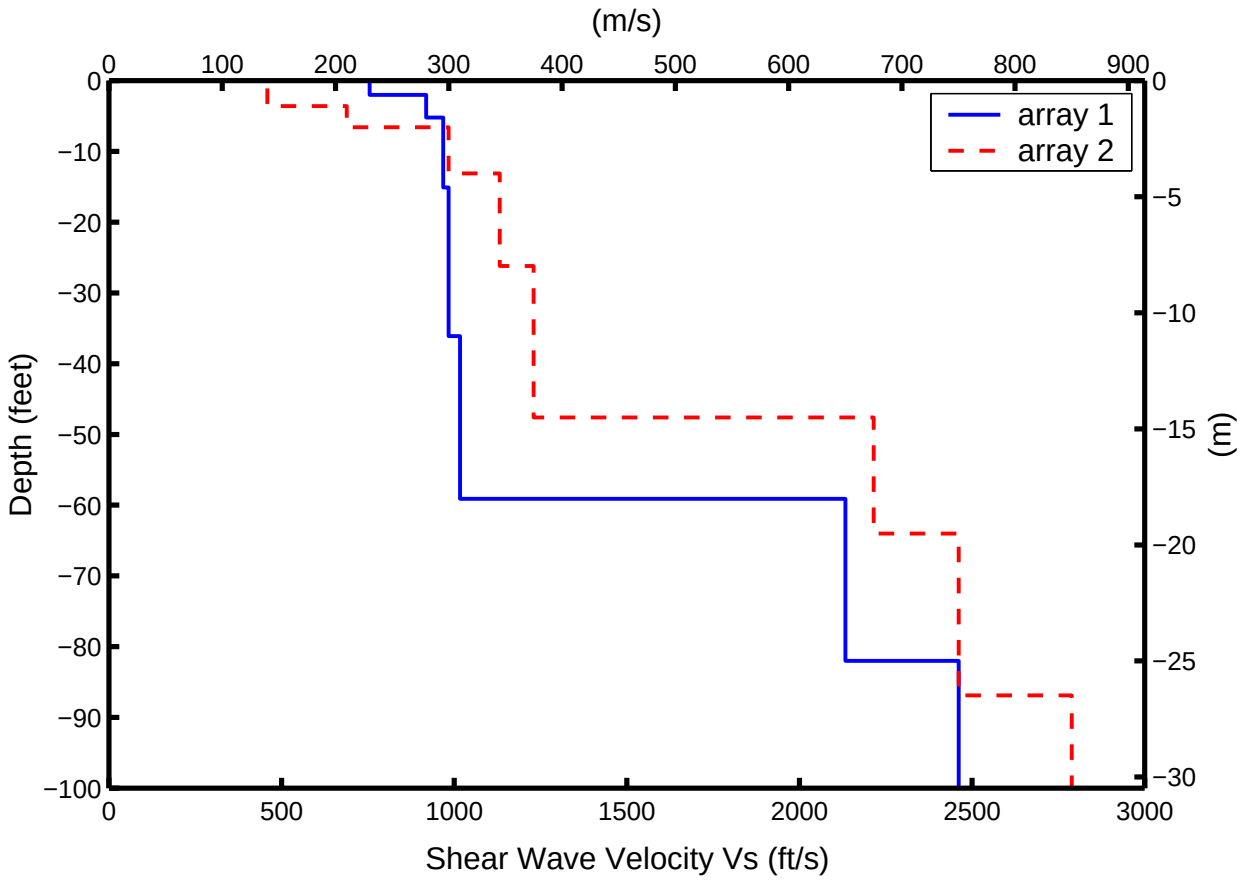

Fig. 4.4 Vs Profile from SASW Testing along Array 1 and Array 2

4.2.3 Shear Strength Profile

The site is mainly underlain by hard to very stiff sandy clay, medium dense sandy silt, and dense clayey sand. The undrained shear strength S_u profile estimated from unconfined compression (UC) test is shown in Fig. 4.5 for Test Area 1, together with the standard penetration test blow counts per feet (SPT N-value). The SPT N-values range from 24 at shallow depth to 54 at depth of 8 m. The shear strength profile shows fairly high undrained shear strength of the soil close to the surface, indicating that the soil is overly consolidated. The high OCR (over-consolidation ratio) may be attributed to desiccation and the unloading of overburden pressure during deep excavation when the parking lot was constructed. The

average undrained shear strength for simple shear is estimated around 100 kPa over the pier length. Unfortunately, a shear strength profile in Test Area 2 is not available.

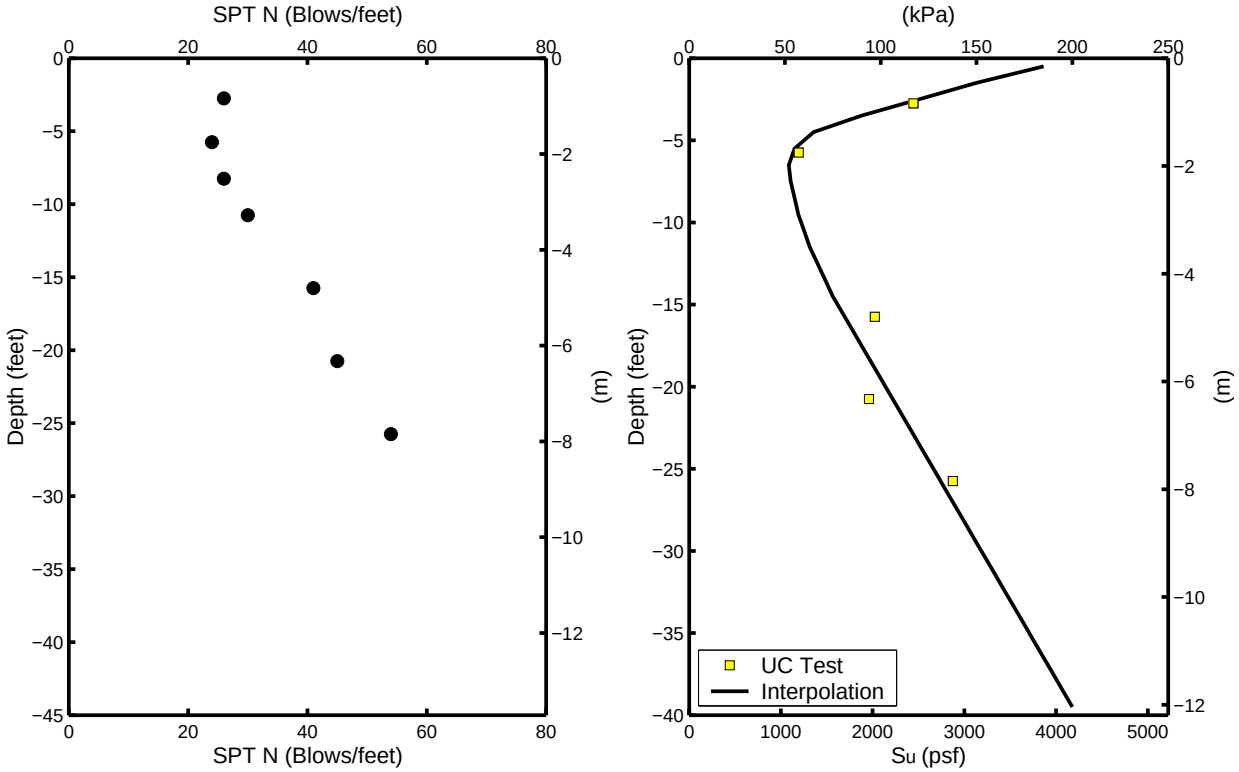

(a) SPT N-value (b) Strength Profile

Fig. 4.5 SPT N-value and Undrained Shear Strength Profile for Test Area 1

4.3 DRILLED PIER LOAD TESTS

4.3.1 The Test Program

Fig. 4.6 shows the detailed arrangement of test piers in each test area, where three piers were installed in each group (Kasali, 2002). In Test Area 1, a 30-inch diameter, 19-foot long pier is flanked by two 24-inch diameter, 20-foot long piers, with spacing of about 12 feet to the middle pier. In Test Area 2, the middle pier is 24 inches in diameter and 30 feet long, with one 24-inch diameter, 20-foot long pier installed about 12 feet to the west, and another 24-inch diameter, 25-foot long pier about 12 feet away to the east. The spacing was chosen to be sufficiently large to avoid pier to pier interaction (group effect) under axial loadings.

All the concrete piers were cast in place during September 10-14, 2001. Conventional

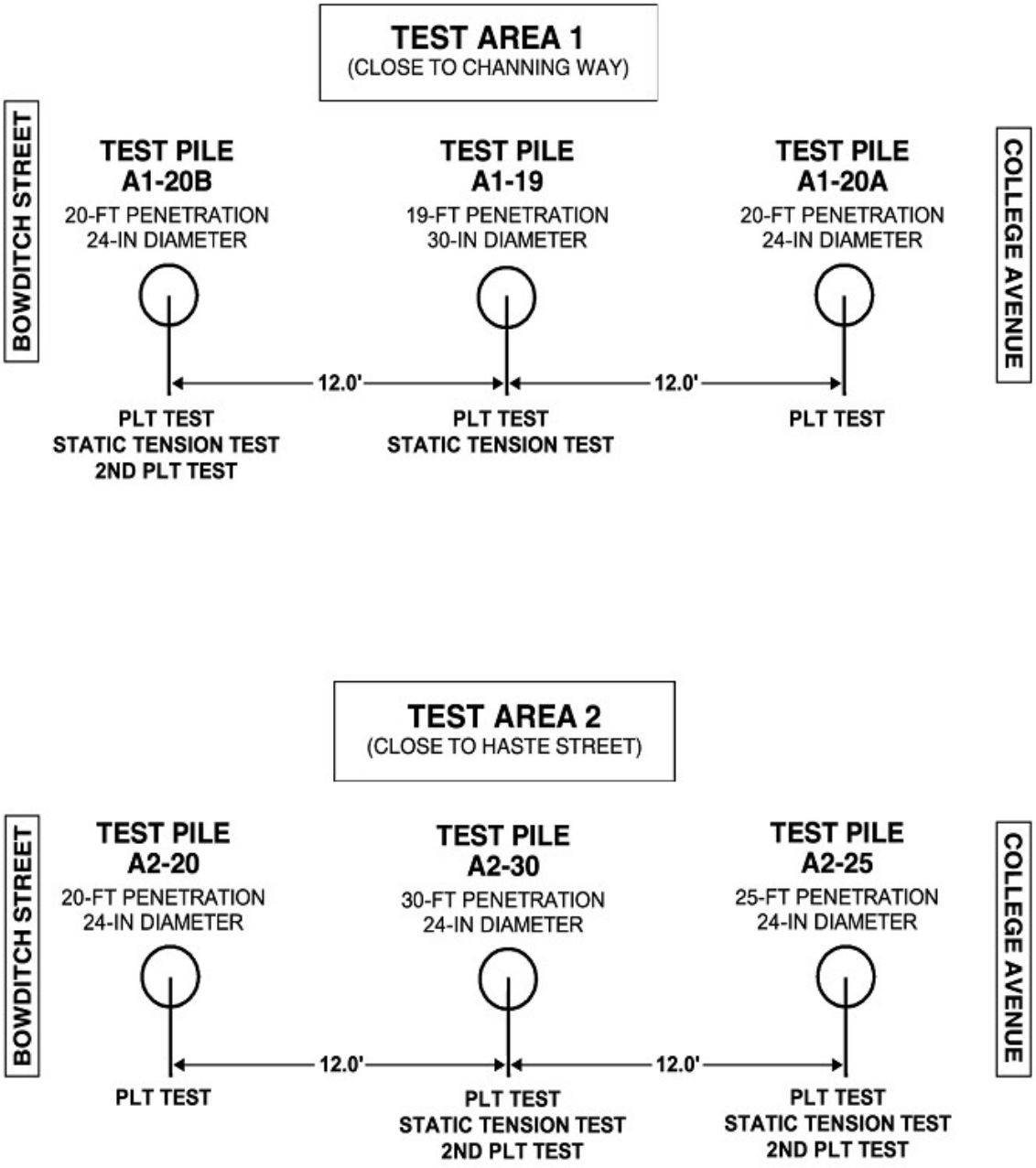

Fig. 4.6 Arrangement of Test Piers, from Kasali (2002)

flight augers were used to drill the pier holes and concrete was placed in each hole at the same day of drilling. Sonotubes were used on all piers to form pier heads about 18 inches above the ground surface, which was necessary to perform the dynamic load test. Beneath all 24-inch diameter piers, compressible materials were placed to ensure that the load was predominately transferred by the side friction, with only one exception that the 30-inch diameter, 19-foot long pier in Test Area 1 (Pier A1-19) was installed with downhole cleaning to ensure end bearing capacity.

After curing for a minimum of 18 days, the concrete piers were loaded according to a predetermined loading sequence. The test program consisted of dynamic pier load tests (called PLT in short) and static compression or tension load tests on six test piers, by American Piledriving, Inc. (API) of Pleasanton, California, under the direction of Rutherford & Chekene Consulting Engineers.

Three kinds of tests were performed between 1 October and 5 October 2001. First, dynamic PLT tests were performed on all piers. The PLT is a relatively new testing method and was pioneered by Fundex of Belgium, as discussed in detail in the following section. For each test pier, the PLT test would obtain dynamic load-displacement information. Second, quick static compression and tension tests were performed based on the ASTM D1143 and ASTM D3689 Quick Load Method. To evaluate the impact of the pier test sequence on the results, the dynamic PLT tests were performed again to explore the differences in pier capacities and stiffness between the first and second PLTs. A pier-by-pier summary of the test program is listed in Table 4.1.

Table 4.1 Summary of Pier Load Test Program

Test Area 1			Test Area 2		
A1-20B (D 24″, L 20′) West Frictional Pier	A1-19 (D 30″, L 19′) Middle With End-bearing	A1-20A (D 24″, L 20′) East Frictional Pier	A2-20 (D 24″, L 20′) West Frictional Pier	A2-30 (D 24″, L 30′) Middle Frictional Pier	A2-25 (ϕ 24″, L 25′) East Frictional Pier
1^{st} PLT (10/01/2001)	PLT (10/02/2001)	PLT (10/02/2001)	PLT (10/03/2001)	1^{st} PLT (10/03/2001)	1^{st} PLT (10/03/2001)
Static Tension Test (10/04/2001)	Static Compression Test (10/03/2001)			Static Tension Test (10/05/2001)	Static Tension Test (10/05/2001)
2^{nd} PLT (10/04/2001)				2^{nd} PLT (10/05/2001)	2^{nd} PLT (10/05/2001)

Note: D = pier diameter, L = pier length

4.3.2 The PLT Test

The PLT test was designed to produce "long-lasting" blows on the pier head. Fig 4.7 provides field photos for the test setup. To conduct a PLT test, a 25-metric ton mass is hydraulically lifted by the mobile track-mounted load tester to a predetermined height to create the potential energy. The mass is then released and free-falls on a striker plate. Large damping springs spread the impact load over about a 200-millisecond period. The hydraulic system then catches the mass on the rebound to allow only one strike on the pier per drop. The resulting 200 – 400 millisecond duration of the load application reasonably simulates the effective period of earthquake loading, making the device a good predictor of pier behavior in seismic loading regardless of soil type (Schellingerhout and Revoort, 1996).

During the tests, pier head vertical displacements over the duration of the applied load are recorded for each blow. The actual applied force of each drop is recorded by a load cell placed on the pier head. The pier head displacement is measured using an optical diode transmitter (an optical accelerometer) fastened to the face of the test pier. Stereo imaging of the movement of the transmitter's pair of LED diodes is recorded by a camera receiver placed at least 30 feet away to minimize disturbance by vibration.

The PLT test conducted herein should not be confused with other methods of dynamic tests. For example, the non-destructive vibrating test has been widely used in estimating the stiffness, length, and cross-sectional area of intact piles (Davis and Robertson, 1976). The non-destructive test is designed to measure small strain wave reflection inside the test pile, and the amplitude of impact during the test is only tens of kPa, with the duration and the pile head displacement in the order of several millisecond and 10^{-9} – $10^{-7}m$, respectively. On the other hand, the PLT test is quite similar to the STAT*Namic* (Middendorp *et al.*, 1992) pile load in some aspects. The STAT*Namic* test uses high gas pressure generated by burning of fuel inside the device to exert short duration (in order of 100 ms) load on the pile. Thus, the STAT*Namic* test usually fully mobilizes the soil resistance in a single load cycle, and the test has primarily been used for the purpose of determining the equivalent static pile capacity. With well-controlled multiple impacts, the PLT test conducted herein can be used to explore dynamic stiffness, capacity, and energy-dissipation characteristics of

(a) PLT rig

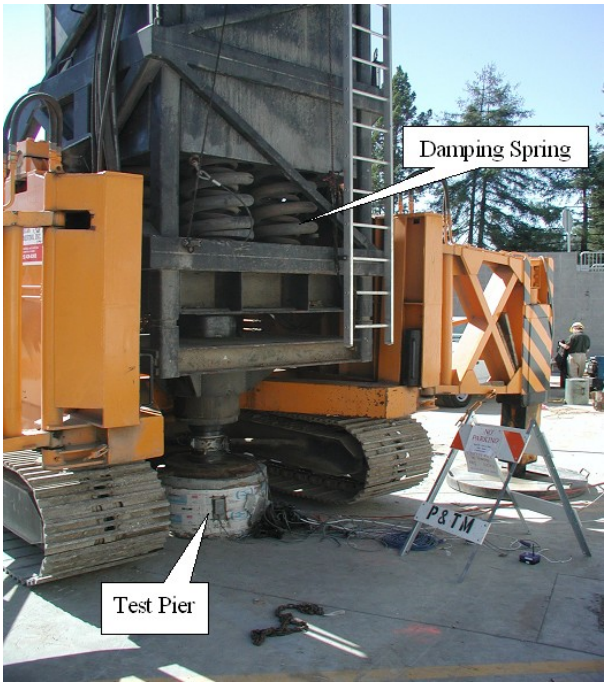

(b) Close-up

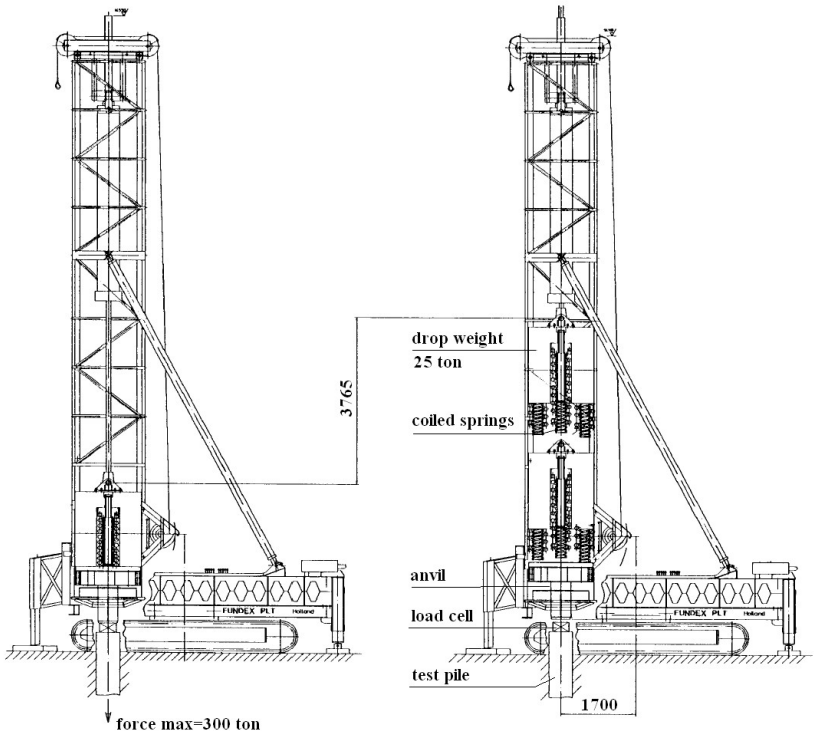

(c) Fundex PLT rig drawing, from Schellingerhout and Revoort (1996)

Fig. 4.7 PLT Test Setup

the soil-pier system. The main results of the pier load test program are summarized in the following section.

4.4 SUMMARY OF PIER LOAD TEST RESULTS

4.4.1 Loading Rate Effects and Cyclic Degradation

Pier A1-19 was 30 inches in diameter, 19 feet long, located at the middle of Test Area 1. As mentioned before, downhole cleaning was performed before installation to ensure the end bearing. The PLT tester impacted the pier with 9 consecutive blows, which progressively loaded the pier from the small strain level to the yield state with increasing magnitude of impact load. The PLT axial load versus pier head displacement curves are shown in Fig. 4.8. A dynamic load displacement envelope is defined to encompass all loading cycles. To examine the effects of loading rate, the PLT test was followed by a static compression test using a reaction beam and flank piers on both sides. The heavy solid line in Fig. 4.8 shows the static load displacement curve, which starts from about 0.5 inch of residual displacement that resulted from the PLT test. To make the comparison of the response for each load increment easier, each cyclic PLT loop and the static curve are re-plotted from the same origin in Fig. 4.9. Each cyclic loop defines a dynamic load-displacement curve, with an initial stiffness that is about twice as high as that of the static curve, and a higher ultimate strength. The difference between dynamic and static response can be attributed to the rate effect of the soil-pier system. The nonlinear load-displacement relationship is pronounced in this plot, and the stiffness of the soil-pier system is dependent on applied load or strain level.

For each PLT load cycle (numbered 1 – 9), the hysteretic energy dissipation, defined as the area enclosed by each cyclic force-displacement loop, is calculated and plotted in Fig. 4.10(a). It is also interesting to plot the energy dissipation in each cycle against the peak load (Fig. 4.10(b)), and the energy dissipation against the residual displacement for each cycle (Fig. 4.10(c)). The slope of the line in Fig. 4.10 (c), designated as F, is 784 kips for Pier A1-19. This linear relationship between energy dissipation and residual displacement implies that energy is primarily dissipated to overcome a constant resistance F, which can therefore be interpreted as the *effective resistance force* of the soil-pier system. The plot of

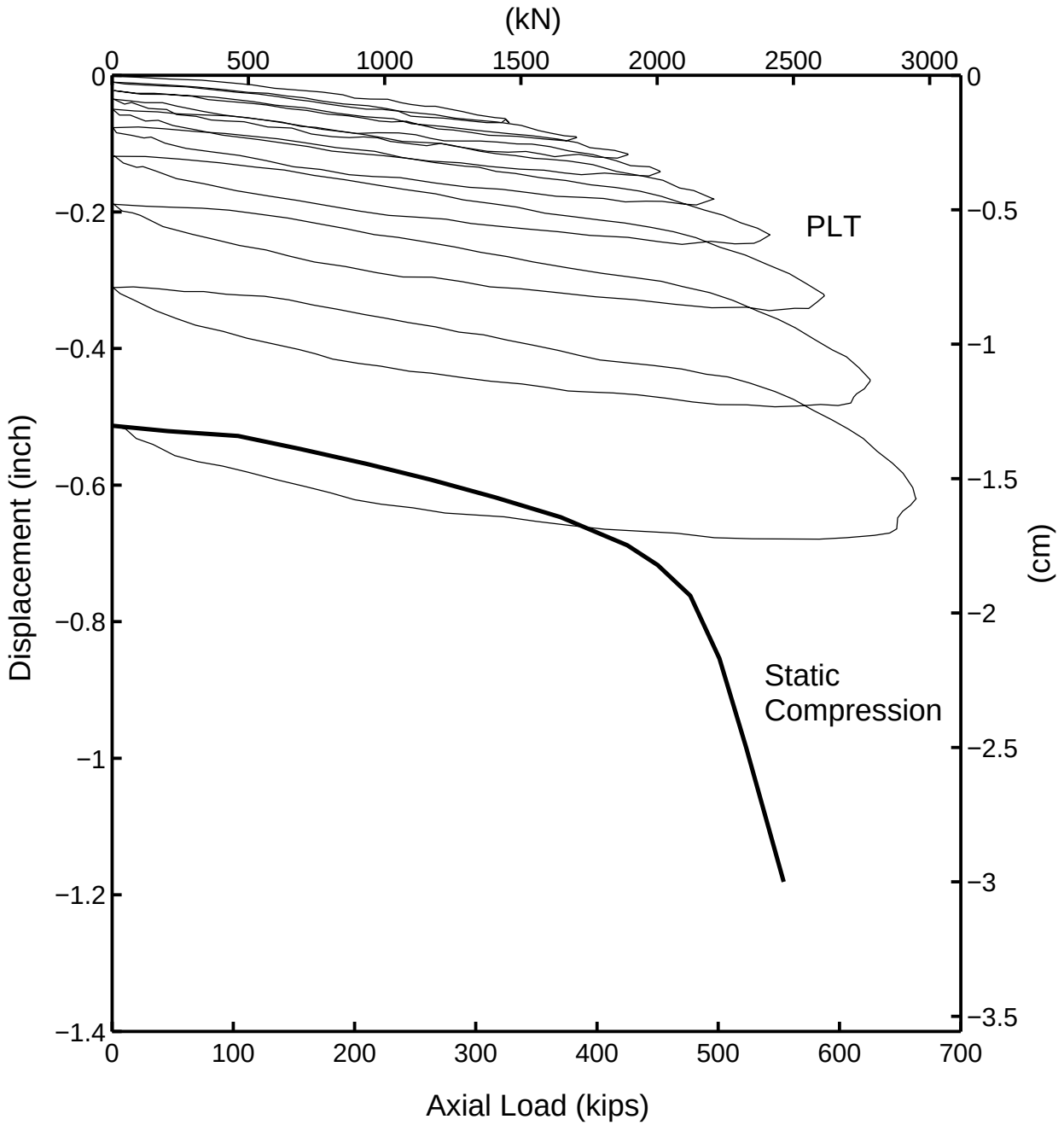

Fig. 4.8 PLT and Static Compression Test Results (Pier A1-19)

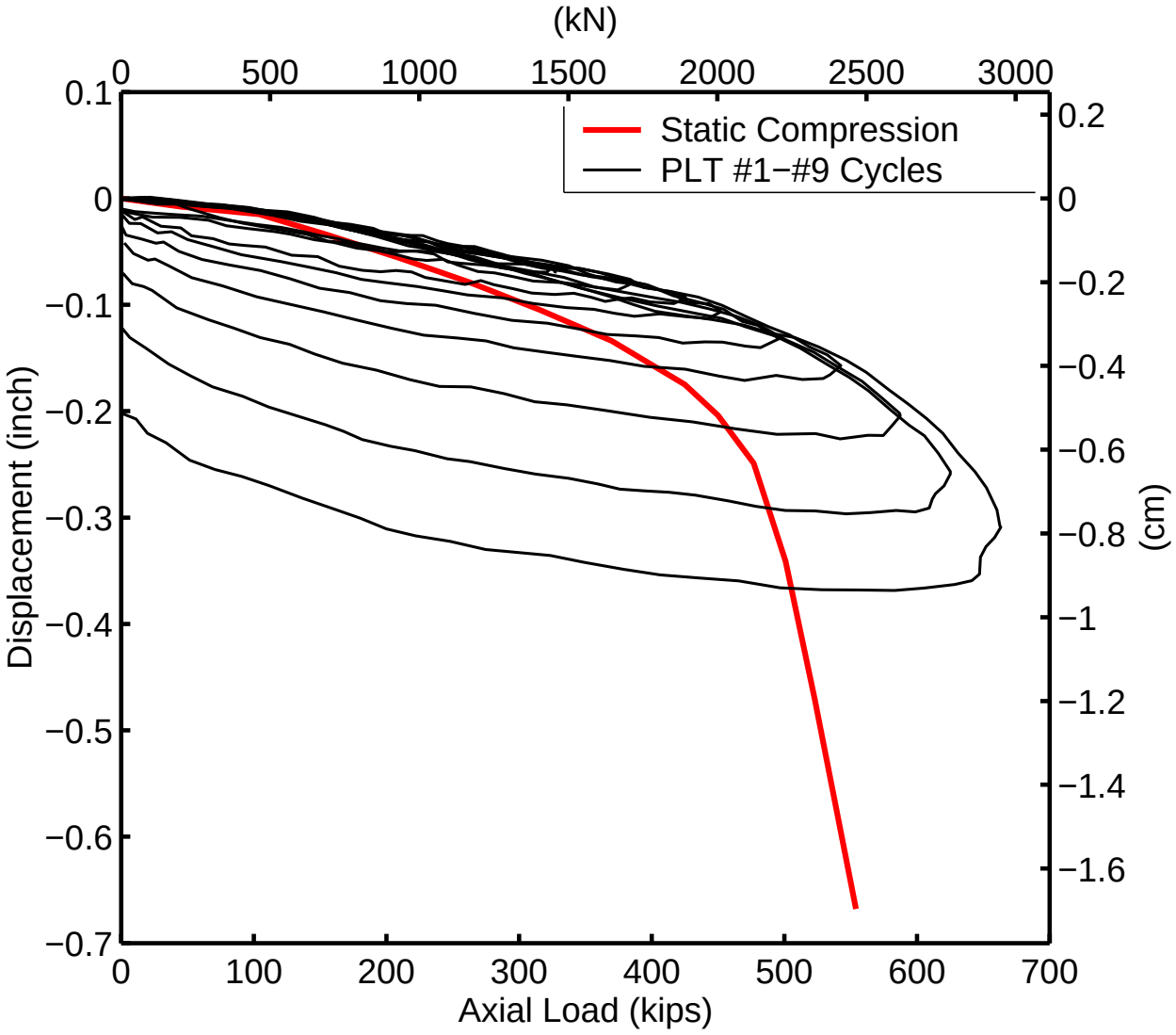

Fig. 4.9. Comparison of Individual PLT Loops and Static Compression (Pier A1-19)

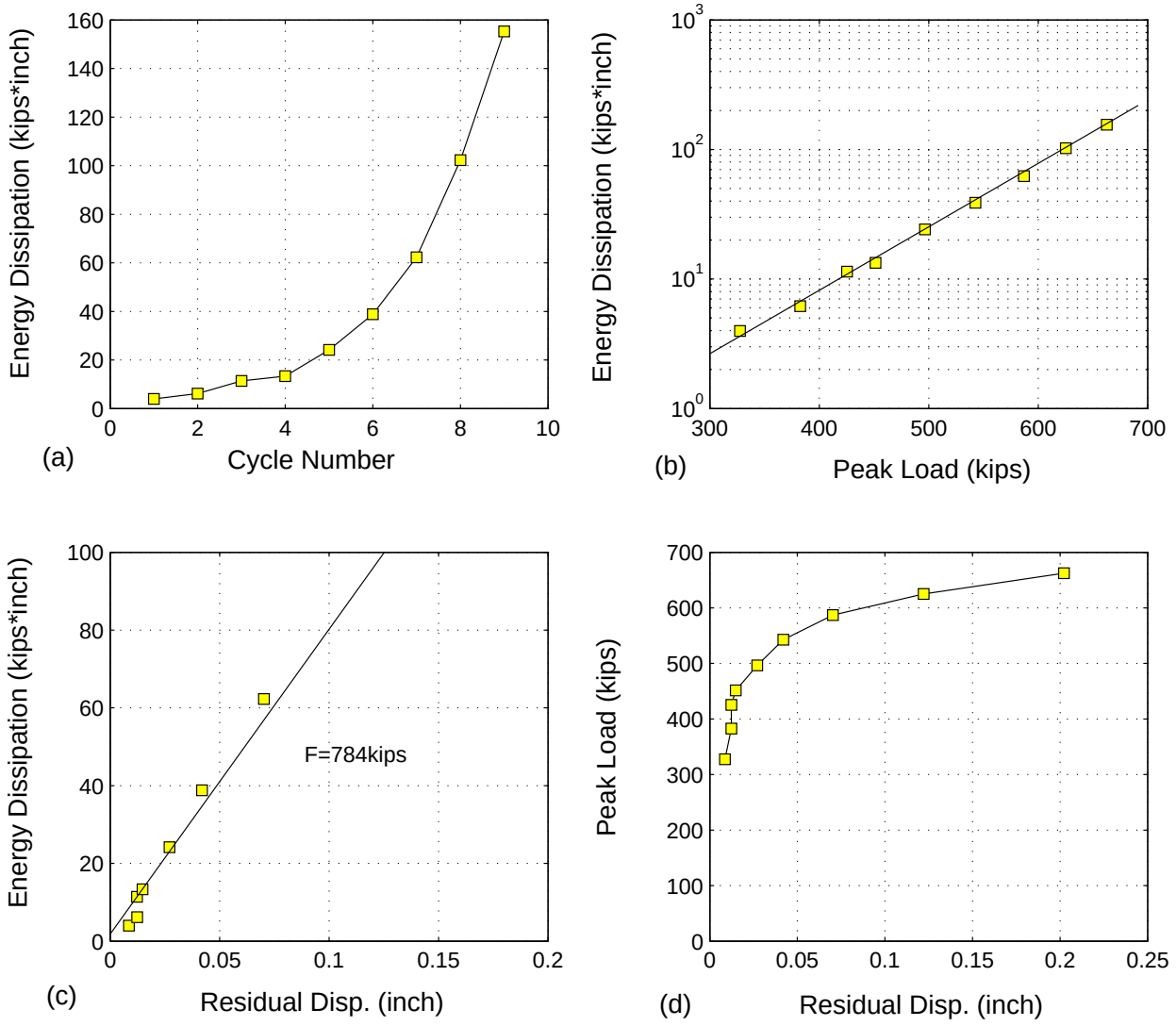

Fig. 4.10 Analysis of Pier A1-19 PLT Test Results

peak loads vs. residual displacement in Fig. 4.10(d) shows that there is an elastic threshold load, below which no residual displacement could accumulate, hence making the pier behavior virtually elastic. The elastic threshold accounted for approximately 30–40% of the ultimate capacity. Once the peak load exceeds the threshold, considerable residual displacement begins to accumulate.

Similar trends can be observed for all other test piers. Figs. 4.11 – 4.13 show the test results for Pier A1-20A, which was 24 inches in diameter, 20 feet long, located at the east of test area 1. The pier was constructed with compressible material in the bottom to eliminate tip resistance. The results show effective resistance force F to be 491 kips for this pier, and the elastic threshold falls into 30–40% of the ultimate capacity.

To examine the effect of stress reversal on the subsequent performance of a single pier, a sequence of load tests was designed for pier A1-20B. The test pier was 24 inches in diameter, 20 feet long, and was located at the west of test area 1. As in the case of A1-20A, the axial load was carried by the shaft resistance only.

First, the PLT test was performed on pier A1-20B. After the PLT test, the pier was subjected to a static tension test. Finally, a second PLT test was performed after the tension test. Fig. 4.14 summarizes the recorded pier head displacement and applied axial load for all tests on performed on pier A1-20B.

In terms of capacity, the static tension capacity of the test pier after the PLT test was reduced to about 70% of the cyclic PLT capacity. The difference can be partially attributed to the different loading rate of these two tests, as well as the influence of the foregoing cyclic PLT compression [2]. As a result of the stress reversal (from compression to tension) up to yield in the tension test, the soil fabric is severely damaged at the soil-pier interface. The effects of cyclic degradation are exhibited in significant stiffness and capacity degradation in the second PLT test, where dynamic capacity was only about 50% of the first PLT test. This

[2]The effect of the compressive load on the uplift capacity of model piles in sands has been previously reported by Dash and Pise (2003). After loaded to 0, 25, 50, 75, 100% of their ultimate capacity in compression, the model piles were subjected to pull out loading tests. The experimental results indicate that the presence of the compressive load tends to decreases the net uplift capacity of a pile. The decrease further depends on the magnitude of the compressive loads, density of the sand, slenderness ratio L/d of the model pile. It is argued that the placement of compressive load may change the fabric of granular soils at the pile soil interface, resulting in a reduction of the soil-pile friction angle up to 4^o – 10^o if the ultimate compressive has been applied. Further, it is observed that the reduction is more in loose sand than in dense sand, and it increases with increasing compressive load intensity for both cases.

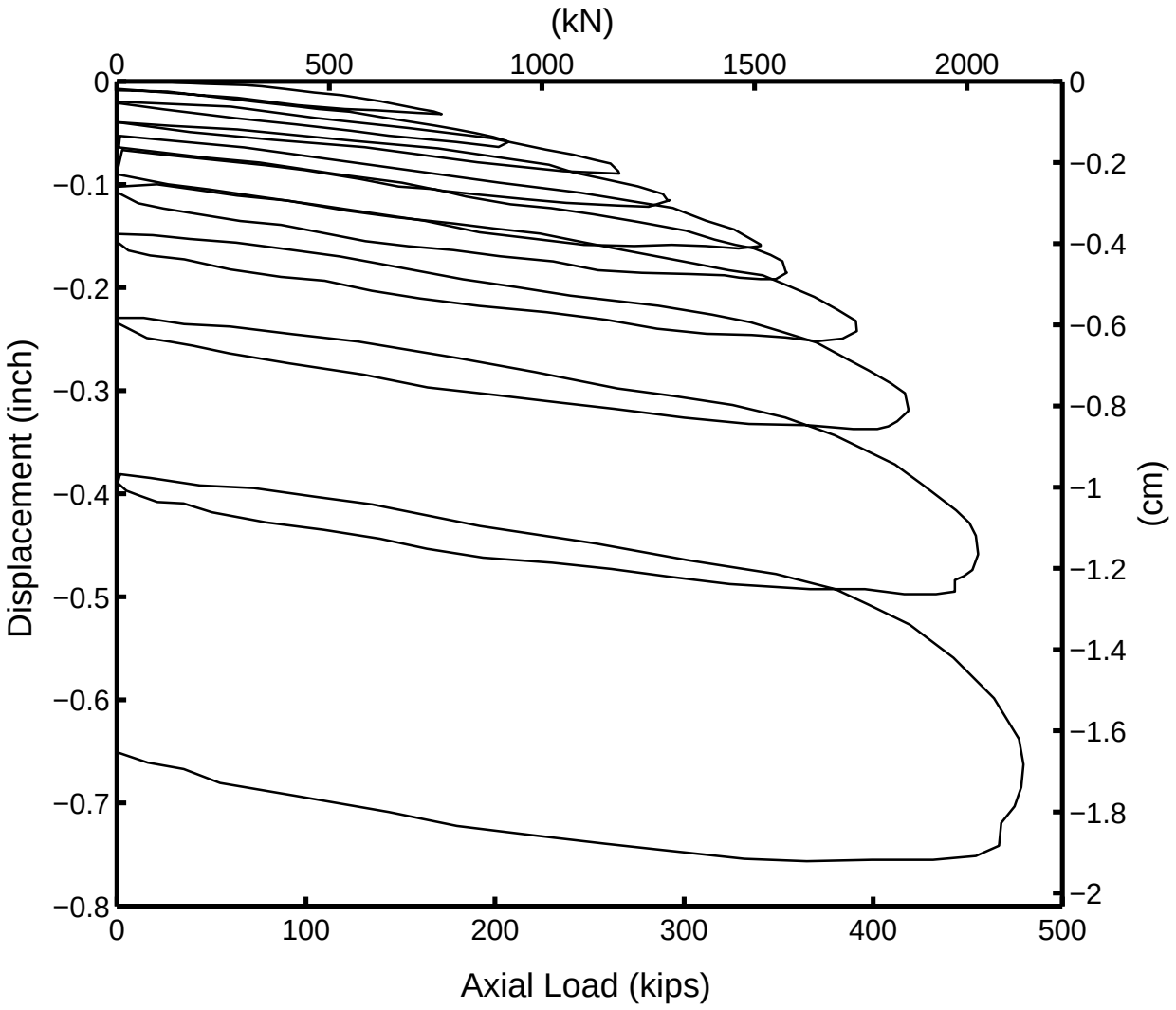

Fig. 4.11 PLT Test Results (Pier A1-20A)

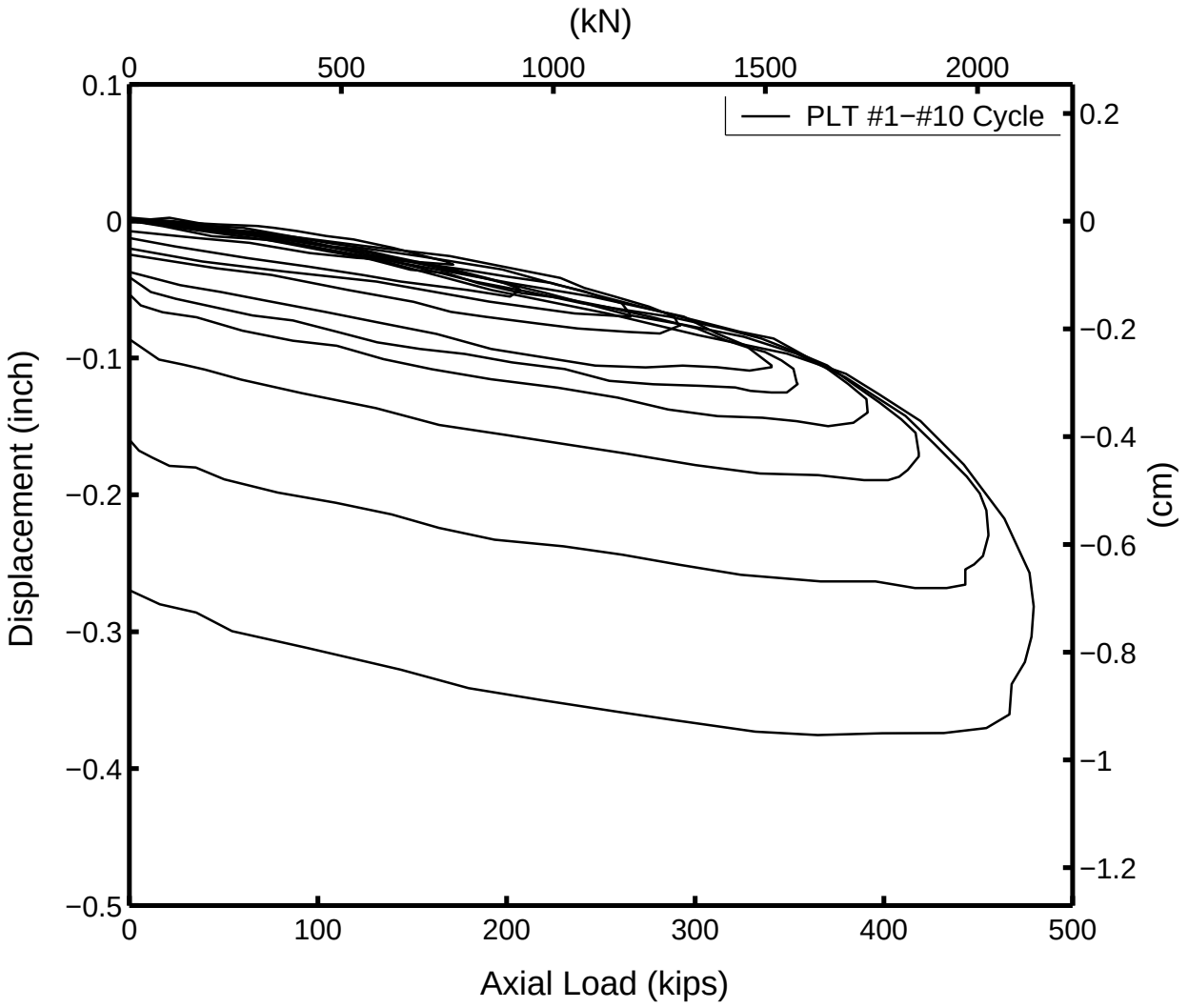

Fig. 4.12 Comparison of Individual PLT Loops (Pier A1-20A)

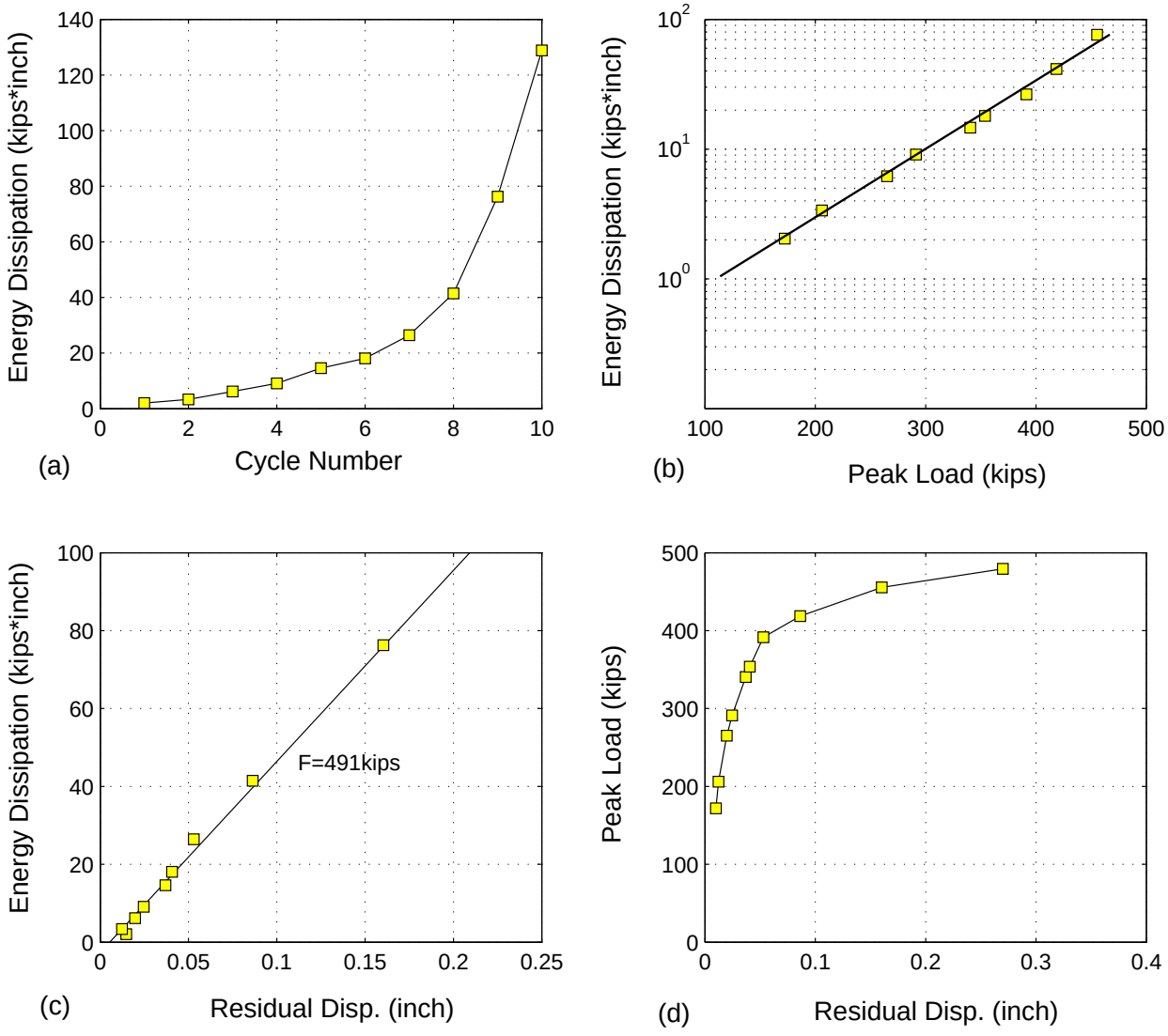

Fig. 4.13 Analysis of Pier A1-20A PLT Test Results

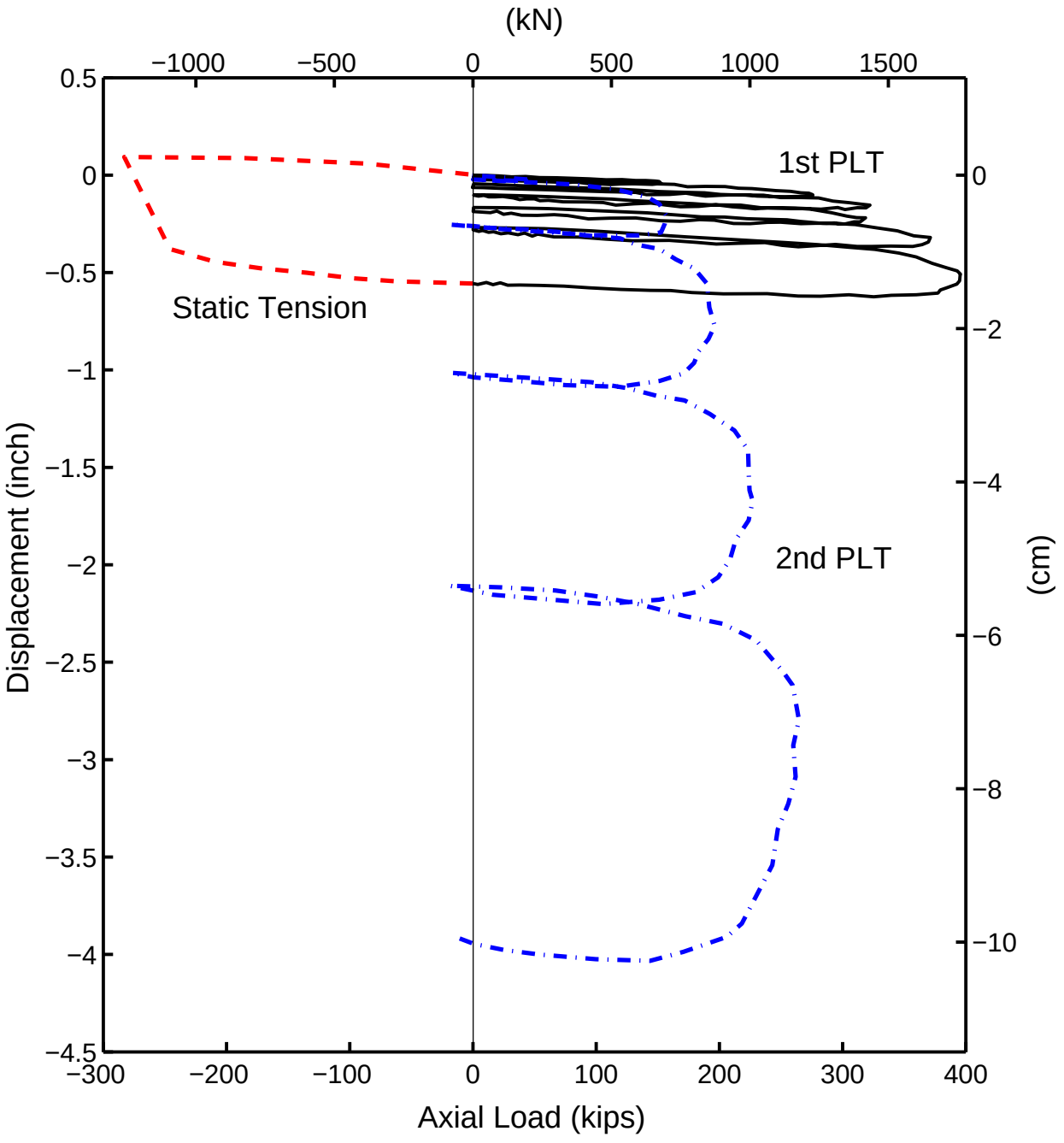

Fig. 4.14 A1-20B 1st PLT, Static Tension and 2nd PLT Tests Results

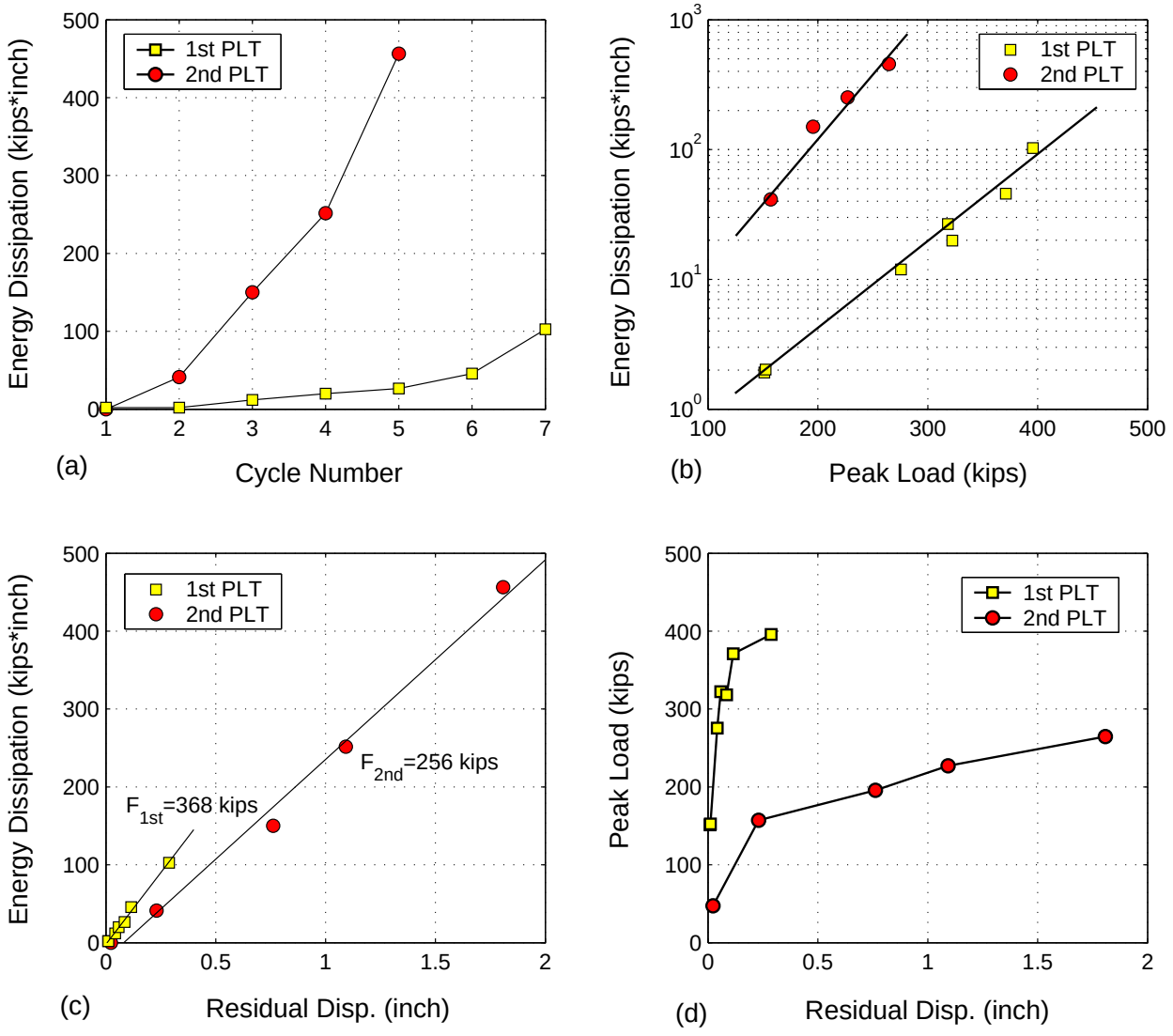

Fig. 4.15 Comparison of A1-20B 1st and 2nd PLT Test Results

finding does suggest that full stress reversal during earthquake loading can lead to significant degradation of the pier capacity and is consistent with soil behavior previously documented under cyclic loading.

Fig. 4.15 compares the energy-dissipation characteristics of the first and second PLT tests. Again, a linear relation can be found between energy dissipation and peak load in a semi-logarithm for both PLT tests. The slope of the linear regression line from the second PLT test data is higher and steeper than that of the first PLT test, indicating a much larger energy dissipation for the damaged system. Consequently the effective resistance force, F, is reduced from 368 kips for the first PLT to about 70% (256 kips) for the second PLT. Similarly, the elastic threshold in the second PLT (50 kips) is only about 1/3 of that of the first PLT (150 kips).

While these tests represent a rather extreme condition of complete load reversal with uplift and they do not address the condition of partial load reversal, they clearly show that such loading could severely reduce the dynamic stiffness and dynamic load capacity of pier foundations subjected to seismic loading.

Table 4.2 summarizes the effective resistance F derived from all PLT tests, see Figs. 4.10, 4.13, 4.15, 4.21, 4.24, 4.28. To allow for comparison between piers of different configurations, the effective resistance per unit area, f, is also given in the table,

$$f = \frac{F}{\pi D L} \tag{4.1}$$

where D and L are pier diameter and pier length, respectively. The effective resistance is also found in the range of about 100% – 120% of ultimate dynamic capacity in each test based on Davisson Offset Limit method.

4.4.2 Normalized Pier Response

To allow for better comparison of all results from the test program, the load-displacement curves are normalized. The total per resistance is divided by surface area of the pier to obtain an averaged unit pier resistance. Since only pier A1-30 has end bearing resistance, that resistance has been subtracted from the total resistance before normalization. For

Table 4.2 Summary of Effective Resistance for PLT Tests

Pier	Length	Diameter	F	f	
	ft	ft	kips	kips/ft^2	kPa
A1-19	19	2.5	784*	5.25	251
A1-20A	20	2.0	491	3.90	187
A1-20B (1st)	20	2.0	368	2.92	140
A1-20B (2nd)			256	2.04	98
A2-20	20	2.0	579	4.61	221
A2-25	25	2.0	825	5.25	252
A2-30	30	2.0	986	5.23	250

*including end-bearing resistance.

clarity, only the cyclic envelopes for PLT tests are plotted, with each data point representing the peak load in each cyclic loop.

As shown in Fig. 4.16, the normalized PLT curves virtually coincide for all piers in Area 1, except that pier A1-20B yields a lower ultimate resistance. The static compression and static tension curves have almost the same initial slope, but the mobilized ultimate resistance in tension is about 60% of the ultimate resistance in compression. The loading rate effect is evident when comparing the PLT tests with the static compression and static tension tests. The PLTs show that 20% – 40% higher ultimate resistance is mobilized in dynamic cases. The initial stiffness of PLT curves is found about twice as much as the initial stiffness of static test curves. Load reversal leads to 50% reduction in both stiffness and ultimate resistance comparing the second PLT test with the first. The mobilized ultimate resistance for each pier test is listed in Table 4.3.

The measured stiffness of the soil-pier system from the field test can be compared with the elastic solution proposed by Randolph and Wroth (1978). As derived in Chapter 2, system stiffness from shaft reaction depends on soil modulus and pier geometry. When normalized by surface area of the shaft, it can be expressed as follows,

$$\bar{k}_s = \frac{G_s}{r_0 \ln\left(\frac{r_m}{r_0}\right)} \tag{4.2}$$

where r_0 is pier radius, $r_m = 2.5L(1-\nu)$, L is pier length, ν = Poisson's ratio of the soil, which is chosen as 0.4 as the soil is partially saturated. Considering soil nonlinearity, G_s is an effective soil modulus that can be related to the maximum shear modulus G_{max} through

a modulus ratio η, defined as

$$\eta = \frac{G_s}{G_{max}} \tag{4.3}$$

where G_{max} can be estimated from the shear wave velocity profile. Figures 4.17 and 4.18 compare field data with the elastic solution for varying modulus ratio. The modulus ratio was back-analyzed from field data. The results presented in Table 4.4 show that modulus ratio between 0.3 – 0.5 can reasonably approximate the dynamic PLT stiffness over the range of the working load. The modulus ratio of static compression and tension is around 0.2, while for the second PLT test, the ratio has been reduced to 0.15 due to stiffness degradation. Eqs. (4.2-4.3) and recommended values in Table 4.4 provided a simple means for estimating the system stiffness under various loading conditions.

Table 4.3 Mobilized Ultimate Shaft Resistance (in kPa)

Test Pier	PLT Test		Static Test	
	1st	2nd	Compression	Tension
A1-19	177		148	
A1-20A	182			
A1-20B	151	75		108

Table 4.4 Effective Shear Modulus Ratio

Test Pier	PLT Test		Static Test	
	1st	2nd	Compression	Tension
A1-19	0.3 – 0.5		0.2	
A1-20A	0.3 – 0.5			
A1-20B	0.3 – 0.5	0.15		0.2

Figures 4.19 – 4.30 summarize the test results for piers A2-20, A2-25, and A2-30 in Test Area 2. All these test piers are frictional piers of 24 inches in diameter, with penetration to 20 ft, 25 ft, and 30 ft, respectively. The effect of cyclic degradation was also measured on piers A2-25 and A2-30. The dynamic PLT test, followed by a static tension test, and then a second round of PLT tests were conducted for both piers. Similar to the findings in Test Area 1, pseudo-cyclic overall response curves are plotted in Figures 4.25 and 4.29. The loading rate effects and severe stiffness and strength degradations after full loading reversal can be systematically compared using normalized curves in Fig. 4.30.

In summary, prototype load tests on cast-in-place concrete piers were performed to examine dynamic and static responses of the soil-pier system under axial loading. In particular, loading rate effects and cyclic effects as well as characteristics of hysteretic energy dissipation were studied. The field data provide valuable information for earthquake design of pier foundations. At this point, the findings presented herein are restricted to current site condition, pile type, and loading program. Additional field data for other site conditions and pile types are still needed. Systematic evaluation of such data should ultimately provide guidelines for performance-based earthquake design of deep foundations.

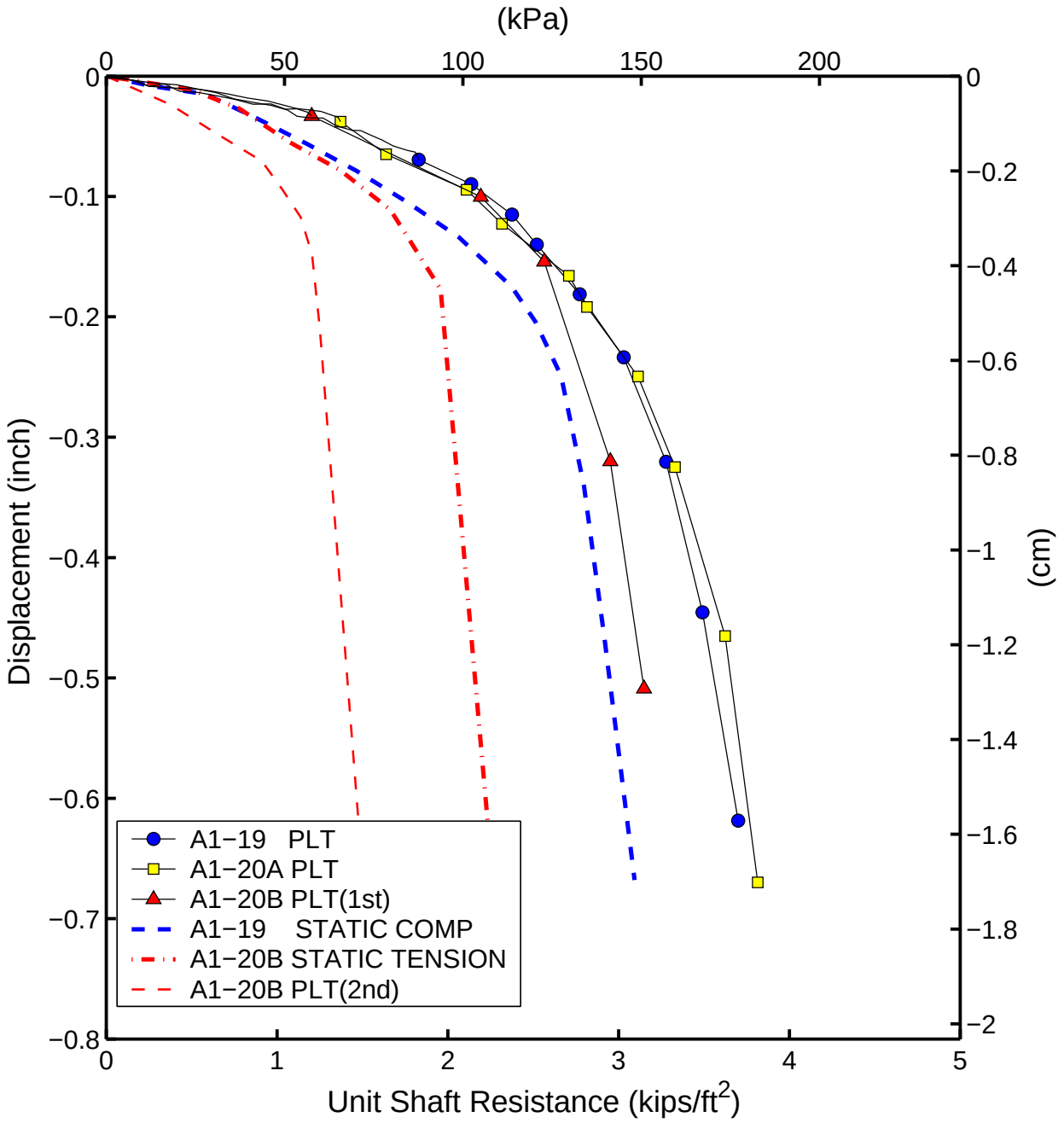

Fig. 4.16 Normalized Pile Load Response (Test Area 1)

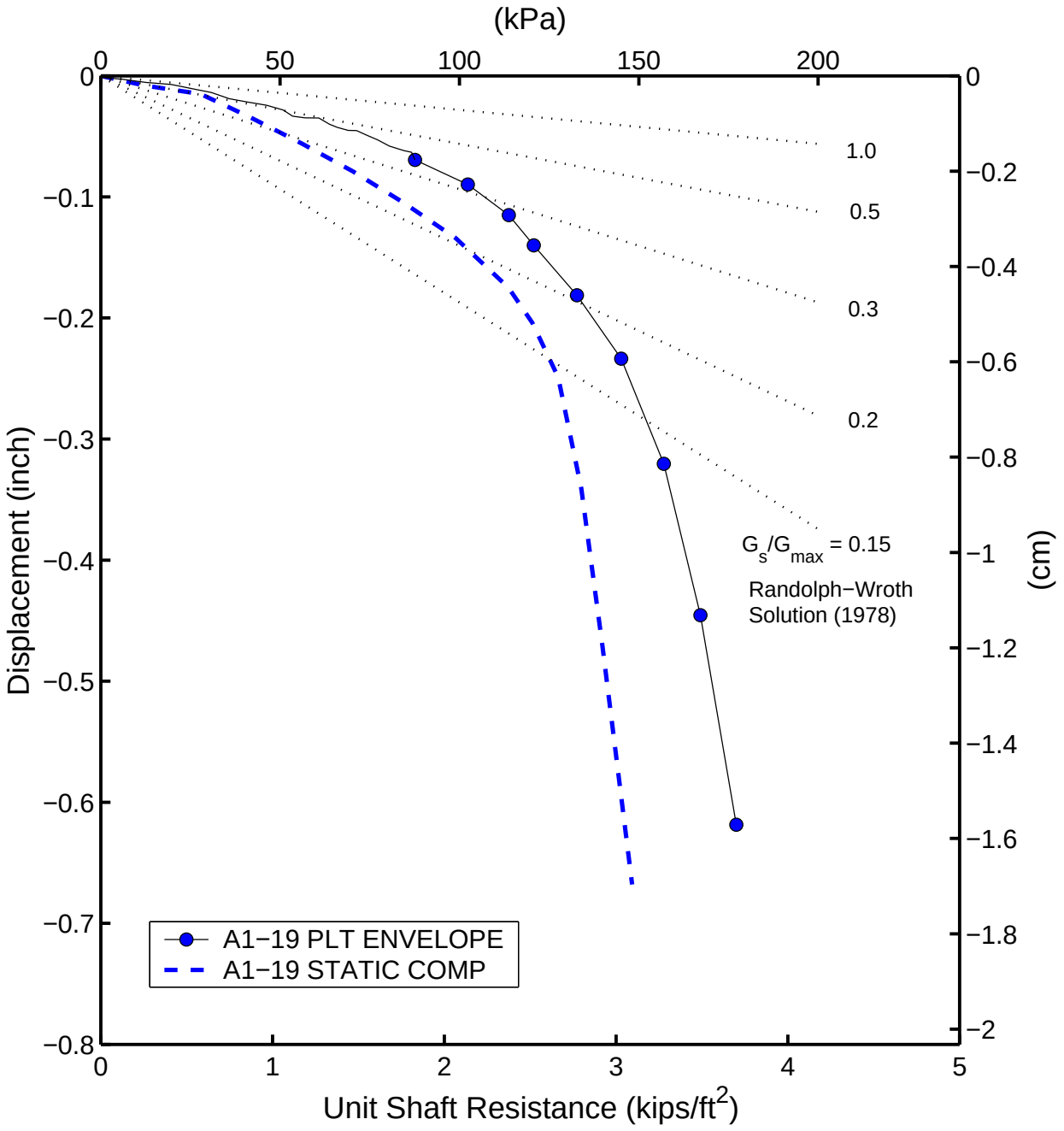

Fig. 4.17. Comparison of Normalized Pile Load Response with Elastic Solution (Pier A1-19)

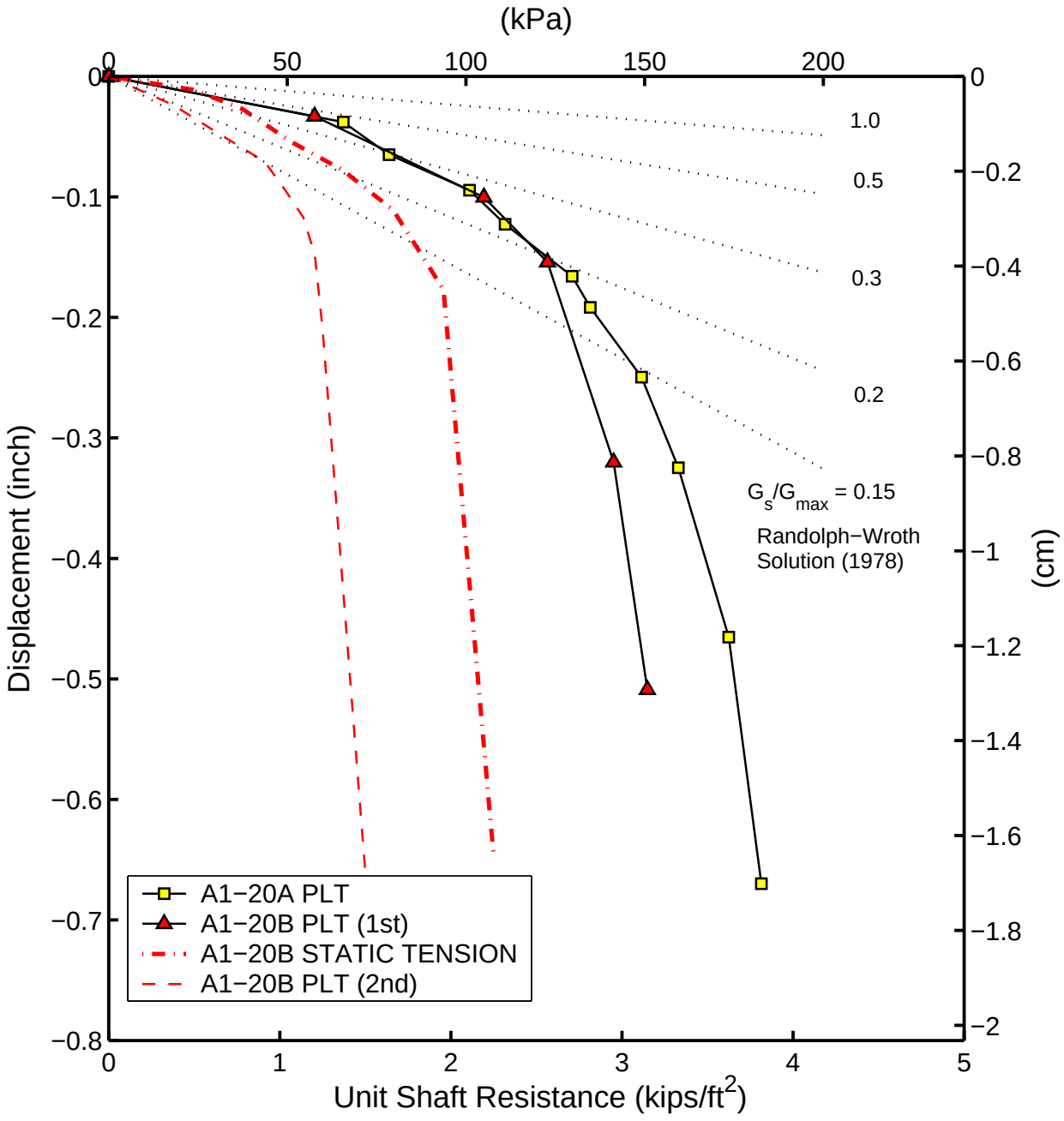

Fig. 4.18. Comparison of Normalized Pile Load Response with Elastic Solution (Pier A1-20AB)

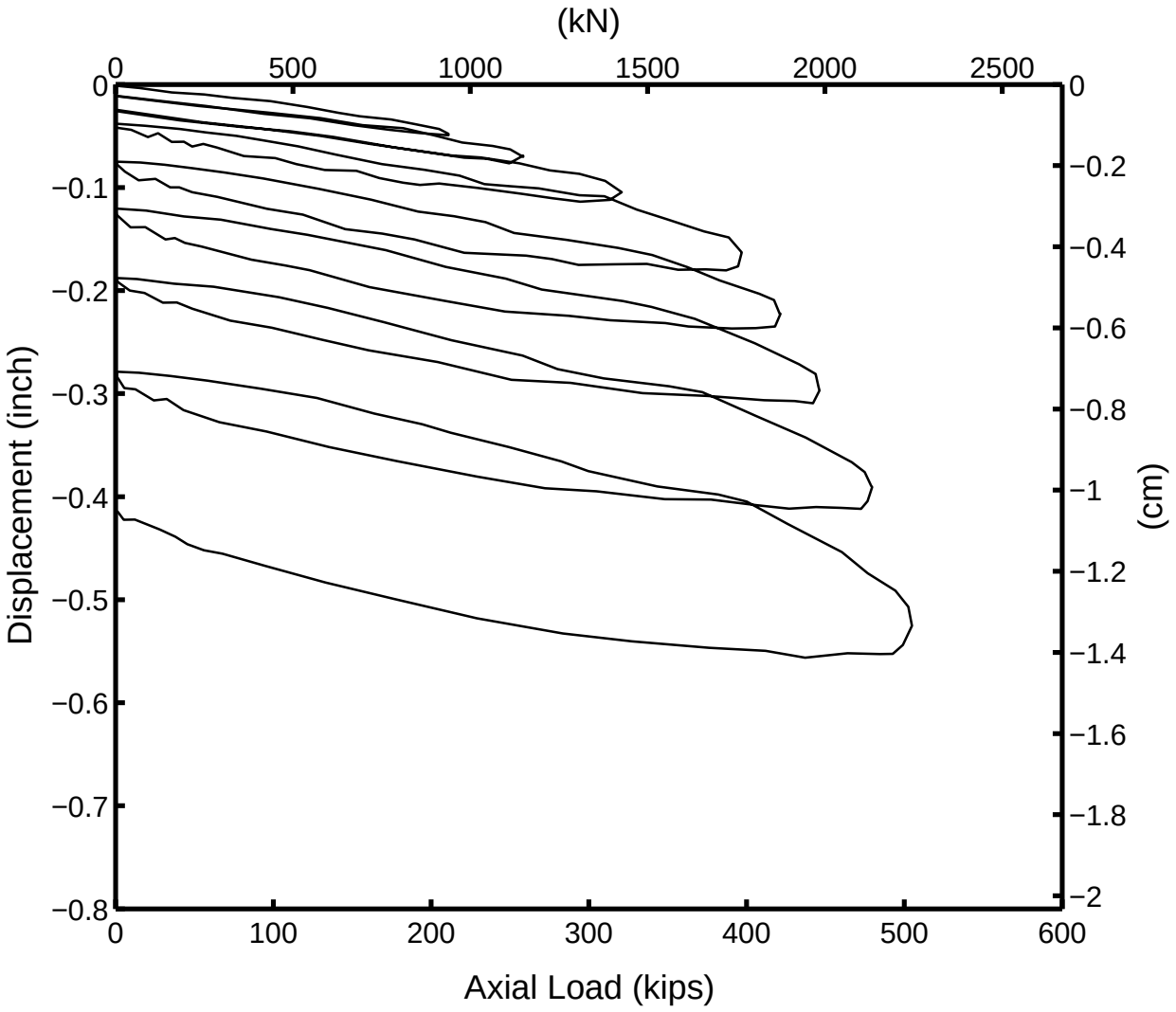

Fig. 4.19 PLT Test Results (Pier A2-20)

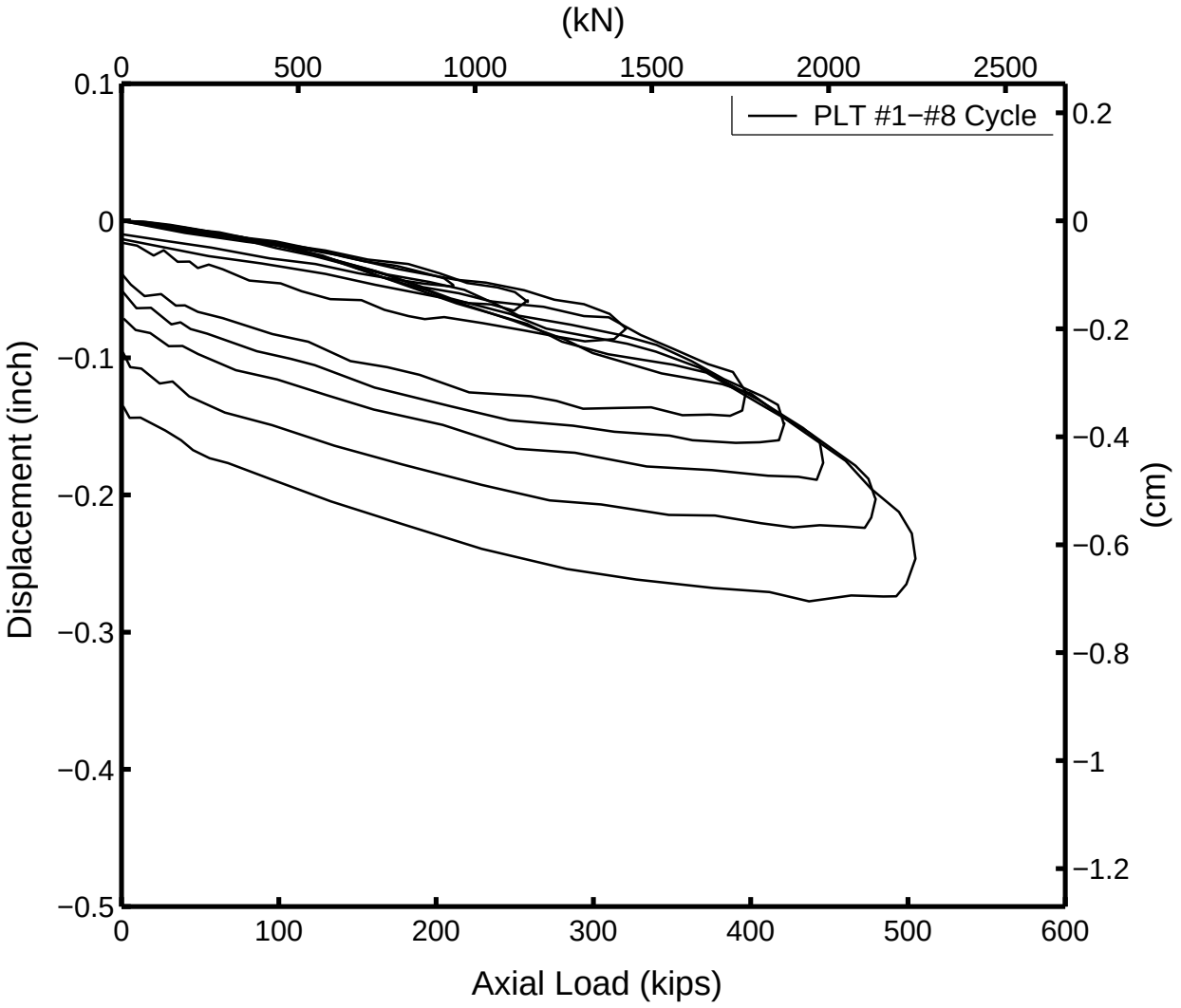

Fig. 4.20 Comparison of Individual PLT Loops (Pier A2-20)

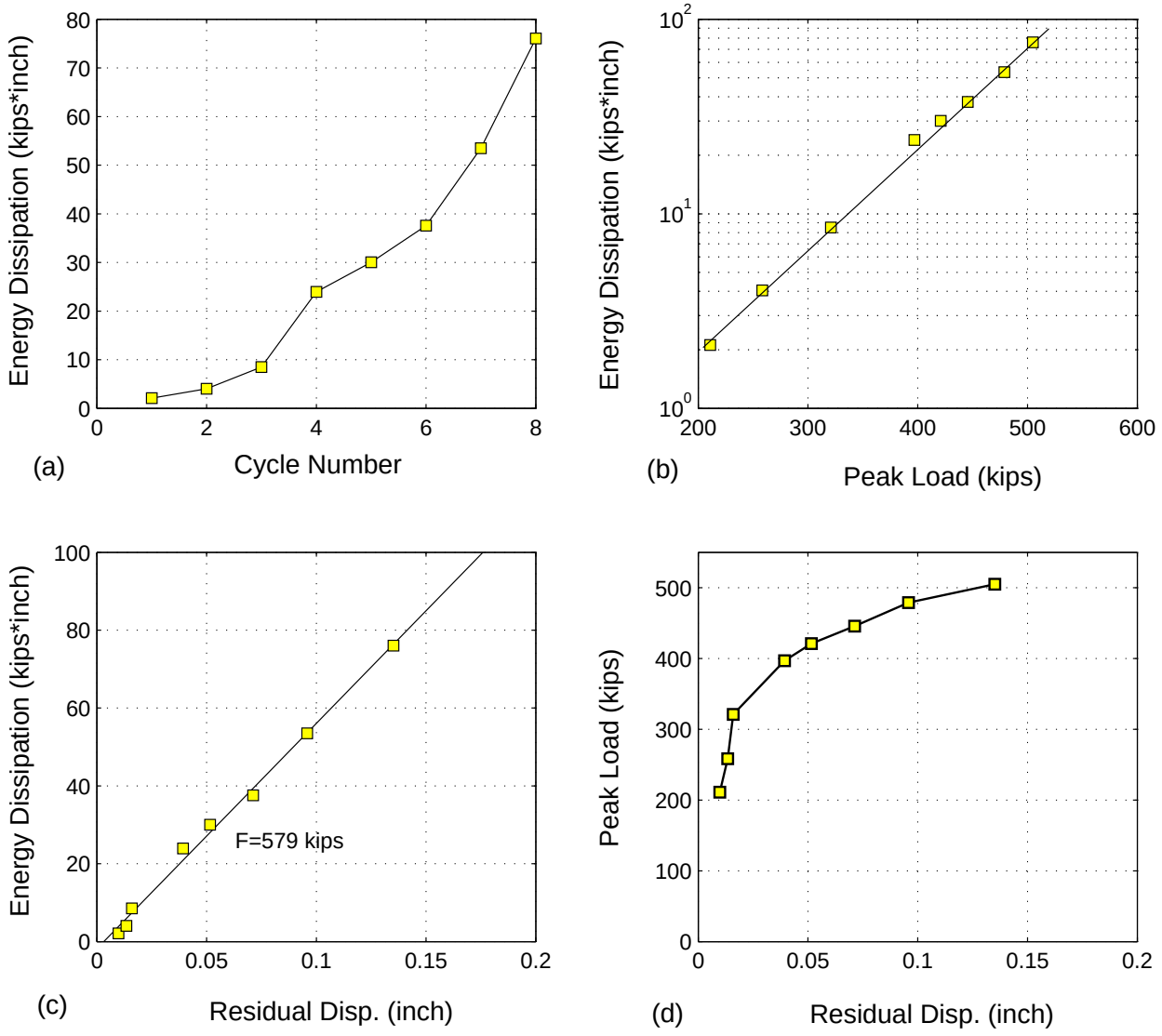

Fig. 4.21 Analysis of Pier A2-20 1st PLT Test Results

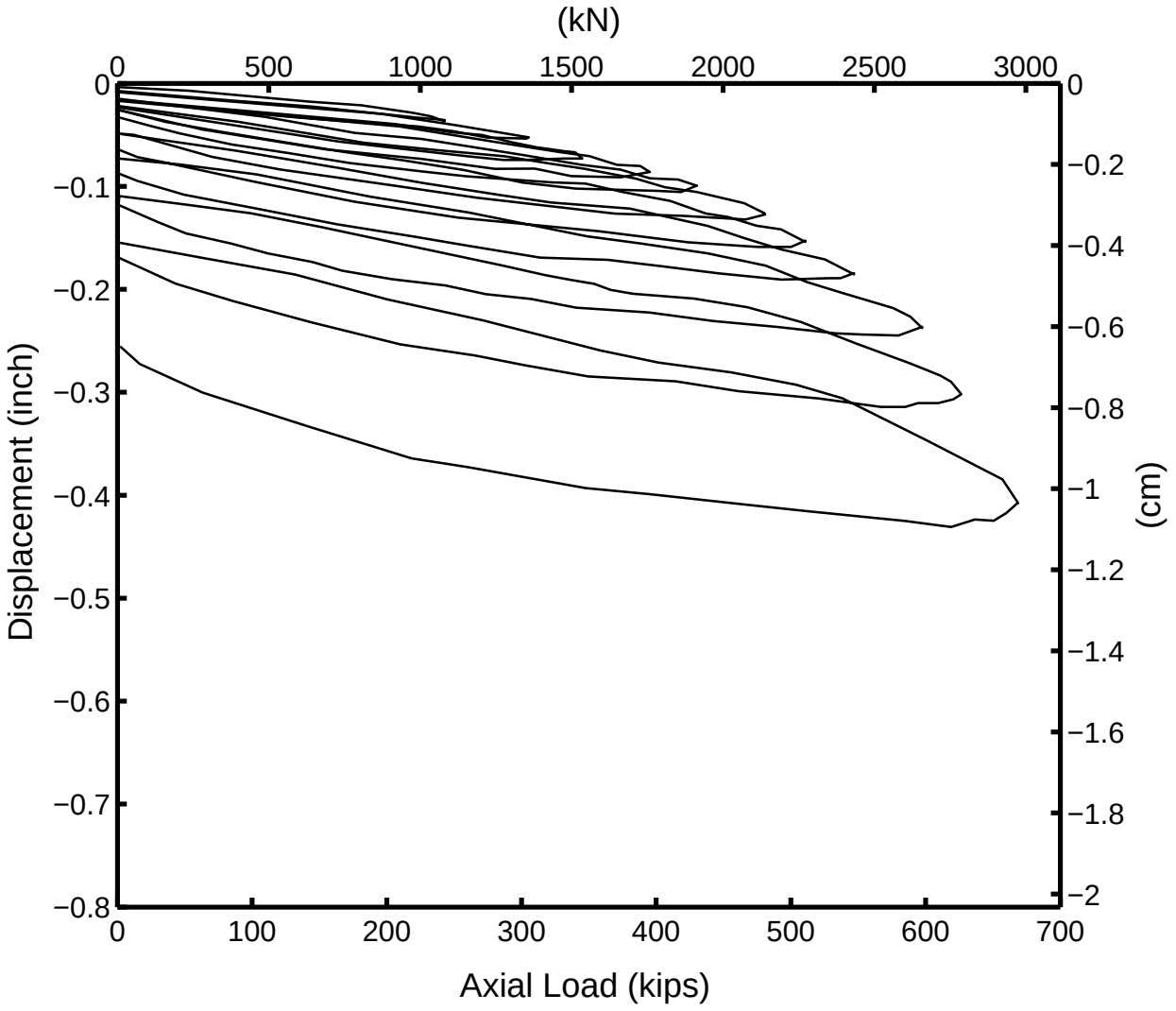

Fig. 4.22 PLT Test Results (Pier A2-25)

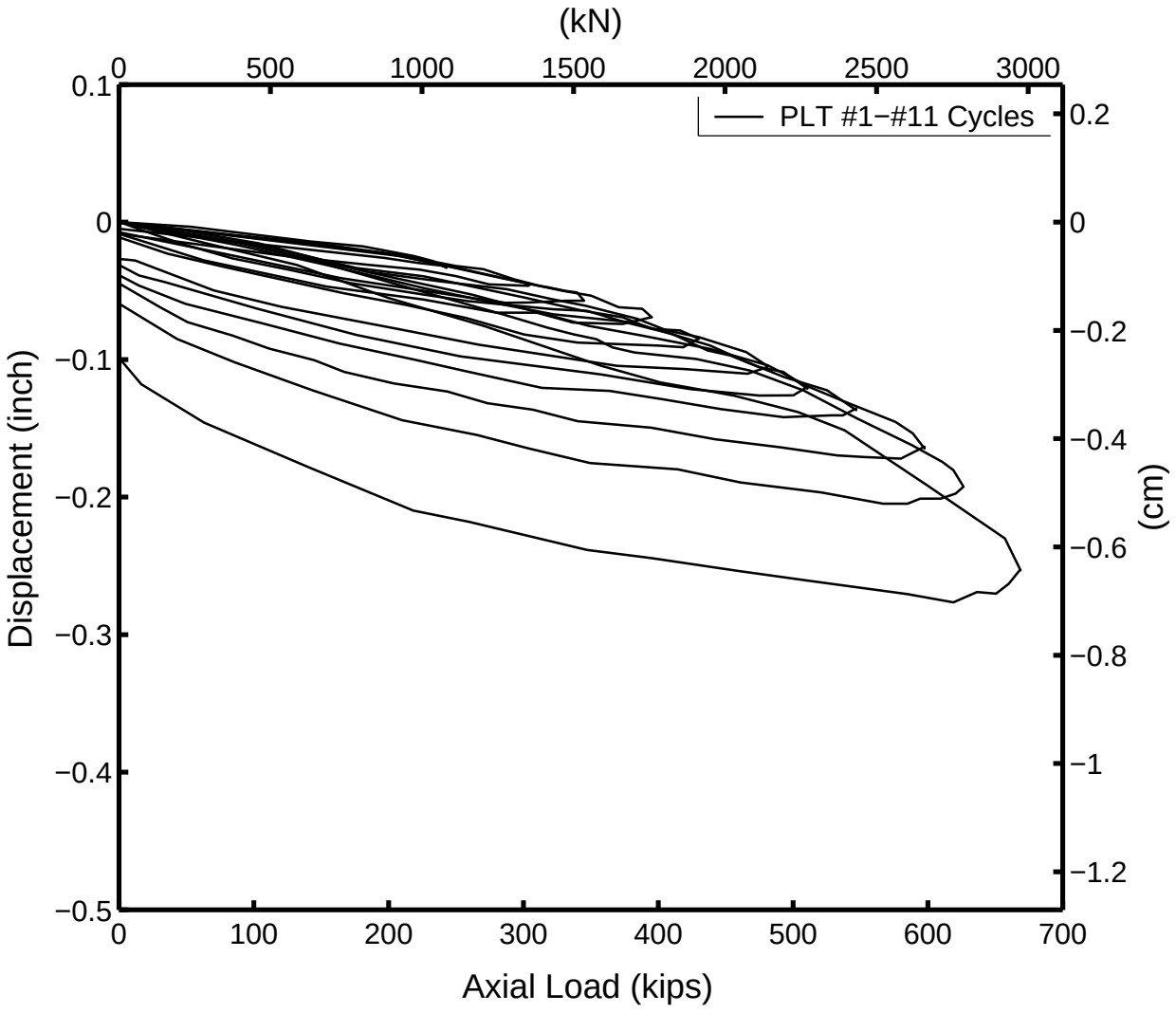

Fig. 4.23 Comparison of Individual PLT Loops (Pier A2-25)

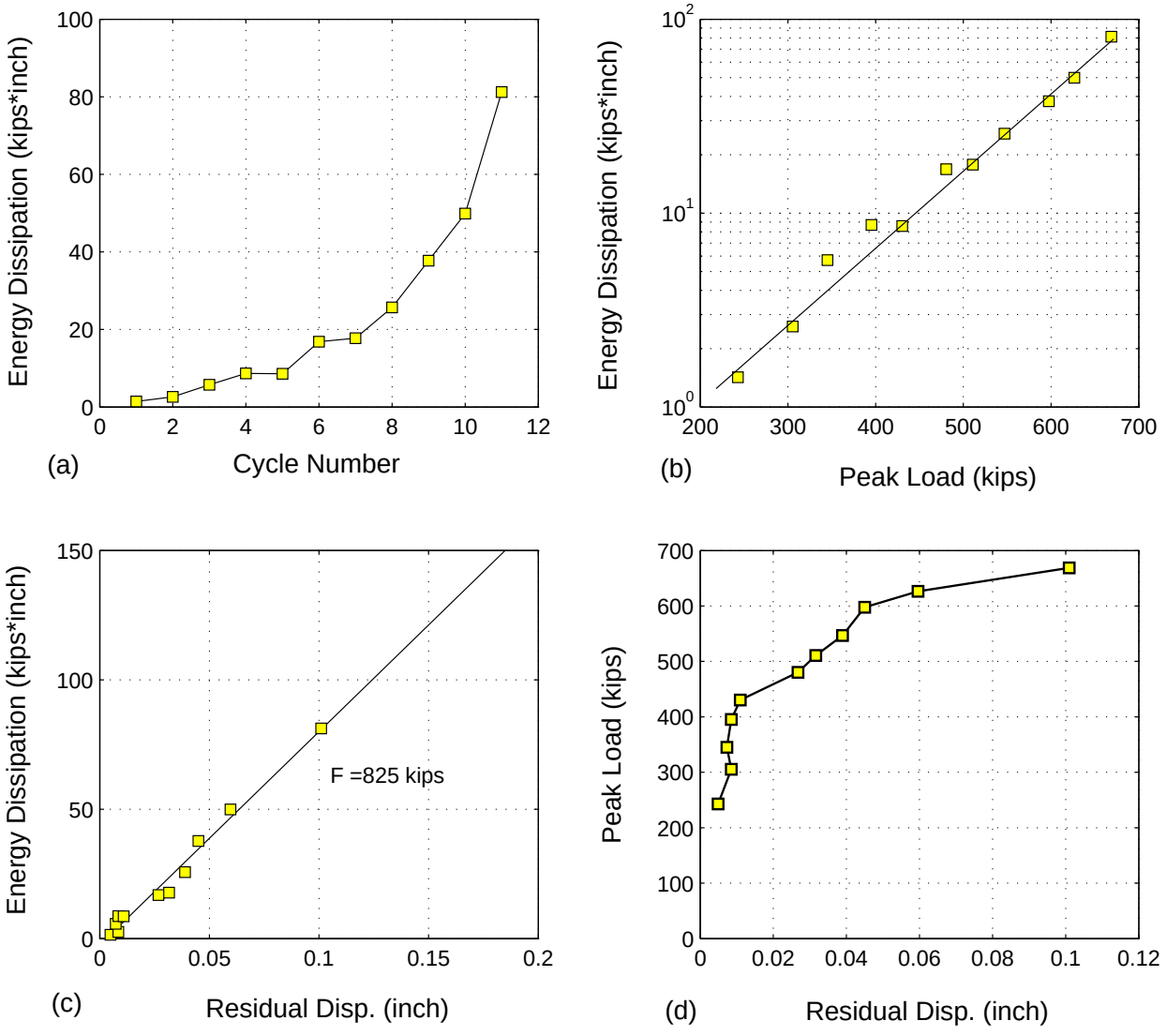

Fig. 4.24 Analysis of Pier A2-25 1st PLT Test Results

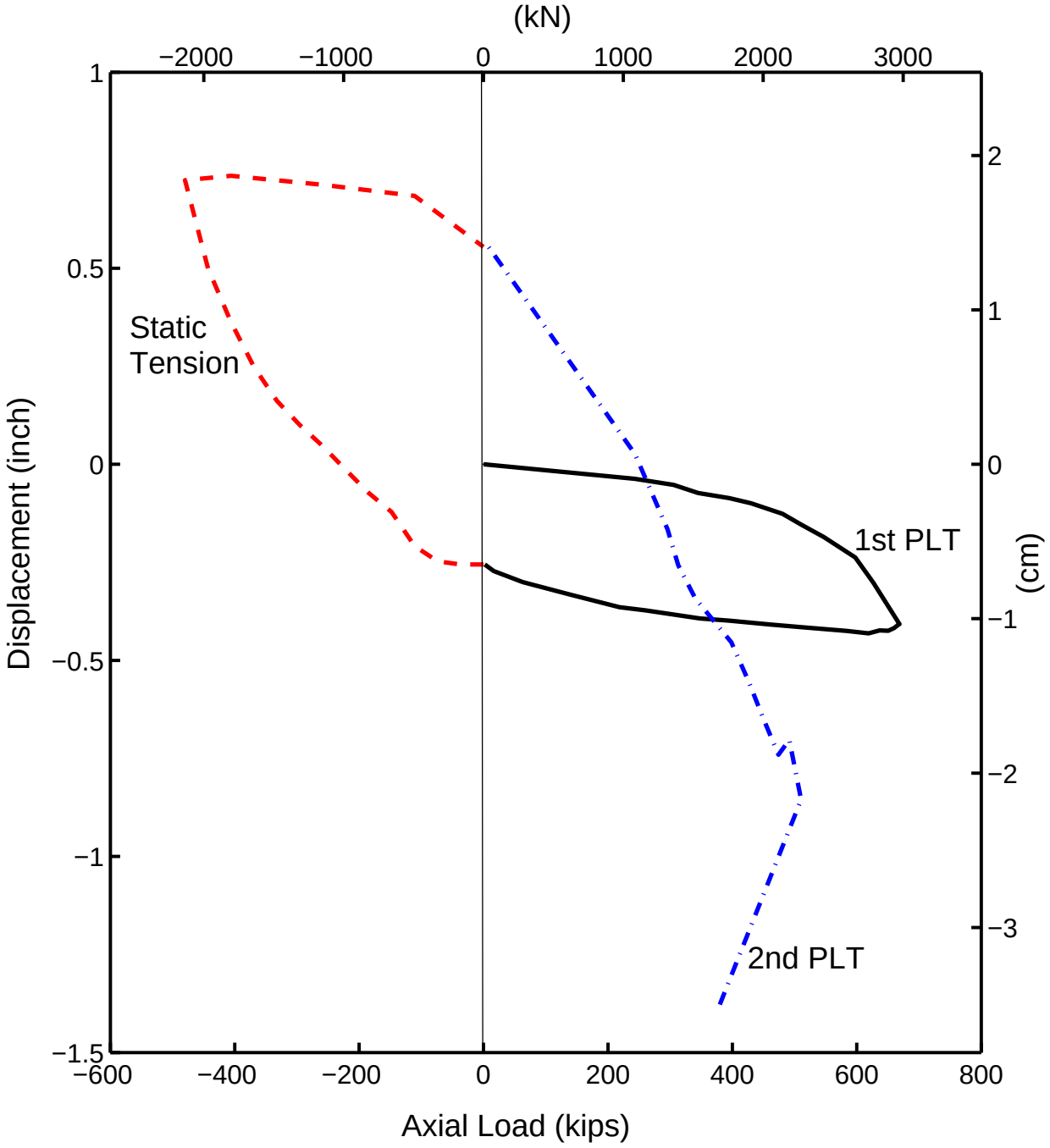

Fig. 4.25. 1st PLT, Static Tension and 2nd PLT Tests Strength Envelope (Pier A2-25)

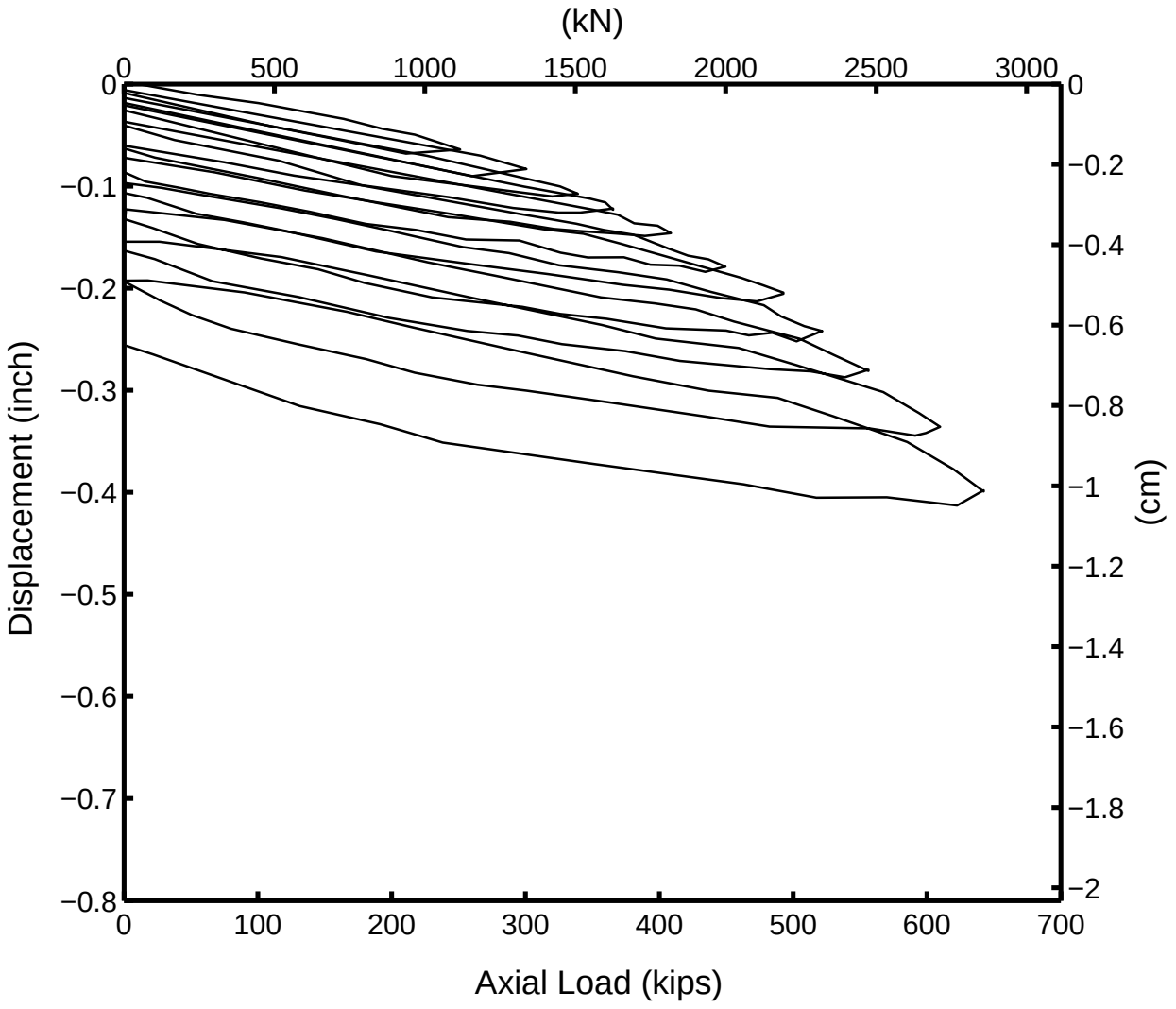

Fig. 4.26 PLT Test Results (Pier A2-30)

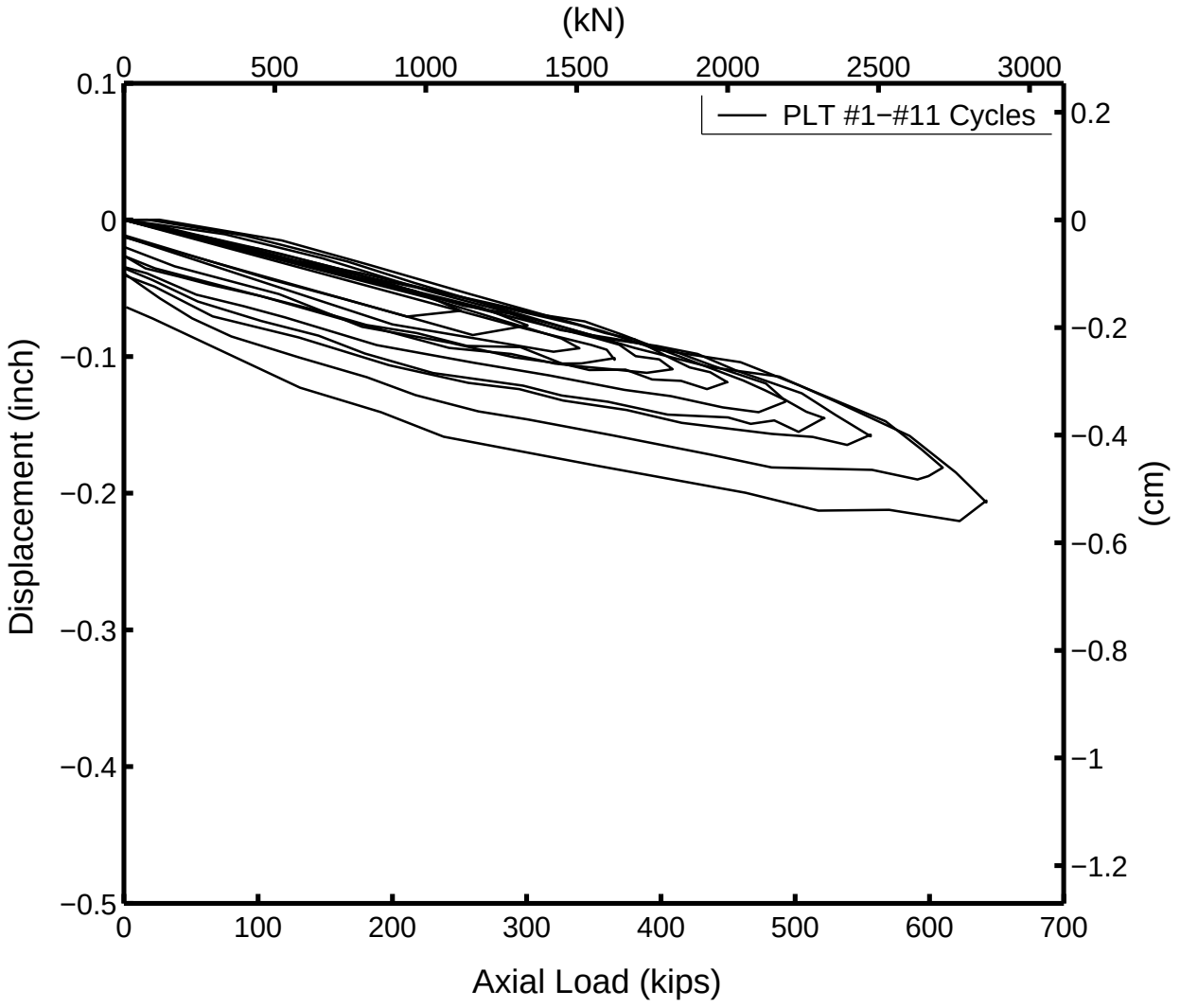

Fig. 4.27 Comparison of Individual PLT Loops (Pier A2-30)

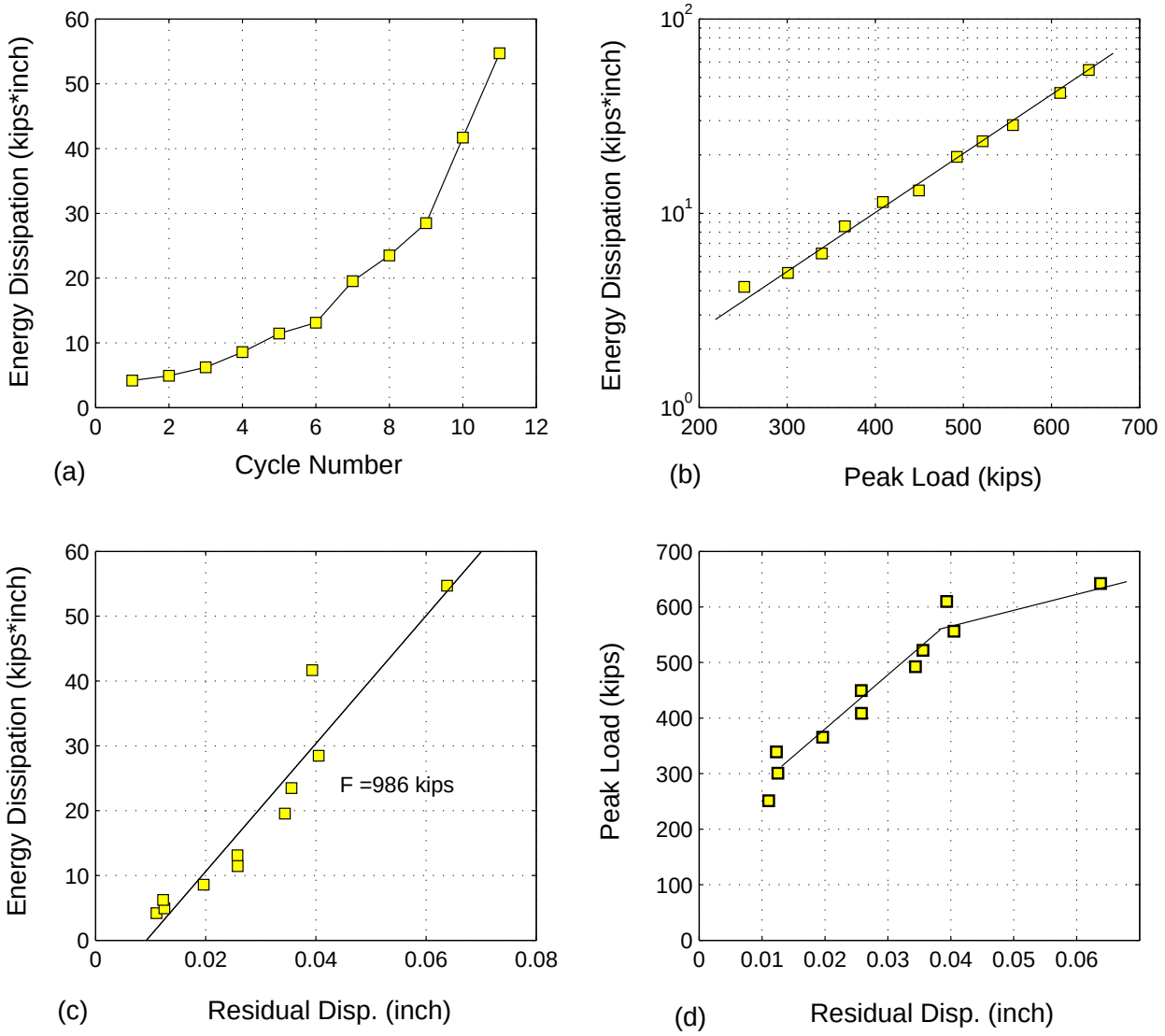

Fig. 4.28 Analysis of Pier A2-30 1st PLT Test Results

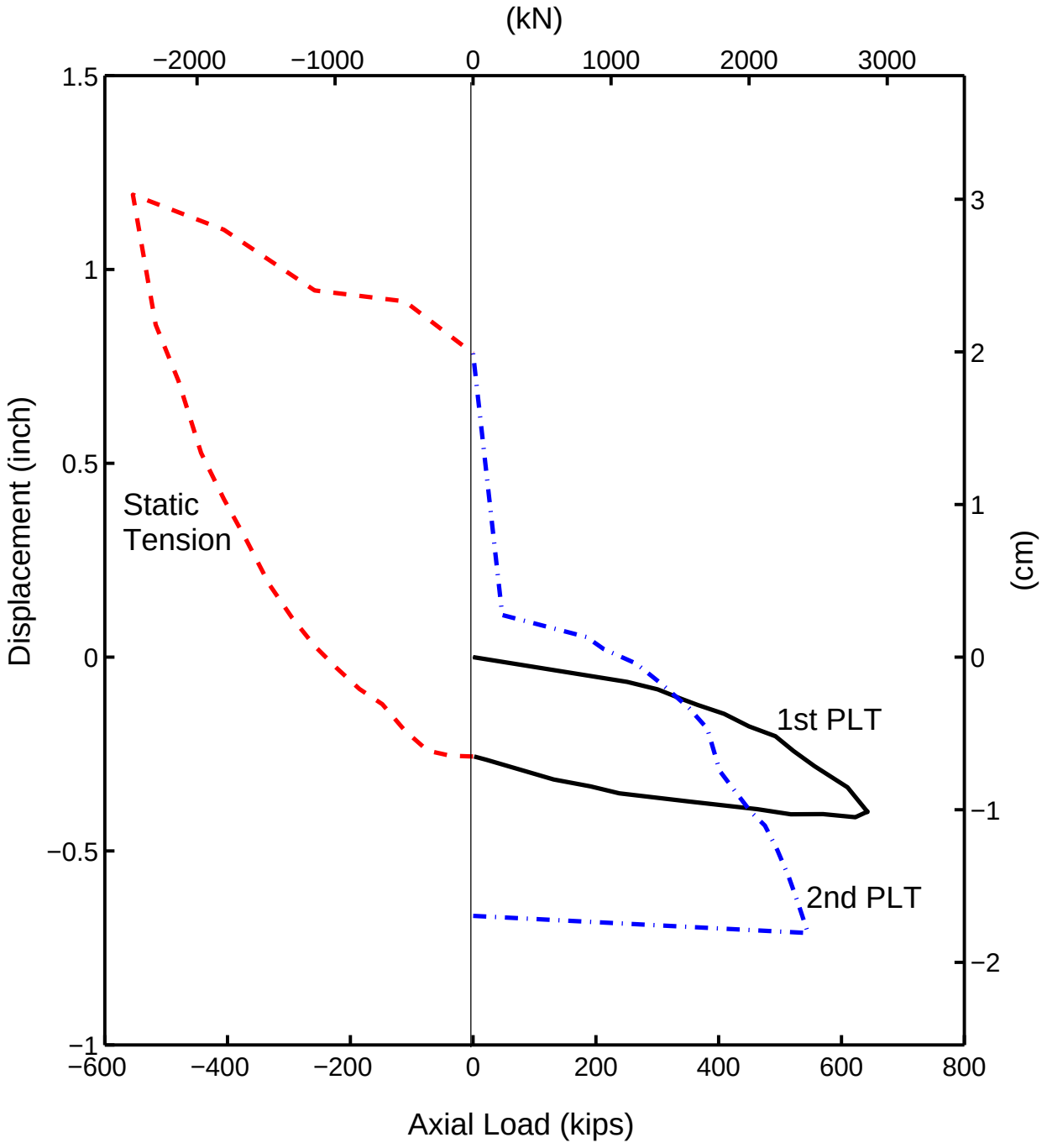

Fig. 4.29. 1st PLT, Static Tension and 2nd PLT Tests Strength Envelope (Pier A2-30)

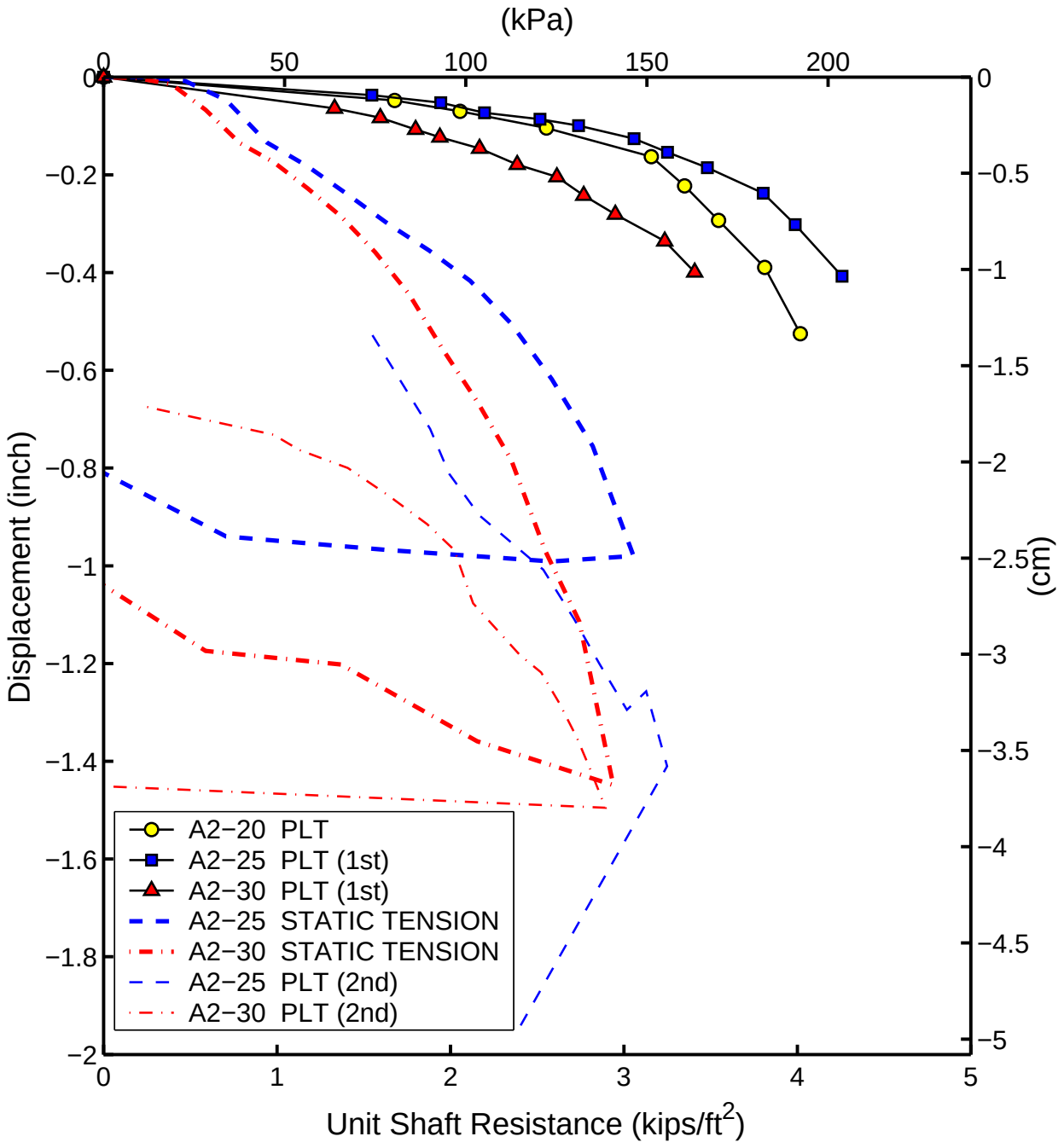

Fig. 4.30 Normalized Pile Load Response (Test Area 2)

5 Nonlinear Static and Dynamic Finite Element Analyses

The nonlinear cyclic soil model, as described in Chapter 3, was implemented in a general finite element framework called OpenSees (2005). The resulting code implementation is suitable for analysis of static and dynamic soil-structure interaction problems. In this chapter, it is used to simulate the prototype pier load test described in Chapter 4.

5.1 MODEL PARAMETERS FOR STATIC AND DYNAMIC ANALYSES

5.1.1 Dynamic Modulus Reduction Curves

The soil modulus reduction and damping factors during cyclic loadings depend on a number of factors including: the amplitude of cyclic strain developed in the soil, as well as the plasticity index (PI), void ratio, overconsolidation ratio (OCR), confining pressure, and frequency and shape of the cyclic loading-time history (Seed *et al.*, 1984; Sun *et al.*, 1988; Hsu and Vucetic, 2002; Vucetic *et al.*, 1998a,b). The emerging trends of laboratory tests include the extrapolation of cyclic stress-strain behavior to both very small and very large strain regimes, where existing test data are relatively scarce (Vucetic, 2004).

For cohesive soils, the plasticity index (PI) has an important influence on the modulus reduction curves (Zen *et al.*, 1978; Vucetic and Dobry, 1991). Clays with higher PI tend to behave more elastically than low PI soils, resulting in a slower rate of modulus reduction and lower damping ratio. Similarly, the modulus of sands reduces much faster than that of clays, and the damping ratio for sands is generally larger. Although it is most appropriate to determine the modulus reduction curve on a site-specific basis, with limited site information, we follow the guidelines suggested by Vucetic and Dobry (1991). Fig. 5.1 outlines the generic

modulus reduction curve used in dynamic analysis. Since the soil in the test area is of low plasticity, the generic curve (solid line) lies in the low plasticity range of Vucetic & Dobry curves (shown in dashed lines).

5.1.2 Static Modulus Reduction Curves

Recent experimental investigations reveal significant dependence of the form of the modulus reduction curve on the applied strain rate at small cyclic strains (Matesic and Vucetic, 2003; Vucetic and Tabata, 2003). It is recognized that the rate effect on the stiffness and strength of the soil can be attributed to the viscosity in the soil skeleton and associated creeping, stress relaxation process. Due to the rate effect, dynamic and static modulus reduction curves can be quite distinctive especially at small strains, which has been examined through comparisons of monotonic and cyclic laboratory tests at varying strain rate (LoPresti *et al.*, 1993, 1996; Shibuya *et al.*, 1996). Based on experiments, the maximum modulus at small strains is not so influenced by the imposed strain rate. On the other hand, the elastic threshold strain [1] is found to be significantly influenced by the strain rate, such that it is larger for the higher strain rate applied [2]. Beyond the elastic threshold strain, the moduli degrade at a much faster rate for monotonic loading than for dynamic cases. The effect of the loading rate also varies with the soil type. In general, the rate effect is very small in clean sands and non-plastic silts, relatively small in silty and clayey sands, and significant in clayey soils (Matesic and Vucetic, 2003). Moreover, the strain rate effect in clays generally increases with the plasticity index (PI) and water content.

Since the shear modulus reduction curve is rate dependent, the effect has significant implication on our numerical modelling procedure. In general, there can be two ways to take into account the rate effect. One is to develop a rate-dependent constitutive model for the soil such that the rate effect can be simulated by the model. Such a scheme is appealing for accommodating variation in the strain rate during a loading history, but unfortunately, is scarce in the literature and not sufficiently developed for practical use. The second ap-

[1] Elastic threshold strain is defined to be the strain beyond which nonlinear and irreversible deformation occurs.

[2] An exponential form seems appropriate to relate the elastic threshold strain to the strain rate, as proposed by Shibuya *et al.* (1996).

proach used herein, considers different soil parameters for the static case and dynamic case, respectively, such that the dependence of soil parameters on the strain rate can be considered explicitly.

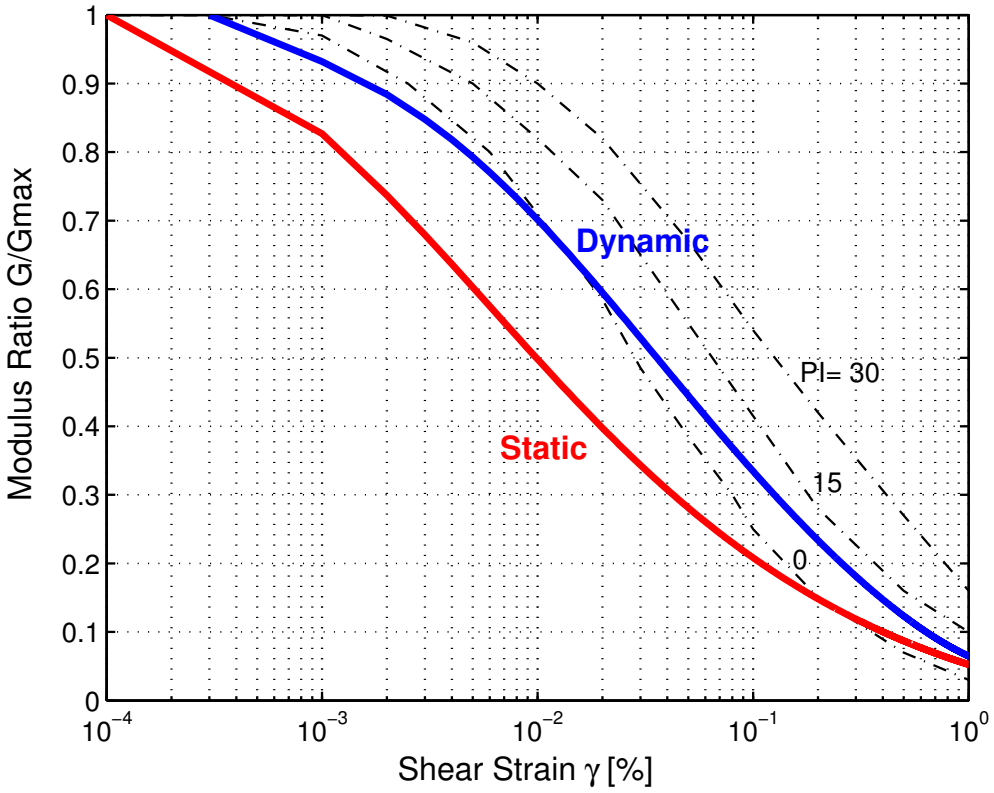

Fig. 5.1. Modulus Reduction Curves Used in the Dynamic and Static Finite Element Simulations

5.1.3 Model Parameters

As discussed in Chapter 3, the nonlinearity of the soil response is modelled by smoothly transforming the tangential shear modulus from the small strain modulus to the plastic yield state through a state-dependent hardening rule. The hardening rule is a continuous exponential mapping function between the current stress state, the last stress reversal point, and the image point on the bounding surface. Two hardening parameters, h and m, are used to adjust the shape of the cyclic curves and can be fitted through the modulus reduction curve of various soil types. In the dynamic simulation, the hardening parameters h and m

are chosen to fit the low PI range of the Vucetic and Dobry (1991) curves. For the static analysis, we back calculate a static modulus reduction curve, which degrades faster than the dynamic curve. The difference is consistent with that observed in the laboratory tests. The stiffness reduction schemes used in the analysis is shown in Fig. 5.1, with the Vucetic and Dobry (1991) curves for PI=0,15,30 shown in dashed lines.

Table 5.1 Summary of Soil Parameters

	Dynamic Analysis	Static Analysis
Soil Density, ρ	$2 \times 10^3 kg/m^3$	
Poisson's Ratio, ν	0.4	
Shear Wave Velocity, V_s	289 m/s	
Max. Shear Modulus, G_{max}	1.67×10^5 kPa	
Undrained Shear Strength, S_u	100 kPa	86 kPa
Hardening Parameter, h	0.70 G_{max}	0.25 G_{max}
Hardening Parameter, m	0.8	0.8
Hardening Modulus, H_o	0	$G_{max}/300$
Viscous Coefficient, β_{ini}	0.0003	–
Time Step, Δt	0.005 sec	–

Table 5.1 summarizes the soil parameters used in the analysis. Based on laboratory tests of soil samples from the site, the soil density was taken as $\rho = 2 \times 10^3 kg/m^3$. Since the average shear wave velocity ($V_s = 289 m/s$) was measured over the pier length, the small strain shear modulus $G_{max} = \rho V_s^2$ was computed using this measured value.

To simplify the simulation, homogeneous soil properties were first assumed. The undrained shear strength for static loading, S_u, was chosen to be 86 kPa over the depth, which is the average of the undrained shear strength over the pier length. To account for the loading rate effect, the undrained shear strength was chosen $S_u = 100$ kPa in dynamic analysis [3]. This simplification will be assessed in subsequent sections, where refined analysis is made using the measured S_u profile that is inhomogeneous.

For the concrete piers, linear elastic material was assumed in the modelling, since the stress developed during the test was well below the tensile and compressive strength of

[3]It was reported that the shear strength of the clay increases typically by a factor of 1.05 – 1.10 for ten-fold increase of the strain rate (Mitchell, 1976). The relationship between soil strength and logarithm of the strain rate can also be approximated by a bilinear relation — beyond the extremely high strain rates of around 20% – 100% /s, the rate effect becomes much more pronounced (Yong and Japp, 1969).

concrete. Young's modulus was assumed 20 GPa, with Poisson's ratio $\nu = 0.1$ and density $2.4 \times 10^3 \text{kg/m}^3$ (150 pcf).

5.2 NONLINEAR FINITE ELEMENT SIMULATION

5.2.1 Finite Element Model

Due to the symmetry of the problem, only one half of the cross section was meshed using an axisymmetric bilinear element which was developed in OpenSees as a part of this study. The mesh, shown as an example in Fig. 5.6(a), extends to 40 feet in depth and 20 feet in length. The base of the mesh is constrained in both directions and only vertical movement is allowed along the right side of the simulation domain and the axis of symmetry (the left side). The size of the mesh was regarded as appropriate for the problem after mesh sensitivity analysis. Since groundwater was found at 21.5 feet in depth at Test Area 1 and 10-11.5 feet in depth at Test Area 2, the degree of saturation varies considerably throughout the site. To alleviate possible volumetric locking at the incompressible limit, B-bar formulation was used in undrained analysis.

Traditionally, frictional contact elements (zero length) can be placed along the pier-soil interface to allow for slippage between pairs of pier and soil elements. Frictional contact elements essentially enforce Mohr-Coulomb type failure criterion along the material interface, which needs an additional set of parameters. However, many field observations reveal that the failure surface of cast-in-place concrete piers does not occur exactly on the material interface but some distance inside the surrounding soil. Instead of utilizing zero-length contact elements, the interface behavior was modelled through a thin layer of nonlinear interface elements adjacent to the pier shaft. Although distinct constitutive behavior can be assigned to the interface elements, they were chosen to have the same properties as the nonlinear soil. To minimize the bias due to element size, a very fine mesh was used in the interface region.

Important for the ensuing analysis, the initial in-situ stress state should be properly developed. A staged loading process was designed to enforce the in-situ stress state of soil elements: The soil elements were initially assumed to be linearly elastic, with Poisson's ratio

determined by $\nu = K_0/(1+K_0)$, where K_0 is the coefficient of earth pressure, approximately 0.5 for normally consolidated clays. After vertical consolidation under self weight to generate the desired K_0 profile, the soil elements were allowed to respond nonlinearly.

During a PLT test, a dynamic load $F(t)$ was applied on the top of the test pier. A typical load history measured during the test of a single load pulse (Fig. 5.2) can be reasonably approximated by a trigonometric function as

$$F(t) = \frac{P}{4}\left[1 - \cos\left(\frac{2\pi\ t}{T}\right)\right]^2 \tag{5.1}$$

where P and T are the magnitude and duration of the load pulse. During the analysis, load pulses were repeatedly applied on the pier top, with magnitude P for each pulse taken as the value of actual measurement, and duration T assumed to be 0.3 second for all pulses. The load was uniformly distributed on the pier head to eliminate point load singularity such that the vertical movements of all top surface nodes of the pier were identical.

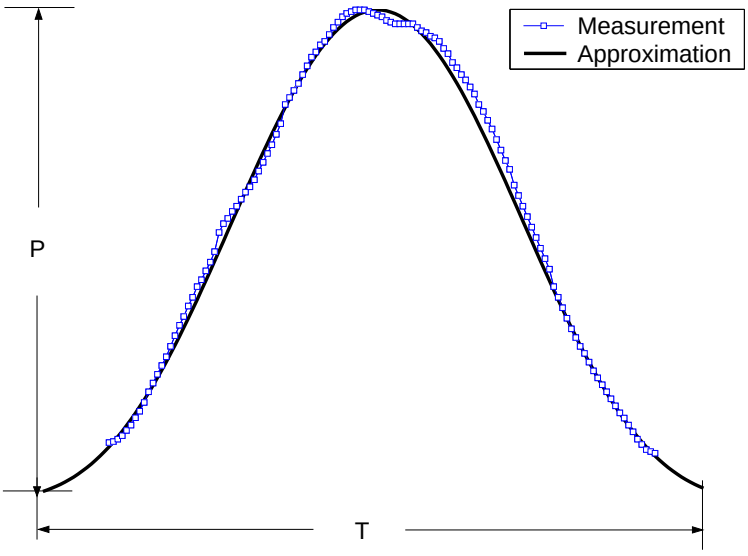

Fig. 5.2 Approximation of PLT Pulse

5.2.2 Simulation of Dynamic PLT Tests

The sequence of PLT test on Pier A1-19 was simulated first. The pier is 19 feet long, 2.5 feet in diameter, with end bearing capacity. Fig. 5.3 shows the recorded and predicted PLT

curves for pier head displacement versus the applied load history. The plot shows that the dynamic soil-pier stiffness for loading and unloading as well as residual displacements and energy dissipation for all nine loops can be simulated reasonably well. The overall strength envelope, which encompasses all these loops, closely follows the actual measurement. It should be noted that during the test, there was considerable rebound at the end of each PLT loop, which cannot be adequately simulated. The lack of rebound accumulates to produce the apparently larger predicted total residual displacement (0.7 inches predicted against 0.5 inches measured).

Fig. 5.4 further juxtaposes the computed displacement, velocity, and acceleration time histories of the top node in reaction to the applied load. When the load increases, the pier accelerates downward, accumulating velocity and displacement. Displacement achieves its maximum value at the point when velocity passes through zero, and reduces afterwards. It is evident that the peak displacement lags slightly behind the peak load point due to the inertial effect. A similar pattern is repeated with increasing magnitude of the cyclic peak load applied. In the last two pulses, the downward peak velocity reaches $0.1m/s$, and the acceleration reaches $2m/s^2$ downward and $6m/s^2$ upward.

A detailed response of the soil element adjacent to the pile wall at middle depth is presented in Fig. 5.5. With increasing load, the element *loads* from its initial stress state, and its shear modulus degradates from the maximum value (small strain modulus) to the current value according to the bounding surface mapping rule. Upon stress *unloading*, the current stress state is set as the new unloading point, and the shear modulus is set back to the maximum value, mapping back in the opposite direction afterwards. The unloading point in the element corresponds to the point of maximum displacement, i.e., where the strain increment changes direction, but not the applied peak load point. The plastic states during the whole analysis are also monitored, where 0 stands for the current stress moving inside the bounding surface, 1 for a full plastic state on the bounding surface, 2 for stress state moving from the interior onto the bounding surface – for that case, the operator split algorithm was performed. The time history of the plastic state indicates that the full plastic stage was reached in the element during the last four pulses, where the shear modulus decreased to zero, and considerable strain was accumulated in that range. To measure the intensity of the strain developed within the element, L_2 norm ($\|\boldsymbol{\epsilon}\| = \sqrt{\boldsymbol{\epsilon} : \boldsymbol{\epsilon}}$) was also plotted. The strain

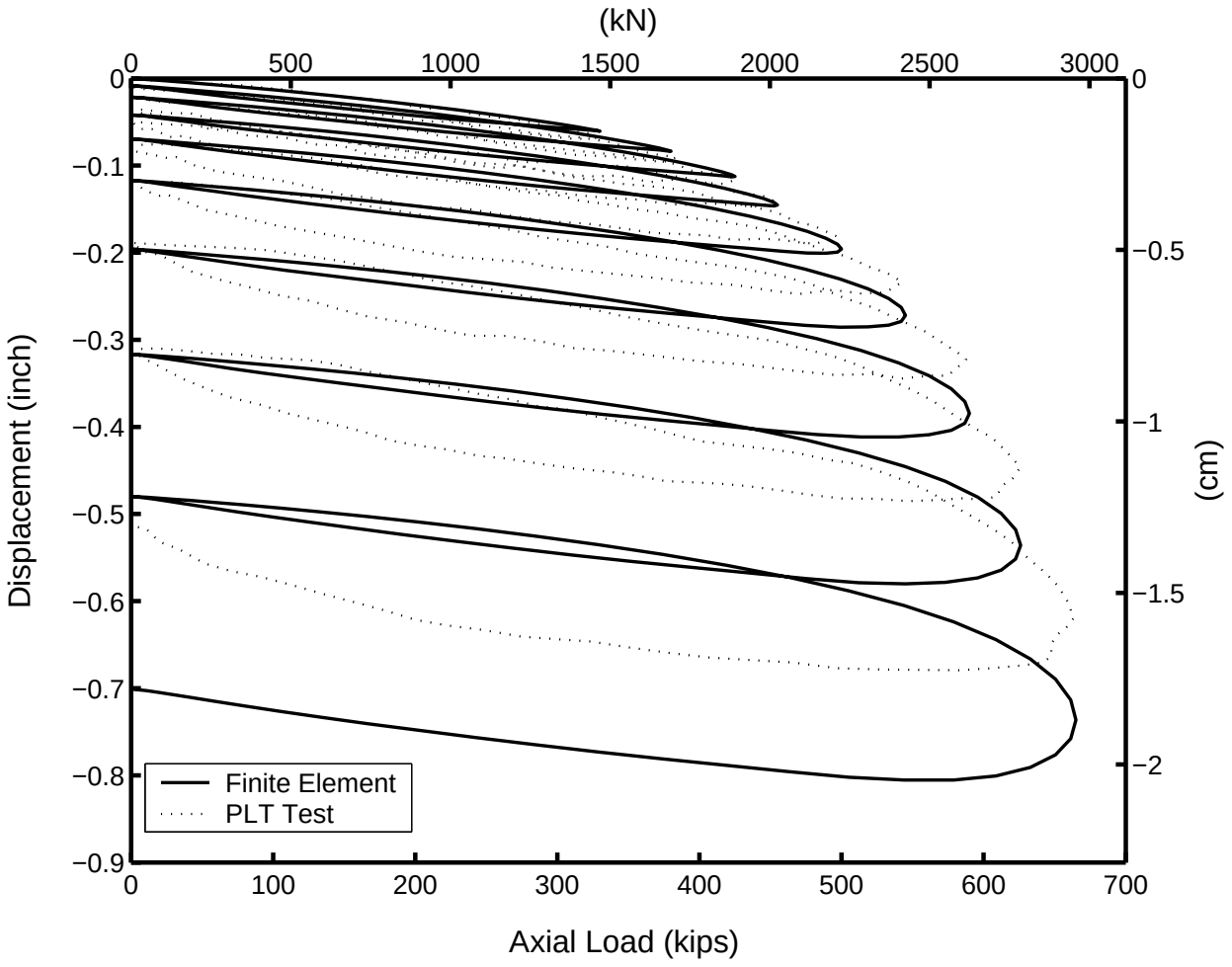

Fig. 5.3. Simulated Pier Head Displacement under Cyclic Loading (Pier A1-19 Homogeneous Profile)

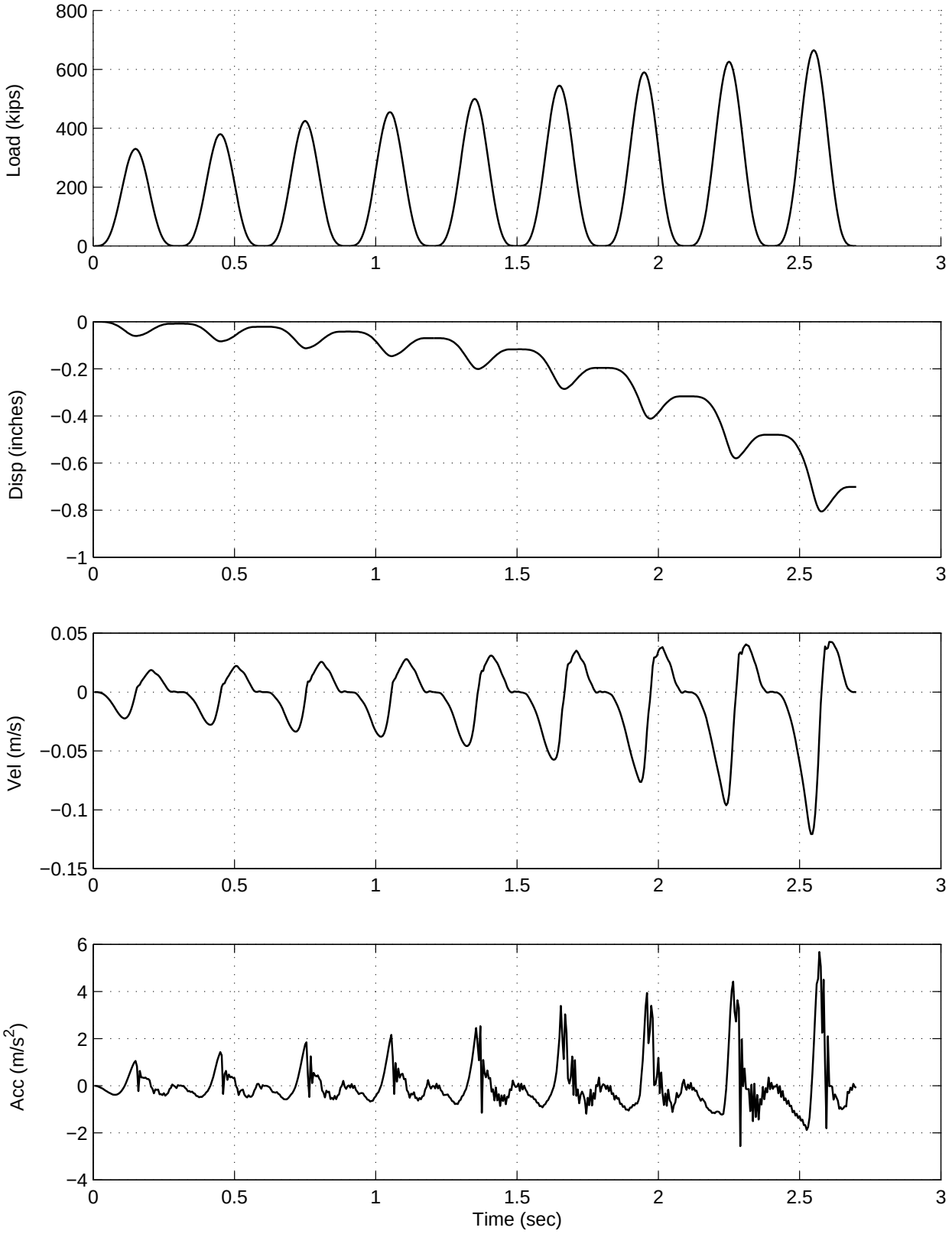

Fig. 5.4 Computed Top Node Reaction (Pier A1-19 Homogeneous Profile)

level in the element ranges from very small to relatively large (up to 1%) under the cyclic loading.

The displacement and stress fields at the peak load point of the last cycle of loading are plotted in Fig. 5.6. In view of the vertical displacement, the pier as a whole penetrates the soil like a rigid body. Underneath the pier end, a conical soil wedge is formed and moves together with the pier, with a slip line of about 45^o inclination. Significant displacement and shear stress gradients are localized within one pier radius distance in the soil. Due to the assumption of homogeneous soil profile, the shear stress along the pier shaft is rather uniform, except for a small area of high stress concentration around the tip. Fig. 5.7 illustrates the residual displacement and stress fields after the PLT test. Upon removal of the applied load on the pier head, about 10% of the peak vertical stress is locked beneath the pier end, and the residual shear stress is also concentrated in that area.

The above analysis was made under the assumption of a homogeneous soil profile, where the averaged soil strength was used. To assess the influence of soil nonhomgeneity, the model was re-analyzed using a more realistic undrained shear strength distribution, as shown in Fig. 5.9 (a). A static strength profile was deduced from the (static) unconfined compression test, in which the surface crust over the top 8 feet is over-consolidated and has a higher strength. The S_u profile for dynamic analysis was assumed to be 16% higher pointwise than the static profile to account for strain rate effect. It may be noted that the layered profile has an average strength value of 86 kPa for the static case and 100 kPa for the dynamic case, the same as used before. As shown in Fig. 5.8, the refined analysis using layered profile predicts very similar pier head response as in Figs. 5.3. This result suggests that the nonhomogeneity of undrained shear strength distribution is not critical for a stiff clay site, especially for short piers. However, the detailed stress distribution is quite different, as shown in Figs. 5.9 and 5.10. In general, larger stresses are mobilized and locked in the upper overconsolidated region.

To further validate the model, the *same* set of parameters was used to model the PLT test conducted on another Pier A1-20A. This pier was 20 feet long, 2.0 feet in diameter, and subjected to ten PLT pulses applied on the top. Since the pier was designed as purely frictional, the elements right underneath were assumed to have very small elastic modulus.

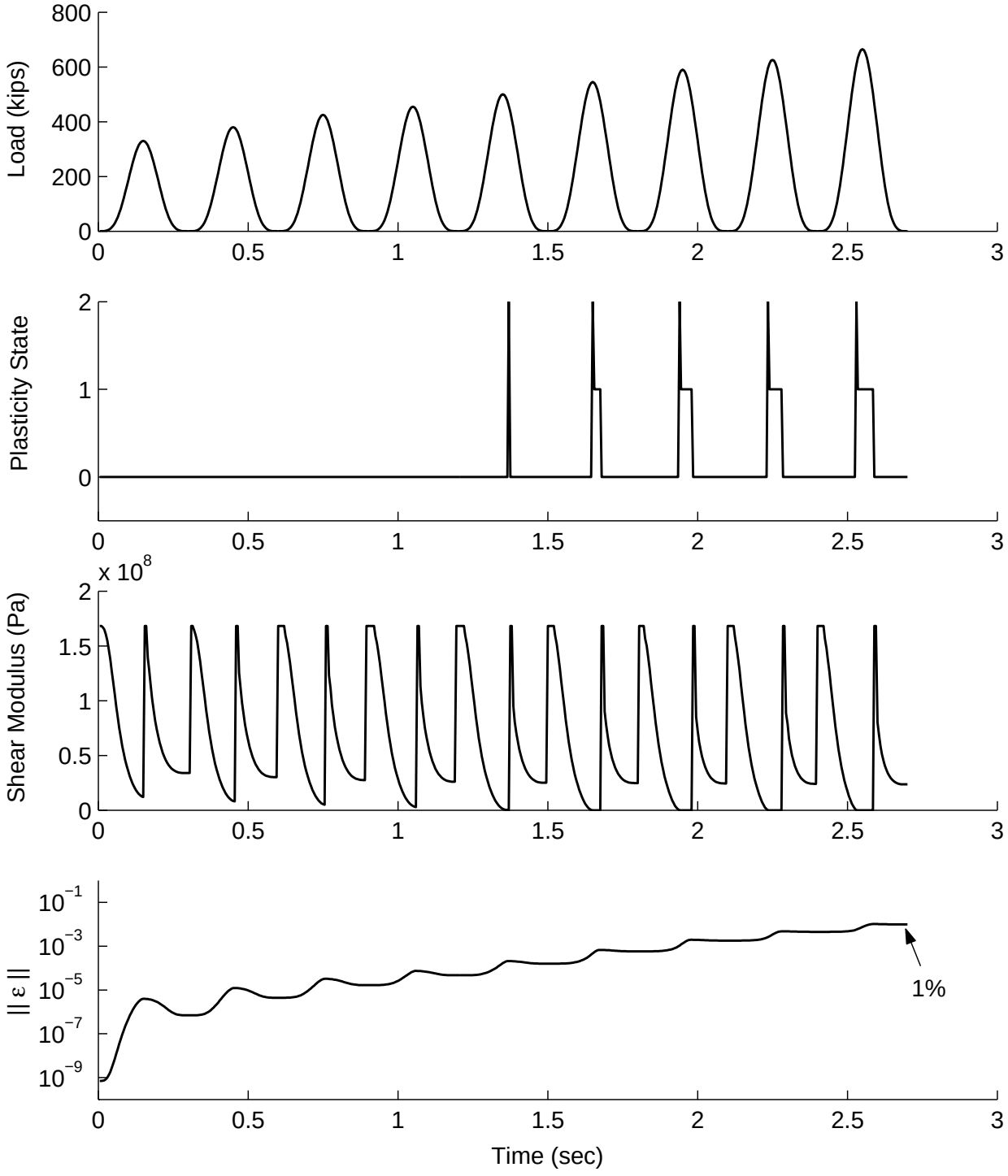

Fig. 5.5 Details of an Element (Pier A1-19 Homogeneous Profile)

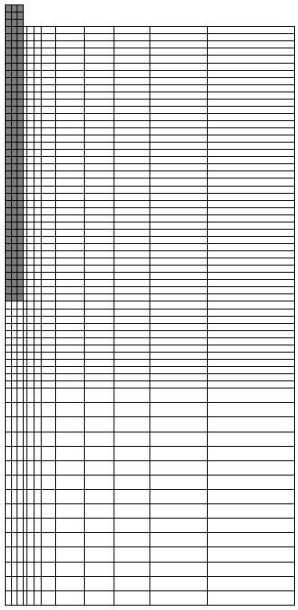

(a) FEM Mesh

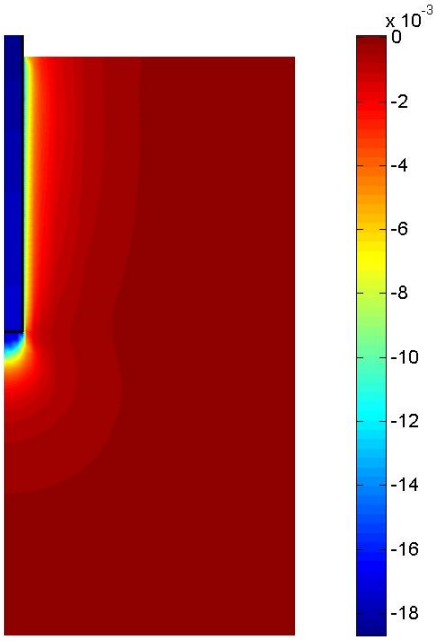

(b) Vertical Displacement Field (m)

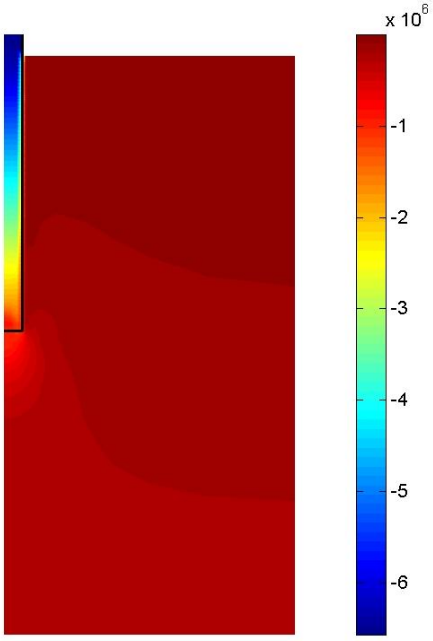

(c) Vertical Stress Field (Pa)

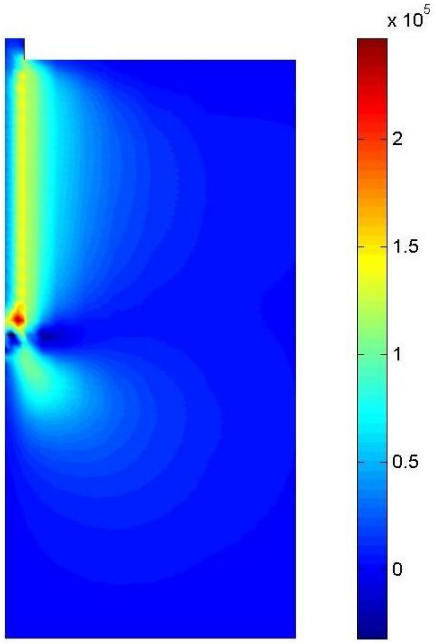

(d) Shear Stress Field (Pa)

Fig. 5.6. Displacement and Stress Fields at Peak of Last PLT Loop (Pier A1-19 Homogeneous Profile)

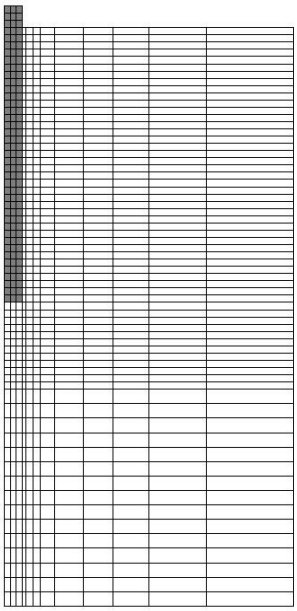

(a) FEM Mesh

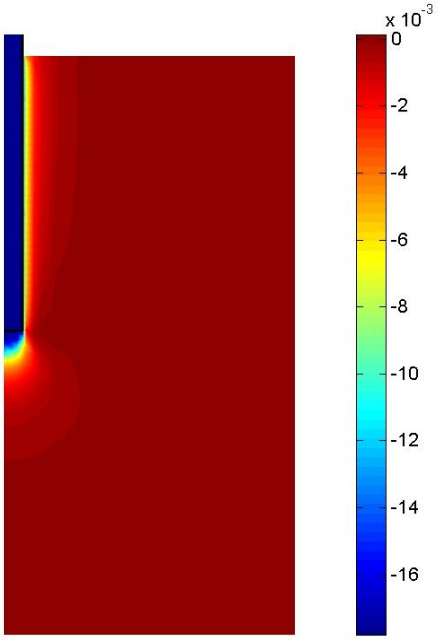

(b) Vertical Displacement Field (m)

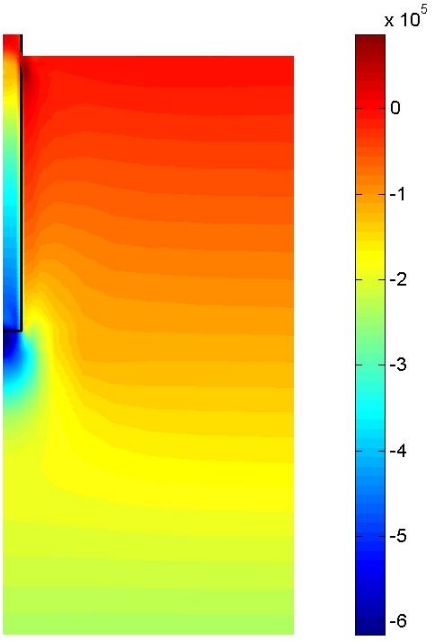

(c) Vertical Stress Field (Pa)

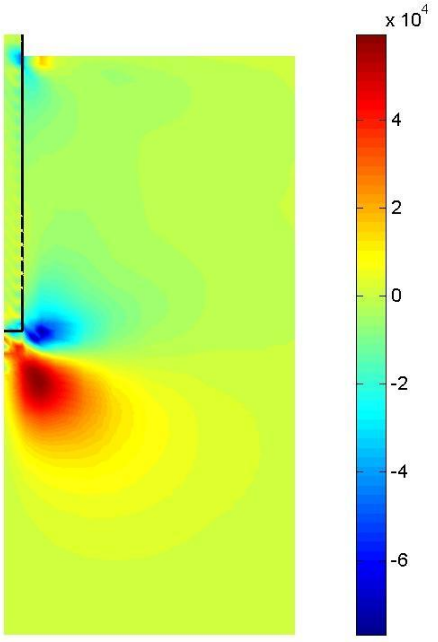

(d) Shear Stress Field (Pa)

Fig. 5.7. Residual Displacements and Stress Fields after Last PLT Loop (Pier A1-19 Homogeneous Profile)

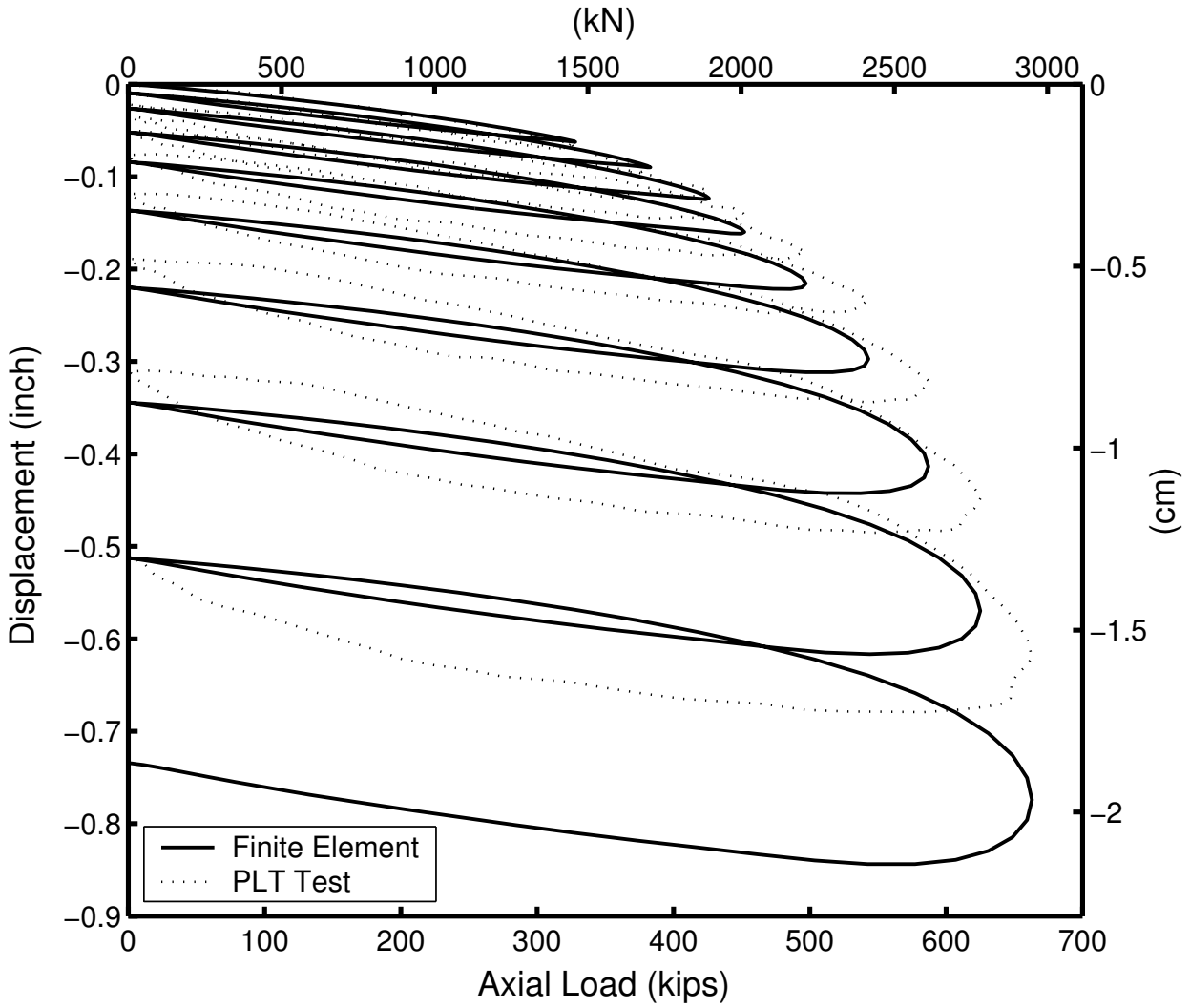

Fig. 5.8. Simulated Pier Head Displacement under Cyclic Loading (Pier A1-19, Layered Profile)

Figs. 5.11 – 5.13 summarize the predicted pier head response, as well as displacement and stress fields. Similar to the previous case, the model agrees very well with the test data.

5.2.3 Simulation of Static Compression Test

As described in Chapter 4, the static compression test was performed after the PLT test on Pier A1-19. The PLT load history, i.e., the influence of residual displacement and stress condition, should be properly taken into account in the finite element analysis.

In our static analysis, the pier was first loaded and unloaded to generate the desired

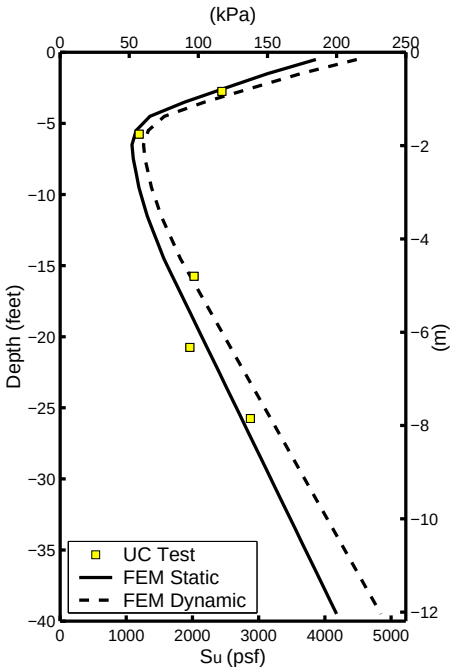

(a) S_u Profile

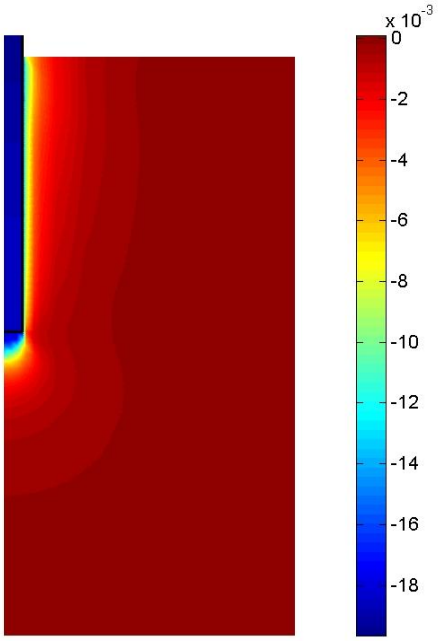

(b) Vertical Displacement Field (m)

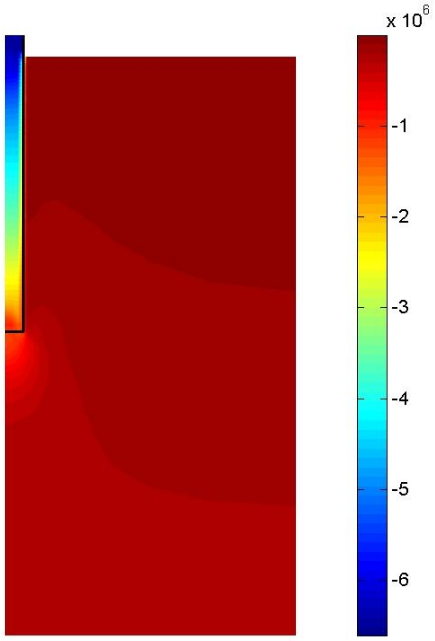

(c) Vertical Stress Field (Pa)

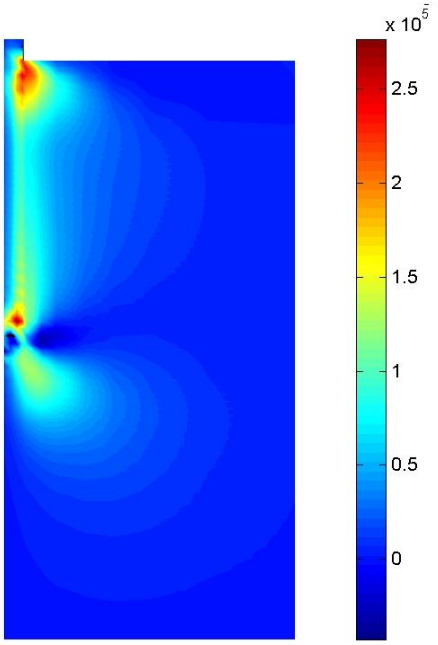

(d) Shear Stress Field (Pa)

Fig. 5.9. Displacement and Stress Fields at Peak of Last PLT Loop (Pier A1-19 Layered Profile)

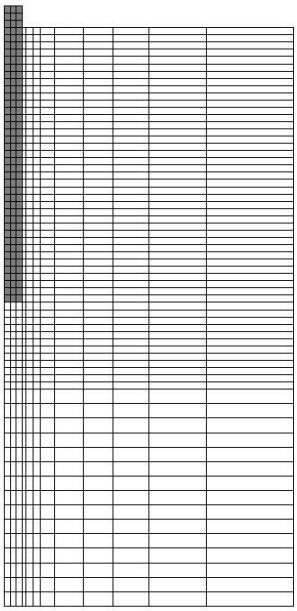

(a) FEM Mesh

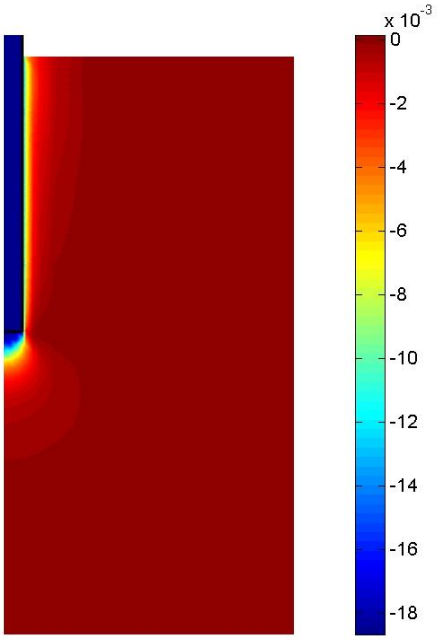

(b) Vertical Displacement Field (m)

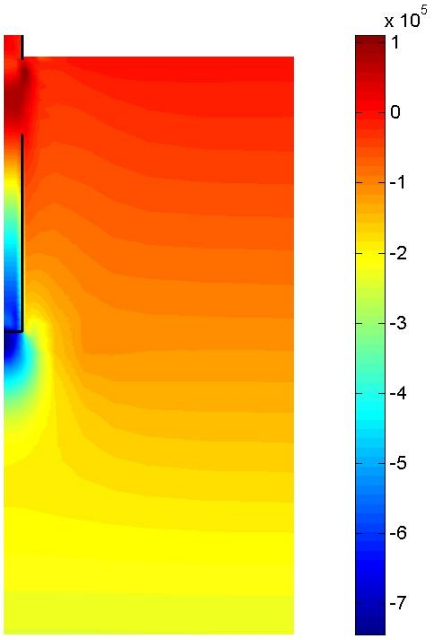

(c) Vertical Stress Field (Pa)

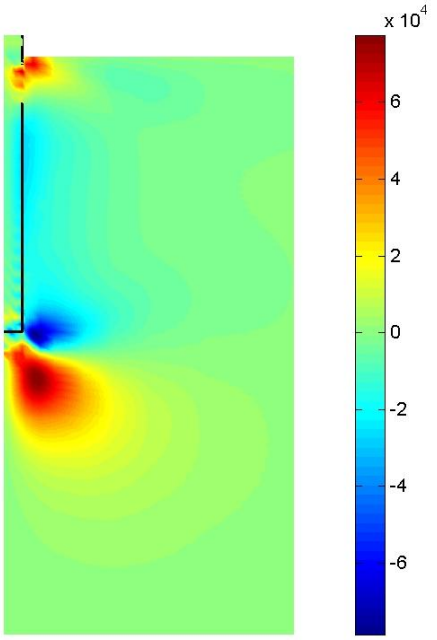

(d) Shear Stress Field (Pa)

Fig. 5.10. Residual Displacements and Stress Fields after Last PLT Loop (Pier A1-19 Layered Profile)

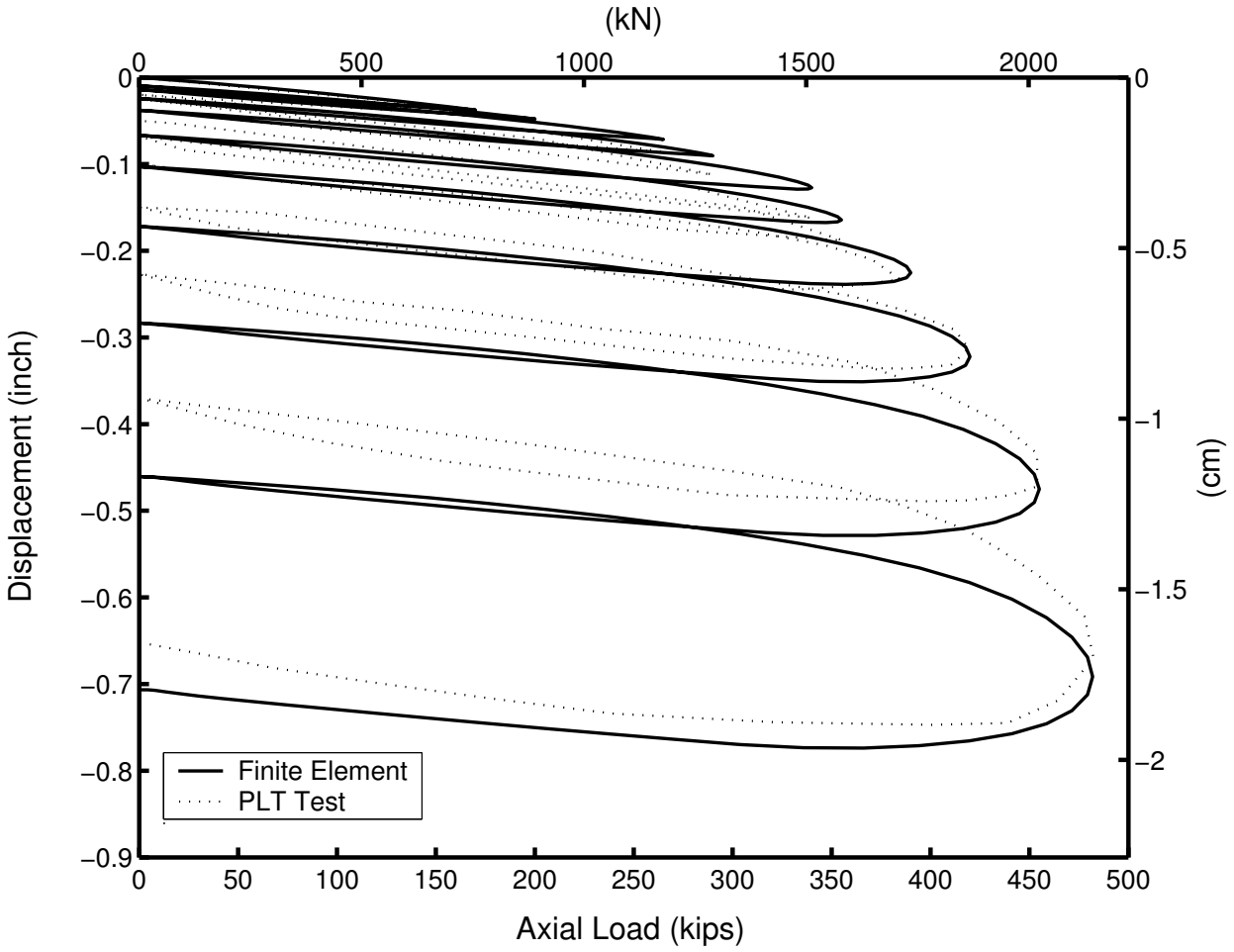

Fig. 5.11 Simulation of Pier A1-20A under Cyclic Loading

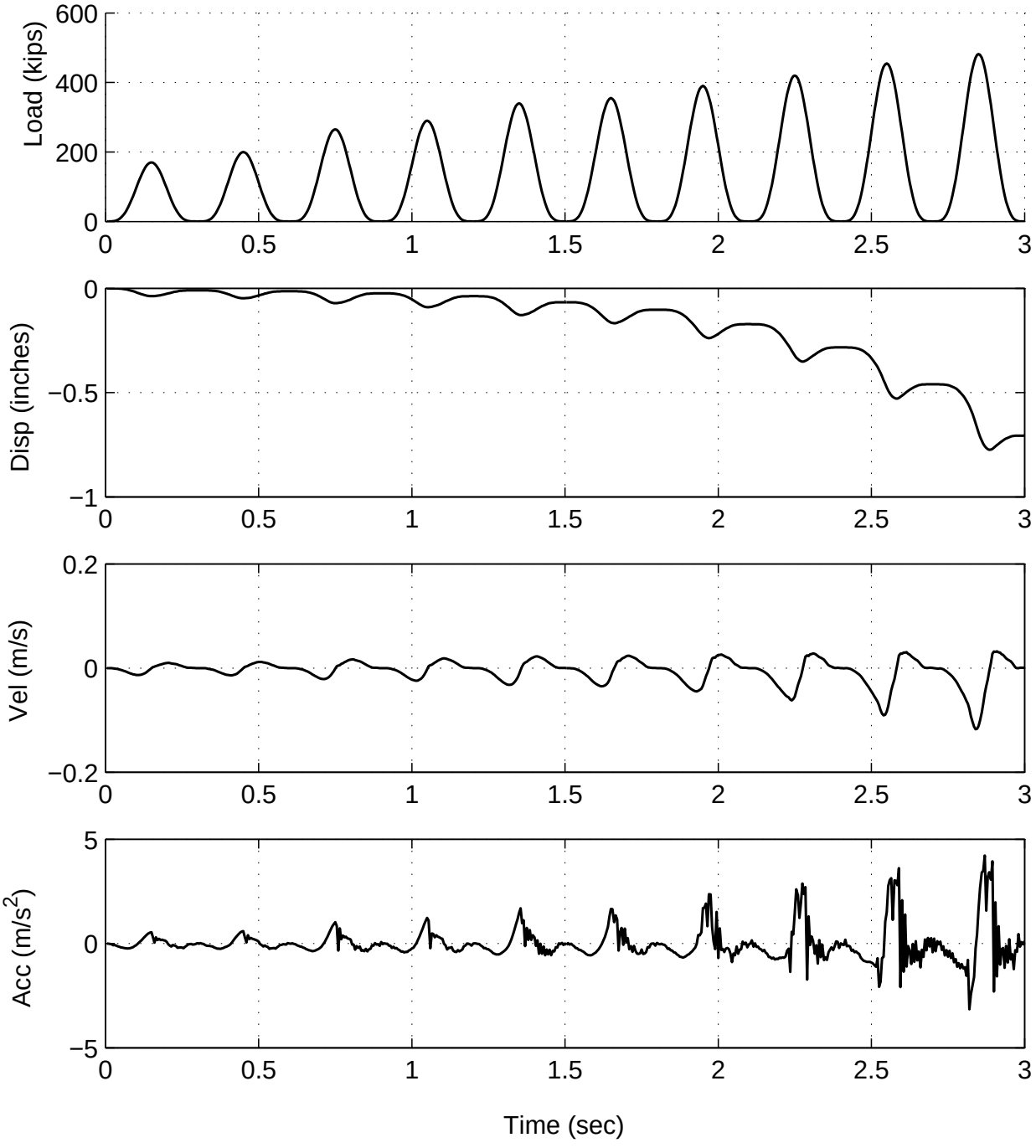

Fig. 5.12 Computed Top Node Reaction (Pier A1-20A, Homogeneous Profile)

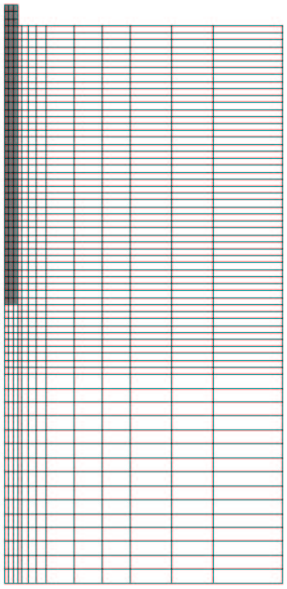

(a) FEM Mesh

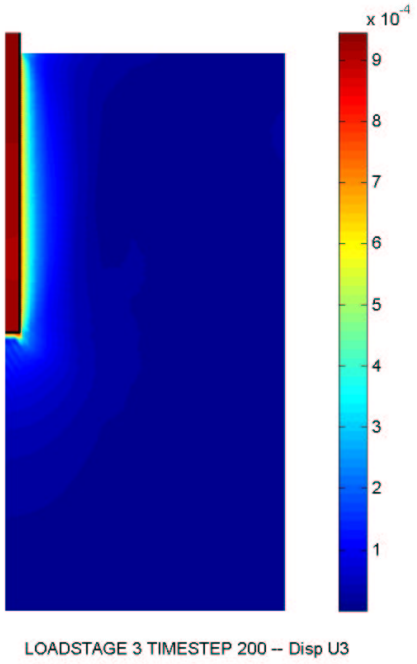

(b) Vertical Displacement Field (m)

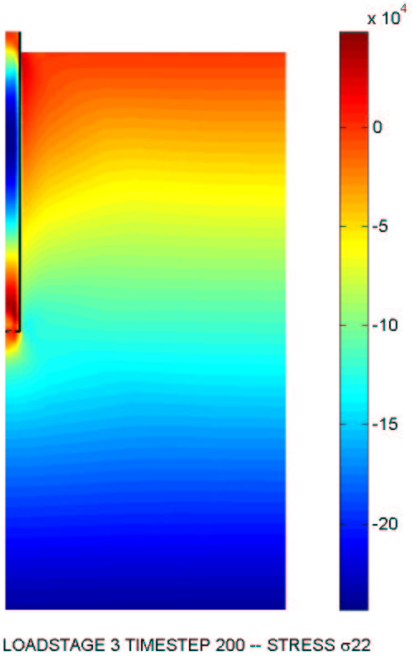

(c) Vertical Stress Field (Pa)

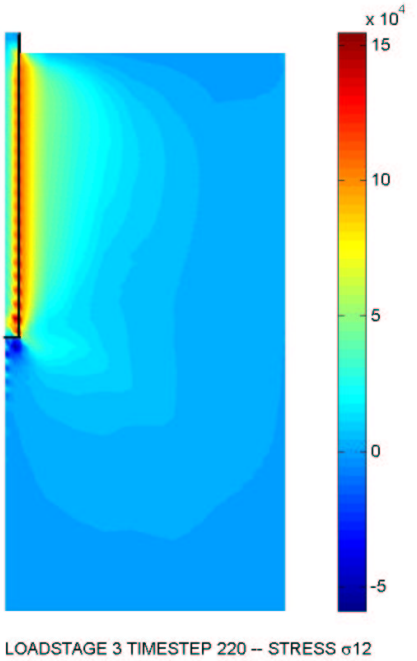

(d) Shear Stress Field (Pa)

Fig. 5.13. Residual Displacements and Stress Fields (Pier A1-20A, Homogeneous Profile)

residual displacement. The pier was then loaded again and the prediction was compared with the measured data. Fig. 5.14 presents the simulated pier head load displacement response using static soil properties in Table 5.1. The prediction closely matches the test data, except that the end bearing capacity is slightly underestimated. The compressive load in the pier can be integrated over Gaussian points, as shown in Fig. 5.15, in which the spatial gradient of the load corresponds to the shear stress of the soil mobilized along the shaft. Due to the assumption of a homogeneous soil profile, the load transfer curve is straight with depth. The load displacement response can be more accurately captured using a layered soil strength profile. As shown in Fig. 5.16, we have obtained excellent prediction in terms of both total capacity and end bearing capacity. Correspondingly, the load transfer curve in Fig. 5.17 appears more realistic.

Fig. 5.18 provides details of displacement and stress fields at the peak load point, where the observation is very similar to what was presented before. The deformed mesh (magnified by a factor of 10) is also illustrated. It is worth mentioning that although the displacement gradient is highly concentrated close to the shaft, the maximum shear strain developed in these elements reaches only about 3%. So the small strain formulation of the constitutive model remains valid.

5.2.4 General Remarks

The results shown in the previous sections validate the numerical model and the material parameters for the dynamic and static soil-pier interaction analysis. The model was also used to perform a series of parametric studies on the influence of different parameters. An extended parametric study is not presented here for brevity, but a number of general remarks are worth enumerating:

In general, the strain dependent modulus reduction scheme of the soil is very critical to the successful prediction of system stiffness. Here different schemes were used for static and dynamic tests, respectively, to address the effect of loading rate explicitly. In general, the loading rate effect can not be fully attributed to linear viscosity. Also it is very difficult to separate the exact amount of viscosity contribution from the test data. In fact, the viscous

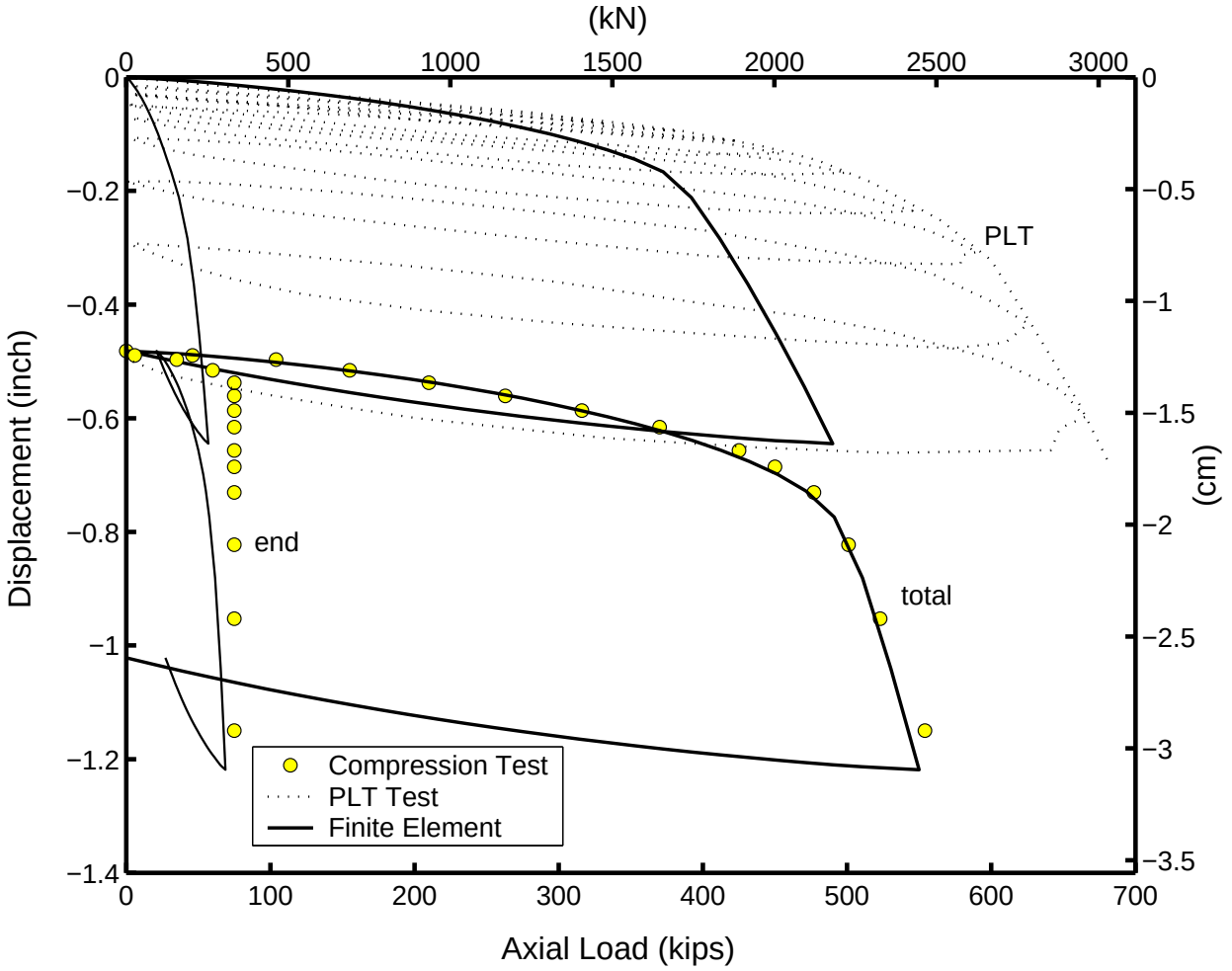

Fig. 5.14. Simulated Pier Head Displacement under Static Compression (Pier A1-19, Homogeneous Profile)

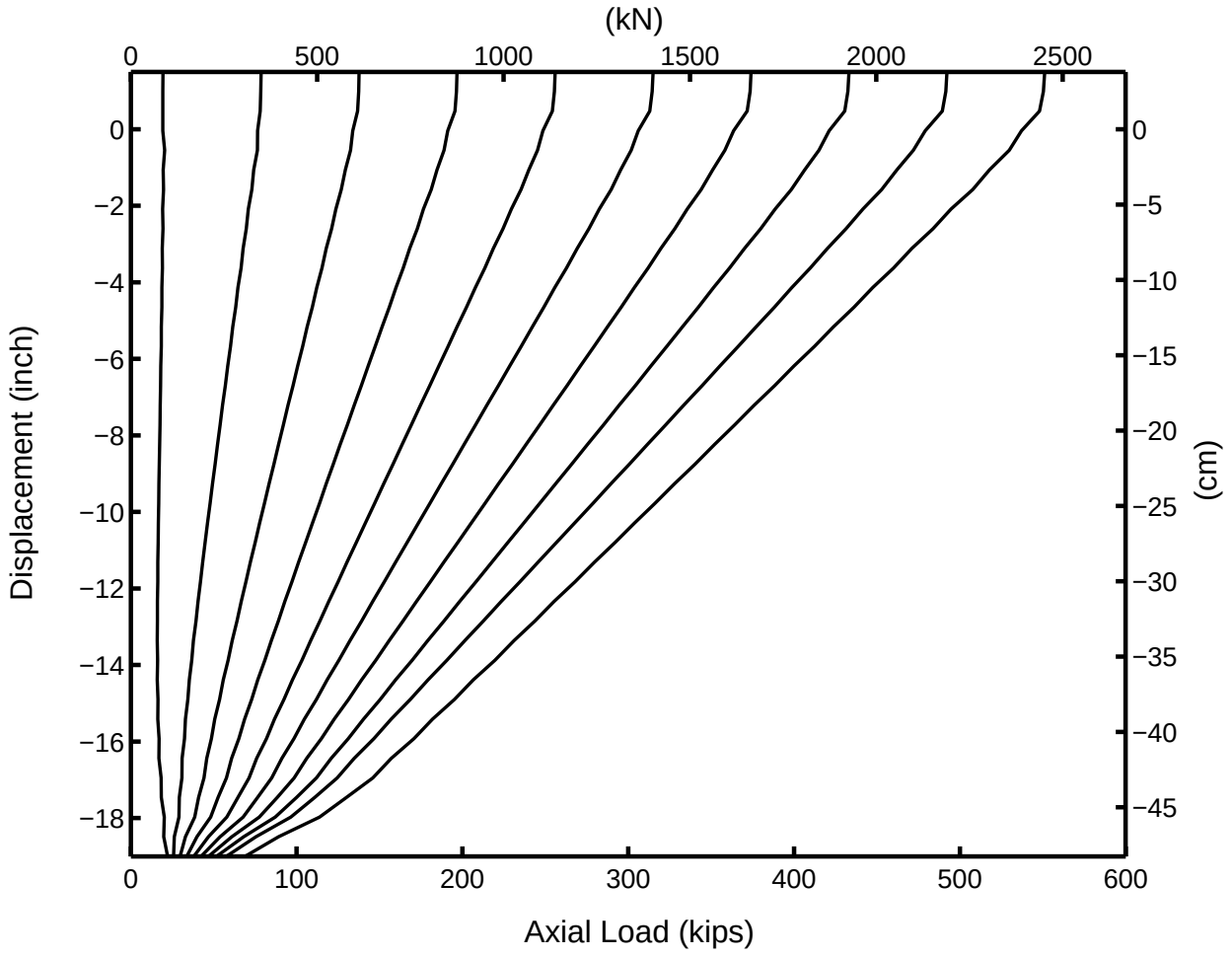

Fig. 5.15. Load Transfer under Static Compression (Pier A1-19, Homogeneous Profile)

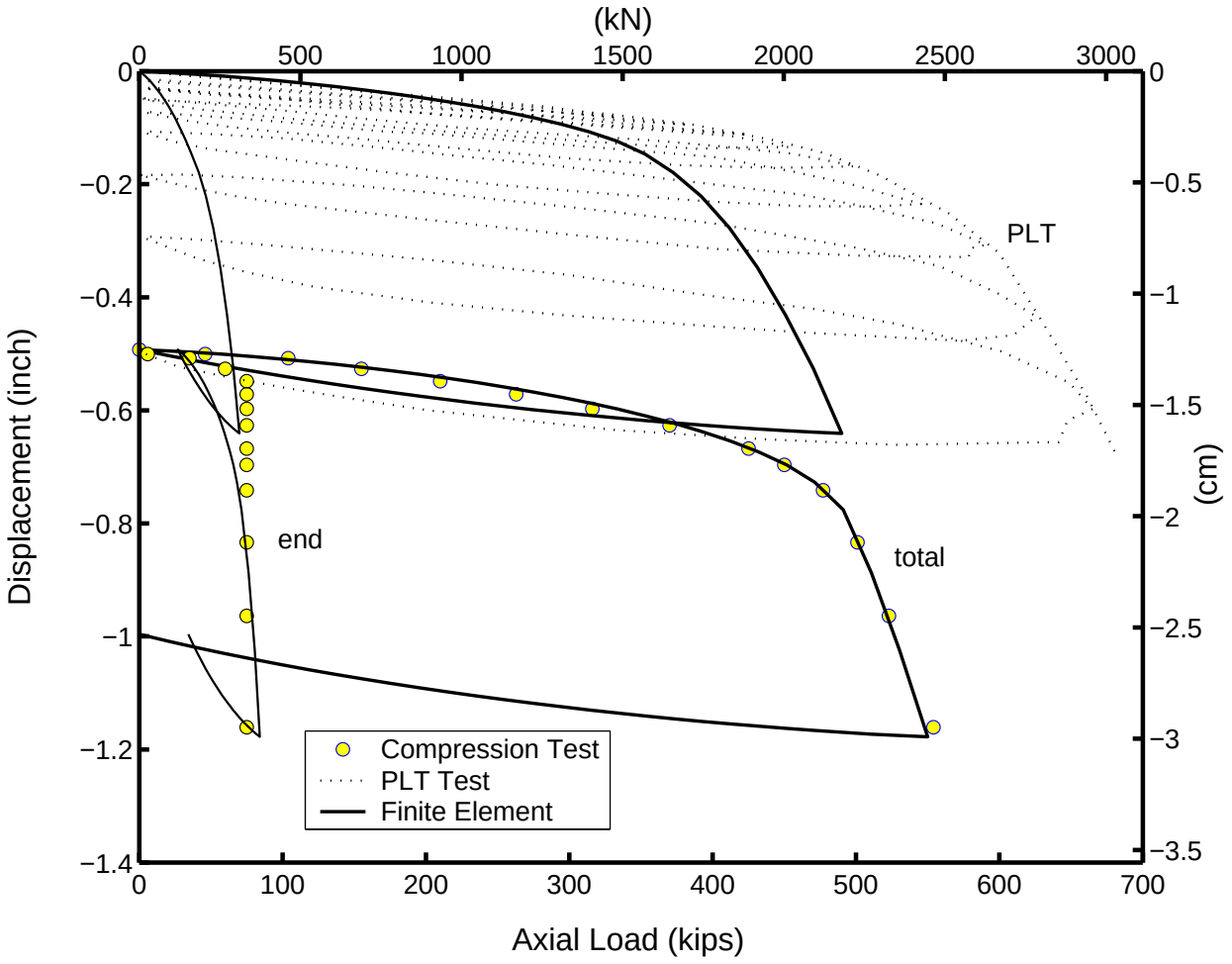

Fig. 5.16. Simulated Pier Head Displacement under Static Compression (Pier A1-19, Layered Profile)

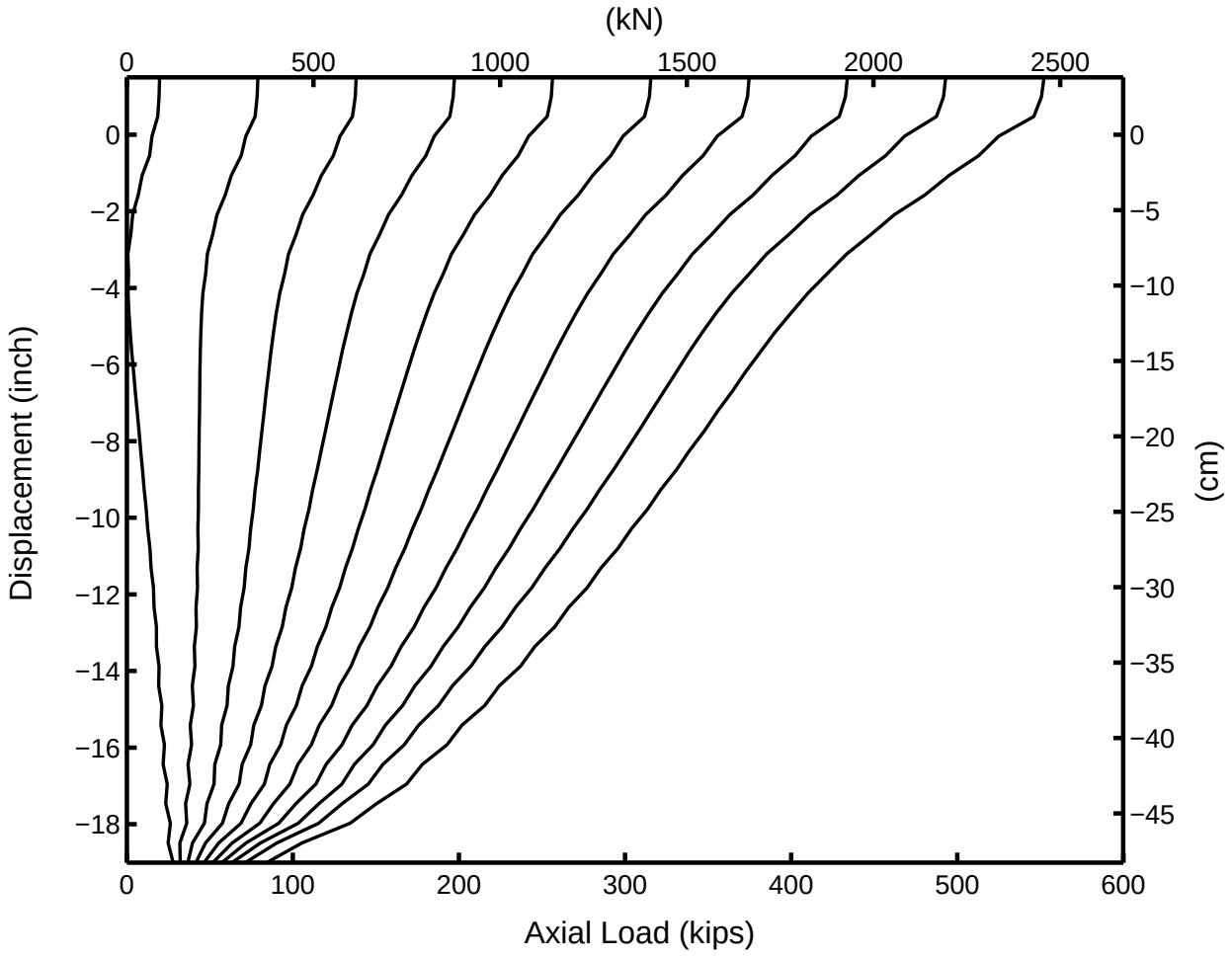

Fig. 5.17. Load Transfer under Static Compression (Pier A1-19, Layered Profile)

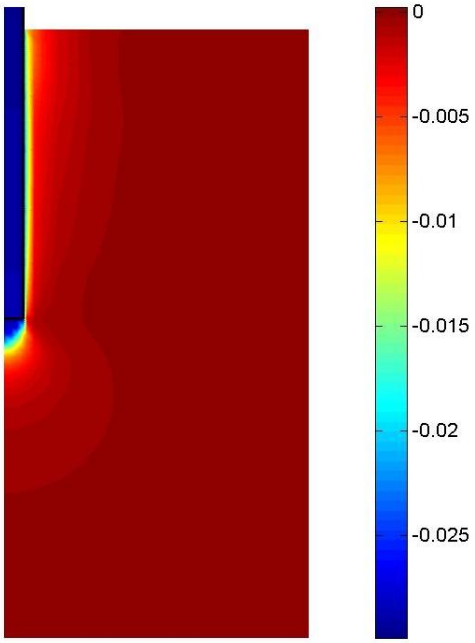

(a) Vertical Displacement Field (m)

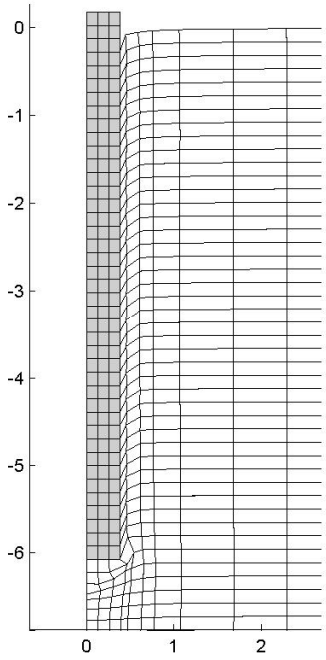

(b) Deformed Mesh (× 10, in m)

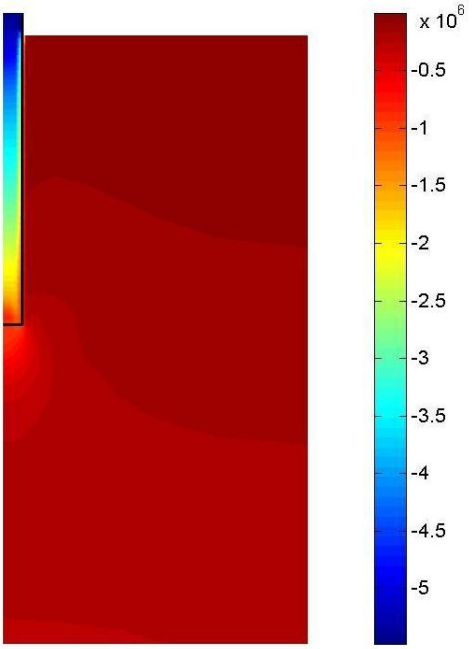

(c) Vertical Stress Field (Pa)

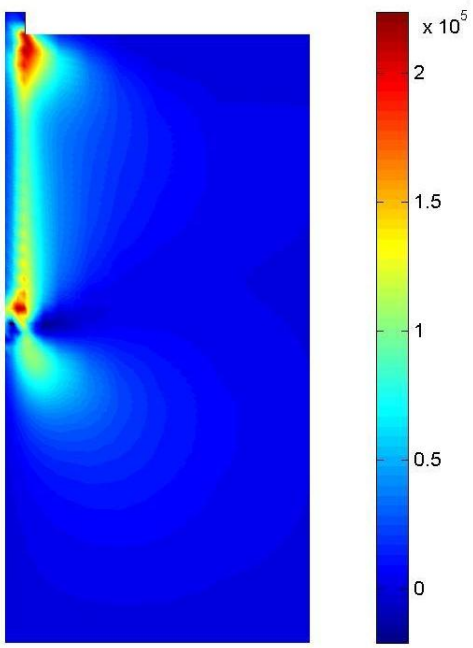

(d) Shear Stress Field (Pa)

Fig. 5.18. Displacement and Stress Fields at Peak Static Load (Pier A1-19, Layered Profile)

damping coefficient used in the dynamic analysis is very small, and is mainly used to control the solution at high strain levels.

The dynamic and static capacity of the system are primarily controlled by the static and dynamic undrained shear strength of the soil. For the cast-in-place piers which we have analyzed, no soil strength reduction is warranted for the prediction. Since local yielding has occurred at the large strain levels, the response is very sensitive to a number of parameters. Given that the analysis is essentially load controlled, slight reduction in the soil strength as well as viscous damping will lead to a larger residual displacement for each loop, leading to an apparent lower dynamic strength envelope.

Changing the time step does not significantly change the pier head response. However, smaller time steps can capture more high-frequency content of the applied force, enriching especially the high-frequency component of the acceleration. The time step 0.005 sec employed here is sufficient in view of the frequency range of the input motion and the size of the element. In the analysis, the applied force history assumed is a very smooth function of time, although, the actual pulse generated in the test is quite irregular and when it is taken into account, the high-frequency response can also be enriched.

The effectiveness of the finite element model can be directly measured by the convergence rate for each time step. Table 5.2 illustrates an example of the rate of convergence with respect to the L_2 norm of the displacement increment. The rate of convergence is found to be better than linear, but it is not quadratic. Ideally, the global Newton-Raphson iteration should provide a quadratic rate of convergence if a consistent algorithmic tangent is used (Simo and Taylor, 1985). However, because the constitutive soil model is highly nonlinear in nature (H' is in exponential form), the discrete algorithm cannot be linearized to provide a completely consistent algorithmic tangent. Instead, the trapezoidal rule used for constitutive integration is slightly strain-step dependent. It also must be mentioned that the lack of a quadratic convergence rate does not affect the accuracy of the solution. The accuracy depends only on the prescribed tolerance in the convergence test. The general performance of the model is robust and reasonably fast. For example, the total run time was approximately 12 minutes for a full analysis consisting of 789 elements and 540 time steps on a personal computer (Pentium IV 2G HZ CPU).

Table 5.2 An Example of Rate of Convergence

Iteration	Displacement Increment Norm
1	7.56×10^{-4}
2	1.83×10^{-4}
3	1.50×10^{-6}
4	1.61×10^{-8}
5	2.01×10^{-10}
6	2.19×10^{-11}

6 Conclusions and Recommendations

6.1 SUMMARY AND CONCLUSIONS

Prototype load tests on cast-in-place concrete piers were performed to examine dynamic and static responses of a soil-pier system under axial loading. In particular, loading rate effects and cyclic effects as well as characteristics of hysteretic energy dissipation have been systematically evaluated from the field data. For the test conducted herein, the dynamic capacity of the piers is 20% – 40% higher than the static resistance, and the dynamic stiffness is about twice as high as the static stiffness observed. The multiple PLT tests conducted on the same drilled pier also indicate that a shaft might experience significant stiffness and strength degradation when subjected to full load reversal.

The successful application of the test program to the Resident Units project indicates that results from static and PLT can be effectively used to assess the axial response of drilled piers under gravity and seismic loads, and the test suggests lower foundation deflections under seismic loads compared to that under static loads. So use of PLT data in performance-based design can lead to substantial savings in foundation costs. For the Resident Units project, Moore *et al.* (2003) reported that utilizing the design parameters derived from the test data resulted in between $400,000 and $600,000 savings in foundation costs over the $125,000 cost of the test program. Since the PLT test is fast and easy to perform, the test procedure is economical even for relatively small projects.

To simulate nonlinear dynamic and static soil-pier interaction, a numerical model was developed within the framework of the finite element method. The cyclic soil model is based on a 3D bounding surface plasticity theory, and it is enhanced from the original model proposed by Borja and Amies (1994). A fully nonlinear implicit algorithm has been

formulated in 3D stress space for numerical implementation. The model requires minimal parameters that can be easily calibrated through conventional field investigation.

Using this model, the load-displacement-capacity of a soil-pier system under static and dynamic axial loading was simulated and prototype pier load tests were analyzed. The numerical model reasonably captured system nonlinearity across the full range of applied loads. Overall, the model shows great promise for use in simulation of coupled soil-foundation-structure interaction problems in the time domain.

6.2 RECOMMENDATIONS AND FUTURE WORK

Soil-foundation-structure interaction is a highly complicated phenomenon, and the fundamental mechanism to this problem is still not well understood. Both physical modeling and numerical modeling of this problem should continue to be pursued in future work, and the following recommendations are made for improvement of this research.

Since the present field data are limited to the case of a stiff clay site and bored concrete piers under axial loading, additional field data for other site conditions, pile/pier types, configurations, and loading conditions are much needed. Other important influential factors, such as the effects of loading history and the soil-pier interface properties, should also be properly measured during field tests. It is our hope that systematic evaluation of such data can provide general guidelines for earthquake design of deep foundations, and can also improve reliability in numerical simulations.

Although the present bounding surface model can reasonably capture system nonlinearity, stiffness, and strength degradation due to full stress reversal is absent in constitutive formulation. This feature can be important for system prediction in the case of extreme loading conditions. A damage material model should be properly incorporated in current bounding surface theory to extend the model capacity.

Significant pore pressure buildup during earthquake excitation is often experienced, especially in liquefiable ground. However, the current numerical model is based on total stress analysis, and cannot predict pore pressure generation. The use of an effective stress model can overcome this problem and enhance the model capacity. A coupled formulation

of fluid-soil mixture is also necessary to model the fluid phase and soil phase simultaneously during earthquake excitations. Moreover, large deformations associated with liquefaction can not be accurately modeled using current small strain formulation. Geometric nonlinearity and frame invariance should be properly reflected in a finite deformation version of bounding surface model.

Full three-dimensionality of the current model capacity should be further explored by coupled simulation of the soil-pier-structure system under multi-directional shaking. Large-scale field tests, shaking table tests, or centrifuge tests for this case are ultimately needed to calibrate the model solution in both time and frequency domains. Parametric studies on model parameters against experimental data need to be performed to identify key components governing system response. Moreover, a systematic way to determine model parameters is highly desirable. Due to the relative simplicity of the model, sensitivity and reliability analyses should also be performed using an advanced statistical finite element technique.

REFERENCES

Amir, JM. and M. Sokolov (1976). Finite element analysis of piles in expansive soils. *ASCE J. Soil Mech. Fnd. Div.* $\mathbf{102}$, 701–720.

Anandarajah, A., H. Rashidi, and K. Arulanandan (1995). Elasto-plastic finite element analyses of a soil-structure system under earthquake excitations. *Computers and Geotechnics* $\mathbf{17}$, 301–325.

API (1984). *Recommended Practice for Planning, Designing and Constructing Fixed Offshore Platforms – Working Stress Design* (15 ed.). American Petroleum Institute.

API (2002). *Recommended Practice for Planning, Designing and Constructing Fixed Offshore Platforms – Working Stress Design* (21 ed.). American Petroleum Institute.

Armero, F. and E. Petocz (1998). Formulation and analysis of conserving algorithms for frictionless dynamic contact/impact problems. *Comp. Meth. Appl. Mech. Eng.* $\mathbf{158}$, 269–300.

Armero, F. and E. Petocz (1999). A new dissipative time-stepping algorithm for frictional contact problems: Formulation and analysis,. *Comp. Meth. Appl. Mech. Eng.* $\mathbf{179}$, 151–178.

Audibert, J.M.E. and A.R. Dover (1982). Discussion of $pile\ load\ tests\ -\ cyclic\ loads\ and\ varying\ load\ rates$ by kraft et. al. *ASCE J. Geotech. Eng. Div. 108*(3), 501–505.

Basu, U. and A.K. Chopra (2003). Perfectly matched layers for time-harmonic elastodynamics of unbounded domains: Theory and finite-element implementation. *Comput. Methods Appl. Mech. Engrg.* $\mathbf{192}$, 1337–1375.

Basu, U. and A.K. Chopra (2004). Perfectly matched layers for transient elastodynamics of unbounded domains. *Int. J. Numer. Meth. Engng.* $\mathbf{59}$, 1039–1074.

Bea, R.G. (1980). Dynamic response of piles in offshore platforms. In M.W. O'Neill & R. Dobry (Ed.), *Special technical publication on dynamic response of pile foundations: analytical aspects*, pp. 80–109. New York: ASCE.

Bea, R.G. (1992). Pile capacity for axial cyclic loading. *ASCE J. Geotech. Eng. 118*(1), 34–50.

Bea, R.G., J.M.E. Audibert, and A.R. Dover (1980). Dynamic response of laterally and axially loaded piles. In *Proc. 12th Offshore Technology Conference*, OTC 3749, pp. 129–139. Houston, TX.

Bea, R.G. and E.H. Doyle (1975). Parametrs affecting axial capacity of piles in clay. In *Proc. 7th Offshore Technology Conference*, OTC 2307, pp. 611–623. Houston, TX.

Bea, R.G., R.W. Litton, S. Nour-Omid, and J.Y. Chang (1984). A specialized design and research tool for the modeling near-field pile-soil interactions. In *Proc. 16th Offshore Technology Conference*, OTC 4806, pp. 249–262. Houston, TX.

Bentley, K.J. and M.H. El Naggar (2000). Numerical analysis of kinematic response of single piles. *Can. Geotech. J.* **37**, 1368–1382.

Borja, R.I. (1988). Dynamics of pile driving by the finite elmenet method. *Computers and Geotechnics* **5**, 39–49.

Borja, R.I. and A.P. Amies (1994). Multiaxial cyclic plasticity model. *ASCE J. Geotech. Eng. 120*(6), 1051–1070.

Borja, R.I., H. Chao, F.J. Montans, and CH. Lin (1999a). Nonlinear ground response at Lotung LSST site. *ASCE J. Geotech. and Geoenviron. Enrg. 125*(3), 187–197.

Borja, R.I., H. Chao, F.J. Montans, and CH. Lin (1999b). SSI effects on ground motion at Lotung LSST site. *ASCE J. Geotech. and Geoenviron. Enrg. 125*(9), 760–770.

Borja, R.I., C. Lin, and F. J. Montans (2001). Cam-clay plasiticity, part IV: implicit integration of anisotropic bounding surface model with nonlinear hyperelasticity and ellipsoidal loading function. *Comput. Methods Appl. Mech. Engrg.* **190**, 3293–3323.

Borja, R.I., C.H. Lin, K.M. Sama, and G.M. Masada (2000). Modelling non-linear ground response of non-liquefiable soils. *Earthquake Engng Struct. Dyn.* **29**, 63–83.

Borja, R.I. and W-H. Wu (1994). Vibration of foundation on incompressible soils with no elastic region. *ASCE J. Geotech. Eng. 120*(9), 1570–1592.

Bouckovalas, G. (1996). Evaluation of cyclic model tests on anchor piles in clay. *Soils and Foundations 36*(4), 57–70.

Boulanger, R.W., C.J. Curras, B.L. Kutter, D.W. Wilson, and A.Abghari (1999). Seismic soil-pile-structure interaction experiments and analysis. *ASCE J. Geotech. and Geoenviron. Enrg. 125*(9), 750–759.

Boulon, M. and R. Nova (1990). Modelling of soil-structure interface behavior, a comparison between elastoplastic and rate type laws. *Computers and Geotechnics* **9**, 21–46.

Briaud, J.L. (1986). Pressuremeter and foundation design. In *Use of in situ Tesing in Geotechnical Engineering*. ASCE Speciality Conference: Blacksburg, VA.

Briaud, J.L. and G.Y. Fellio (1986). Cyclic axial loads on piles: Analysis of existing data. *Can. Geotech. J.* **23**, 362–371.

Briaud, J.L. and L.M. Tucker (1984). Piles in sand: a method including residual stresses. *ASCE J. Geotech. Engrg 110*(11), 1666–1680.

Briaud, J.L. and L.M. Tucker (1988). Measured and predicted axial response of 98 piles. *ASCE J. Geotech. Eng.* **114**, 984–1001.

Burland, J.B. (1969). Contribution to discussion on comparision of full-scale performance with in situ and laboratory measurements. In *Brithish Geotechnical Society Conference on In-Situ Investigations of Soils and Rock*, pp. 61. London, England.

Burland, J.B. and R.W. Cooke (1974, July). The design of bored piles in stiff clays. *Ground Engineering 7*(4).

Bustamante, M. and L. Gianeselli (1982). Prevision de la capacite portante des pieux par la methode pressiometrique. Laboratoire Central des Ponts et Chaussees (in French).

Bustamante, M. and L. Gianeselli (1983). Prevision de la capacite portante des pieux par la methode penetrometrique. *Compte Rendu de Recherche F.A.E.R.1.05.02.2*, Laboratoire Central des Ponts et Chaussees (in French).

Cai, Y.X., P.L. Gould, and C.S. Desai (2000). Nonlinear analysis of 3d seismic interaction of soil-pile-structure system and application. *Engng. Struct. 22*(2), 191–199.

Chan, K.S., P. Karasudhi, and S.L. Lee (1974). Force at a point in the interior of layered elastic half-space. *Int. J. Solids Struct.* $\mathbf{10}$, 1179–1199.

Cheung, Y.K. and P.K.K. Lee (1991). Elastoplastic analysis of soil-pile interaction. *Computers and Geotechnics*, 115–132.

Chin, J.T., , Y.K. Chow, and H.G. Poulos (1990). Numerically analysis of axially loaded vertical piles and pile groups. *Computers and Geotechnics* $\mathbf{9}$, 273–290.

Chin, J.T. and H.G. Poulos (1991). Axially loaded vertical piles and pile groups in layered soil. *Int. J. Numer. Anal. Meth. Geomech. 15*(7), 497–511.

Chow, Y.K. (1986). Analysis of vertically loaded pile groups. *Int. J. Numer. Anal. Meth. Geomech. 10*(1), 59–72.

Clisby, B.M. (1978). An evaluation of pile bearing capacities. Report to the mississippi state highway department, Civil Engineering, Mississippi State Univeristy.

Clough, G.W. and J.M. Duncan (1971). Finite element analyses of retaining wall behavior. *ASCE J. Soil Mech. Fnd. Div. 97*(12), 1657–1673.

Coyle, H.M. and R. Castello (1981). New design correlations for piles in sand. *ASCE J. Geotech. Eng. Div. 107*(GT7), 965–986.

Coyle, H.M. and G.C. Gibson (1970). Empirical damping constants for sands and clays. *ASCE J. Soil Mech. Fnd. Div. 96*(3), 949–965.

Dafalias, Y.F. and L.R. Herrmann (1986). Bounding surface plasticity. ii. application to isotropic cohesive soils. *ASCE Journal of Engineering Mechnics* $\mathbf{112}$, 1263–1291.

Dafalias, Y.F. and E.P. Popov (1977). Cyclic loading for materials with a vanishing elastic region. *Nuclear Engrg. and Des.* $\mathbf{41}$, 293–302.

Dash, B.K. and P.J. Pise (2003). Effect of compressive load on uplift capacity of model piles. *ASCE J. Geotech. and Geoenviron. Enrg. 129*(11), 987–992.

Datta, M., S.K. Gulhati, and G.V. Rao (1980). An appraisal of the existing practice of determining the axial load capacity of deep penetration piles in calcareous sands. In *Proc. 12th Offshore Technology Conference*, OTC 3867, pp. 119–130. Houston, TX.

Davies, T.G. and P.K. Banerjee (1978). The displacement filed due to a point load at the interface of a two layer elastic half-space. *ASCE J. Geotech. Eng. Div. 28*(1), 43–56.

Davis, A.G. and S.A. Robertson (1976). Vibration testing of piles. *Struct. Eng. 54*(6), A7–A10.

de Mello, V.F.B. (1969). Foundations of buildings on clay. In *Proc. 7th Int. Conf. Soil Mech. and Fndn. Eng., States of the Art Report*, pp. 49–136. Mexico City.

De Ruiter, J. and F.L. Beringen (1979). Pile foundation for large north sea structures. *Marine Geotech. 3*(3).

Desai, C.S. (1974). Numerical design-analysis for piles in sands. *ASCE J. Geotech. Eng. Div. 100*(GT6), 613–635.

Desai, C.S and C. Shao (2000). Implementation of dsc model and application for analysis of field pile tests under cyclic loading. *Int. J. Numer. Anal. Meth. Geomech.* 24, 601–624.

Desai, C.S., G.W. Wathugalai, and H. Matlock (1993). Constitutive model for cyclic behavior of clays. II: Application. *ASCE J. Geotech. Eng. 119*(4), 730–748.

Desai, C.S., N.M. Zaman, J.G. Lightner, and H.J. Siriwardane (1984). Thin-layer element for interface and joints. *Int. J. Numer. Anal. Meth. Geomech.* 8, 19–43.

Drucker, D.C. and W. Prager (1952). Soil mechanics and plastic analysis or limit design. *Quat. Appl. Math.* 10, 157–165.

Dubose, L.A. (1955). Discussion of $the\ action\ of\ soft\ clay\ along\ friction\ piles$ by H.B. Seed and L.C. Reese. *Transactions of the American Society of Civil Engineers* 128, 755–757.

Duncan, J.M. and C.Y. Chang (1970). Nonlinear analysis of stress and strain in soils. *ASCE J. Soil Mech. Fnd. Div. 96*(SM5), 1629–1653.

El Naggar, M.H. (2004). The 2002 canadian geotechnical colloquium: The role of soil-pile interaction in foundation engineering. *Can. Geotech. J.* 41, 485–509.

El Naggar, M.H. and M. Novak (1994a). Non-linear axial interaction in pile dynamics. *ASCE J. Geotech. Eng. 120*(4), 678–696.

El Naggar, M.H. and M. Novak (1994b). Non-linear model for dynamic axial pile response. *ASCE J. Geotech. Eng. 120*(2), 308–329.

Elgamal, A., ZH. Yang, and E. Parra (2002). Computational modeling of cyclic mobility and post-liquefaction site response. *Soil Dyn. Earthq. Eng. 22*(4), 259–271.

Elgamal, A., ZH. Yang, E. Parra, and A. Ragheb (2003). Modeling of cyclic mobility in saturated cohesionless soils. *International Journal of Plasticity 19*(6), 883–905.

Ellison, R.D., E. D'Appolonia, and G.R. Thiers (1971). Load-deformation mechanism for bored piles. *ASCE J. Geotech. Eng. Div. 97*(4), 661–678.

Fahey, M. and J.P. Carter (1993). A finite element study of the pressuremeter test in sand using non-linear elastic plastic model. *Can. Geotech. J. 30*(2), 348–362.

Floess, C.H. (1979). *Direct Simple Shear Behavior of Fine Grained Soil Subjected to Repeated Loads*. Ph.D. thesis, Rensselaer Polytechnical Institute, Troy, NY.

Fox, E.N. (1948). The mean elastic settlement of a uniformly loaded area at a depth below ground surface. In *2nd International Conference on Soil Mechanics and Foundation Engineering*. London, England.

Fuller, F.M. and H.E. Hoy (1970). Pile load tests including quick-load test method, conventional methods, and interpretations. *Highway Research Record* (3), 74–86.

Gazetas, G. and R. Dobry (1984). Simple radiation damping model for piles and footings. *ASCE J. Engrg. Mech. 110*(6), 937–956.

Geordiadis, K., D.M. Potts, and L. Zdravkovic (2003). The influence of partial soil saturation on pile behaviour. *Géotechnique 53*(1), 11–25.

Ginzburg, L. (1973). Resistance of sandy clay during dynamic testing. *Soil Mechanics and Foundation Engineering* (1), 18–21.

Gomez, J.E., G.M. Filz, and R.M. Ebeling (2003). Extended hyperbolic model for sand-to-concrete interfaces. *ASCE J. Geotech. and Geoenviron. Enrg. 129*(11), 993–1000.

Goncharov, B.V. (1966). Soil resistance when jacking piles. *Soil Mechanics and Foundation Engineering* (4), 255–257.

Goodman, R.E., R.L. Taylor, and T.L. Brekke (1968). A model for the mechanics of jointed rock. *ASCE J. Soil Mech. Fnd. Div.* $\mathrm{SM3}$, 637–659.

Grosch, J.J. and L.C. Reese (1980). Field tests of small-scale pile segments in a soft clay deposit under repeated axial loading. In *Proc. 12th Offshore Technology Conference*, OTC 3869, pp. 143–151. Houston, TX.

Guo, W.D. (2000a). Vertically loaded single piles in gibson soil. *ASCE J. Geotech. and Geoenviron. Enrg. 126*(2), 189–193.

Guo, W.D. (2000b). Visco-elastic load transfer models for axially loaded piles. *Int. J. Numer. Anal. Meth. Geomech.* 24, 135–163.

Guo, W.D. and M.F. Randolph (1997). Vertically loaded piles in nonhomogeneous media. *Int. J. Numer. Anal. Meth. Geomech. 21*(8), 507–532.

Hardin, B.O. and V.P. Drnevich (1972). Shear modulus and damping in soils: Design equations and curves. *ASCE J. Soil Mech. Fnd. Div. 98*(7), 667–692.

Hsu, C.C. and M. Vucetic (2002, January). Dynamic and cyclic behavior of soils over a wide range of shear strains in ngi-type simple shear testing device. Technical Report No. ENG-02-228, University of California, Los Angeles.

Hu, L. and J. Pu (2004). Testing and modeling of soil-structure interface. *ASCE J. Geotech. and Geoenviron. Enrg. 130*(8), 851–860.

Hughes, T.J.R. (1987). *The Finite Element Method – Linear Static and Dynamic Finite Element Analysis* (1 ed.). Englewood Cliffs, New Jersey: Prentice-Hall.

Hunt, C.E., J.M. Pestana, J.D. Bray, and M. Riemer (2002). Effect of pile driving on static and dynamic properties of soft clay. *ASCE J. Geotech. and Geoenviron. Enrg. 128*(1), 13–24.

Hussein, M.H. and G.G. Goble (2004). A brief history of the application of stress-wave theory to piles. *Practices and Trends in Deep Foundations 142*(11), 186–201.

Idriss, I.M., R. Dobry, and R.D. Singh (1978). Nonlinear behavior of soft clays during cyclic loading. *ASCE J. Geotech. Eng. Div. 104*(GT12), 1427–1447.

Idriss, I.M. and J. Sun (1991). *User's manual for SHAKE91*. Center for Geotechnical Modeling, Dept. of Civil and Environ. Engrg., Univeristy of California, Davis.

Jones, R.E. and P. Papadopoulos (2001). A novel three-dimensional contact finite element based on smooth pressure interpolations. *Int. J. Num. Meth. Engrg.* **51**, 791–811.

Kaliakin, V.N. and Y.F. Dafalias (1989). Simplifications to the bounding surface model for cohesive soil. *Int. J. Numer. Anal. Meth. Geomech. 13*(1), 91–100.

Karabatakis, D.A. and T.N. Hatzigogos (2002). Analysis of creep behaviour using interface elements. *Computers and Geotechnics* **29**, 257–277.

Kasali, Gyimah (2002). Geotechnical investigation report for units 1 and 2 housing project. Technical Report to University of California, Berkeley No. 2001.022G, Rutherford & Chekene, Oakland, California.

Kishida, H. (1967). Ultimate bearing capacity of piles driven in loose sand. *Soil and Foundations 7*(3), 20–29.

Kondner, R.L. (1963). Hyperbolic stress-strain response: Cohesive soil. *ASCE J. Soil Mech. Fnd. Div. 189*(1), 115–143.

Kraft, L.M., W.R. Cox, and E.A. Verner (1981). Pile load tests - cyclic loads and varying load tests. *ASCE J. Geotech. Eng. Div. 107*(1), 1–19.

Kraft, L.M., J.A. Focht, and S.F. Amerasinghe (1981). Frictional capacity of piles driven into clays. *ASCE J. Geotech. Eng. Div.*.

Kraft, L.M., R.P. Ray, and T. Kagawa (1981). Theretical t-z curves. *ASCE J. Geotech. Eng. Div. 107*(GT11), 1543–1561.

Kuhlemeyer, R.L. (1979). Static and dynamic laterally loaded floating piles. *ASCE J. Geotech. Eng. Div. 105*(2), 289–304.

Laursen, T. A. and J. C. Simo (1993). A continuum-based finite element formulation for the implicit solution of multibody, large deformation frictional contact problems. *Int. J. Numer. Methods Eng.* **36**, 3451–3485.

Lee, C.J., M.D. Bolton, and A. Al-Tabbaa (2002). Numerical modelling of group effects on the distribution of dragloads in pile foundations. *Géotechnique 52*(5), 325–335.

Lee, C.Y. and H.G. Poulos (1990). Axial response analysis of piles in vertically and horizontally non-homogeneous soils. *Computers and Geotechnics* **9**, 133–148.

Lee, C.Y. and H.G. Poulos (1993). Cyclic analysis of axially loaded piles in calcareous soils. *Can. Geotech. J.* **30**, 82–93.

Lee, J.H. and R. Salgado (1999). Determination of pile base resistance in sands. *ASCE J. Geotech. and Geoenviron. Enrg. 125*(8), 673–683.

Likins, G. (2004). Pile testing – selection and economy of safety factors. *Practices and Trends in Deep Foundations, ASCE 142*(14), 239–252.

Litkouhi, S. and T.J. Poskitt (1980). Damping constants for pile driveability calculations. *Géotechnique 30*(1), 77–86.

Liyanapathirana, D.S., A.J. Deeks, and M.F. Randolph (2000). Numerical modelling of large deformations associated with driving of open-ended piles. *Int. J. Numer. Anal. Meth. Geomech.* **24**, 1079–1101.

Liyanapathirana, D.S., A.J. Deeks, and M.F. Randolph (2001). Numerical modelling of the driving response of thin-walled open-ended piles. *Int. J. Numer. Anal. Meth. Geomech.* **25**, 933–953.

LoPresti, D.C.F., M. Jamiolkowski, O. Pallara, and A. Cavallaro (1996). Rate and creep effect on the stiffness of soils. *ASCE Geotechnical Special Publication* (61), 166–180.

LoPresti, D.C.F., O. Pallara, R. Lancellotta, M. Armandi, and R. Maniscalco (1993). Monotonic and cyclic loading behavior of two sands at small strains. *ASTM Geotechnical Testing Journal 16*(4), 409–424.

Lysmer, J. and R.L. Kuhlemeyer (1969). Finite dynamic model for infinite media. *ASCE J. Engrg. Mech. Div. 95*(EM4), 859–877.

Mabsout, M.E., L.C. Reese, and J.L. Tassoulas (1995). Study of pile driving by finite-element method. *ASCE J. Geotech. Eng. Div. 121*(7), 535–543.

Mabsout, M. and S. Sadek (2003). A study of the effect of driving on pre-bored piles. *Int. J. Numer. Anal. Meth. Geomech.* **27**, 133–146.

Mabsout, M.E., S. Sadek, and T.E. Smayra (1999). Pile driving by numerical cavity expansion. *Int. J. Numer. Anal. Meth. Geomech.* **23**, 1121–1140.

Maheshwari, B.K., K.Z. Truman, P.L. Gould, and M.H. El Naggar (2005). Three-dimensional nonlinear seismic analysis of single piles using finite element: Effects of plasticity of soil. *ASCE International Journal of Geomechanics 5*(1), 35–44.

Maheshwari, B.K., K.Z. Truman, M.H. El Naggar, and P.L. Gould (2004). Three-dimensional nonlinear analysis for seismic soil-pile-structure interaction. *Soil Dyn. Earthquake Eng.* **24**, 343–356.

Matesic, L. and M. Vucetic (2003). Strain-rate effect on soil secant shear modulus at small cyclic strains. *ASCE J. Geotech. Eng. Div. 129*(6), 536–549.

Matlock, H. (1970). Correlations for design of laterally loaded piles in soft clay. In *Proc. 2nd Offshore Technology Conference*, OTC 1204, pp. 577–594. Houston.

Matlock, H. and D.V. Homquist (1976). A model study of axially loaded piles in soft clay. Technical report, Report to the American Petroleum Institute, The University of Texas, Austin.

McClelland, B. (1974). Design of deep penetration piles for ocean structures. *ASCE J. Geotech. Eng. Div. 100*(GT7), 705–747.

Meyerhof, G.G. (1959). Compaction of sands and bearing capacity of piles. *ASCE J. Soil Mech. Fnd. Div. 85*(SM6), 1–29.

Meyerhof, G.G. (1976). Bearing capacity and settlement of pile foundations. *ASCE J. Geotech. Eng. Div. 102*(GT3), 195–228. The Eleventh Terzaghi Lecture.

Michaelides, O., G. Gazeas, G. Bouckovalas, and E. Chrysikou (1997). Approximate non-linear dynamic axial response of piles. *Géotechnique 48*(1), 33–53.

Middendorp, P., P. Berminghammer, and B. Kuiper (1992). Statnamic load testing of foundation piles. In *4th International Conference of Applications of Stress-wave Theory to Piles*, pp. 581–588. The Hague, The Netherlands.

Mindlin, R.D. (1936). Force at a point in the interior of a semi-infinite solid. *Physics* **7**, 195–202.

Mitchell, J.K. (1976). *Fundamentals of Soil Behavior* (1st ed.). New York: Wiley.

Mohamedzein, YE-A., M.G. Mohamed, and A.E. El Sharief (1999). Finite element analysis of short piles in expansive soils. *Computers and Geotechnics*, 231–243.

Montans, F.J. (2000a). Bounding surface plasticity model with extended masing behavior. *Comput. Methods Appl. Mech. Engrg.* **182**, 125–162.

Montans, F.J. (2000b). Implicit algorithms for multilayer J_2 plasticity. *Comput. Methods Appl. Mech. Engrg.* **189**, 673–700.

Montans, F.J. (2001). Implicit multilayer J_2-plasticity using prager's translation rule. *Int. J. Numer. Meth. Engng* **50**, 347–375.

Montans, F.J. (2004). Implicit plane stress algorithm for multilayer J_2-plasticity using the prager-ziegler translation rule. *Int. J. Numer. Meth. Engng 59*(3), 409–418.

Montans, F.J. and R.I. Borja (2002). Implicit J_2-bounding surface plasticity using prager's translation rule. *Int. J. Numer. Meth. Engng* **55**, 1129–1166.

Moore, K.S., C.D. Comartin, G. Kasali, and W.A. Lopez (2003). The benefits of physical testing: Two case studies at the University of California, Berkeley. SEAONC (Structural Engineers Association of Northern California) Convention, Lake Tahoe, California.

Mosher, R.L. and W.P. Dawkins (2000). Theoretical manual for pile foundations. Final Report ERDC/ITL TR-00-5, US Army Corps of Engineers, Engineering Research and Development Center, Washington DC.

Mostafa, Y.E. and M.H. El Naggar (2002). Dynamic analysis of laterally loaded pile groups in sand and clay. *Can. Geotech. J.* **39**, 1358–1383.

Mroz, Z., V.A. Norris, and O.C. Zienkiewicz (1979). Application of an anisotropic hardening model in the analysis of elastoplastic deformation of soils. *Géotechnique 29*(1), 1–34.

MSHD (1972). *Soil Design Manual*. Mississippi State Highway Department.

Murff, J.D. (1980). Pile capacity in a softening soil. *Int. J. Numer. Anal. Meth. Geomech. 4*(2), 185–189.

Mylonakis, G. (2001). Winkler modulus for axially loaded piles. *Géotechnique 51*(5), 455–461.

Novak, M. and H. Mitwally (1988). Tranmitting boundary for axisymmetrical dilation problems. *ASCE J. Engrg. Mech. Div. 114*(1), 181–187.

Novak, M., T. Nogami, and F. Aboul-Ella (1978). Dynamic soil reactions for plane strain case. *ASCE J. Engrg. Mech. Div. 104*(4), 953–959.

Novak, M. and M. Sheta (1980). Approximate approach to contact effects of piles. In M.W. O'Neill & R. Dobry (Ed.), *Special technical publication on dynamic response of pile foundations: analytical aspects*, pp. 53–79. New York: ASCE.

Oden, J. T. and E. B. Pires (1983). Nonlocal and nonlinear friction laws and variational principles for contact problems in elasticity. *J. Appl. Mech.* **50**, 67–76.

O'Neill, M. and J. Murchison (1983). An evaluation of p-y relationships in sands. Technical Report GT-DF02-83, Dept. of Civil Eng., Univeristy of Houston.

OpenSees (2005). Open system for earthquake engineering simulation. University of California, Berkeley. http://opensees.berkeley.edu.

Ottaviani, M. (1975). Three-dimensional finite element analysis of vertically loaded pile groups. *Géotechnique 25*(2), 159–174.

Papadopoulos, P. and R.L. Taylor (1992). A mixed formulation for the finite element solution of contact problems. *Comp. Meth. Appl. Mech. Eng.* **94**, 373–389.

Papadopoulos, P. and R.L. Taylor (1993). A simple algorithm for three-dimensional finite element analysis of contact problems. *Comp. Struct.* **46**, 1107–1118.

Peck, R.B., W.E. Hanson, and T.H. Thornburn (1974). *Foundation Engineering* (2nd ed.). New York, N.Y.: John Wiley & Sons.

Pestana, J.M., C.E. Hunt, and J.D. Bray (2002). Soil deformation and excess pore pressure field around a closed-end pile. *ASCE J. Geotech. and Geoenviron. Enrg. 128*(1), 1–12.

Potts, D.M. and L. Zdravkovic (1999). *Finite Element Analysis in Geotechnical Engineering, Vol. 1: Theory*. Thomas Telford Publishing.

Potts, D.M. and L. Zdravkovic (2001). *Finite Element Analysis in Geotechnical Engineering, Vol. 2: Application*. Thomas Telford Publishing.

Poulos, H.G. (1968). Analysis of the settlement of pile groups. *Géotechnique 18*(4), 449–471.

Poulos, H.G. (1979). Settlement of single piles in non-homogeneous soil. *ASCE J. Geotech. Eng. Div. 105*(GT5), 627–641.

Poulos, H.G. (1981). Cyclic axial response of single piles. *ASCE J. Geotech. Eng. Div. 107*(GT1), 41–58.

Poulos, H.G. (1988). Cyclic stability diagram for aixally loaded piles. *ASCE J. Geotech. Eng. Div. 114*(8), 877–895.

Poulos, H.G. (1989). Pile behaviour – theory and application. *Géotechnique 39*(3), 365–415. 29th Rankine Lecture.

Poulos, H.G. and E.H. Davis (1980). *Pile Foundation Analysis and Design*. New York: John Wiley and Sons.

Prager, W. (1956). A new method of analyzing stresses and strains in work-hardening plastic solids. *ASME J. Appl. Mech* 78, 493–496.

Pressley, J.S. and H.G. Poulos (1986). Finite element analysis of mechanisms of pile group behavior. *Int. J. Numer. Anal. Meth. Geomech. 10*(2), 213–221.

Prevost, J.H. (1977). Mathematical modelling of monotonic and cyclic undrained clay behaviour. *Int. J. Numer. Anal. Meth. Geomech. 1*(2), 195–216.

Prevost, J.H. (1985). A simple plasticity theory for frictional cohesionless soils. *Soil Dyn. Earthquake Eng. 4*(1), 9–17.

Randolph, M.F., J.P. Carter, and C.P. Wroth (1979). Driven piles in clay – the effects of installation and subsequent consolidation. *Géotechnique 29*(4), 361–393.

Randolph, M.F. and A.J. Deeks (1992). Keynote lecture: Dynamic and static soil models for axial pile response. In Frans B.J. Barends (Ed.), *Proceedings of the 4th International Conference on the Application of Stress-wave Theory to Piles*, pp. 3–14. The Hague, the Netherlands.

Randolph, M.F. and B.S. Murphy (1985). Shaft capacity in driven piles in clay. In *Proc. 17th Offshore Technology Conference*, Number OTC 4883, pp. 371–378. Houston, TX.

Randolph, M.F. and C.P. Wroth (1978). Analysis of deformation of vertically loaded piles. *ASCE J. Geotech. Eng. Div. 104*(GT12), 1465–1488.

Rausche, F. (1970). *Soil response from dyanmic analysis and measurements on piles*. Ph.D. thesis, Divison of Solid Mechanics, Structures and Mechanical Design, Case Western Reserve University.

Rausche, F., G.G. Goble, and G.E. Likins (1985). Dynamic determination of pile capacity. *ASCE J. Geotech. Eng. Div. 111*(3), 367–383.

Rausche, F., F. Moses, and G.G. Goble (1972). Soil resistance predictions from pile dynamics. *ASCE J. Soil Mech. Fnd. Div. 98*(SM9), 917–937.

Reese, L., W. Cox, and F. Koop (1974). Analysis of laterally loaded piles in sand. In *Proc. 6th Offshore Technology Conference*, Volume 2, OTC 2080, pp. 473–483. Houston, TX.

Reese, L., W. Cox, and F. Koop (1975). Field testing and analysis of laterally loaded piles in stiff clays. In *Proc. 7th Offshore Technology Conference*, Volume 2, OTC 2312, pp. 671–690. Houston, TX.

Robinsky, E.I. and C.E. Morrison (1964). Sand displacement and compaction around model friction piles. *Can. Geotech. J. 1*(2), 81.

Rodriguez-Marek, A. (2000). *Near-fault seismic site response*. Ph.D. thesis, University of California, Berkeley.

Schellingerhout, A.J.G. and E. Revoort (1996). Pseudo static pile load tester. In Hussein Townsend and McVay (Eds.), *Proceedings of the 5th International Conference on the Application of Stresswave Theory to Piles*. Univeristy of Florida, Orlando FL.

Schmertmann, J.H. (1978). *Guidelines for Cone Penetration Test: Performance and Design* (FHWA-TS-209 ed.). Washington, D.C.: U.S. Department of Transportation, Federal Highway Administration.

Schnabel, P.B., J. Lysmer, and HB. Seed (1970). SHAKE– a computer program for earthquake response analysis of horizontally layered sites. Technical Report EERC No. 72-12, Earthquake Engineering Research Center, University of California, Berkeley.

Seed, H.B. and I.M. Idriss (1982). Ground motions and soil liquefaction during earthquakes. Technical report, Earthquake Engineering Research Institute, University of California, Berkeley.

Seed, H.B. and L.C. Reese (1955). The action of soft clay along friction piles. *Transactions of the American Society of Civil Engineers* 122, 731–754.

Seed, H.B., R.T. Wong, I.M. Idriss, and K. Tokimatsu (1984). Moduli and damping factors for dynamic analyses of cohesionless soils. Technical Report UCB/EERC-84/14, Earthquake Engineering Research Center, University of California, Berkeley.

Shahrour, I. and F. Rezaie (1997). An elastoplastic constitutive relation for the soil-structure interface under cyclic loading. *Computers and Geotechnics 21*(1), 21–39.

Shibuya, S., T. Mitachi, A. Hosomi, and S.C. Hwang (1996). Strain rate effects on stress-strain behaviour of clay as observed in monotonic and cyclic triaxial tests. *ASCE Geotechnical Special Publication* (61), 214–227.

Simo, J.C. and T.J.R. Hughes (1997). *Computational Inelasticity*. Interdisciplinary Applied Mathematics, Vol. 7. Springer.

Simo, J.C. and R.L. Taylor (1985). Consistent tangent operators for rate-independent elastoplasticity. *Comp. Meth. Appl. Mech. Eng.* 48, 101–108.

Smith, E.A.L. (1960). Pile-driving analysis by the wave equation. *ASCE J. Soil Mech. Fnd. Div. 86*(SM4), 35–61.

Stevens, J. and J. Audibert (1979). Re-examination of p-y curve formulations. In *Proc. 11th Offshore Technology Conference*, Volume 1, OTC 3402, pp. 397–403. Houston, TX.

Sun, J.I., R. Golesorkhi, and H.B. Seed (1988). Dynamic moduli and damping ratios for cohesive soils. Technical Report UCB/EERC-88/15, Earthquake Engineering Research Center, University of California, Berkeley.

Taylor, D.W. (1942). Reasearch on consolidation of clays. Technical Report 82, Department of Civil and Sanitary Engineering, Massachusetts Institute of Technology.

Taylor, R.L. (2002). *FEAP – A Finite Element Analysis Program, Version 7.4 User Manual*. Department of Civil and Environmental Engineering, University of California at Berkeley.

Terzaghi, K. (1943). *Theoretical Soil Mechanics*. New York: John Wiley and Sons.

Tham, L.G., C.K. Chu, and Z.X. Lei (1996). Analysis of the transient response of vertically loaded single piles by time-domain bem. *Computers and Geotechnics 19*(2), 117–136.

Timoshenko, S. and J.N. Goodier (1951). *Theory of Elasticity* (2nd ed.). McGraw-Hill Book Co., Inc.

Tomlinson, M.J. (1994). *Pile Design and Construction Practice* (Fourth ed.). E & FN SPON.

Trochanis, A.M., J. Bielak, and P.P. Christiano (1991). Three-dimensional nonlinear study of piles. *ASCE J. Geotech. Eng. 117*(3), 429–447.

Tumay, M.T. and M. Fakhroo (1981). Pile capacity in soft clays using electric QCPT data. In G.M. Norris and R.D. Holtz (Eds.), *Cone Penetration Testing and Experience Convention*, pp. 434–455. ASCE, St. Louis.

Vesic, A.S. (1961). Bending of beams resting on isotropic elastic solids. *ASCE J. Engrg. Mech. Div. 87*(2), 35–53.

Vucetic, M. (2004, March 18-19). Emerging trends in dynanic simple shear testing. In *International Workshop on Uncertainties in Nonlinear Soil Properties and their Impact on Modeling Dynamic Soil Response*. PEER Headquaters, University of California, Berkeley.

Vucetic, M. and R. Dobry (1991). Effect of soil plasticity on cyclic response. *ASCE J. Geotech. Eng. Div. 117*(1), 89–107.

Vucetic, M., G. Lanzo, and M. Doroudian (1998a). Damping at small strains in cyclic simple shear test. *ASCE J. Geotech. and Geoenviron. Enrg. 124*(7), 585–593.

Vucetic, M., G. Lanzo, and M. Doroudian (1998b). Effect of the shape of cyclic loading on damping ratio at small strains. *Soils and Found. 38*(1), 111–120.

Vucetic, M. and K. Tabata (2003). Influence of soil type on the effect of strain rate on small-strain cyclic shear modulus. *Soils and Foundation 43*(5), 161–173.

Wang, G. and N. Sitar (2004). Numerical analysis of piles in elasto-plastic soils under axial loading. In *Proc. 17th ASCE Engineering Mechanics Conference*. University of Delaware, Newark, DE.

Wang, S., B.L. Kutter, M.J. Chacko, D.W. Wilson, R.W. Boulanger, and A. Abghari (1998). Nonlinar seismic soil-pile structure interaction. *Earthquake Spectra 14*(2), 377–396.

Wathugala, G.W. and C.S. Desai (1993). Constitutive model for cyclic behavior of clays. I: Theory. *ASCE J. Geotech. Eng. 119*(4), 714–729.

Wu, A.K.H., R.L. Kuhlemeyer, and C.W.S. To (1989). Validity of smith model in pile driving analysis. *ASCE J. Geotech. Eng. 115*(9), 1285–1302.

Wu, G. and W.D.L. Finn (1997). Dynamic nonlinear analysis of pile foundations using finite element method in the time domain. *Can. Geotech. J.* **34**, 44–52.

Yang, Z. and B. Jeremic (2002). Numerical analysis of pile behavior under lateral loads in layered elasto-plastic soil. *Int. J. Numer. Anal. Geomech. 26*(14), 1385–1406.

Yang, Z. and B. Jeremic (2005). Study of soil layering effects on lateral loading behavior of piles. *ASCE J. Geotech. and Geoenviron. Enrg. 131*(6), 762–770.

Yong, R.N. and R.D. Japp (1969). Vibration effects of earthquakes on soils and foundations. *Stress-strain Behavior of Clays in Dynamic Compression, ASTM Special Technical Publication* (450), 233–262.

Zeghal, M. and T.B. Edil (2002). Soil structure interaction analysis: Modeling the interface. *Can. Geotech. J.* **39**, 620–628.

Zen, K., Y. Umehara, and K. Hamada (1978). Laboratory tests and in-situ seismic survey on vibratory shear modulus of clayey soils with various plaxticities. In *Proceedings, Fifth Japan Earthquake Engineering Symposium*, pp. 721–728. Tokyo, Japan.

Zienkiewicz, O.C., A.HC. Chan, M. Pastor, BA. Schrefler, and T. Shiomi (1999). *Computational Geomechanics with Special Reference to Earthquake Engineering*. John Wiley & Sons.

Zienkiewicz, O.C. and R.L. Taylor (2000). *Finite Element Method: volume 1, The Basic; volume 2: Solid Mechanics* (Fifth ed.). McGraw-Hill.

PEER REPORTS

PEER reports are available from the National Information Service for Earthquake Engineering (NISEE). To order PEER reports, please contact the Pacific Earthquake Engineering Research Center, 1301 South 46th Street, Richmond, California 94804-4698. Tel.: (510) 665-3405; Fax: (510) 665-3420.

PEER 2006/06 *Nonlinear Analysis of a Soil-Drilled Pier System under Static and Dynamic Axial Loading.* Gang Wang and Nicholas Sitar. November 2006.

PEER 2006/04 *Probabilistic Seismic Evaluation of Reinforced Concrete Structural Components and Systems.* Tae Hyung Lee and Khalid M. Mosalam. August 2006.

PEER 2006/02 *Pacific Earthquake Engineering Research Center Highway Demonstration Project.* Anne Kiremidjian, James Moore, Yue Yue Fan, Nesrin Basoz, Ozgur Yazali, and Meredith Williams. April 2006.

PEER 2006/01 *Bracing Berkeley. A Guide to Seismic Safety on the UC Berkeley Campus.* Mary C. Comerio, Stephen Tobriner, and Ariane Fehrenkamp. January 2006.

PEER 2005/16 *Seismic Response and Reliability of Electrical Substation Equipment and Systems.* Junho Song, Armen Der Kiureghian, and Jerome L. Sackman. April 2006.

PEER 2005/15 *CPT-Based Probabilistic Assessment of Seismic Soil Liquefaction Initiation.* R. E. S. Moss, R. B. Seed, R. E. Kayen, J. P. Stewart, and A. Der Kiureghian. April 2006.

PEER 2005/14 *Workshop on Modeling of Nonlinear Cyclic Load-Deformation Behavior of Shallow Foundations.* Bruce L. Kutter, Geoffrey Martin, Tara Hutchinson, Chad Harden, Sivapalan Gajan, and Justin Phalen. March 2006.

PEER 2005/13 *Stochastic Characterization and Decision Bases under Time-Dependent Aftershock Risk in Performance-Based Earthquake Engineering.* Gee Liek Yeo and C. Allin Cornell. July 2005.

PEER 2005/12 *PEER Testbed Study on a Laboratory Building: Exercising Seismic Performance Assessment.* Mary C. Comerio, editor. November 2005.

PEER 2005/11 *Van Nuys Hotel Building Testbed Report: Exercising Seismic Performance Assessment.* Helmut Krawinkler, editor. October 2005.

PEER 2005/10 *First NEES/E-Defense Workshop on Collapse Simulation of Reinforced Concrete Building Structures.* September 2005.

PEER 2005/09 *Test Applications of Advanced Seismic Assessment Guidelines.* Joe Maffei, Karl Telleen, Danya Mohr, William Holmes, and Yuki Nakayama. August 2006.

PEER 2005/08 *Damage Accumulation in Lightly Confined Reinforced Concrete Bridge Columns.* R. Tyler Ranf, Jared M. Nelson, Zach Price, Marc O. Eberhard, and John F. Stanton. April 2006.

PEER 2005/07 *Experimental and Analytical Studies on the Seismic Response of Freestanding and Anchored Laboratory Equipment.* Dimitrios Konstantinidis and Nicos Makris. January 2005.

PEER 2005/06 *Global Collapse of Frame Structures under Seismic Excitations*. Luis F. Ibarra and Helmut Krawinkler. September 2005.

PEER 2005//05 *Performance Characterization of Bench- and Shelf-Mounted Equipment.* Samit Ray Chaudhuri and Tara C. Hutchinson. May 2006.

PEER 2005/04 *Numerical Modeling of the Nonlinear Cyclic Response of Shallow Foundations.* Chad Harden, Tara Hutchinson, Geoffrey R. Martin, and Bruce L. Kutter. August 2005.

PEER 2005/03 *A Taxonomy of Building Components for Performance-Based Earthquake Engineering.* Keith A. Porter. September 2005.

PEER 2005/02 *Fragility Basis for California Highway Overpass Bridge Seismic Decision Making*. Kevin R. Mackie and Bozidar Stojadinovic. June 2005.

PEER 2005/01 *Empirical Characterization of Site Conditions on Strong Ground Motion.* Jonathan P. Stewart, Yoojoong Choi, and Robert W. Graves. June 2005.

PEER 2004/09 *Electrical Substation Equipment Interaction: Experimental Rigid Conductor Studies.* Christopher Stearns and André Filiatrault. February 2005.

PEER 2004/08 *Seismic Qualification and Fragility Testing of Line Break 550-kV Disconnect Switches.* Shakhzod M. Takhirov, Gregory L. Fenves, and Eric Fujisaki. January 2005.

PEER 2004/07 *Ground Motions for Earthquake Simulator Qualification of Electrical Substation Equipment.* Shakhzod M. Takhirov, Gregory L. Fenves, Eric Fujisaki, and Don Clyde. January 2005.

PEER 2004/06 *Performance-Based Regulation and Regulatory Regimes.* Peter J. May and Chris Koski. September 2004.

PEER 2004/05 *Performance-Based Seismic Design Concepts and Implementation: Proceedings of an International Workshop.* Peter Fajfar and Helmut Krawinkler, editors. September 2004.

PEER 2004/04 *Seismic Performance of an Instrumented Tilt-up Wall Building.* James C. Anderson and Vitelmo V. Bertero. July 2004.

PEER 2004/03 *Evaluation and Application of Concrete Tilt-up Assessment Methodologies.* Timothy Graf and James O. Malley. October 2004.

PEER 2004/02 *Analytical Investigations of New Methods for Reducing Residual Displacements of Reinforced Concrete Bridge Columns.* Junichi Sakai and Stephen A. Mahin. August 2004.

PEER 2004/01 *Seismic Performance of Masonry Buildings and Design Implications.* Kerri Anne Taeko Tokoro, James C. Anderson, and Vitelmo V. Bertero. February 2004.

PEER 2003/18 *Performance Models for Flexural Damage in Reinforced Concrete Columns.* Michael Berry and Marc Eberhard. August 2003.

PEER 2003/17 *Predicting Earthquake Damage in Older Reinforced Concrete Beam-Column Joints.* Catherine Pagni and Laura Lowes. October 2004.

PEER 2003/16 *Seismic Demands for Performance-Based Design of Bridges.* Kevin Mackie and Božidar Stojadinovic. August 2003.

PEER 2003/15 *Seismic Demands for Nondeteriorating Frame Structures and Their Dependence on Ground Motions.* Ricardo Antonio Medina and Helmut Krawinkler. May 2004.

PEER 2003/14 *Finite Element Reliability and Sensitivity Methods for Performance-Based Earthquake Engineering.* Terje Haukaas and Armen Der Kiureghian. April 2004.

PEER 2003/13 *Effects of Connection Hysteretic Degradation on the Seismic Behavior of Steel Moment-Resisting Frames.* Janise E. Rodgers and Stephen A. Mahin. March 2004.

PEER 2003/12 *Implementation Manual for the Seismic Protection of Laboratory Contents: Format and Case Studies.* William T. Holmes and Mary C. Comerio. October 2003.

PEER 2003/11 *Fifth U.S.-Japan Workshop on Performance-Based Earthquake Engineering Methodology for Reinforced Concrete Building Structures.* February 2004.

PEER 2003/10 *A Beam-Column Joint Model for Simulating the Earthquake Response of Reinforced Concrete Frames.* Laura N. Lowes, Nilanjan Mitra, and Arash Altoontash. February 2004.

PEER 2003/09 *Sequencing Repairs after an Earthquake: An Economic Approach.* Marco Casari and Simon J. Wilkie. April 2004.

PEER 2003/08 *A Technical Framework for Probability-Based Demand and Capacity Factor Design (DCFD) Seismic Formats*. Fatemeh Jalayer and C. Allin Cornell. November 2003.

PEER 2003/07 *Uncertainty Specification and Propagation for Loss Estimation Using FOSM Methods.* Jack W. Baker and C. Allin Cornell. September 2003.

PEER 2003/06 *Performance of Circular Reinforced Concrete Bridge Columns under Bidirectional Earthquake Loading*. Mahmoud M. Hachem, Stephen A. Mahin, and Jack P. Moehle. February 2003.

PEER 2003/05 *Response Assessment for Building-Specific Loss Estimation.* Eduardo Miranda and Shahram Taghavi. September 2003.

PEER 2003/04 *Experimental Assessment of Columns with Short Lap Splices Subjected to Cyclic Loads*. Murat Melek, John W. Wallace, and Joel Conte. April 2003.

PEER 2003/03 *Probabilistic Response Assessment for Building-Specific Loss Estimation.* Eduardo Miranda and Hesameddin Aslani. September 2003.

PEER 2003/02 *Software Framework for Collaborative Development of Nonlinear Dynamic Analysis Program.* Jun Peng and Kincho H. Law. September 2003.

PEER 2003/01 *Shake Table Tests and Analytical Studies on the Gravity Load Collapse of Reinforced Concrete Frames.* Kenneth John Elwood and Jack P. Moehle. November 2003.

PEER 2002/24 *Performance of Beam to Column Bridge Joints Subjected to a Large Velocity Pulse.* Natalie Gibson, André Filiatrault, and Scott A. Ashford. April 2002.

PEER 2002/23 *Effects of Large Velocity Pulses on Reinforced Concrete Bridge Columns.* Greg L. Orozco and Scott A. Ashford. April 2002.

PEER 2002/22 *Characterization of Large Velocity Pulses for Laboratory Testing.* Kenneth E. Cox and Scott A. Ashford. April 2002.

PEER 2002/21 *Fourth U.S.-Japan Workshop on Performance-Based Earthquake Engineering Methodology for Reinforced Concrete Building Structures*. December 2002.

PEER 2002/20 *Barriers to Adoption and Implementation of PBEE Innovations.* Peter J. May. August 2002.

PEER 2002/19 *Economic-Engineered Integrated Models for Earthquakes: Socioeconomic Impacts.* Peter Gordon, James E. Moore II, and Harry W. Richardson. July 2002.

PEER 2002/18 *Assessment of Reinforced Concrete Building Exterior Joints with Substandard Details.* Chris P. Pantelides, Jon Hansen, Justin Nadauld, and Lawrence D. Reaveley. May 2002.

PEER 2002/17 *Structural Characterization and Seismic Response Analysis of a Highway Overcrossing Equipped with Elastomeric Bearings and Fluid Dampers: A Case Study.* Nicos Makris and Jian Zhang. November 2002.

PEER 2002/16 *Estimation of Uncertainty in Geotechnical Properties for Performance-Based Earthquake Engineering.* Allen L. Jones, Steven L. Kramer, and Pedro Arduino. December 2002.

PEER 2002/15 *Seismic Behavior of Bridge Columns Subjected to Various Loading Patterns.* Asadollah Esmaeily-Gh. and Yan Xiao. December 2002.

PEER 2002/14 *Inelastic Seismic Response of Extended Pile Shaft Supported Bridge Structures.* T.C. Hutchinson, R.W. Boulanger, Y.H. Chai, and I.M. Idriss. December 2002.

PEER 2002/13 *Probabilistic Models and Fragility Estimates for Bridge Components and Systems.* Paolo Gardoni, Armen Der Kiureghian, and Khalid M. Mosalam. June 2002.

PEER 2002/12 *Effects of Fault Dip and Slip Rake on Near-Source Ground Motions: Why Chi-Chi Was a Relatively Mild M7.6 Earthquake.* Brad T. Aagaard, John F. Hall, and Thomas H. Heaton. December 2002.

PEER 2002/11 *Analytical and Experimental Study of Fiber-Reinforced Strip Isolators*. James M. Kelly and Shakhzod M. Takhirov. September 2002.

PEER 2002/10 *Centrifuge Modeling of Settlement and Lateral Spreading with Comparisons to Numerical Analyses***.** Sivapalan Gajan and Bruce L. Kutter. January 2003.

PEER 2002/09 *Documentation and Analysis of Field Case Histories of Seismic Compression during the 1994 Northridge, California, Earthquake.* Jonathan P. Stewart, Patrick M. Smith, Daniel H. Whang, and Jonathan D. Bray. October 2002.

PEER 2002/08 *Component Testing, Stability Analysis and Characterization of Buckling-Restrained Unbonded Braces™*. Cameron Black, Nicos Makris, and Ian Aiken. September 2002.

PEER 2002/07 *Seismic Performance of Pile-Wharf Connections.* Charles W. Roeder, Robert Graff, Jennifer Soderstrom, and Jun Han Yoo. December 2001.

PEER 2002/06 *The Use of Benefit-Cost Analysis for Evaluation of Performance-Based Earthquake Engineering Decisions*. Richard O. Zerbe and Anthony Falit-Baiamonte. September 2001.

PEER 2002/05 *Guidelines, Specifications, and Seismic Performance Characterization of Nonstructural Building Components and Equipment*. André Filiatrault, Constantin Christopoulos, and Christopher Stearns. September 2001.

PEER 2002/04 *Consortium of Organizations for Strong-Motion Observation Systems and the Pacific Earthquake Engineering Research Center Lifelines Program: Invited Workshop on Archiving and Web Dissemination of Geotechnical Data, 4–5 October 2001*. September 2002.

PEER 2002/03 *Investigation of Sensitivity of Building Loss Estimates to Major Uncertain Variables for the Van Nuys Testbed.* Keith A. Porter, James L. Beck, and Rustem V. Shaikhutdinov. August 2002.

PEER 2002/02 *The Third U.S.-Japan Workshop on Performance-Based Earthquake Engineering Methodology for Reinforced Concrete Building Structures*. July 2002.

PEER 2002/01 *Nonstructural Loss Estimation: The UC Berkeley Case Study.* Mary C. Comerio and John C. Stallmeyer. December 2001.

PEER 2001/16 *Statistics of SDF-System Estimate of Roof Displacement for Pushover Analysis of Buildings.* Anil K. Chopra, Rakesh K. Goel, and Chatpan Chintanapakdee. December 2001.

PEER 2001/15 *Damage to Bridges during the 2001 Nisqually Earthquake.* R. Tyler Ranf, Marc O. Eberhard, and Michael P. Berry. November 2001.

PEER 2001/14 *Rocking Response of Equipment Anchored to a Base Foundation.* Nicos Makris and Cameron J. Black. September 2001.

PEER 2001/13 *Modeling Soil Liquefaction Hazards for Performance-Based Earthquake Engineering.* Steven L. Kramer and Ahmed-W. Elgamal. February 2001.

PEER 2001/12 *Development of Geotechnical Capabilities in OpenSees.* Boris Jeremi . September 2001.

PEER 2001/11 *Analytical and Experimental Study of Fiber-Reinforced Elastomeric Isolators*. James M. Kelly and Shakhzod M. Takhirov. September 2001.

PEER 2001/10 *Amplification Factors for Spectral Acceleration in Active Regions.* Jonathan P. Stewart, Andrew H. Liu, Yoojoong Choi, and Mehmet B. Baturay. December 2001.

PEER 2001/09 *Ground Motion Evaluation Procedures for Performance-Based Design*. Jonathan P. Stewart, Shyh-Jeng Chiou, Jonathan D. Bray, Robert W. Graves, Paul G. Somerville, and Norman A. Abrahamson. September 2001.

PEER 2001/08 *Experimental and Computational Evaluation of Reinforced Concrete Bridge Beam-Column Connections for Seismic Performance*. Clay J. Naito, Jack P. Moehle, and Khalid M. Mosalam. November 2001.

PEER 2001/07 *The Rocking Spectrum and the Shortcomings of Design Guidelines*. Nicos Makris and Dimitrios Konstantinidis. August 2001.

PEER 2001/06 *Development of an Electrical Substation Equipment Performance Database for Evaluation of Equipment Fragilities*. Thalia Agnanos. April 1999.

PEER 2001/05 *Stiffness Analysis of Fiber-Reinforced Elastomeric Isolators.* Hsiang-Chuan Tsai and James M. Kelly. May 2001.

PEER 2001/04 *Organizational and Societal Considerations for Performance-Based Earthquake Engineering.* Peter J. May. April 2001.

PEER 2001/03 *A Modal Pushover Analysis Procedure to Estimate Seismic Demands for Buildings: Theory and Preliminary Evaluation.* Anil K. Chopra and Rakesh K. Goel. January 2001.

PEER 2001/02 *Seismic Response Analysis of Highway Overcrossings Including Soil-Structure Interaction.* Jian Zhang and Nicos Makris. March 2001.

PEER 2001/01 *Experimental Study of Large Seismic Steel Beam-to-Column Connections.* Egor P. Popov and Shakhzod M. Takhirov. November 2000.

PEER 2000/10 *The Second U.S.-Japan Workshop on Performance-Based Earthquake Engineering Methodology for Reinforced Concrete Building Structures.* March 2000.

PEER 2000/09 *Structural Engineering Reconnaissance of the August 17, 1999 Earthquake: Kocaeli (Izmit), Turkey*. Halil Sezen, Kenneth J. Elwood, Andrew S. Whittaker, Khalid Mosalam, John J. Wallace, and John F. Stanton. December 2000.

PEER 2000/08 *Behavior of Reinforced Concrete Bridge Columns Having Varying Aspect Ratios and Varying Lengths of Confinement.* Anthony J. Calderone, Dawn E. Lehman, and Jack P. Moehle. January 2001.

PEER 2000/07 *Cover-Plate and Flange-Plate Reinforced Steel Moment-Resisting Connections.* Taejin Kim, Andrew S. Whittaker, Amir S. Gilani, Vitelmo V. Bertero, and Shakhzod M. Takhirov. September 2000.

PEER 2000/06 *Seismic Evaluation and Analysis of 230-kV Disconnect Switches.* Amir S. J. Gilani, Andrew S. Whittaker, Gregory L. Fenves, Chun-Hao Chen, Henry Ho, and Eric Fujisaki. July 2000.

PEER 2000/05 *Performance-Based Evaluation of Exterior Reinforced Concrete Building Joints for Seismic Excitation.* Chandra Clyde, Chris P. Pantelides, and Lawrence D. Reaveley. July 2000.

PEER 2000/04 *An Evaluation of Seismic Energy Demand: An Attenuation Approach.* Chung-Che Chou and Chia-Ming Uang. July 1999.

PEER 2000/03 *Framing Earthquake Retrofitting Decisions: The Case of Hillside Homes in Los Angeles.* Detlof von Winterfeldt, Nels Roselund, and Alicia Kitsuse. March 2000.

PEER 2000/02 *U.S.-Japan Workshop on the Effects of Near-Field Earthquake Shaking.* Andrew Whittaker, ed. July 2000.

PEER 2000/01 *Further Studies on Seismic Interaction in Interconnected Electrical Substation Equipment.* Armen Der Kiureghian, Kee-Jeung Hong, and Jerome L. Sackman. November 1999.

PEER 1999/14 *Seismic Evaluation and Retrofit of 230-kV Porcelain Transformer Bushings*. Amir S. Gilani, Andrew S. Whittaker, Gregory L. Fenves, and Eric Fujisaki. December 1999.

PEER 1999/13 *Building Vulnerability Studies: Modeling and Evaluation of Tilt-up and Steel Reinforced Concrete Buildings.* John W. Wallace, Jonathan P. Stewart, and Andrew S. Whittaker, editors. December 1999.

PEER 1999/12 *Rehabilitation of Nonductile RC Frame Building Using Encasement Plates and Energy-Dissipating Devices.* Mehrdad Sasani, Vitelmo V. Bertero, James C. Anderson. December 1999.

PEER 1999/11 *Performance Evaluation Database for Concrete Bridge Components and Systems under Simulated Seismic Loads.* Yael D. Hose and Frieder Seible. November 1999.

PEER 1999/10 *U.S.-Japan Workshop on Performance-Based Earthquake Engineering Methodology for Reinforced Concrete Building Structures.* December 1999.

PEER 1999/09 *Performance Improvement of Long Period Building Structures Subjected to Severe Pulse-Type Ground Motions*. James C. Anderson, Vitelmo V. Bertero, and Raul Bertero. October 1999.

PEER 1999/08 *Envelopes for Seismic Response Vectors.* Charles Menun and Armen Der Kiureghian. July 1999.

PEER 1999/07 *Documentation of Strengths and Weaknesses of Current Computer Analysis Methods for Seismic Performance of Reinforced Concrete Members.* William F. Cofer. November 1999.

PEER 1999/06 *Rocking Response and Overturning of Anchored Equipment under Seismic Excitations.* Nicos Makris and Jian Zhang. November 1999.

PEER 1999/05 *Seismic Evaluation of 550 kV Porcelain Transformer Bushings.* Amir S. Gilani, Andrew S. Whittaker, Gregory L. Fenves, and Eric Fujisaki. October 1999.

PEER 1999/04 *Adoption and Enforcement of Earthquake Risk-Reduction Measures.* Peter J. May, Raymond J. Burby, T. Jens Feeley, and Robert Wood.

PEER 1999/03 *Task 3 Characterization of Site Response General Site Categories.* Adrian Rodriguez-Marek, Jonathan D. Bray, and Norman Abrahamson. February 1999.

PEER 1999/02 *Capacity-Demand-Diagram Methods for Estimating Seismic Deformation of Inelastic Structures: SDF Systems*. Anil K. Chopra and Rakesh Goel. April 1999.

PEER 1999/01 *Interaction in Interconnected Electrical Substation Equipment Subjected to Earthquake Ground Motions.* Armen Der Kiureghian, Jerome L. Sackman, and Kee-Jeung Hong. February 1999.

PEER 1998/08 *Behavior and Failure Analysis of a Multiple-Frame Highway Bridge in the 1994 Northridge Earthquake.* Gregory L. Fenves and Michael Ellery. December 1998.

PEER 1998/07 *Empirical Evaluation of Inertial Soil-Structure Interaction Effects.* Jonathan P. Stewart, Raymond B. Seed, and Gregory L. Fenves. November 1998.

PEER 1998/06 *Effect of Damping Mechanisms on the Response of Seismic Isolated Structures.* Nicos Makris and Shih-Po Chang. November 1998.

PEER 1998/05 *Rocking Response and Overturning of Equipment under Horizontal Pulse-Type Motions.* Nicos Makris and Yiannis Roussos. October 1998.

PEER 1998/04 *Pacific Earthquake Engineering Research Invitational Workshop Proceedings, May 14–15, 1998: Defining the Links between Planning, Policy Analysis, Economics and Earthquake Engineering.* Mary Comerio and Peter Gordon. September 1998.

PEER 1998/03 *Repair/Upgrade Procedures for Welded Beam to Column Connections.* James C. Anderson and Xiaojing Duan. May 1998.

PEER 1998/02 *Seismic Evaluation of 196 kV Porcelain Transformer Bushings.* Amir S. Gilani, Juan W. Chavez, Gregory L. Fenves, and Andrew S. Whittaker. May 1998.

PEER 1998/01 *Seismic Performance of Well-Confined Concrete Bridge Columns.* Dawn E. Lehman and Jack P. Moehle. December 2000.